ISBN 978-82-326-1976-4 (printed ver.)
ISBN 978-82-326-1977-1 (electronic ver.)
ISSN 1503-8181

NTNU
Norwegian University of
Science and Technology

Doctoral thesis

Kjetil Eik Haavik

Doctoral theses at NTNU, 2016:319

NTNU
Norges teknisk-naturvitenskapelige universitet
Thesis for the Degree of
Philosophiae Doctor
Faculty of Engineering Science and Technology
Department of Petroleum Engineering
and Applied Geophysics

NTNU

Doctoral theses at NTNU, 2016:319

Kjetil Eik Haavik

Source-Depth Diversity for Enhanced Marine Seismic Imaging

NTNU
Norwegian University of
Science and Technology

Kjetil Eik Haavik

Source-Depth Diversity for Enhanced Marine Seismic Imaging

Thesis for the Degree of Philosophiae Doctor

Trondheim, November 2016

Norwegian University of Science and Technology
Faculty of Engineering Science and Technology
Department of Petroleum Engineering and Applied Geophysics

NTNU
Norwegian University of
Science and Technology

NTNU
Norwegian University of Science and Technology

Thesis for the Degree of Philosophiae Doctor

Faculty of Engineering Science and Technology
Department of Petroleum Engineering and Applied Geophysics

ISBN 978-82-326-1976-4 (printed ver.)
ISBN 978-82-326-1977-1 (electronic ver.)
ISSN 1503-8181

IMT-report 2016:319

Doctoral theses at NTNU, 2016:319

Printed by NTNU Grafisk senter

Preface

This thesis is submitted to the Norwegian University of Science and Technology (NTNU) for partial fulfilment of the requirements for the degree of philosophiae doctor.

This doctoral work has been performed at the Department of Petroleum Engineering and Applied Geophysics, NTNU, Trondheim, with Professor Martin Landrø as supervisor.

The research was funded by Lundin Norway AS.

Acknowledgements

First of all, I would like to thank my supervisor, Prof. Martin Landrø, for many inspiring conversations, guidance and hospitality during this three year period. Martin has been a source of inspiration and motivation when needed.

Thanks to Dr. Vetle Vinje, Dr. Johan O. A. Robertsson and Dr. Børge Arntsen for serving on my thesis committee.

Thanks to Per Eivind Dhelie, Jan Erik Lie and Vidar Danielsen at Lundin Norway for being helpful with comments and data. I would like to acknowledge Lundin Norway for financial support that made this project possible.

I am grateful to the Norwegian Petroleum directorate for accommodating me with an office. Furthermore, I am grateful to the people at to the Norwegian Petroleum directorate for their hospitality during my year-and-a-half long period there.

Thanks to Mari, who has supported me during these years.

I want to thank my colleagues at IPT for scientific discussion and great fun on trips to various destinations in the world.

Contents

Chapter 1

Introduction

Broadband seismic data has become the new standard of seismic data used in geophysical prospecting. The main goal of the work performed during this PhD project has been to examine the potential of acquiring marine seismic data with variations in the source depth from shot to shot to further improve marine broadband seismic data. In conventional seismic data acquisition, the source has been kept at a constant depth. The source depth influence the frequency content of the resulting seismic data. There are at least two reasons for this: The first reason, independent of what kind of source that is used, is interference between the waves propagating directly downwards from the source and the waves propagating downwards after they have reflected from the air-water interface. This interference cause energy in some frequency bands to increase, while energy in other frequency bands will be reduced. At particular frequencies, there will be close to no energy. These frequencies are referred to as notch frequencies. Throughout this thesis, the waves that has been reflected from the air-water interface will be referred to as the ghost reflection. The reason for this is that it appears to come from a position above the air-water interface. The second reason why the source depth influence the frequency content of marine seismic data is because the nature of the most common source used in marine seismic: Which is the air gun. The air gun is based on generating an oscillating air bubble that expands rapidly and generates acoustic pressure. Air-gun arrays consisting of up to 40 air guns may be used as source. The frequency content of the acoustic energy will depend, among several parameters, on the pressure of the surrounding water. A bubble that is oscillating at a greater depth (having higher surrounding pressure) will produce a more high-frequency signal than a bubble that is oscillating at shallower depth.

The motivation for varying the source depths during marine seismic acquisition is that, in theory, it could yield a data set where the energy is distributed more evenly over all frequencies within the seismic bandwidth. No narrow frequency band will suffer from having less energy due to the source ghost.

In addition to acquiring seismic data with a broader bandwidth, modern seismic acquisition is often performed with more than one source used at the same time. This way, more data can be acquired in a given time window, yielding more cost-efficient seismic acquisition. Acquiring seismic data with simultaneous sources result in data where the wavefield from the different sources are overlapping in time. Separation of these wavefields must be carried out prior to conventional imaging.

This thesis is a collection of several independent papers organized in chapters. The remaining part of this Chapter consist of an introduction to some theory and concepts that are relevant as background for the work presented, a motivation for the work that has been performed and a brief summary of the publications that have been published or submitted to peer-reviewed journals.

1.1 Marine seismic acquisition

The goal of seismic data acquisition is to obtain information about the geology in subsurface. The most common marine seismic experiment is the towed streamer experiment (see Figure 1.1). This kind of seismic acquisition usually consists of one or more seismic sources that emit acoustic energy that propagate as waves from the source, and one or several cables with sensors distributed along them that measure acoustic wavefield generated by the source. These cables are referred to as streamers. The sources and the streamers are towed behind a seismic vessel. If one streamer is used, the experiment is referred to as 2D seismic acquisition, and if more than one streamer is used, it is referred to as 3D seismic acquisition. Conventionally, the sensors in the streamers have been hydrophones that measure the pressure variations in the water due to the acoustic wave. Nowadays, it is also becoming more common to use multi-component streamers that measure particle motion in addition to pressure. Other marine seismic acquisition strategies exist. Examples of this are ocean bottom seismic (OBS), where the recording devices are placed on the seafloor and vertical seismic profiling (VSP), where the receivers are positioned in well bores.

The seismic data must be processed in order to obtain images of the subsurface that resembles geological boundaries (referred to as imaging or migration) or rock parameters (referred to as inversion). In exploration geophysics, the goal is to obtain images and physical parameters of the subsurface so geologists can perform interpretation of the geology. The foundation for high-quality images and inversion results is related to quality of the raw seismic data.

1.2 Marine broadband seismic data

Marine broadband seismic acquisition shares the same experiment setup as conventional marine seismic acquisition, *e.g.*, sources in front of streamers. The main differences are in the ways the source arrays are designed, the type and geometry of the streamers used, and in the processing of the resulting data. As the name implies, broadband seismic provide data with a broader bandwidth than conventional seismic. The geology we want

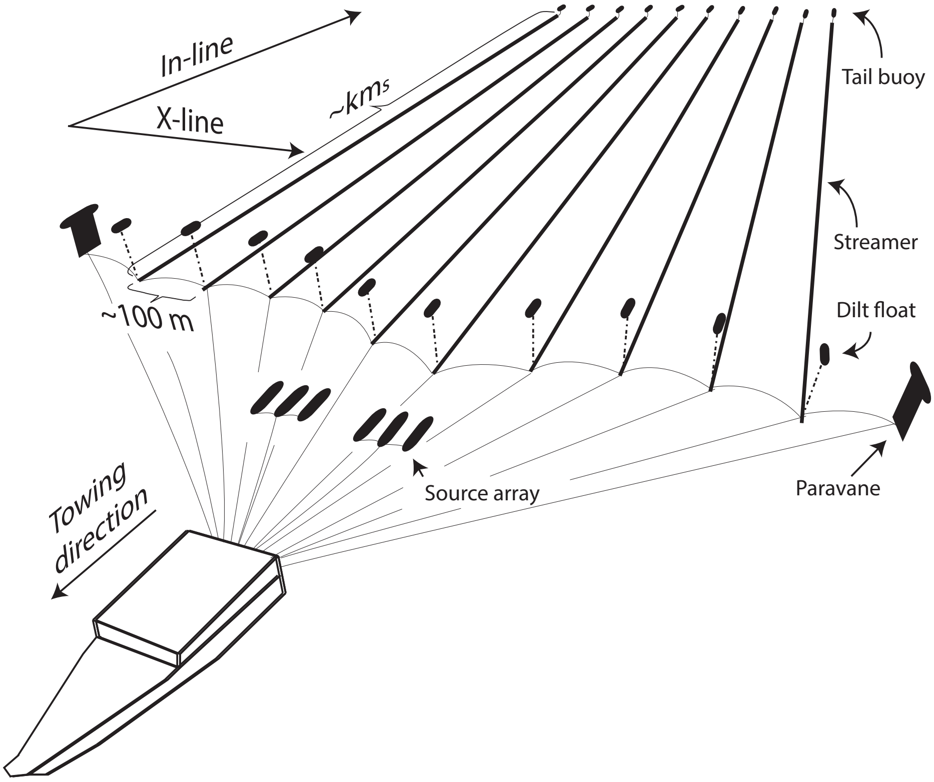

Figure 1.1: A sketch of towed-streamer marine 3D seismic acquisition. Two source arrays, each consisting of three sub arrays, are illustrated. The streamer can be up to 12 km long, and their depths typically range between 5 to 50 m. The distance between the sources and the first recording channel in the streamer is typically 50 to 200 m depending on the acquisition type. The paravanes to the sides are used to pull the streamers out to the sides.

to image have variations on all scales, all the way from molecular composition; to pores in sandstone; to large variations in rocks deposited over millions of years. By increasing the bandwidth in the seismic data, we obtain information about variations in the geology on more length scales. Ideally, we want to have an infinite bandwidth with equal distribution of energy with respect to frequency so that what we record is the impulse response of earth. For exploration seismic in a marine setting, a bandwidth from 2 to 200 Hz is considered very good. If we assume that this bandwidth is the "visible" bandwidth of seismic, an analogy to light can be made: A familiar concept in optics is how light refracts through a prism. If we use a white light beam, we are able too see the full spectrum of the light on the other side of the prism. However, if we use a coloured light beam, we are only be able to see this part of the spectrum on the other side of the prism. This is illustrated in Figure 1.2. If the bandwidth of the seismic data is limited, we will not be able to image the variations in geology on all the desired length scales.

In reflection seismic we can only obtain information about the scales corresponding to the bandwidth of the seismic source and the bandwidth that we may record. There are several factors in seismic acquisition that affect the total bandwidth:

- Total output from the source:
  - Bandwidth of air-gun array
  - Array directivity
  - Source ghost
- The recording equipment:
  - Instrument response
  - Receiver grouping
  - Receiver ghost
- The signal-to-noise ratio

The two first bullet points in the list above, without going into details, are to a certain degree known in seismic acquisition. To correct for and/or reduce the impact of these factors is probably the biggest difference between old seismic and modern broadband seismic acquisition and processing. Measures can be done in acquisition, and type of acquisition equipment, to reduce the impact of the ghost reflections. Processing must be performed to remove its effect on the data. The signal-to-noise ratio (S/N) is a measure

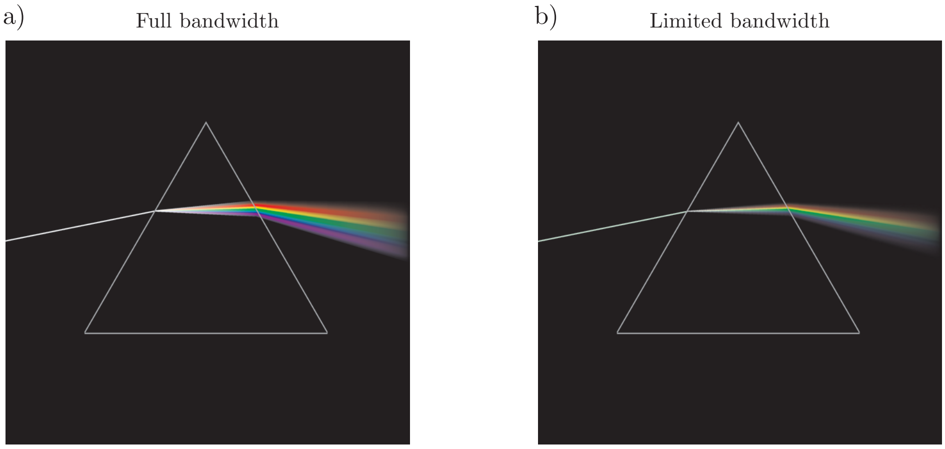

Figure 1.2: a) How white light refracts in a prism. b) How colored light refracts in a prism.

of the relative amount of signal compared to noise in the data. The S/N is frequency dependent, and a high S/N is desired over the full bandwidth. If no noise is present, it would be straight forward to remove the effect of all the factors limiting the bandwidth within the bandwidth of the source. However, noise is always present during seismic acquisition, and the S/N is the key parameter in determining whether or not it is reasonable to correct for the different factors in a given frequency band.

The motivation for acquiring data with a broader bandwidth can be seen in the following example: A photograph of small scale structural geology (modified from Fossen and Gabrielsen, 2005) is used as a geological model. Reflection coefficients are based on the relative color difference vertically in the photograph. For each lateral position, a reflection series is calculated:

$$R_i = \frac{I_{i+1} - I_i}{I_{i+1} + I_i}, \tag{1.1}$$

where R_i is the reflectivity at depth i, and I_i is a value based on the intensity of the color in the photograph, and can be thought of as the acoustic impedance (product of the velocity and the density of the medium) at depth i. The velocity is assumed constant (2000 m/s, 1m = 1 ms) for simplicity. Synthetic seismic sections, or reflection images, are generated by convolving the reflectivity series with bandpass filters. The geological model and the reflection images for three different frequency bands are shown in Figure 1.3. Figure 1.3b shows a reflection image where a bandpass filter with corner frequencies 10-15-45-55 Hz is used, this image provides high resolution, and most of the boundaries seen in Figure 1.3a is visible. Figure 1.3c shows an image where a bandpass filter with corner frequencies 2-3-10-15 Hz is used, here the resolution is not as good as in Figure 1.3b, and most of the thin layers are not resolved. However, the large scale differences are clearer defined, compared to Figure 1.3b. Figure 1.3c shows an image where a bandpass filter with corner frequencies 2-3-45-55 Hz is used. Here, we observe that the resolution is even better than in Figure 1.3b, and it is easier to distinguish the boundaries between geology with large contrast (e.g. very dark or very light). For interpretation, we see that the section in Figure 1.3d is preferred.

Equation 1.1 gives the relative difference in the geology. If we would like to go back to the I, we must invert thee equation. An approximation to this is to take the cumulative sum, or integrate each trace to obtain a relative impedance. Figure 1.4b,c and d show the relative "impedance" of the corresponding reflection images in Figure 1.3. We observe that when a broader bandwidth is used, we obtain an image that is closer to the geological model.

In the examples above, attenuation has not been included. Attenuation is the term used for frequency dependent damping of the seismic signal (e.g. Knopoff, 1964; Futterman, 1962; Kjartansson, 1979). Attenuation of the seismic signal can be related at least to two different phenomena: 1) Intrinsic absorption of energy and 2) Scattering due to heterogeneity. A commonly used model for attenuation is the constant-Q model:

$$A(r,\omega) = A_0(\omega)e^{\frac{-\pi\omega r}{Q_c}}, \tag{1.2}$$

where $A(r, \omega)$ is the signal recorded at a distance r away from the source with strength $A_0(\omega)$, Q is the quality factor, c is the velocity and $\omega = 2\pi f$ is the angular frequency, where f is the frequency. Equation 1.2 shows that higher frequencies are attenuated more than low frequencies. Figure 1.5 shows the corresponding images as in Figure 1.3 when $Q = 50$ is included. We observe that the section in Figure 1.5b has very low amplitudes at large times, and that the section with low frequencies, in Figure 1.5c, is less affected by attenuation.

Although these examples are simple and unphysical, they clearly demonstrate the effect of bandwidth in seismic data. It is obvious from the example that both low and high frequencies are desired for a better understanding of the subsurface. Low frequencies illuminate the larger variations in geology and are less affected by attenuation due to absorption and scattering, while the high frequencies are illuminating smaller variations in geology. For inversion and imaging of deep structures, the low frequencies play an important role.

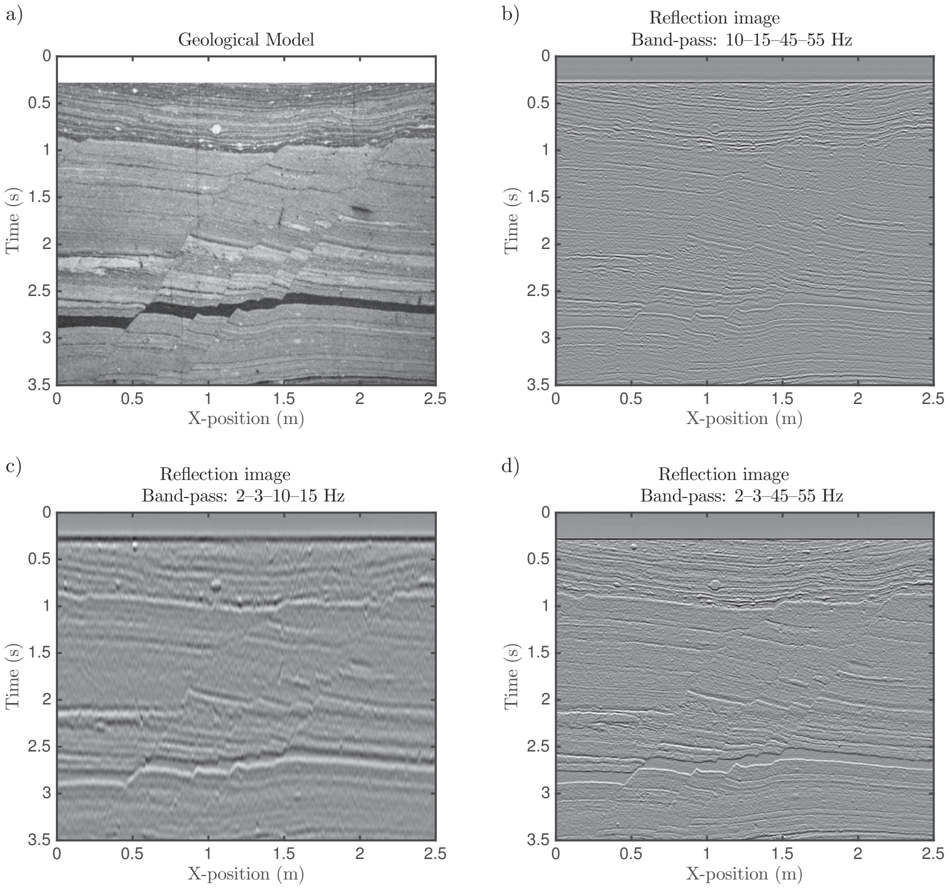

Figure 1.3: a) Geological model based on photograph from Fossen and Gabrielsen (2005). b), c) and d) shows synthetic seismic sections obtained by convolution modeling, where different band-pass filters (indicated above the respective figures) are used as source.

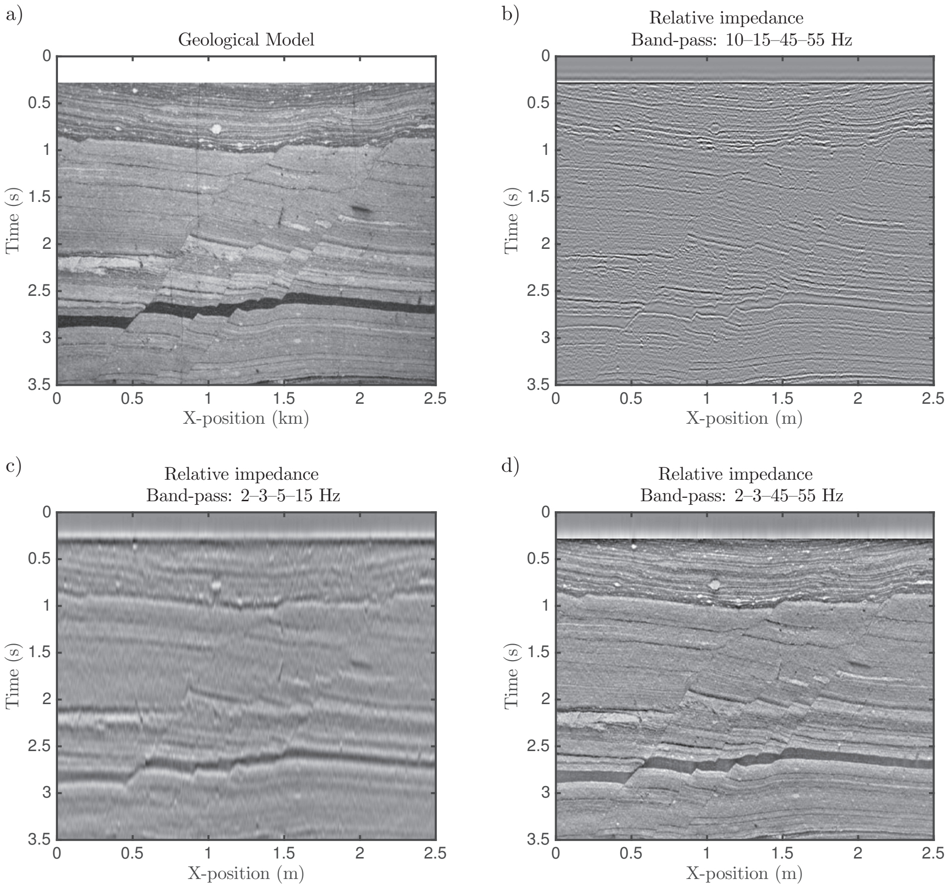

Figure 1.4: a) Geological model based on photograph from Fossen and Gabrielsen (2005). b), c) and d) shows relative impedance sections obtained by integrating each of the traces in Figure 1.3b), c) and d). We observe that d), with a broad bandwidth, results in an image that is closer to the true model.

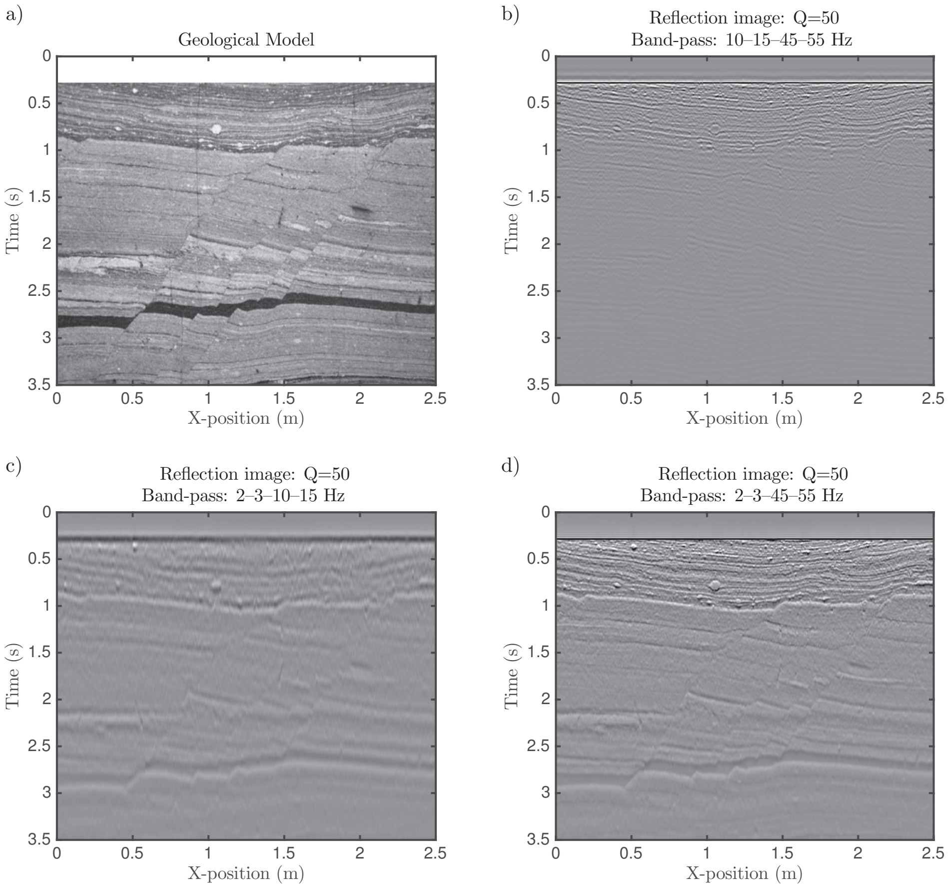

Figure 1.5: Geological model based on photograph from Fossen and Gabrielsen (2005). b), c) and d) shows synthetic seismic sections obtained by convolution modeling, where different band-pass filters (indicated above the respective figures) are used as source. Constant-Q attenuation (Kjartansson, 1979) is applied.

1.2.1 The ghost reflection

The ghost reflection is the term used for the wavefield that has been reflected at the free surface, *i.e.*, the air-water interface for marine seismic data (van Melle and Weathernurm, 1953). The contrast in acoustic properties (density and velocity of sound) is large between water and air. The amplitude of the reflected wave is given by the reflection coefficient as:

$$R_0 = \frac{\rho_a c_a - \rho_w c_w}{\rho_a c_a + \rho_w c_w}, \tag{1.3}$$

where ρ and c are the density and velocity of sound, respectively, and the subscripts denote air (a) and water (w). The typical density and velocity of sound in water is 1000 kg/m^3 and 1500 m/s, respectively, while the same parameters for air is 1.2 kg/m^3 and 330 m/s. The reflection coefficient from the air-water interface is thus R_0 =-0.99945 $\approx$ -1. This shows that all up-going waves will be reflected at the free-surface and propagate down with approximately the same strength, but opposite polarity. The air-water interface works as a mirror for seismic waves. When the seismic data is recorded, we record both the up-going waves as they pass the receivers, and the down-going wave that has been reflected at the free surface. The latter appears in the data as it was recorded at a ghost receiver that is positioned above the free surface. The wavefield from a source at a given depth, will consist of the direct wave and the ghost reflection. Figure 1.6 shows how this will appear for an impulse source positioned at 10 m depth in different domains. We observe that there is a diversity of notch frequencies with respect to angle for a single source depth (Figure 1.6b).

The wavefield recorded at position $\mathbf{r}$ from a source at position $\mathbf{r}_s$ is given as:

$$s(\mathbf{x};\mathbf{x}_s,t) = \frac{1}{|\mathbf{x}-\mathbf{x}_s|} w(t-\tau) + \frac{R_0}{|\mathbf{x}-\mathbf{x}'_s|} w(t-\tau') \tag{1.4}$$

where $w(t)$ is the source signature, $\mathbf{x} = (x, y, z)$, $\mathbf{x}_s = (x_s, y_s, z_s)$, $\mathbf{x}'_s = (x_s, y_s, -z_s)$, are the recording, source and ghost-source positions, respectively, $\tau = |\mathbf{x} - \mathbf{x}_s|/c$ and $\tau = |\mathbf{x} - \mathbf{x}'_s|/c$ are the travel times from the source and ghost source to the recording position, respectively, and c is the velocity in the medium. If we assume $(x - x_s)/z \ll 1$, $z_s/z \ll 1$ and $R_0 = -1$, we can approximate equation 1.4 as:

$$s(\mathbf{x};\mathbf{x}_s,t) \approx \frac{1}{|\mathbf{x}-\mathbf{x}_s|} \Big[w(t-\tau) - w(t-\tau-\Delta\tau) \Big]. \tag{1.5}$$

Here, $\Delta\tau$ is the difference in the travel time between the primary and ghost events:

$$\Delta\tau \approx \frac{2 z_s \cos\theta}{c}.$$

By taking the Fourier transform of equation 1.5 we obtain:

$$S(\omega) = \frac{e^{i\omega\tau}}{|\mathbf{x}-\mathbf{x}_s|} W(\omega) \Big[1 - e^{i\omega\Delta\tau} \Big], \tag{1.6}$$

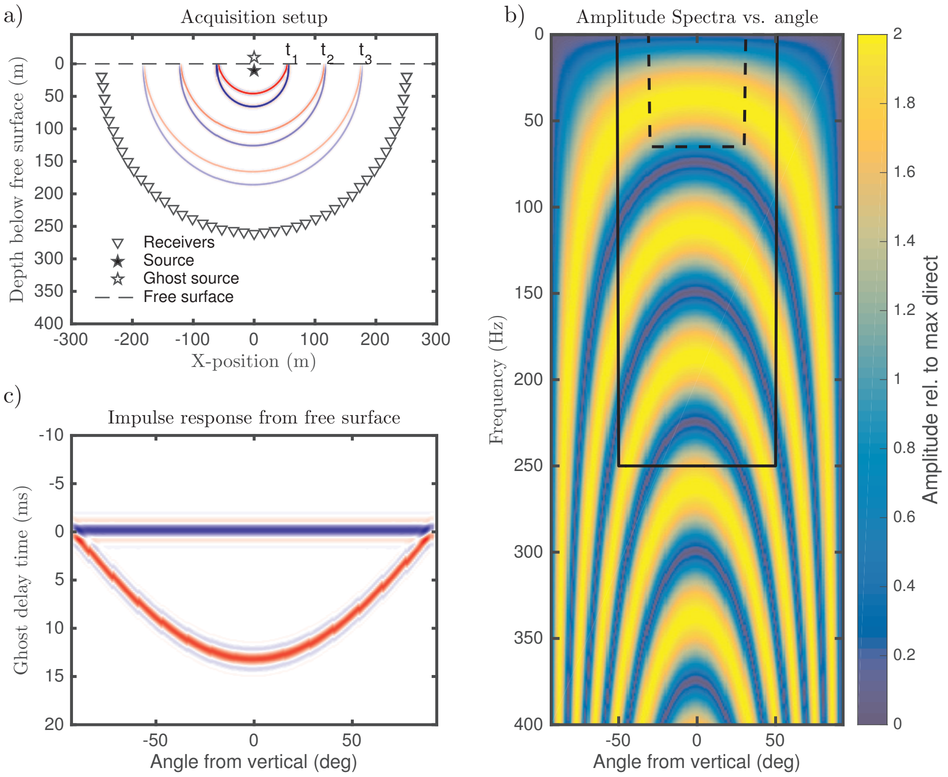

Figure 1.6: a) A source positioned 10 m below a free surface. Receivers are positioned 250 m away from the source at angles -90° to -90° from vertical. The resulting wavefield is illustrated at three different times (t_1, t_2 and t_3), where blue and red illustrates the direct and ghost, respectively. b) Amplitude spectra versus angle, where the amplitudes are normalized to the maximum value of the direct wave. The periodicity and position of the ghost notches vary with angle. The solid black box shows a typical region of frequencies and angles that is used in imaging of shallow geology. The dashed box indicates the region that is typical for deep imaging. c) Impulse response from the source positioned 10 m below the free surface. The time axis is centered on the time for the direct wave.

where $\omega = 2\pi f$ is the angular frequency. This equation can be written as the follows:

$$S(\omega) = R(\omega)G(\omega), \tag{1.7}$$

with

$$R(\omega) = \frac{e^{i\omega\tau}}{|\mathbf{x} - \mathbf{x}_s|}W(\omega) \qquad \text{and} \qquad G(\omega) = 1 - e^{i\omega\Delta\tau},$$

being the signal that we would have recorded without a ghost and the ghost filter, respectively. The ghost filter describes how the free surface alter, or filter, the seismic signal.

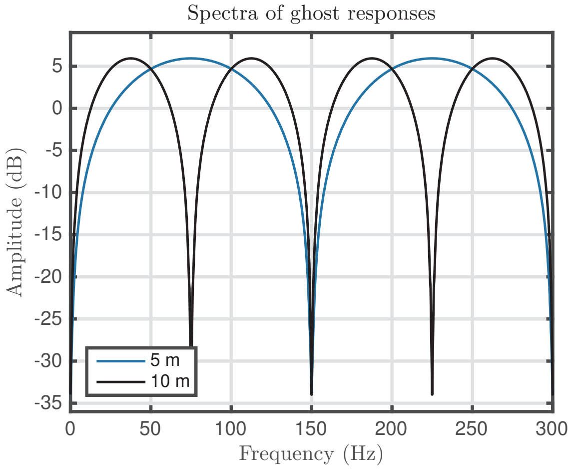

Figure 1.7: The amplitude spectra of vertical ghost responses for source depths 5 m (blue) and 10 m (black). The amplitude scale is in decibel (dB relative to 1).

The ghost spectrum is given as:

$$|G(\omega)| = 2\left|\sin\left(\frac{\omega\Delta\tau}{2}\right)\right|. \tag{1.8}$$

We see that the maximum and minimum value of $|G(\omega)|$ are 2 and 0, respectively. Figure 1.7 shows the vertical ($\theta = 0$) ghost spectra for source depths 5 and 10 m. We observe that the ghost reflection give rise to notches in the spectrum, and that the position of these notches are dependent on the source depth. The position of the notches are given by:

$$f_n = \frac{c}{2z} \cdot n \quad \text{for} \quad n = 0, 1, 2, \ldots. \tag{1.9}$$

The scale that is used for the amplitudes in Figure 1.7 is the decibel scale given as:

$$A_{dB} = 20 \log_{10}\left(\frac{A}{A_0}\right),$$

where A is the amplitude of the signal and A_0 is a reference amplitude. If the A is twice the magnitude of A_0, A_{dB} is close to 6.

1.2.2 Source-side deghosting

Source-side deghosting is the process where the ghost reflection on the source side is attempted removed. To remove the ghost, an inverse ghost filter can be applied to the recorded seismic data, $S(\omega)$, in equation 1.7:

$$R(\omega) = G^{-1}(\omega)S(\omega) = \frac{S(\omega)}{G(\omega)}. \tag{1.10}$$

A problem with this process, is that $G(\omega)$ is zero at the notch frequencies, making this highly unstable in the presence of noise. A more robust approach is to use Wiener deconvolution:

$$G^{-1}(\omega)S(\omega) \approx \frac{G^{*}(\omega)S(\omega)}{|G(\omega)|^2 + \epsilon^2}, \tag{1.11}$$

where superscript * indicates complex conjugate and ϵ is a regularization term, related to the noise level in the data, used to avoid division by zero. Equation 1.11 gives the correct phase-shifts to the data, but will not correctly restore the amplitudes. Figure 1.8 illustrates how different values of ϵ affect the deghosting result. Figure 1.8a shows a trace where a Ricker wavelet with peak frequency of 40 Hz is used, the same trace with a ghost corresponding to a source depth of 10 m and the ghosted trace with noise. Figure 1.8b shows the amplitude spectra of the trace with no ghost, with ghost and the noise. Figure 1.8c shows the deghosted result for different constant values of ϵ with the true trace overlaid, and Figure 1.8d shows the corresponding amplitude spectra. We observe, in Figure 1.8d, that the amplitudes of the deghosted result in the areas where the S/N is low are amplified too much ($f < 5Hz$ and $f > 105Hz$). The ϵ parameter can be chosen frequency dependent to better represent the S/N for different frequencies. This illustrates source-side deghosting for a wave that has traveled vertically. A seismic shot gather contain traces where the take-off angle, or angle of emergence, is deviating from vertical (see Figure 1.6b). The vertical approximation is often used in processing of seismic data, but better results can be achieved if this deviation is included in the deghosting filters.

Receiver-side deghosting is an equally important process for obtaining broadband seismic images. However, since the focus of this thesis is on the source side, no detailed description will be given for the receiver-side deghosting. For further reading on receiver-side deghosting, the reader is referred to Amundsen (1993); Fokkema and van den Berg (1993); Posthumus (1993); Tenghamn et al. (2007); Soubaras (2012).

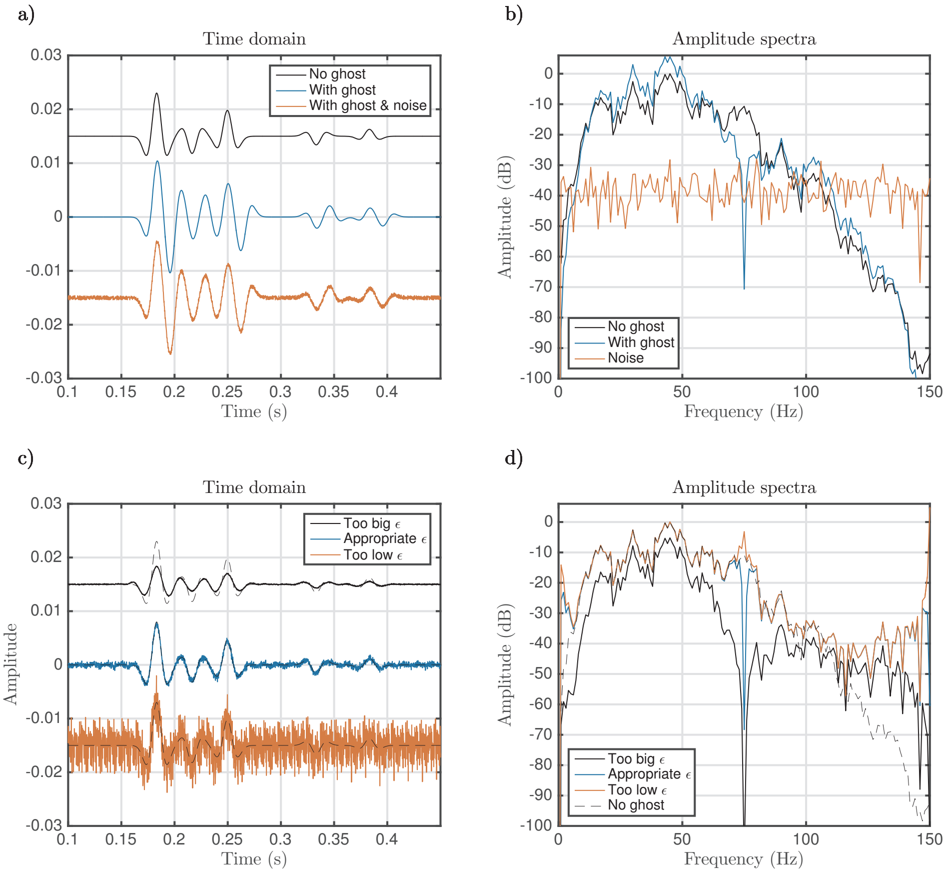

Figure 1.8: a) Synthetic seismic trace, ghosted trace and ghosted trace with noise. b) Amplitude spectra of the trace, ghosted trace and noise. c) Deghosting of the trace with ghost and noise using different constant values of ϵ. A trace without the ghost is overlain for comparison (dashed). d) The amplitude spectra of the deghosted results in c).

1.3 Air gun as acoustic source

The most common source of acoustic signal used in marine seismic acquisition today is the air gun, or arrays of multiple air guns. The air gun was developed in the 1960's by Stephen Chelminski, who also co-founded Bolt technologies. An air gun works in the way that pressurized air is filled in a chamber. When this air is released, it forms a bubble of air that will expand rapidly. As the bubble expands, the pressure inside the bubble decrease. When the pressure is lower than the pressure in the water surrounding it, the bubble slows down, and will eventually start to contract. As it contracts, the pressure inside the bubble will again increase and eventually start expanding. The bubble oscillates like this until it dissolves or breaks the air-water interface. In this section, the fundamentals of how the air-gun source works is described. The physics of such a bubble was first described by Rayleigh (1917).

1.3.1 Rayleigh equation for bubble motion

Let us now examine how an expanding bubble in an incompressible fluid will affect the particle motion of its surroundings. Let us assume that there are no boundaries in this fluid and that the motion has spherical symmetry with respect to the centre of the bubble. We denote R as the radius of the bubble and U the velocity of the bubble wall. The relationship between R and U is given by:

$$U = \frac{dR}{dt}. \tag{1.12}$$

The rate of the volume of fluids pushed away as the bubble expands a small radius dR over a short time dt is given as

$$\frac{dV}{dt} = 4\pi R^2 \frac{dR}{dt}, \tag{1.13}$$

where $4\pi R^2$ is the area of a sphere with radius R. The rate of volume going through a shell at a radius r away from the centre of the bubble due to the same expansion must therefor be:

$$\frac{dV}{dt} = 4\pi r^2 \frac{dr}{dt}. \tag{1.14}$$

This gives a relationship between the particle velocity at a distance r and the bubble-wall velocity when the bubble radius is R:

$$u = \frac{dr}{dt} = \frac{UR^2}{r^2}. \tag{1.15}$$

The total kinetic energy in the liquid surrounding the bubble is given as the integral:

$$E_k = \int_R^\infty \frac{1}{2} 4\pi \rho u^2 dr, \tag{1.16}$$

which is evaluated to:

$$E_k = 2\pi\rho U^2 R^3. \tag{1.17}$$

The potential energy of this system equals the work done by the bubble when it expands from the initial radius R_0 to R:

$$W = \int_{R_0}^{R} (p - p_\infty) 4\pi R^2 dR. \tag{1.18}$$

The total energy of the system is therefore given by:

$$E = E_k + W = 2\pi\rho U^2 R^3 + \int_{R_0}^{R} (p - p_\infty) 4\pi R^2 dR. \tag{1.19}$$

The total energy of this system must be constant with respect to time, if we assume that there is no loss of energy to the surroundings (dissipation), hence

$$\frac{dE}{dt} = 0. \tag{1.20}$$

We now, for simplicity, ignore the time dependency of the pressure inside the bubble (*i.e.* $\frac{dp}{dt} = 0$) and we find:

$$2\rho \left(2\frac{dR}{dt}\frac{d^2R}{dt^2}R^3 + 3\left(\frac{dR}{dt}\right)^3 R^2 \right) = 4\left(p - p_\infty\right) R^2 \frac{dR}{dt}. \tag{1.21}$$

By rearranging this equation we obtain the Rayleigh equation for bubble motion:

$$R\frac{d^2R}{dt^2} + \frac{3}{2}\left(\frac{dR}{dt}\right)^2 = \frac{p - p_\infty}{\rho}. \tag{1.22}$$

This equation is a non-linear differential equation, that must be solved numerically. The pressure, p, inside the bubble is often approximated by assuming a gas law that relates the pressure and volume of the gas at different stages of the expansion. A common approximation is to assume that the air expands adiabatically:

$$p = p_0 \left(\frac{R_0}{R}\right)^{3\gamma}. \tag{1.23}$$

Here, R_0 and p_0 is the initial radius of the bubble and the initial pressure inside the bubble, respectively. The parameter γ is the adiabatic constant for air (diatomic gas) is $\gamma = 7/5$. The Rayleigh equation is derived under many assumptions: Incompressible fluid, no energy dissipation and that the change in pressure with respect to time is very small. The Rayleigh equation serves as a good model for understanding the basics of bubble motion, but cannot be used to model air-gun bubbles. There are several other models for bubble-motion (e.g. Kirkwood and Bethe, 1942; Gilmore, 1952; Ziolkowski, 1970; Plesset and Prosperetti, 1977). These models are derived using more complicated physics that take into account, for instance, compressibility of the fluid, mass- and heat-transfer, and/or other energy dissipation effects. Even though these models are more complicated, it is often required to calibrate them to observed data. An example of such calibration is to introduce damping terms in the Rayleigh equation:

$$R\frac{d^2R}{dt^2} + \frac{3}{2}\left(\frac{dR}{dt}\right)^2 - \alpha\frac{dR}{dt} + \beta\left(\frac{dR}{dt}\right)^2 = \frac{p - p_\infty}{\rho}. \tag{1.24}$$

Here, α and β are damping parameters that controls how fast the signal decays, and the bubble-time period, respectively (inspired by Landrø and Sollie, 1992).

Examples of bubble motion as predicted by the Rayleigh equation, with and without damping, are shown in Figure 1.9 for source depths of 5 m and 10 m. In this example, we observe that both the period at which the bubbles oscillates and the maximum radius are different for the 5 m and 10 m case.

The nature of the air-gun bubble is oscillatory, as seen in Figure 1.9. Rayleigh (1917) studied the collapse time of small cavities. Cavities are small bubbles, or voids in the water, that form when the pressure in the water drops below the vapor pressure. Rayleigh (1917) assumes the pressure inside these cavities is very low ($p \approx 0$) and found:

$$\tau_c = 0.91468R_0\sqrt{\frac{\rho}{p_\infty}} \tag{1.25}$$

This equation gives the time for an empty cavity to collapse from its maximum radius. For a bubble that oscillates, this will correspond to half a period. Willis (1941) assumed adiabatic expansion of the air inside the bubble and found the following bubble-time period:

$$\tau_{RW} = 1.3625\rho^{1/2}\frac{p_0^{1/3}V_0^{1/3}}{p_\infty^{5/6}}, \tag{1.26}$$

where $V_0 = 4/3\pi R_0^3$ is the initial volume of the air bubble. This equation is known as the Rayleigh-Willis equation. We see that the bubble-time period will decrease as the surrounding pressure increases.

1.3.2 Acoustic pressure from an oscillating bubble

The acoustic pressure generated by an oscillating bubble can be given as (Gilmore, 1952):

$$p_a(r) = \rho\frac{R}{r}\left(H + \frac{1}{2}\left|\frac{dR}{dt}\right|^2\right), \tag{1.27}$$

where r is the distance from the centre of the bubble, ρ is the density of the water, R is the radius of the bubble and H is the enthalpy at the bubble wall given as:

$$H = \int_{p_\infty}^{p} \frac{dp}{\rho}. \tag{1.28}$$

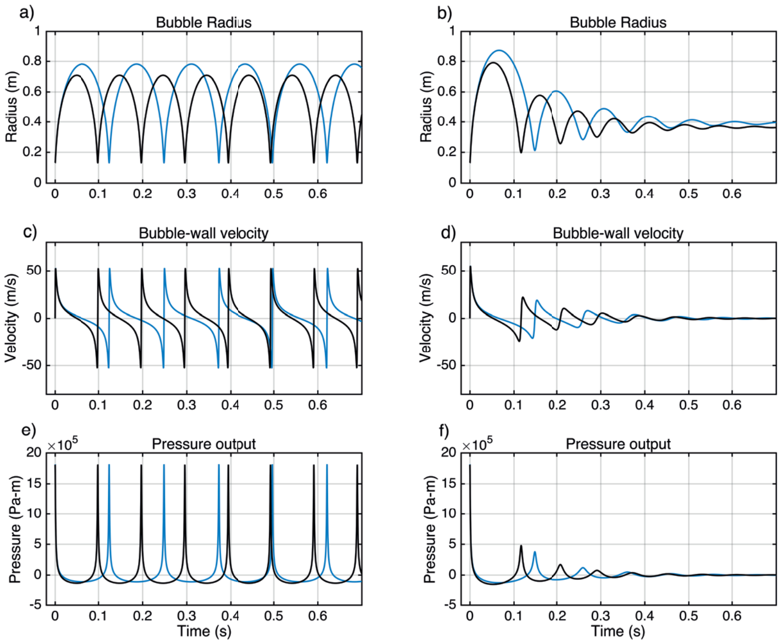

Figure 1.9: Results from modeling of bubble motion using the Rayleigh (left) and damped Rayleigh equations. The initial volume of the modeled bubble is 600 inch^3 (9.8 l), the initial pressure is 2000 psi (137.9 bar) and the external pressure (p_∞) corresponds to the pressure at water depths of 5 m and 10 m, approximately 1.5 bar and 2 bar, respectively. a) and b) The radius of the bubble. c) and d) The bubble-wall velocity. e) and f) The pressure output at 1 m. The blue lines are for a source depth of 5 m and the black lines are for a source depth of 10 m.

The empirical Tait-equation is often used to evaluate H (Ziolkowski, 1970; Landrø and Sollie, 1992; Landrø et al., 1993b). If we assume that the density of water is independent of the pressure, *i.e.* incompressible, then H can be approximated as:

$$H \approx \frac{p - p_\infty}{\rho}. \tag{1.29}$$

Here p is the pressure inside the bubble and p_∞ is the hydrostatic pressure.

1.3.3 Air-gun arrays

A single air-gun is often considered too weak as a source in seismic acquisition. Normally, arrays of up to 40 to 50 air guns and air-gun clusters (two or three air guns that are placed close together) are used (Dragoset, 2000). The air-gun arrays are usually organized in sub-arrays that might be up to 20 m long and separated by up to 10 m. The volumes of the air guns are chosen so that the bubble-time periods are not interfering constructively, so that combined signature is as close to an impulse as possible. This is referred to as a tuned array (Kologinczak, 1974; Dragoset, 2000; Landrø and Amundsen, 2010). When several closely spaced air guns are fired simultaneously, the pressure and water movement from nearby air guns will affect the movement of the bubbles, and the resulting pressure signature will be different than if the guns were fired separately. This non-linear interaction is described in Ziolkowski et al. (1982). Superposition of air-gun signatures fired separately will therefore not provide the correct description of the total source signature from an air-gun array. The source signature from an array can be described through the superposition of equivalent non-interacting signatures, referred to as notional source signatures (Ziolkowski et al., 1982; Parkes et al., 1984). Figure 1.10 shows notional source signatures from an air-gun array consisting of 28 air guns modeled with a commercial air-gun modeling software. The modeled air-gun array is 16 m long, in three sub-arrays. Figure 1.11a and b shows the source signatures and the amplitude spectra, respectively, from the air-gun array in Figure 1.10 vertically below the source and at an angle of 20 degrees from vertical in the in-line direction (along sub-array). The ghost reflection is not included in this example. We observe that the source signature is dependent on the angle, but is similar for frequencies up to 60–70 Hz. This directivity is dependent on the length of the array, and the ghost reflection will also influence the directivity. The recorded seismic data will have the source signature imprinted on each event. Ideally, we would like to have seismic data from an impulse source. The shape of the source signature can be removed from the recorded data in a similar fashion as we remove the source ghost (section 1.2.2). This is referred to as designature or debubbling (Wood et al., 1978).

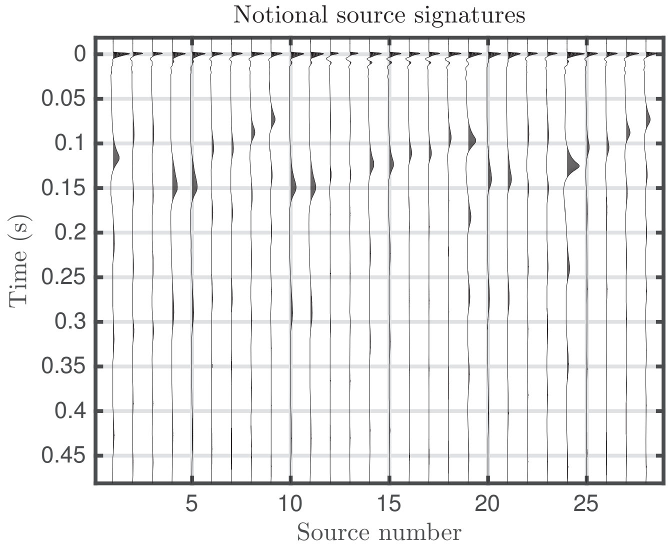

Figure 1.10: Notional source signatures from 28 air guns in an air-gun array.

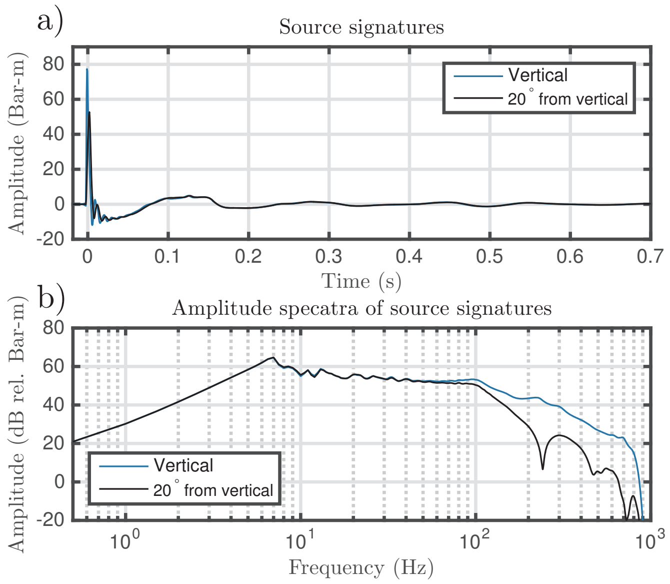

Figure 1.11: a) Source signature from the 28-gun air-gun array. Vertically below the array (blue) and 20 degrees from vertical (black) in the in-line direction (along the sub-arrays). b) The corresponding amplitude spectra of a). No ghost is included.

1.4 Seismic wave propagation

Seismic waves are small disturbances in pressure or stress that propagate through or at the boundary of a medium (Ewing, 1957). The equations that describe seismic wave propagation are the equation of motion, and a constitutive relationship between stress and strain (Hooke's law).

1.4.1 Equation of motion

The equations of motion are given as

$$\rho \frac{d^2\mathbf{u}}{dt^2} = \nabla \boldsymbol{\sigma}, \tag{1.30}$$

where $\mathbf{u} = \mathbf{u}(\mathbf{x}, t)$ is the particle displacement vector, $\rho = \rho(\mathbf{x})$ is the density and $\boldsymbol{\sigma} = \boldsymbol{\sigma}(\mathbf{x}, t)$ is the stiffness tensor, at position $\mathbf{x}$ and time t (dependencies omitted), given respectively as:

$$\mathbf{u} = \begin{bmatrix} u_1 \\ u_2 \\ u_3 \end{bmatrix} \qquad \text{and} \qquad \boldsymbol{\sigma} = \begin{bmatrix} \sigma_{11} & \sigma_{12} & \sigma_{31} \\ \sigma_{12} & \sigma_{22} & \sigma_{32} \\ \sigma_{13} & \sigma_{23} & \sigma_{33} \end{bmatrix}.$$

The subscripts indicate the directions, *i.e.*, $1 = x$, $2 = y$ and $3 = z$. For the stress, σ_{ij} describes the stress applied in the i direction on surface with normal j. For an acoustic medium, where no shear forces exist, σ_{ij}, reduce to a diagonal tensor with the pressure, p:

$$\boldsymbol{\sigma} = \begin{bmatrix} -p & 0 & 0 \\ 0 & -p & 0 \\ 0 & 0 & -p \end{bmatrix}.$$

1.4.2 Hooke's law

The relationship between stress and strain is given as:

$$\sigma_{ij} = \tilde{C}_{ijkl}\epsilon_{kl}, \tag{1.31}$$

where $\tilde{C}_{ijkl} = \tilde{C}_{ijkl}(\mathbf{x})$ is the fourth-order stiffness tensor and

$$\epsilon_{kl} = \frac{1}{2}\left(\frac{\partial u_k}{\partial x_l} + \frac{\partial u_l}{\partial x_k}\right), \tag{1.32}$$

is the strain tensor. Einstein summation convention is used. Due to symmetry of the stress and strain tensors, the number of independent stiffnesselements reduces from 81 to

21, equation 1.31 can be written in Voigt notation ($11 \rightarrow 1$, $22 \rightarrow 2$, $33 \rightarrow 3$, $23 \rightarrow 4$, $13 \rightarrow 5$ and $12 \rightarrow 6$) as:

$$\begin{bmatrix} \sigma_1 \\ \sigma_2 \\ \sigma_3 \\ \sigma_4 \\ \sigma_5 \\ \sigma_6 \end{bmatrix} = \begin{bmatrix} C_{11} & C_{21} & C_{31} & C_{41} & C_{51} & C_{61} \\ C_{12} & C_{22} & C_{32} & C_{42} & C_{52} & C_{62} \\ C_{13} & C_{23} & C_{33} & C_{43} & C_{53} & C_{63} \\ C_{14} & C_{24} & C_{34} & C_{44} & C_{54} & C_{64} \\ C_{15} & C_{25} & C_{35} & C_{45} & C_{55} & C_{65} \\ C_{16} & C_{26} & C_{36} & C_{46} & C_{56} & C_{66} \end{bmatrix} \begin{bmatrix} \epsilon_1 \\ \epsilon_2 \\ \epsilon_3 \\ \epsilon_4 \\ \epsilon_5 \\ \epsilon_6 \end{bmatrix}.$$

We see that there are 21 different stiffness coefficients in $\mathbf{C}$. For a homogeneous, isotropic elastic medium, $\mathbf{C}$ reduce to

$$\mathbf{C} = \begin{bmatrix} \lambda + 2\mu & \lambda & \lambda & 0 & 0 & 0 \\ \lambda & \lambda + 2\mu & \lambda & 0 & 0 & 0 \\ \lambda & \lambda & \lambda + 2\mu & 0 & 0 & 0 \\ 0 & 0 & 0 & \mu & 0 & 0 \\ 0 & 0 & 0 & 0 & \mu & 0 \\ 0 & 0 & 0 & 0 & 0 & \mu \end{bmatrix}, \tag{1.33}$$

where λ and μ are the Lamé parameters. The parameter μ is a measure of the elastic mediums ability to resist shear movement, and is referred to as the shear modulus. The elastic mediums ability to resist compression is the bulk modulus, which is related to the Lamé parameters as: $K = \lambda + 2/3\mu$.

1.4.3 Wave equation

By combining equation 1.30 and equation 1.31 we obtain an equation that describes wave propagation. For an elastic medium, this equation is given as (Aki and Richards, 2002):

$$\rho \frac{\partial^2 \mathbf{u}}{\partial t^2} = (\lambda + 2\mu) \nabla (\nabla \cdot \mathbf{u}) - \mu \nabla \times (\nabla \times \mathbf{u}), \tag{1.34}$$

Here, $\cdot$ denotes inner product and $\times$ is the cross product. The displacement vector, $\mathbf{u}$, can be written in terms of potentials:

$$\mathbf{u} = \nabla \phi + \nabla \times \mathbf{\Theta}, \tag{1.35}$$

where ϕ is a scalar potential and $\mathbf{\Theta}$ is a vector potential. By inserting equation 1.35 into equation 1.34, it can be shown that the potentials are solutions to the following wave equations:

$$\frac{1}{c_p^2} \frac{\partial^2 \phi}{\partial t^2} = \nabla^2 \phi \tag{1.36}$$

and

$$\frac{1}{c_s^2} \frac{\partial^2 \mathbf{\Theta}}{\partial t^2} = \nabla^2 \mathbf{\Theta}, \tag{1.37}$$

where the velocities, c_p and c_s, are given, respectively, by

$$c_p = \sqrt{\frac{\lambda + 2\mu}{\rho}} \qquad \text{and} \qquad c_s = \sqrt{\frac{\mu}{\rho}}.$$

The two potentials are describing different parts of the wavefield: The scalar potential is describing P-waves, or compressional waves, and the vector potential is describing, S-waves, or shear waves. In a homogeneous elastic media, these are not coupled, but for a heterogeneous media conversions between P- and S-Waves occur (Aki and Richards, 2002).

1.4.4 Solution to the wave equation for an impulse source

For simplicity, an isotropic and acoustic medium ($\mu = 0$) is considered. The solution to the acoustic wave equation for an impulse source is of special interest:

$$\frac{1}{c^2}\frac{\partial^2 g(\mathbf{x}, t; \mathbf{x}_0)}{\partial t^2} - \nabla^2 g(\mathbf{x}, t; \mathbf{x}_0) = \delta(\mathbf{x} - \mathbf{x_0})\delta(t). \tag{1.38}$$

The right-hand side of the equation is a source term, where $\delta(x)$ is the Dirac delta function, which is given as:

$$\delta(x) = \begin{cases} 1, & \text{if } x = 0 \\ 0, & \text{otherwise.} \end{cases}$$

This source is an impulse source at position $\mathbf{x} = \mathbf{x_0}$. The solution to equation 1.38 is called a Green function, and is the impulse response of the medium. For an unbounded, homogeneous and isotropic medium, the Green function is given as

$$g(\mathbf{x}, t; \mathbf{x}_0) = \frac{\delta(t - t_0)}{4\pi|\mathbf{x} - \mathbf{x_0}|}, \tag{1.39}$$

where the $|\mathbf{x} - \mathbf{x_0}|$ is the distance between the points $\mathbf{x}$ and $\mathbf{x_0}$, and $t_0 = |\mathbf{x} - \mathbf{x_0}|/c$ is the time it takes for the wave to travel the distance $|\mathbf{x} - \mathbf{x_0}|$. The Green function holds information about the amplitude and the travel-time of the wavefield between two points in the medium. Analytical Green functions for complex media are more complicated and in general difficult to obtain.

1.4.5 Reciprocity theorem

We now consider the two equations:

$$\frac{1}{c^2}\frac{\partial^2 p_1(\mathbf{x}, t; \mathbf{x}_1)}{\partial t^2} - \nabla^2 p_1(\mathbf{x}, t; \mathbf{x}_1) = \delta(\mathbf{x} - \mathbf{x}_1) f_1(t) \tag{1.40}$$

and

$$\frac{1}{c^2}\frac{\partial^2 p_2(\mathbf{x},t;\mathbf{x}_2)}{\partial t^2} - \nabla^2 p_2(\mathbf{x},t;\mathbf{x}_2) = \delta(\mathbf{x}-\mathbf{x}_2)f_2(t). \tag{1.41}$$

A Fourier transformation over time of equations 1.40 and 1.41 yields:

$$\frac{\omega^2}{c^2}P_1(\mathbf{x},\omega;\mathbf{x}_1) + \nabla^2 P_1(\mathbf{x},\omega;\mathbf{x}_1) = -\delta(\mathbf{x}-\mathbf{x}_1)F_1(\omega) \tag{1.42}$$

and

$$\frac{\omega^2}{c^2}P_2(\mathbf{x},\omega;\mathbf{x}_2) + \nabla^2 P_2(\mathbf{x},\omega;\mathbf{x}_2) = -\delta(\mathbf{x}-\mathbf{x}_2)F_2(\omega). \tag{1.43}$$

Here, $P_1(\mathbf{x};\mathbf{x}_1,\omega)$, $P_2(\mathbf{x};\mathbf{x}_2,\omega)$, $F_1(\omega)$ and $F_2(\omega)$ are the Fourier transforms of $p_1(\mathbf{x};\mathbf{x}_1,t)$ $p_2(\mathbf{x};\mathbf{x}_2,t)$, $f_1(t)$ and $f_2(t)$, respectively. The dependency on ω is omitted in P_1 and P_2 for simplicity. Let us introduce the vector:

$$\mathbf{F} = P_1(\mathbf{x};\mathbf{x}_1)\nabla P_2(\mathbf{x};\mathbf{x}_2) - P_2(\mathbf{x};\mathbf{x}_2)\nabla P_1(\mathbf{x};\mathbf{x}_1) \tag{1.44}$$

The divergence of $\mathbf{F}$ is given as:

$$\nabla\cdot\mathbf{F} = P_1(\mathbf{x};\mathbf{x}_1)\nabla^2 P_2(\mathbf{x};\mathbf{x}_2) - P_2(\mathbf{x};\mathbf{x}_2)\nabla^2 P_1(\mathbf{x};\mathbf{x}_1) \tag{1.45}$$

By inserting equations 1.42 and 1.43 into equation 1.45, we obtain:

$$\nabla\cdot\mathbf{F} = P_2(\mathbf{x};\mathbf{x}_2)\delta(\mathbf{x}-\mathbf{x}_1)F_1(\omega) - P_1(\mathbf{x};\mathbf{x}_1)\delta(\mathbf{x}-\mathbf{x}_2)F_2(\omega). \tag{1.46}$$

Now, by using the divergence theorem

$$\int_V \nabla\cdot\mathbf{F}dV = \oint_S \mathbf{F}\cdot\mathbf{n}dS, \tag{1.47}$$

where V is the volume closed by the surface S, and $\mathbf{n}$ is the outward pointing normal vector to S, we obtain:

$$\int_V \big[P_1(\mathbf{x};\mathbf{x}_1)\delta(\mathbf{x}-\mathbf{x}_2)F_2(\omega) - P_2(\mathbf{x};\mathbf{x}_2)\delta(\mathbf{x}-\mathbf{x}_1)F_1(\omega)\big]dV = \\ \oint_S \big[P_1(\mathbf{x};\mathbf{x}_1)\nabla P_2(\mathbf{x};\mathbf{x}_2) - P_2(\mathbf{x};\mathbf{x}_2)\nabla P_1(\mathbf{x};\mathbf{x}_1)\big]\cdot\mathbf{n}dS. \tag{1.48}$$

This integral is Rayleigh's reciprocity theorem between two independent wavefields in the same acoustic medium. From this equation it is possible to derive several useful representations, depending on the choice of boundary conditions, the source type and the causality of the wavefield with respect to time. By choosing the surface S to be infinite away from $\mathbf{x}_1$ or by choosing S as a free or rigid boundary we get

$$P_1(\mathbf{x}_2;\mathbf{x}_1)F_2(\omega) = P_2(\mathbf{x}_1;\mathbf{x}_2)F_1(\omega). \tag{1.49}$$

If the source functions are equal, we obtain the best known formulation of the reciprocity relationship: The source-receiver reciprocity given as

$$P_1(\mathbf{x}_2;\mathbf{x}_1) = P_2(\mathbf{x}_1;\mathbf{x}_2). \tag{1.50}$$

This equation shows that the acoustic wavefield due to a source at $\mathbf{x}_1$ recorded at $\mathbf{x}_2$ is the same as the acoustic wavefield due to a source at $\mathbf{x}_2$ recorded at $\mathbf{x}_1$, if the same source function is used. If we now choose $f_2(t) = \delta(t)$, in equation 1.41, which gives $p_2(\mathbf{x}, t; \mathbf{x}_2) = g(\mathbf{x}, t; \mathbf{x}_2)$, equation 1.49 reduces to:

$$P_1(\mathbf{x}_2; \mathbf{x}_1) = G(\mathbf{x}_2; \mathbf{x}_1) F_1(\omega) \tag{1.51}$$

This result shows that if we know the Green function between the two points $\mathbf{x}_1$ and $\mathbf{x}_2$, and the source function $F_1(\omega)$, we can predict the pressure at the position $\mathbf{x}_1$ due to a source at the position $\mathbf{x}_2$ with source function $F_1(\omega)$. By choosing the source position $\mathbf{x}_1$ to lie outside S, again with $f_2(t) = \delta(t)$, equation 1.48 reduces to the acoustic Kirchhoff integral

$$P_1(\mathbf{x}_2; \mathbf{x}_1) = \oint_S \big[G(\mathbf{x}_2; \mathbf{x}) \nabla P_1(\mathbf{x}; \mathbf{x}_1) - P_1(\mathbf{x}; \mathbf{x}_1) \nabla G(\mathbf{x}_2; \mathbf{x}) \big] \cdot \mathbf{n} dS. \tag{1.52}$$

The Kirchhoff integral allows us to extrapolate the wavefield recorded on the surface S forwards or backwards in time, depending on what Green function we choose, the causal (forward) and anti-causal (backward), respectively. We observe that the dependency on the source position in equation 1.52 is not necessary, as long as we now the Green function between $\mathbf{x}$ to $\mathbf{x}_2$, and have recordings of P and $\mathbf{n} \cdot \nabla P$ on the surface S.

In conventional seismic data acquisition, only the pressure is recorded. Both pressure and the normal derivative of the pressure ($\mathbf{n} \cdot \nabla P$) are recorded in multi-component seismic data acquisition. If we only know either the pressure or the normal derivative of pressure, we cannot know which direction the wavefield came from. When both are known, it is possible to perform more advanced processing of seismic data (Amundsen, 1993; Ikelle and Amundsen, 2005; Amundsen and Robertsson, 2014), including separation of the recorded wavefield in up- and downgoing wavefields (receiver-side deghosting). More details on acoustic and elastic reciprocity can be found in Fokkema and van den Berg (1993) and Arntsen and Carcione (2000); Aki and Richards (2002); Ikelle and Amundsen (2005).

1.5 Finite-difference method

The wave equation can only be solved analytically for some specific models, boundary conditions and initial conditions. For complex models, numerical methods must be used. Modeling of seismic wave propagation is an important part in seismic imaging and inversion. The most common way of solving the wave equation for complex models is by replacing the derivatives in the equations of motion and Hooke's law with finite-difference (FD) approximations:

$$\frac{df(x)}{dx} \approx \frac{1}{\Delta x} \sum_{n=-N}^{N} a_n f(x \pm n\Delta x). \tag{1.53}$$

Where f(x) is the function we want to find the derivative of, x is a position in a specified dimension, Δx is a step length in the same dimension. The coefficients a_n are the finite-difference coefficients. Higher accuracy of the FD-approximation is obtained when more points $(2N)$ are included in equation 1.53 or a smaller step length Δx is used. By increasing the number of points used for differentiation or decreasing the step length, the computational time also increase. The most common ways of finding the finite difference coefficients are either through Taylor expansion, where the FD-operator will be accurate to the order of $2N$ in Δx for central difference operatord, or by trying to minimize the grid dispersion (e.g. Holberg, 1987). Given initial and boundary conditions, the particle motion and stress propagation can be solved using FD-methods on a discrete points in space and for a discrete number of times.

An example of a modeled seismic shot record is shown together with the acoustic velocity model in Figure 1.12. The evolution of the corresponding acoustic wave propagation is shown in Figure 1.13. Here, a staggered-grid approach using central difference operators (Virieux, 1986) is used to solve for the wavefield.

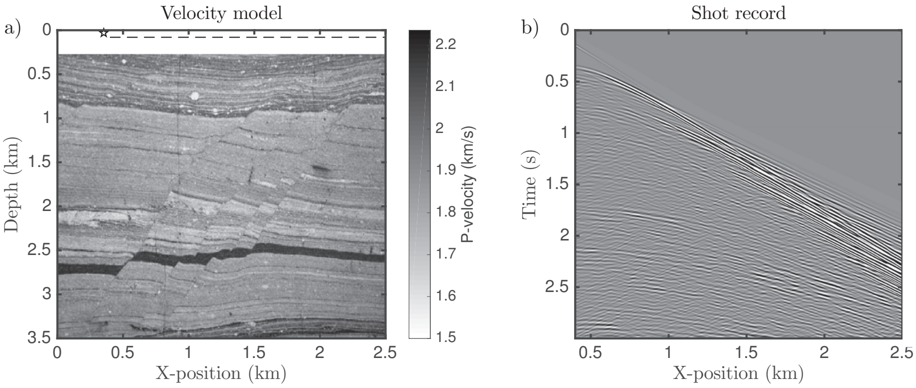

Figure 1.12: a) The velocity model used for modeling of seismic data. b) The recorded wavefield from the dashed line in a), resulting from a source positioned at the star in a). The amplitudes have been gained with a factor corresponding to the travel-time to the power of 1.5.

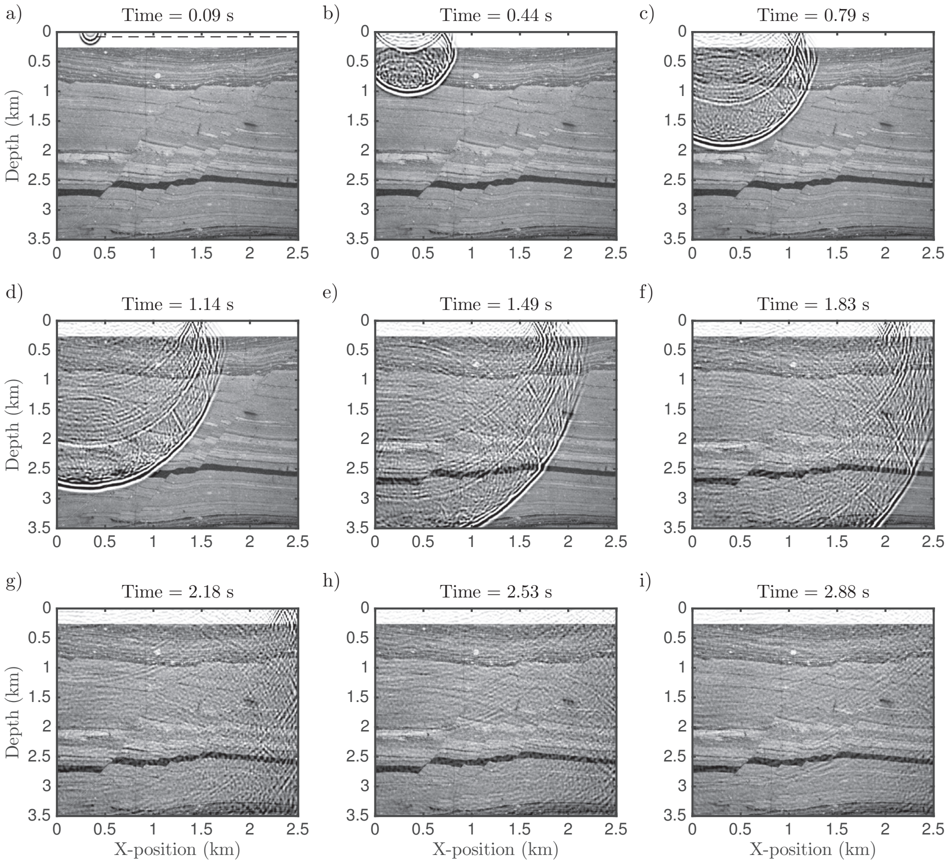

Figure 1.13: Seismic wave propagation. Evolution of the acoustic wavefield overlaid the velocity model. The times from the onset of the source is indicated above each figure.

1.6 Sampling Theory

All data being recorded digitally is sampled. By sampling, we refer to observing a continuous physical quantity only at some discrete points in time or space. The separation between samples in time or space must be chosen carefully so that the recorded data make sense to us. Sampling theory is fundamental for a vast scientific, technical and everyday applications. The basis of sampling theory is the Comb function or sampling function:

$$c(t, \Delta t) = \sum_{m=-\infty}^{\infty} \delta(t - m\Delta t), \tag{1.54}$$

where $\delta(t)$ is Dirac's delta function and Δt is the sampling period. Equation 1.54 can be written in terms of a Fourier series as:

$$c(t, \Delta t) = \sum_{n=-\infty}^{\infty} c_n e^{\frac{2\pi i n t}{\Delta t}}, \tag{1.55}$$

where $i = \sqrt{-1}$ is the imaginary unit and c_n is the complex Fourier-series coefficients given as:

$$c_n = \frac{1}{\Delta t} \int_{-\Delta t/2}^{\Delta t/2} c(t) e^{\frac{-2\pi i n t}{\Delta t}} = \frac{1}{\Delta t} \int_{-\Delta t/2}^{\Delta t/2} \sum_{m=-\infty}^{\infty} \delta(t - m\Delta t) e^{\frac{-2\pi i n t}{\Delta t}} = \frac{1}{\Delta t}. \tag{1.56}$$

Thus, the Comb function can be written as:

$$c(t, \Delta t) = \frac{1}{\Delta t} \sum_{n=-\infty}^{\infty} e^{\frac{2\pi i n t}{\Delta t}}. \tag{1.57}$$

The Fourier transform of the Comb function is given by:

$$C(f) = \int_{-\infty}^{\infty} c(t) e^{-2\pi f t} dt = \frac{1}{\Delta t} \sum_{n=-\infty}^{\infty} \int_{-\infty}^{\infty} e^{-2\pi t (f - n/\Delta t)} dt \tag{1.58}$$

This integral can be found through the frequency-shift property of the Fourier transform, and is given as:

$$C(f) = \frac{1}{\Delta t} \sum_{n=-\infty}^{\infty} \delta\left(f - \frac{n}{\Delta t}\right) \tag{1.59}$$

This shows that the Fourier transform of a Comb function in the time (or space) domain corresponds to a Comb function in the frequency (or wavenumber) domain.

A sampled signal can be written as the product between a continuous signal and the Comb function:

$$s(t) = g(t) c(t, \Delta t) \tag{1.60}$$

where $s(t)$ is the sampled function and $g(t)$ is the continuous function. If we take the Fourier transform of $s(t)$, we obtain:

$$S(f) = G(f) * C(f) \tag{1.61}$$

where $*$ denotes convolution. This shows that the whole frequency spectrum of $G(f)$ will reoccur around every frequency that is an integer multiple of Δt^{-1}. This is shown in Figure 1.14 for a 200 Hz Ricker (Figure 1.14a) wavelet for two different sampling intervals of 0.5 ms (Figure 1.14e) and 1 ms (Figure 1.14d), respectively. The highest frequency of the 200 Hz Ricker wavelet is around 750 Hz. The corresponding amplitude spectra are shown in Figure 1.14b,c and d. We observe that when the signal is sampled densely (0.5 ms) the reoccurring amplitude spectra do not overlap. When the signal is sampled more coarsely (1 ms), the spectra overlap. The blue thin lines in Figure 1.14f shows the original spectra around $f = -1000$ Hz, 0 Hz and 1000 Hz for reference.

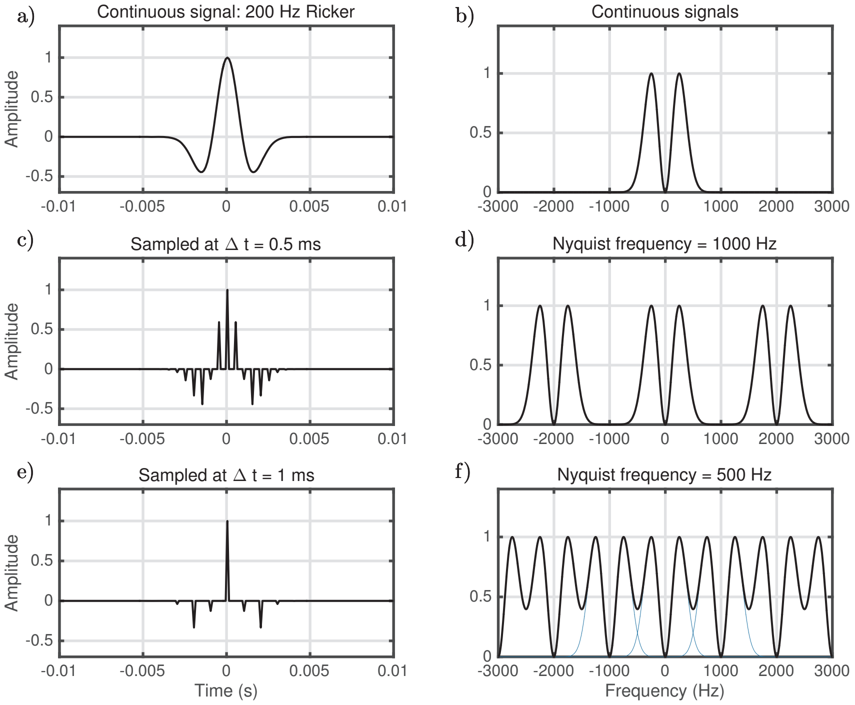

Figure 1.14: a) A continuous signal in time: 200 Hz Ricker wavelet. b) The amplitude spectra of the signal in a). c) Signal in a) sampled every 0.5 ms. d) The amplitude spectra of the signal in c). e) Signal in a) sampled every 1 ms. f) The amplitude spectra of the signal in e). The blue thin lines in f) shows the original spectra around $f = -1000$ Hz, 0 Hz and 1000 Hz.

There are restrictions on how high frequencies the continuous signal can contain when we perform sampling. The highest frequency that can be in the signal, and still be sampled correctly, is the Nyquist frequency given by (Nyquist, 1926):

$$f_N = \frac{1}{2\Delta t}. \tag{1.62}$$

If the signal is sampled correctly, it is possible to reconstruct the continuous signal using sinc-interpolation (Shannon, 1949). If the signal is not sampled correctly, we say that the signal is aliased, i.e. energy that originally had a given frequency will appear at another frequency. Seismic recording equipment usually contains an analog low-pass filter that removes energy at frequencies higher than the Nyquist frequency to avoid aliasing. In seismic acquisition, aliasing is not a problem for sampling in time domain. However, for spatial dimensions, and especially sampling in the X-line, aliasing is abundant.

1.7 Motivation for VSDA

Broadband seismic data acquisition is the new standard for marine seismic acquisition. Data with a broad bandwidth is desirable for interpretation and inversion of seismic data, as illustrated in section 1.2. In marine seismic acquisition, the ghost reflections on the receiver and source side limit the fidelity of the recorded seismic data. Removing the ghost reflections is one of the most important processes to recover the full bandwidth of the seismic data. The ghost reflections have been known for a long time (e.g. van Melle and Weathernurm, 1953), but it has taken more than 50 years for broadband seismic acquisition to become reality. Several solutions for mitigating the ghost reflections on the receiver side exist, including multi-component streamers, slanted streamers and streamers at two depths (over/under acquisition). In the past two decades, all these methods have been successfully commercialized. The first tests presented of marine broadband seismic streamer acquisition system was the over/under system (Sonneland and Berg, 1985; Brink and Svendsen, 1987; Posthumus, 1993). However, the over/under acquisition was not very successful in the 80's and early 90's, this was because the acquisition systems did not have proper control of the streamer positions. The first commercial broadband seismic success was the Geo-Streamer provided by PGS. The GeoStreamer is a streamer that consist of both hydrophones and geophones (Tenghamn et al., 2007), utilizing an old idea (Pavey and Pearson, 1966) for separating the recorded wavefield into up- and down-going wavefields. The up-going wavefield corresponds to the receiver-ghost free wavefield. In response to this, CGG introduced their Broadseis acquisition system and WesternGeco (now part of Schlumberger) introduced two acquisition systems: ObliQ and DISCover. Both the Broadseis and ObliQ systems are based on the idea of slanting the streamers to obtain ghost notch diversity (Ray and Moore, 1982). The data acquired with this type of streamer geometry are processed to output receiver-ghost free data (Soubaras and Dowle, 2010; Moldoveanu et al., 2012). The DISCover acquisition system is based on over/under streamers (Parrack, 1974; Posthumus, 1993), that are steerable to better control the positioning (Kragh et al., 2010). Broadband processing of conventional single-level, hydrophone-only, seismic data by means of inverse ghost filtering (e.g. Fokkema and van den Berg, 1993; Amundsen, 1993) or/and by using inversion based "bootstrap" methods (Wang and Peng, 2012; Wang et al., 2013) have also resulted in major uplift in the quality of the resulting seismic images (e.g. Zhou et al., 2012; Dhelie et al., 2014). In 2014, Schlumberger launched their IsoMetrix seismic acquisition system (Robertsson et al., 2008a). The IsoMetrix system consists of multi-component streamers, measuring pressure and particle acceleration in both vertical and horizontal directions. This makes it possible to separate the wavefield into up- and down-going wavefields, as for the GeoStreamer technology. Furthermore, the particle accelerations can be used to obtain spatial gradients of the pressure wavefield (equation 1.30 with p= $-\sigma$), and by using the multichannel sampling theorem (Linden, 1959), it is possible to reconstruct the wavefield in cross-line direction with very high fidelity (see Robertsson et al., 2008a).

The seismic acquisition strategies described above are developed mainly to mitigate the problem of the receiver ghost in marine seismic acquisition. The source-side ghost is also degrading the recorded seismic data. A major difference between source-side and receiver-side deghosting is related to the angle of incidence. For data recorded on a streamer, with some length and sampling interval, it is possible to tell at what angle the wave-fronts passed the streamer. Knowledge of this angle is crucial for the deghosting process as the time-delay of the ghost is angle dependent. For source-side deghosting, it is the angle of emergence that controls the source-ghost delay time. The emergence angle from the source is in general not known from the recorded data. It is often assumed that the earth consist of horizontal layers so that the angle of emergence from the source equals the angle of incidence at the streamer. This way, source-side deghosting can be applied in frequency-wavenumber or tau-p domains (e.g. Amundsen, 1993; Agudo et al., 2016). A problem with deghosting in general is that the process involves a division by zero in the frequency domain (see equation 1.10). This makes deghosting very sensitive to noise. For source-side deghosting, several solutions have been proposed and commercialized, and all involve deconvolution. A popular way of making this deconvolution stable has been to use multi-level sources to fill the deep ghost notch (Moldoveanu, 2000; Sablon et al., 2013; Shen et al., 2014). This is analogous to using over/under streamers for receiver-side deghosting, but is not quite the same. This is because data acquired with over/under streamers consist of separate recordings at two levels, while for the multi-level source, the signal from the sources are not separated since the sources are fired at about the same time. Another approach for source-side deghosting is the inversion-based bootstrap method (Wang et al., 2015; Fu et al., 2015), which inverts for the deghosted (and designatured) data, and can be applied for both the source and receiver sides.

An ideal seismic source, would be a combination of monopole and dipole sources. If the signal from the two were designed properly, it would result in a purely down-going wave, *i.e.*, ghost free. This is analogous to multi-component recordings where we measure the vertical motion (dipole) and pressure (monopole) at one level. However, making powerful marine dipoles is not trivial, and research on this is topic is ongoing (e.g. Meier et al., 2015).

The source-side analogy to slanted-streamer acquisition involves changing the source depth on a shot-to-shot basis: Variable source-depth acquisition (VSDA). Research on this is at least limited, and to my knowledge, no publications on this topic existed prior to this PhD project. There are probably several reasons for this: It is operationally difficult to change the source depths with current technology, the far-field source signature will be different from shot to shot, thus making processing more difficult, and no research has shown the benefit of performing this kind of acquisition. The first part of this thesis is devoted to exploring the potential of variable source-depth acquisition of seismic data. Several aspects and implications related to VSDA are presented.

1.8 Simultaneous source separation

In addition to increasing the usable bandwidth of seismic data, optimizing acquisition with respect to quality and cost is important in modern seismic acquisition. This section is not linked to VSDA, but serves as a brief introduction to simultaneous source separation.

It is becoming more common to acquire seismic data using simultaneous sources during acquisition (Beasley, 2008; Hampson et al., 2008; Abma et al., 2015; Kumar et al., 2015; Zhan et al., 2015; Langhammer and Bennion, 2016), also known as blended acquisition (Berkhout, 2008). By using simultaneous sources it is possible to cover a larger area over the same time period, to achieve data with denser shot sampling and data richer in azimuths. A problem that arises when acquiring data with several sources fired (almost) simultaneously, is that the recorded data consist of wavefields from more than one source. Before the data can be processed into images or inverted in the normal fashion, separation of the wavefields from the respective sources must be carried out. There exist different methods for doing so: Using time-dithered sources (Moore et al., 2008; Hampson et al., 2008; Abma et al., 2015), source encoding (e.g. Robertsson et al., 2008b; Mueller et al., 2015), and the recent signal apparition method (Robertsson et al., 2016a). The most common method has been to use time-dithered sources, for example, two sources that are fired with scheduled time-dithers (delays) apart. The time-dithering is varied from shot to shot, but always known. There are at least two different ways of separating this kind of data: 1) The recorded data can be sorted into appropriate domains where the interfering signal from the other source can be treated as noise and filtered out. 2) The use of inversion to predict and subtract the interfering signal (Abma et al., 2015). In the source encoding approach, the individual source elements of a source array (e.g. air gun for marine acquisition) are fired in an encoded sequence rather than simultaneously. By using two source arrays with orthogonal source encoding in simultaneous acquisition, separation can be achieved by cross-correlating the data with the respective source encodings (Mueller et al., 2015). The seismic apparition, or signal apparition, method proposed by Robertsson et al. (2016a), rely on different, but periodic sampling in shot domain. If a signal consists of two signals that are sampled differently, they have different periodicity in the frequency domain (see section 1.6), and separation can be achieved by carefully picking out different parts of the FK-spectra. In work, not related to VSDA, performed during this PhD, the potential of using the apparition methodology to separation of simultaneous source towed-streamer seismic data is proposed.

1.9 Thesis structure

The main part of the thesis comprises 6 independent papers, either published or submitted to peer-reviewed journals, that are organized in chapters. Because of this, there are to some extent overlapping introductions and different notation. The four first chapters consist of the work related to VSDA. Chapter 6 and Appendix A consist of work that have been performed during this PhD period, but not particularly related to VSDA. A brief summary of the papers are given below:

In Chapter 2, variable source-depth acquisition (VSDA) is presented for the first time. An inversion is used to find an optimal sequence of source depths for obtaining a white frequency spectra in final image. An example using measured quasi near-field signatures shows that VSDA can provide a whiter frequency spectra when data from several source depths are stacked in the final image.

Chapter 3 describes an empirical relationship between source signatures from an air gun fired at different depths. A correction factor to the Rayleigh-Willis equation for sources close to the free surface is also presented here. Tests of the empirical relationship show that the method works well as long as the difference in source depth is not too large ($< \pm$ 10 m). Furthermore, the corrections factor improves the predicted source signatures for sources that are position shallow.

Chapter 4 is a modeling study of three different source strategies for marine seismic acquisition: Single-level source (conventional acquisition), multi-level source and variable source-depth acquisition. This study provides useful insight into the potentials of VSDA. Although the modeling is relatively simple, it shows that ghost-notch diversity in VSDA results in better signal-to-noise ratio in a broad bandwidth compared to the other strategies. The variations in source signature between successive shots in VSDA results in lower quality data in low-fold areas, e.g., for very shallow geology, but is not apparent in deeper parts of the image ($t > 0.3$ s)

Chapter 5 describes a method for implementing arbitrary marine source wavefields in finite difference methods. The method is a hybrid approach where an analytical source wavefield is injected on to the finite difference grid. The analytical wavefield is based on notional source signatures that are assumed to be known. This can be used to implement sources that does not coincide with with the grid points in finite difference methods.

The apparition methodology (Robertsson et al., 2016a) is used to perform wavefield separation on synthetic simultaneous-source towed-streamer data in Chapter 6. The separation is performed in the common-offset domain. The examples show that the separation process works quite well on the given examples. We propose to use this for separation of site survey and conventional seismic data acquired simultaneously.

Appendix A is a study of shallow gas accumulations in the Central North Sea. A new trapping mechanism for shallow gas is proposed. The study is mostly based on interpretation in conventional 3D seismic data.

1.10 Contributions

The contributors to the papers in the thesis are as follows:

- **Paper 1, Chapter 2:** Variable source depth acquisition for improved marine broadband seismic data *Published in Geophysics, Vol. 80, No. 3. A69–A73.*
  This work was performed by Kjetil Eik Haavik as the lead author and researcher. Martin Landrø participated as a supervisor.
- **Paper 2, Chapter 3:** Estimation of source signatures from air guns fired at various depths: A field test of the source scaling law. *Published in Geophysics, Vol. 81, No. 3, P27–P36.*
  This work was performed by Kjetil Eik Haavik as the lead author and researcher. Martin Landrø participated as a supervisor.
- **Paper 3, Chapter 4:** Variable source depth acquisition for (an overall) improved signal-to-noise ratio in marine broadband seismic data: A modeling study. *Submitted to Geophysics*
  This work was performed by Kjetil Eik Haavik as the lead author and researcher. Martin Landrø participated as a supervisor.
- **Paper 4, Chapter 5:** Implementation of marine seismic source wavefields in finite-difference methods using wavefield injection. *Published in Geophysics, Vol. 81, No.5, T211–T219*
  This work was performed by Kjetil Eik Haavik as the lead author and researcher. Espen Birger Raknes provided his FWI code which was modified to incorporate the method suggested in the paper. Martin Landrø participated as a supervisor.
- **Paper 5, Chapter 6:** Wavefield separation using seismic apparition on towed streamer data with distributed source arrays: Site survey and conventional survey in one go? *Submitted to Geophysics*
  This work was performed by Kjetil Eik Haavik as the lead author and researcher. Martin Landrø participated as a supervisor.
- **Paper 6, Appendix A:** Iceberg ploughmarks illuminated by shallow gas in the Central North Sea. *Published in Quaternary Science Reviews, Vol.103, P43–50*
  This work was performed by Kjetil Eik Haavik as the lead author and researcher. Martin Landrø participated as a supervisor.

Chapter 2

Variable source depth acquisition for improved marine broadband seismic data*

Kjetil Eik Haavik and Martin Landrø
Norwegian University of Science and Technology, Trondheim, Norway

2.1 Abstract

In marine seismic data acquisition, varying the source depth along a sail line gives diversity in sequential shot gather frequency spectra. Undesired alterations of the frequency spectra are created by the source ghost and by air-gun bubble oscillations. By deliberately varying the source depth along a sail line, it is possible to obtain a seismic data set that will have energy more evenly distributed within the main frequency band of the source output. This is obtained when data acquired with different source depths are stacked in imaging. We formulate a simple inverse problem that seeks to find the optimal distribution of source depths over a sequential series of shots that shape the amplitude spectrum of the final image into a desired shape. We assumed that the data are receiver-side deghosted, that designature could be applied to each shot gather, and that the shot gathers could be redatumed to a common datum prior to imaging.

---

[*] *Paper published in GEOPHYSICS, Volume. 80, number 3 (May-June 2015); P. A69–A73. DOI:10.1190/geo2014-0437.1*

2.2 Introduction

Recent interest in broadband seismic, and especially the low-frequency end, has triggered several seismic acquisition solutions. Increasing the bandwidth of the seismic signal in the low end of the frequency spectrum improves penetration and resolution in reflection seismic data, and it is beneficial in waveform and impedance inversion (ten Kroode et al., 2013). Marine seismic acquisition systems that provide seismic data with broader bandwidth have been developed, and the most important feature of these systems is their ability to eliminate the ghost reflections from the free surface. The ghost reflections causes deep notches in the amplitude spectra of the recorded data at frequencies determined by the depths of the source and the receivers. Improvements in positioning systems, recording devices, computer power and new processing algorithms are probably the most important factors that have made it possible to realize older ideas dealing with the ghost (e.g. Berni, 1982; Ray and Moore, 1982; Sonneland and Berg, 1985). For the receiver side, broadband acquisition systems can be divided into two main categories: (1) Multicomponent recordings (e.g. Loewenthal et al., 1985; Robertsson et al., 2008a; Vaage et al., 2008; Day et al., 2013) and (2) slanted streamer profiles (e.g. Ray and Moore, 1982; Soubaras and Dowle, 2010; Moldoveanu et al., 2012), which allows for deghosting by wavefield separation and deconvolution, respectively. However, deghosting of conventional seismic data, i.e. pressure measurements at constant streamer depth, also result in improvements of the final image compared to non-deghosted data (Zhou et al., 2012; Dhelie et al., 2014). The source side deghosting algorithms used today rely on predictive deconvolution and/or by using multi-level sources to avoid the notches introduced by the ghost reflection (Moldoveanu, 2000; Hopperstad et al., 2008a; Sablon et al., 2013; Halliday, 2013).

Here, we present a new strategy for acquiring seismic data for improving the ghost notch and bubble notch diversity related to the air-gun source. As a reciprocal experiment to the slanted streamer, the source depth is varied along a sail line to obtain notch diversity in the amplitude spectra. Furthermore, by choosing the source depths carefully it is possible to optimize the shape of the frequency spectrum for the final seismic image.

Theory

2.2.1 Notches in the air gun spectrum

The acoustic signal generated by an air gun has been studied extensively (Giles, 1968; Ziolkowski, 1970; Vaage et al., 1983; Ziolkowski et al., 1982; Landrø et al., 2011; Barker and Landrø, 2013). The low frequency output from an air-gun array is primarily related to the bubble that expands and contracts several times before it dissolves or breaks the air-water interface. The bubble-time period is dependent on the firing pressure P, air-gun volume V and source depth z in meters, and is given by the Rayleigh-Willis formula(Rayleigh, 1917; Willis, 1941):

$$\tau = const.\frac{P^{\frac{1}{3}}V^{\frac{1}{3}}}{(10+z)^{\frac{5}{6}}}. \tag{2.1}$$

The low frequency output will have a maximum at the frequency $f_b = \tau^{-1}$. The bubble also create notches, or depressions, in the frequency spectrum that are periodic related to the bubble time period as (Landrø and Amundsen, 2014a):

$$f_{bn} = \frac{n+\frac{1}{2}}{\tau}, \quad n = 0, 1, 2, \dots\ . \tag{2.2}$$

Interference between the primary downgoing wavefield and wavefield reflected at the free surface causes notches in the frequency spectrum. Assuming that the signal is recorded vertically below the air gun, the notches are positioned at the frequencies given by:

$$f_{gn} = \frac{c}{2z}n, \quad n = 0, 1, 2, \dots\ , \tag{2.3}$$

where c is the sound velocity of water and z is the source depth. Thus, the far-field amplitude spectrum from an air gun will have notches related to both bubble oscillations and the free surface. The notches, or depressions, due to the bubble oscillations are small compared to the notches caused by the ghost reflection. This is because a tuned air-gun array has a diversity of bubble periods. The severity of these notches and depressions depends on the free-surface reflection coefficient for the ghost notches and the primary to bubble ratio for the bubble related notches, respectively.

The low frequency output from an air-gun array is almost unaffected by the source depth (Hegna and Parkes, 2011; Hopperstad et al., 2012; Landrø and Amundsen, 2014a). There are two major effects related to the depth of the source that influences the low frequency output from an air gun. The bubble time period increases as the source depth decreases; resulting in more low frequency energy. However, the change in ghost response due to the same decrease in source depth will counteract that increase in low frequency output. Hopperstad et al. (2012) showed even greater constraints on the low frequency output from an air-gun cluster: The output well below the lowest bubble resonance frequency is only determined by the total quantity of air released, i.e. the product of firing pressure and the total volume.

2.2.2 Inverting for optimal source depths

Acquiring seismic data with a constant source depth will result in a data set that contains notches due to the ghost reflection and the bubble oscillations at the same frequencies throughout the data set. To avoid this we suggest to use various source depths along sail lines. Our objective is to obtain a data set that, over a sequence of shots, has energy distributed equally amongst all frequencies in the final image. If we, for simplicity, only consider the signal propagating vertically from the source, the total frequency spectrum of the final stacked image from combining data acquired with N different and predefined source depths is given as:

$$\mathbf{s}(f) = \sum_{i=1}^{N} a_i \mathbf{k}_i(f), \tag{2.4}$$

where k_i is the vertical far-field amplitude spectrum from the source fired at depth i, f is the frequency, and a_i is a weight factor at the ith source depth. The choice of a_i will determine the shape of the total frequency spectrum and a_i is used to find the number of sources that should be positioned at depth z_i in a shot sequence. Equation 2.4 can be written in matrix notation as $\mathbf{s} = \mathbf{K}\mathbf{a}$.

We formulate an inverse problem that seeks to find the set of a_i that shape the total frequency spectrum $\mathbf{s}$ of the final image into a desired frequency spectrum $\mathbf{s}_\mathbf{d}$. We define the objective function for this inverse problem as

$$\Phi(\mathbf{a}) = \Phi_d(\mathbf{a}) + \beta\Phi_m(\mathbf{a}), \tag{2.5}$$

where $\mathbf{a}$ is the model vector that contains the weights, Φ_d is the data objective function, β is a regularization parameter (Tikhonov and Arsenin, 1977) and Φ_m is the model objective function. We use the standard least-squares norm for the data and model objective functions, respectively:

$$\Phi_d(\mathbf{a}) = \frac{1}{2}\|\mathbf{W}_d(\mathbf{K}\mathbf{a} - \mathbf{s}_d)\|^2, \tag{2.6}$$

and

$$\Phi_m(\mathbf{a}) = \frac{1}{2}\|\mathbf{W}_m\mathbf{a}\|^2, \tag{2.7}$$

where $\mathbf{W}_d$ is the data weighting matrix and $\mathbf{K}$ is a matrix containing the kernel functions. The kernel functions for this problem are the amplitude spectra for vertical far-field source signatures from sources fired at different depths. $\mathbf{W}_m$ is a weighting matrix in model space. Here, we use $\mathbf{W}_m$ as the differential operator that will penalize rapid variation in $\mathbf{a}$. This is done for practical reasons, as we would like to have a smooth transition between the different source depths during acquisition. A solution that minimizes the objective function in equation 2.5 with respect to $\mathbf{a}$ is given in e.g. Oldenburg and Li (2005) as:

$$\mathbf{a} = \left(\mathbf{K}^T\mathbf{W}_d^T\mathbf{W}_d\mathbf{K} + \beta\mathbf{W}_m^T\mathbf{W}_m\right)^{-1}\left(\mathbf{K}^T\mathbf{W}_d^T\mathbf{W}_d\mathbf{s}_d\right). \tag{2.8}$$

We suggest to design a sequence of source depths (SSD) that will result in an amplitude spectrum of a desired shape. The number of shots within the SSD times an integer should be equal to the common mid point (CMP) fold to ensure that all CMP's contain traces from all source depths within an SSD. It is clear that the depths of sequential sources must be close to make the necessary changes in source depth as smooth and simple as possible. There might be several potential practical solutions to achieve this, but what we foresee is a source depth controller that continuously moves sources up and down in a gentle and smooth manner.

2.3 Optimal source depths using field data

A field experiment was conducted in a Norwegian fjord a few years ago (Landrø and Amundsen, 2014a). A single 600 in^3 air gun was used as source. The water depth at the location is approximately 390 m, and the weather conditions were excellent during tests. The source was positioned at approximately 3, 5, 7, 10, 15, 20, 25, 30, 35 and 40 m, and a hydrophone was positioned 20 m below the source. The far-field signatures from the sources fired at different depths were estimated by the notional source method (Ziolkowski et al., 1982) and then convolved with the source ghost functions for the respective source depths. The data were filtered with a high-cut filter (out-230-250 Hz) and normalized to the highest amplitude. The estimated far-field signatures are shown in Figure 2.1. The far-field signatures in Figure 2.1 show the expected characteristics from sources fired at different depths. The primary pulse is aligned for all source depths (white spike at approximately 0.025 s), and the ghost reflection is seen as the black spike following the primary pulse and is deviating more as the source depths are increasing. The first bubble can be seen at approximately 0.2 s for the first trace, and is shifted towards earlier times as the source depths increase.

We perform two inversions as described in equation 2.8, one with regularization ($\beta \neq 0$) and the second without regularization. The kernel matrix $\mathbf{K}$ contains the frequency spectra of the estimated vertical far-field signatures from each depth and the identity matrix was used for the data weighting matrix $\mathbf{w}_d$. For the desired spectrum $\mathbf{s}_d$, we use a white spectrum within the frequency band of interest (0 - 250 Hz). We would like to find the combinations of source depths that will give the flattest amplitude spectrum using 40 shots. The results from these inversions are compared to the amplitude spectrum of a multilevel source that consists of two air guns at 6 and 9 m and have strengths equivalent to two-thirds and one-third of the air gun used in the inversion, respectively. Because there are no records from sources fired at 6 and 9 m, we use notional source signatures from the sources fired at 5 and 10 m and then convolve them with the ghost response for 6 and 9 m, respectively, and tuned them on peak. This will not give the correct bubble time period, but will give the amplitude spectra closest to the much-used 6 and 9 m configuration. The inversion results are shown in Figure 2.2 and the corresponding distribution of source depths are shown in Figure 2.3.

The inversion results in Figure 2.2 show that the variable source depths (blue and black curves) give whiter amplitude spectra than the multi-level source (red curve). The ghost notches corresponding to source depths of 6 and 9 m are 125 and 83 Hz, respectively, and we observe a large difference in amplitudes between the multi-level source and the inversion results in the vicinity of those frequencies. We observe a significant improvement also for low frequencies, especially around 10 Hz, where the inversion results show an improved amplitude response of up to 12 dB. The notch around 10 Hz, and oscillating behaviour observed in the spectrum of the multi-level source is a result of the the bubble oscillations. This behaviour is far less pronounced in the amplitude spectra estimated from the inversion. The cause for this is the diversity of bubble notches as multiple source

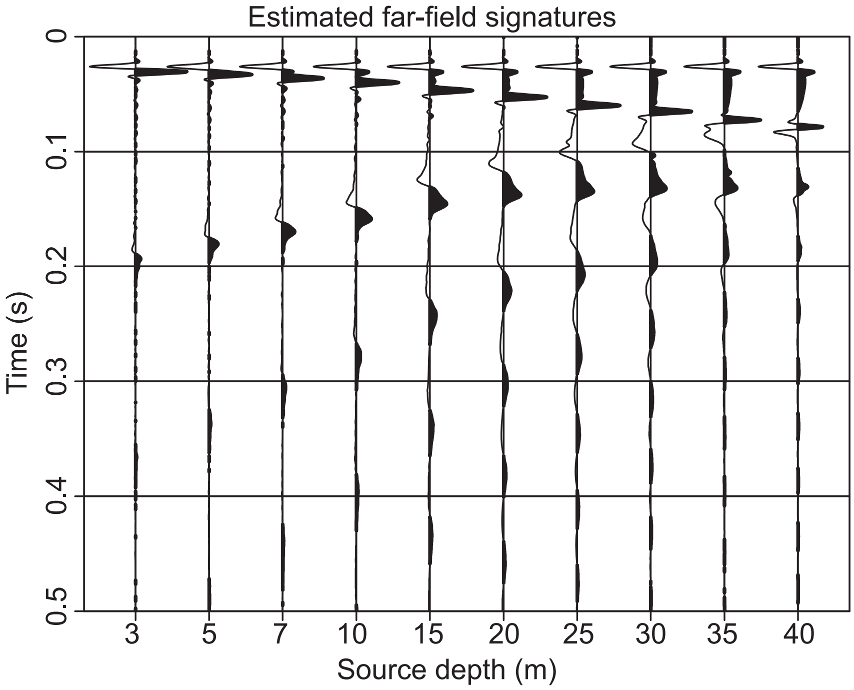

Figure 2.1: The estimated far-field signatures for zero offset from a single 600 in^3 air gun fired at depths ranging from 3 m to 40 m. Note how the bubble pulse delay is reduced as the source depth increases. Also note the free surface ghost and how it is delayed as the source depth increases.

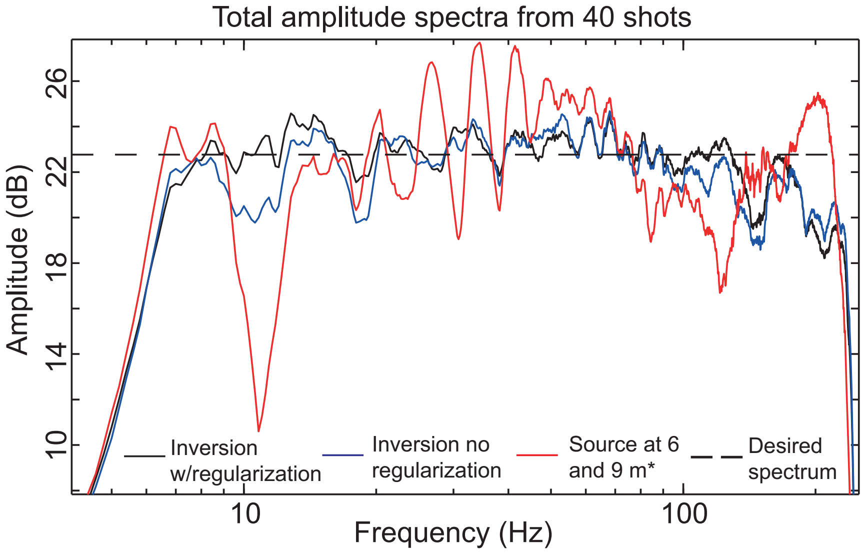

Figure 2.2: The total amplitude spectra from combining data from air guns fired at different depths. The black and blue curves are the amplitude spectra from the inversion with and without regularization, respectively. The red curve is the amplitude spectrum from a multi-level source with sources at 6 and 9 m. Since no source signatures were recorded from sources at 6 and 9 m, we estimated these far-field signatures by convolving the the notional source signatures from 5 and 10 m with the ghost response for source depths of 6 and 9 m, respectively; hence the star.

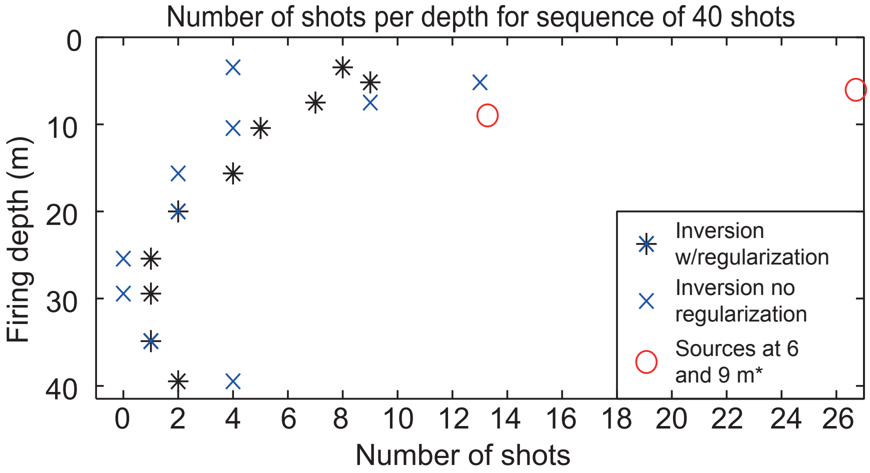

Figure 2.3: The number of shots per source depth in a sequence of 40 shots. The red circles represents the number of the distribution of the strength of the multilevel source with airgun depths of 6 and 9 m.

depths are included. The amplitudes from the multi-level source from 3 - 9 Hz is around 0.5 dB higher, with a maximum difference of approximately 2.5 dB at 7.5 Hz, compared to the amplitudes from the constrained inversion result (black curve). In the frequency band between 170 and 230 Hz we find that the amplitude response from the multi-level source is better than the inversion result. The optimal source depths (Figure 2.3) obtained by inversion show that about 50 % of the shots should be fired at depths in the range 3.4 to 7.5 m, and only 15 % deeper than 15 m. This results aligns well with the discussion in (Landrø and Amundsen, 2014a).

2.4 Discussion

We use the amplitude spectrum resulting from combining data acquired for different source depths for the same take-off angle (vertical). However, a CMP gather contains a signal that left the source with other take-off angles. The optimal source depths in a SSD should therefore be modeled for a specified target. In general, the effect of directivity will influence shallow targets more than deep targets if this is not taken into account in survey design. To be able to benefit the most from variable source depth acquisition (VSDA), each shot gather needs to be redatumed to a common datum, and designature and deghosting should be applied. The two latter processes involve spectral shaping of the data and are fairly common processing steps in modern seismic processing. The term designature often includes debubbling and deghosting. The debubble process is stable because the bubble notches or depressions are small compared with the severe ghost notches.

However, the result of debubbling is dependent on a good estimate of the source signature. The source-side deghosting process consists of deconvolving the recorded data with the ghost response. This process is unstable in the vicinity of the ghost notches, where we have a poor signal-to-noise ratio (S/N) and where we, in practice, divide by zero. If the same source depth is used throughout a seismic survey, it will lead to a data set that suffers from a poor S/N in the vicinity of these frequencies, and we are in a way repeating the same error every shot. VSDA as proposed here will ensure that the final data set has energy distributed more evenly among the frequency band of the source output. Except for the notch present at 0 Hz common for all source depths, notch diversity will ensure that there are no frequency bands within our main signal that have poorer signal to noise ratio than others; i.e., we are not repeating the error. The deghosting process is theoretically sound, but it suffers from a division by zero at the ghost notch frequencies. VSDA is a way to optimize seismic data for processing during acquisition, rather than to do it all during processing. Seismic data acquired with variable source depths will not give a substantial difference on the low-frequency end (less than 6 Hz) of the frequency spectrum compared with other air-gun source configurations. The low-frequency response from an air-gun array is only weakly dependent on the source depth. If we position the source deeper, it will result in a source ghost response more favorable for the low frequencies, but the corresponding reduction in the bubble time period yields less low-frequency output (Hegna and Parkes, 2011; Hopperstad et al., 2012; Landrø and Amundsen, 2014a). However, the main effect and goal of this acquisition strategy is to obtain diversity of the notches related to the ghost and the notches or depressions caused by the bubble. The field data studied here are from a single 600 in^3 airgun, and the bubble is therefore be more pronounced than compared with a tuned air-gun array. Still, is possible to obtain a fairly white spectra. We think that the combination of VSDA and large sources, such as the hypercluster (Hopperstad et al., 2012), will yield data sets that have more low frequency energy and that this can be exploited to improve marine broadband seismic data.

The inversion presented here requires knowledge of the source signatures from each of the source depths. These source signatures should have a high S/N, and ideally be noise free, to prevent the influence of noise in the inversion. Available for this study, we have recordings from a single large air gun fired at depths ranging from 3 to 40 m. This method is not restricted to using a single air gun; as long as the source signatures are known, this method can be used. An alternative to measuring the signatures may be to model them for the different depths. More sophisticated inversions can include source signature modeling as a forward model in an iterative scheme. In such a scheme, more model parameters, such as number of air guns, pressure, and total volume can be included. However, we choose to use the simple inversion here to illustrate the main point of VSDA.

2.5 Conclusions

We suggest gradually changing the source depth along sail lines during acquisition to introduce diversity of the notches and depressions in the frequency spectra caused by the ghost reflection and the bubble oscillation, respectively. Using an inversion to find the optimal source depths over a sequential series of shots, we obtain an amplitude spectrum in the final image that is close to a desired and predefined shape. Here, we specify a white spectrum within the frequency band of the source output as the desired spectrum. The desired shape can be changed to accommodate other shapes, but the final shape is always limited by the bandwidth of the source used.

Based on the recorded seismic data obtained from firing a large single air gun at various source depths, we show that it is possible to use an inversion technique to obtain an optimal sequence of shot depths to produce a close-to-white frequency spectrum. When comparing the spectrum from a multilevel source (6 and 9 m) with the total spectrum of an optimal SSD over 40 shots, we find that the variable source depth spectrum has energy that is more evenly distributed.

2.6 Acknowledgements

Thanks to Lundin Norway AS for financial support to Kjetil E. Haavik's PhD project. We acknowledge Statoil ASA for contributing with the seismic source recordings. Å. S. Pedersen and M. Thomson are acknowledged for designing and conducting the field work. P. E. Dhelie at Lundin Norway AS is acknowledged for useful comments and suggestions that improved this manuscript. The associate editor J. Rickett and two reviewers, including J. F. Hopperstad and one anonymous, are acknowledged for valuable and constructive feedback that have improved this manuscript. Landrø thanks the Norwegian Research Council for financial support.

Chapter 3

Estimation of source signatures from air guns fired at various depths: A field test of the source scaling law*

Kjetil Eik Haavik and Martin Landrø
Norwegian University of Science and Technology, Trondheim, Norway

3.1 Abstract

Recent advances in marine broadband seismic data acquisition have led to a range of new air-gun source configurations. The air-gun arrays have conventionally been kept at a constant depth, but in order to attenuate the source-side ghost reflection new source strategies involving multiple source depths have been proposed. The bubble-time period for an air-gun bubble is dependent on, among many parameters, the firing depth. We use quasi-near-field measurements of air-gun signatures to validate a version of the well-known source scaling law, where the characteristic bubble-time period is used as scale. We find that the source scaling law can be used to estimate a source signature from one depth knowing the source signature at a different depth from the same gun. Furthermore, we present a correction term to the Rayleigh-Willis bubble-time equation to correct for the fact that interaction between the bubble and free surface reduce the bubble-time period. This correction term improve our results significantly for air guns positioned close to the air-water interface. The error between the estimated and measured source signatures is dependent on the difference in source depth. For a depth difference of ±5 m we estimate signatures that have NRMS-differences ranging between 5 and 6 % from the measured signature at the given depth, and 8-12 % when the difference is ±10 m.

---

[*] Paper published in GEOPHYSICS, Volume. 81, number 3 (May-June 2016); P13–P22. DOI: 10.1190/geo2015-0369.1 Parts of this work was presented at the 84th SEG Annual Meeting in 2015

3.2 Introduction

Recent advances in marine broadband seismic technologies have led to several new source configurations. The overall goal of these configurations is to attenuate the ghost reflection from the air-water interface, and therefore reduce the deep notches in the frequency spectra. The different source configurations and acquisition strategies include e.g. multi-level time-synchronized sub arrays (Cambois et al., 2009; Sablon et al., 2013), slanted arrays (Shen et al., 2014; Telling et al., 2014) and variable source depth acquisition (VSDA) where the source depth is varied between successive shots along a sail line (Haavik and Landrø, 2015). A common factor in the new marine source configurations is that they involve sources at more than one depth. It is well known that the bubble-time period of the air-gun bubble is dependent on the hydrostatic pressure, i.e. the Rayleigh-Willis formula. In fact the whole signature is dependent on the hydrostatic pressure and hence the firing depth. Since many of the new marine source configurations involve sources at different depths, we think that it will be of importance to have a tool to easily predict how the source signatures will change when the firing depth is changed. Here we present a simple method for predicting how depth variations will affect the source signatures. This can be used to improve the shot-to-shot de-signature process of seismic data, in particular data acquired with VSDA. However, other applications of this method may be: Calibration between 4D surveys if there are known source depth variations or simply to predict source signatures at various source depths from one measurement. The latter can for instance be used in finding optimal sequence of source depths in VSDA (Haavik and Landrø, 2015) or optimal depths for separate guns in a slanted array (e.g. Shen et al., 2014).

In this work, we show that the source scaling law (e.g. O'Brian, 1969; Giles and Johnston, 1973; Ziolkowski et al., 1980; Ziolkowski, 1986) offers a nice way to estimate the change in signature as the source depth is altered. The source scaling law states that a source signature will change if there are changes in the acquisition parameters, such as initial energy of the bubble or the hydrostatic pressure, and that the new source signature will be a scaled version of the initial signature with respect to amplitude and time. Here we adapt a formulation by Giles and Johnston (1973) which is used to correct air-gun signatures for pressure variations from surrounding seismic sources. Giles and Johnston (1973) used a sample-to-sample correction to the source signature that was based on the change in the bubble-time period due to an external pressure change. The key parameters in the source signature estimation is thus the bubble-time period, and a good understanding of this is crucial. For shallow firing depths we use a correction term to the Rayleigh-Willis formula to estimate the bubble time period. The correction term reduces the bubble-time period and arises from similar effects as to why clustering of air guns increases the bubble-time period. This correction was first described by Herring (1941). To the authors knowledge, this has not been adapted in the exploration geophysics community, even though other work in Herring (1941) has been cited (e.g. Ziolkowski, 1970; Landrø and Sollie, 1992; Ziolkowski et al., 1998). We think it is worthwhile to describe this in some detail here.

We use quasi-near-field measurements of air gun signatures to validate the well-known source scaling law. Air-gun signatures was measured from a 600-in^3 air gun fired at depths ranging from 3 m to 40 m with the same initial pressure of 2000 psi.

Theory

3.2.1 Bubble-time period close to a free surface

The air-bubble generated by an air gun oscillates with a fundamental time period which is dependent on the firing pressure P_i, air-gun volume V_i and the hydrostatic pressure P_∞ at a given water depth, and is given by the Rayleigh-Willis formula (Rayleigh, 1917; Willis, 1941):

$$T_{RW} = const. \frac{P_i^{\frac{1}{3}} V_i^{\frac{1}{3}}}{P_\infty^{\frac{5}{6}}}, \tag{3.1}$$

where

$$P_\infty = p_0 + \rho g z, \tag{3.2}$$

p_0 is the atmospheric pressure which is practically equivalent to a 10 m column of water, ρ is the density of water, g is the acceleration of gravity and z is the source depth in meters below the air-water interface. The physics involved in deriving the Rayleigh-Willis formula consists of a simple model for bubble motion in an incompressible, inviscid and infinite medium (Rayleigh, 1917) and an assumption that the maximum radius can be estimated based on adiabatic expansion (Willis, 1941). Rayleigh's equation for bubble motion is derived assuming there are no constraints from the surroundings. The effect of bubble oscillation close to a free surface or a rigid wall was first described by Herring (1941), who showed that the kinetic energy of the system of a bubble and rigid wall or a bubble and free surface is increasing or decreasing, respectively, compared to the case where the bubble is positioned in an infinite medium. Correspondingly, the bubble-time periods increase and decrease for the two respective cases compared to bubble-time period of a bubble in an infinite medium. Later, many scientists have studied the interactions between an oscillating bubble and a boundary (e.g. Rattray, 1951; Chahine, 1977; Blake and Gibson, 1981; Wang et al., 1996; Barker and Landrø, 2012). In the exploration geophysics community, it is established that clustering of air-guns increase the bubble-time period (e.g. Vaage and Ursin, 1987; Strandenes and Vaage, 1992; Barker and Landrø, 2012), but the reduction in bubble-time period when an air-gun is close to a free surface has not been discussed to the same detail.

The problem of an oscillating bubble or collapse of a cavity close to a free surface has been studied extensively in other scientific communities (e.g. Voinov and Voinov, 1975; Chahine, 1977; Blake and Gibson, 1981; Wang et al., 1996). When the bubble is close to the free surface, its motion will change the shape of the free surface and in addition the shape of the bubble gets distorted due to the non-spherical flow. A key parameter determining this effect is the ratio between the initial depth from the free surface to the center of the bubble (b) and the maximum bubble radius (R_m), $\alpha = b/R_m$. In the absence of gravity, bubbles where $\alpha > 1.5$ tend to remain spherical during most of the life-time (Wang et al., 1996). Chahine (1977) showed that as long as the air bubble is positioned sufficiently away from the air-water interface ($\alpha >> 2.5$), the problem involving a free-surface can be approximated to the first order by describing the system through superposition of a source and a sink potential. In contrast, the problem of an oscillating bubble close to a rigid surface, or equivalently bubbles from two clustered guns, can be described by a system of two similar source potentials. The latter was done by Barker and Landrø (2012) who derived an explicit expression for the bubble-time period for clustered air guns. By using the same type of arguments, we will here derive an expression for the bubble-time period close to a free surface. Barker and Landrø (2012) assumed that the bubble-time period could be approximated using the relationship:

$$T_B = C\frac{R_{EQ}}{U_{EQ}}, \tag{3.3}$$

where C is some gun-type dependent constant, R_{EQ} is the radius of the bubble when the pressure inside the bubble equals the hydrostatic pressure, assuming that the initial state of the bubble is spherical and that it expands adiabatically:

$$R_{EQ} = R_0\left(\frac{P_0}{P_\infty}\right)^{1/3\gamma}, \tag{3.4}$$

and U_{EQ} is the bubble-wall velocity when the radius is R_{EQ}. Here the parameter γ is a gas constant, where we have used $\gamma = 1.13$ equal to the value used in Ziolkowski (1970) and R_0 is the radius of the assumed spherical bubble with volume V_0. Following Barker and Landrø (2012), we use a monopole velocity potential for describing the particle motion in the water surrounding the bubble:

$$\phi = -\frac{UR^2}{r}, \tag{3.5}$$

where R is the bubble radius, U is the bubble-wall velocity and r is the distance away from the center of the bubble. Furthermore, all energy dissipation effects are neglected and it is assumed that the water is inviscid and incompressible. This model will result in the same sort of bubble dynamics as in Rayleigh (1917). As we are interested in the relative changes in the bubble-time period, the error introduced by these assumptions should be small, especially for the time interval it takes the bubble to reach R_{EQ}. By integrating the kinetic energy from the bubble wall to infinity, we find the total kinetic energy in the water surrounding the bubble as:

$$E_k(R, U) = 2\pi\rho U^2 R^3, \tag{3.6}$$

where ρ is the density of water. The potential energy of the bubble can be evaluated to:

$$E_p(R) = -\int_{R_{EQ}}^{R} 4\pi r^2 \left[P(r) - P_\infty\right] dr. \tag{3.7}$$

By assuming adiabatic expansion and that the state where $R = R_{EQ}$ is a state of zero potential energy, equation 3.4 can be used to find:

$$E_p = \frac{4}{3}\pi P_\infty \left[R^3 - R_{EQ}^3 + \frac{\left(\frac{R_{EQ}}{R}\right)^{3\gamma} R^3 - R_{EQ}^3}{\gamma - 1} \right]. \tag{3.8}$$

An expression for U_{EQ} can be obtained by comparing the energy states corresponding to initial conditions $(R = R_0)$ and where there is zero potential energy $(R = R_{EQ})$:

$$2\rho\pi U_{EQ}^2 R_{EQ}^3 = \frac{4}{3}\pi R_0^3 P_\infty \hat{\beta}, \tag{3.9}$$

where

$$\hat{\beta} = 1 - \beta \frac{\beta^{-\frac{\gamma-1}{\gamma}}\gamma - 1}{\gamma - 1} \tag{3.10}$$

and $\beta = P_0/P_\infty$. U_{EQ} is thus found to be:

$$U_{EQ} = \frac{1}{3}\sqrt{\frac{6P_\infty}{\rho}\frac{\hat{\beta}}{\beta^{\frac{1}{\gamma}}}}. \tag{3.11}$$

The bubble-time period for a single air gun fired in an infinite homogeneous medium (equation 3.3) can then be found:

$$T_B = \frac{1}{2} C R_{EQ} \beta^{\frac{1}{2\gamma}} \sqrt{\frac{6\rho}{\hat{\beta} P_\infty}}. \tag{3.12}$$

This equation gives good numerical scales for the Rayleigh equation (Barker and Landrø, 2012). We also note that it is consistent with the bubble-time periods derived in Rayleigh (1917) and Minneart (1933).

So far we have repeated the derivation of Barker and Landrø (2012). We will now consider two non-overlapping bubbles of radius R at a distance $2b$ away from each other. The flow around these bubbles is described by superposition of two single-bubble potentials. In contrast to Barker and Landrø (2012), one of the potentials is scaled with a coefficient r_0:

$$\phi = -\frac{UR^2}{r} - \frac{r_0 U R^2}{\sqrt{r^2 + 4b^2 + 4rb\cos\theta}}, \tag{3.13}$$

where θ is the angle between the depth-axis and a line from $r = 0$. This potential must satisfy the boundary condition mid-way between the bubbles,

$$\hat{\mathbf{n}} \cdot \nabla\phi = 0, \tag{3.14}$$

for a rigid boundary ($r_0 = 1$), and

$$\phi = 0, \tag{3.15}$$

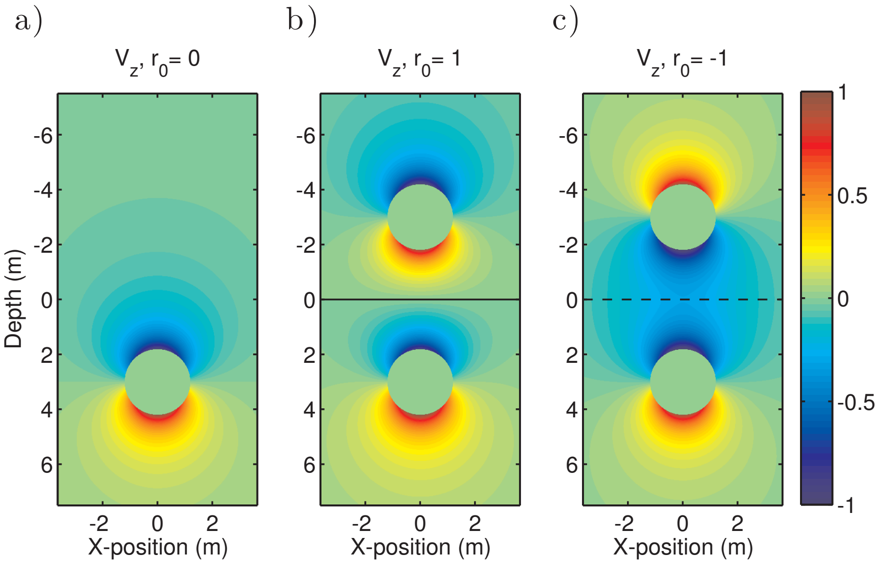

Figure 3.1: The vertical particle velocity surrounding the bubble in a) and infinite medium ($r_0 = 0$), b) a rigid boundary ($r_0 = 1$) and c) a "stationary" free surface ($r_0 = -1$). The color scale is relative to the bubble-wall velocity. It is clear from superposition of potentials that the vertical particle velocities are zero at $z = 0$ in b) and twice the magnitude of a) in c) at $z = 0$.

for free surface ($r_0 = -1$), where $\hat{\mathbf{n}}$ is the unit normal vector to the plane midway between the two bubbles and the dot ($\cdot$) denotes the dot product. We assume that the bubbles are spherical, but the potential in equation 3.13 does not satisfy the boundary condition at the bubble wall(s) for a spherical bubble:

$$\hat{\mathbf{n}} \cdot \nabla\phi = U, \tag{3.16}$$

where $\hat{(\mathbf{n})}$ is the unit normal vector to the bubble wall and U is the bubble-wall velocity. This will be discussed below. Figure 3.1 shows the particle velocities derived from the potential in equation 3.13 for the three different cases where $r_0 = -1, 0, 1$.

We assume that $r_0 = -1$ in equation 3.13 is equivalent to describing bubble motion a distance b away from a free surface. However, compared to a rigid boundary, the air-water interface is free to move. By setting $r_0 = -1$ we specify that the free surface cannot move.

Following Barker and Landrø (2012) we get the following expression for the total energy in the water caused by one of the air bubbles:

$$E_k = \frac{1}{2}\rho \int_{\Omega} |\nabla\phi|^2 \, dV = -\frac{1}{2}\rho \int_{\partial\Omega} \frac{\partial\phi}{\partial r}\phi dS, \tag{3.17}$$

where Ω is the liquid domain and $\partial\Omega$ is its boundary. Using Sommerfeld's radiation condition we can take this boundary to be the bubble wall. The integral can be evaluated to (see Barker and Landrø, 2012):

$$E_k = \frac{1}{2}\pi\rho U^2 R^3 A(\kappa, r_0), \tag{3.18}$$

where

$$A(\kappa, r_0) = \frac{4\kappa + 4r_0 - r_0^2 \ln\left(\frac{\kappa-1}{\kappa+1}\right)}{\kappa} + \frac{2r_0^2}{1-\kappa^2},\ \kappa \geq 4 \tag{3.19}$$

where $\kappa = 2b/R_{EQ}$. This a more general formula compared to Barker and Landrø (2012), and by specifying $r_0 = 1$ we obtain the same equation. When setting $r_0 = -1$ we observe that the total energy in the system decreases, compared to the case where the bubble oscillates in an infinite medium. As in Barker and Landrø (2012), $\lim_{b\to\infty} E_k = 2\pi\rho U^2 R^3$, is consistent with the single-bubble model. We note that this is independent on the coefficient r_0.

The normalized kinetic energy for the three different scenarios $r_0 = -1$, $r_0 = 0$ and $r_0 = 1$ are shown in Figure 3.2 for $1 < \kappa \leq 150$. We observe that the kinetic energy surrounding the bubble behaves differently if the bubble is close to a wall, a free surface or in an infinite medium. We would expect that the normalized E_k should tend to zero when κ goes to 0 for the case where $r_0 = -1$, as this would correspond to two sources of equal strengths with opposite polarity canceling each other. For the case when $r_0 = 1$, it is tempting to think that the normalized E_k should approach 2 as kappa goes to 0. However, this limit cannot be evaluated in this model (see Barker and Landrø, 2012). Although Equation 3.18 is valid for $\kappa > 1$, it is derived under the assumption that the bubbles are non-interacting, i.e. $\alpha > 1$. For a source depth of 3 m Rayleigh modeling gives the relationship $R_m \approx 2R_{EQ}$ and therefore $\kappa > 4$ is the minimum requirement for this theory to be valid. The relationship between R_m and R_{EQ}, κ and α at different depths for a 600-in^3 air gun are shown in Appendix 1.

By comparing the initial energy of the air bubble to the energy when the bubble has reached equilibrium radius (i.e. when there is no potential energy in the bubble), we find the following expression for the bubble-time-period:

$$T_{r_0} = C\frac{1}{4}R_{EQ}\beta^{\frac{1}{2\gamma}}\sqrt{\frac{6\rho}{\hat{\beta}P_\infty}}\sqrt{A(\kappa, r_0)}. \tag{3.20}$$

To find the ratio between the bubble-time period for a bubble in an infinite homogeneous medium and the bubble-time period for a bubble close to a boundary, we divide equation 3.20 by equation 3.12 to obtain:

$$\frac{T_{r_0}}{T_B} = \frac{1}{2}\sqrt{A(\kappa, r_0)}. \tag{3.21}$$

We propose to use equation 3.21 as a correction term to the Rayleigh-Willis formula:

$$T^* = T_{RW}\frac{1}{2}\sqrt{A(\kappa, r_0)}. \tag{3.22}$$

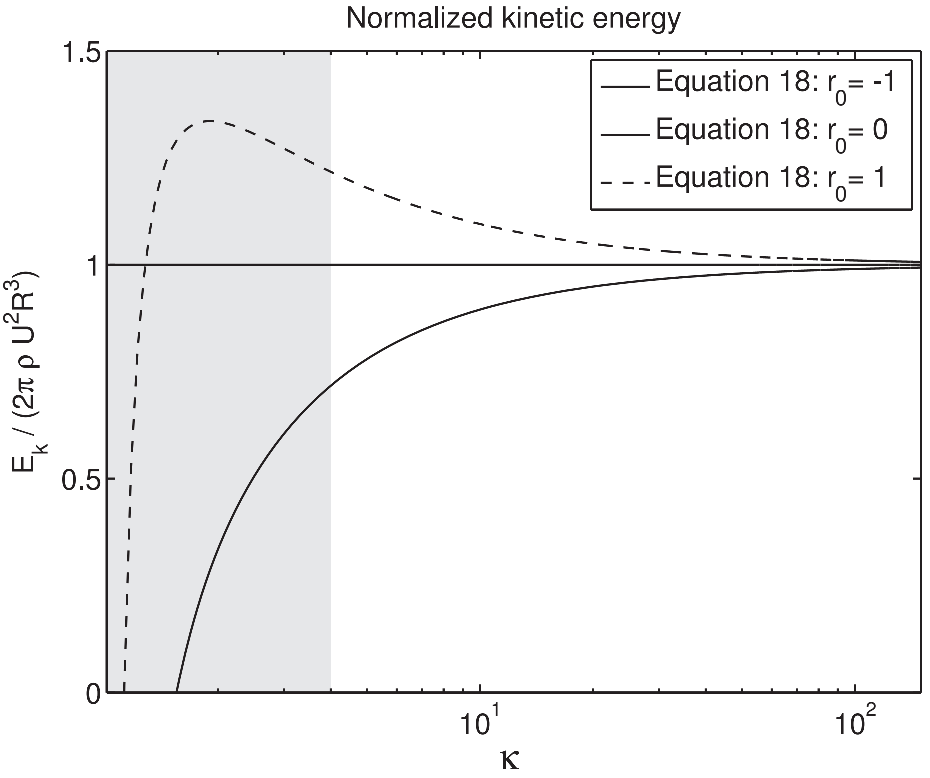

Figure 3.2: Normalized kinetic energy around one of the bubbles in vicinity of a free surface ($r_0 = -1$), a wall ($r_0 = 1$) and in infinite medium ($r_0 = 0$). The shaded area indicates where $\kappa \leq 4$.

It is possible to include more terms in the potential to make it satisfy the boundary condition at the bubble wall (equation 3.16), but this will again cause the potential to break the boundary condition at the rigid/free surface. This was done by Herring (1941) who derived the following equation for the bubble-time period close to a rigid boundary or a free surface, neglecting terms of higher orders in R/b:

$$T_H^* = T_{RW}\left(1 + r_0 \frac{R_a}{4b}\right), \tag{3.23}$$

where R_a is the average bubble radius over a bubble period, $r_0 = 1$ for a rigid surface and $r_0 = -1$ for a free surface. By performing modeling of bubble motion with the Rayleigh equation, we have found an approximate relationship $R_a \approx \frac{3}{2} R_{EQ}$ for a bubble of initial radius corresponding to 600 in^3 fired at different depths with initial pressure of 2000 psi.

The hydrodynamic cause for the change in kinetic energy when the bubble oscillates close to a free surface is that there is less inertia in the fluid surrounding the bubble (Cole, 1948). The effect of the free surface is that it reduces the inertia of the oscillating system without changing the spring constant and therefore reduces the bubble-time period (Herring, 1941).

3.2.2 Source scaling

The source scaling as used here is adapted from Giles and Johnston (1973), who used this to correct source signatures for external pressure variations. Their method involves a sample-to-sample stretch/squeeze and amplitude correction to the source signature. The stretch correction corresponds to multiplying the sampling time with the ratio between the bubble-time period for a given source setup (P_i, V_i and z_i) and the bubble-time period resulting from having external pressure variations from other air-guns in the array in addition. The amplitude correction was deduced by assuming that the output pressure is proportional to $V^{1/3}$ and that the change in bubble-time period could be written in terms of an apparent change in the chamber volume of the gun. The amplitude correction term can, using these assumptions, be shown to be the reciprocal of the ratio between the bubble time periods (Giles and Johnston, 1973). Using these relations we find that:

$$s_2(t) = \frac{1}{a} s_1(at), \tag{3.24}$$

where $s_2(t)$ and $s_1(t)$ are the source signatures from the same air-gun (i.e. same volume and pressure) from depths z_2 and z_1, respectively, and a is the ratio between the bubble-time periods from the the two depths. This result is the well-known source scaling law (O'Brian, 1969; Ziolkowski et al., 1980). More detailed descriptions of the source scaling law can be found in Ziolkowski (1986), Ziolkowski (1993) and Ziolkowski and Bokhorts (1993) who discuss the scaling parameter a in terms of energy of the source. For our purpose, the simple relationship using bubble-time periods given in Giles and Johnston

(1973) is very practical since it incorporates the firing depth which we are concerned with here. The ratio is given as:

$$a = \frac{T_2^*}{T_1^*} \tag{3.25}$$

where the subscripts indicate the different states (e.g. differnt depths) and T^* is the modified Rayleigh-Willis formula given in equation 3.22 or equation 3.23.

To estimate the source signature from an air gun fired at a depth z_2 we use a known source signature from the same air gun fired at a depth z_1 and do the following steps:

1. Measure the near-field or quasi far-field signature from an air-gun fired at depth z_1
2. Obtain the notional source signature using e.g. the method of Ziolkowski et al. (1982).
3. Span the notional source signatures from step 2 on a new time axis ($\hat{t} = at$) using interpolation.
4. Scale the resulting signature with a^{-1}.
5. Use a frequency filter to obtain the source signature in the desired frequency band.

By spanning the notional source signature on a new time axis we are literally stretching or squeezing the signature. The corresponding change in the frequency domain is well known through the scaling property of the Fourier transform. A change in time domain $\hat{t} = at$ will result in a stretch/squeeze in the frequency domain $\hat{f} = f/a$. In step 4, it is important to use correct bandwidths prior to stretch or squeeze. If the highest frequency wanted in the estimated signature is f_m, frequencies up to f_m/a must be present in the signature that is used as basis for the estimation.

3.3 Field data

A field experiment was performed a few years ago (Landrø and Amundsen, 2014a). A single 600-in^3 air gun was fired at depths 3, 5, 7.5, 10, 15, 20, 25, 30, 35 and 40 m and a hydrophone was positioned 20 m vertically below the air gun. The water depth at the location is approximately 390 m. The experiment was repeated two or three times per source depth and the data showed good repeatability (NRMS-difference of $\sim$ 5.5 % between successive shots at same depths). The average source signatures from the respective depths were used to reduce noise. The data was de-ghosted to find the notional source signatures from each depth. An iterative approach was used to find the travel-times and geometrical spreading that resulted in the best deghosting results. The estimated notional source signatures are shown in Figure 3.3. The source signatures exhibit the expected depth dependence; we observe that the bubble pulse delay is reduced as the firing depth is increased, as predicted from equation 3.1.

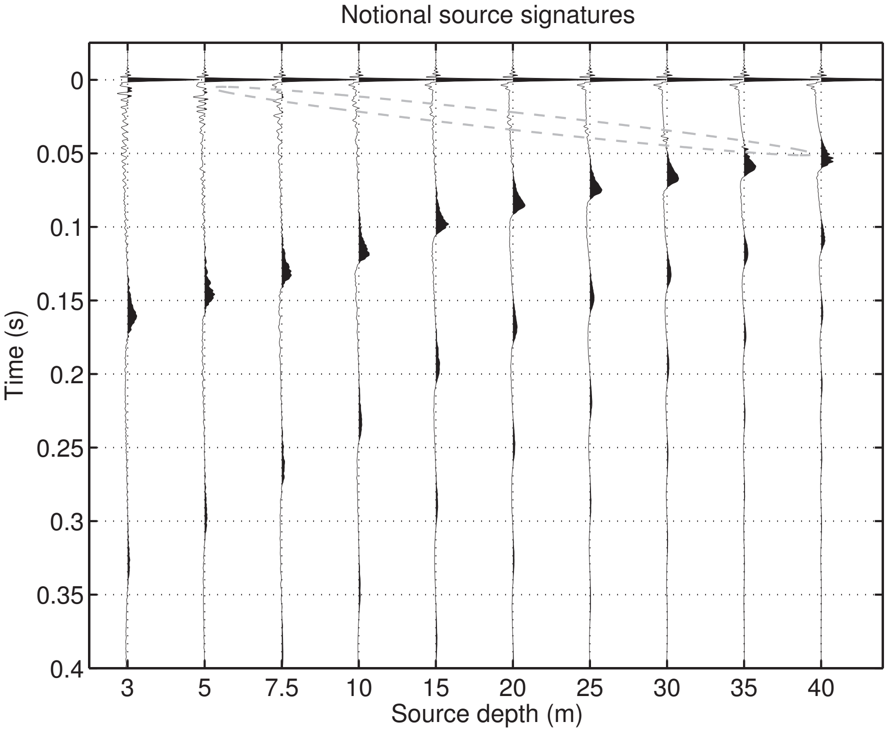

Figure 3.3: The estimated notional sources for different source depths ranging from 3 to 40 m, in the full bandwidth (0 - 500 Hz). Note how the bubble pulse delay is reduced as the source depth increases. Residual ghosts are highlighted in the ellipse (dashed ellipse).

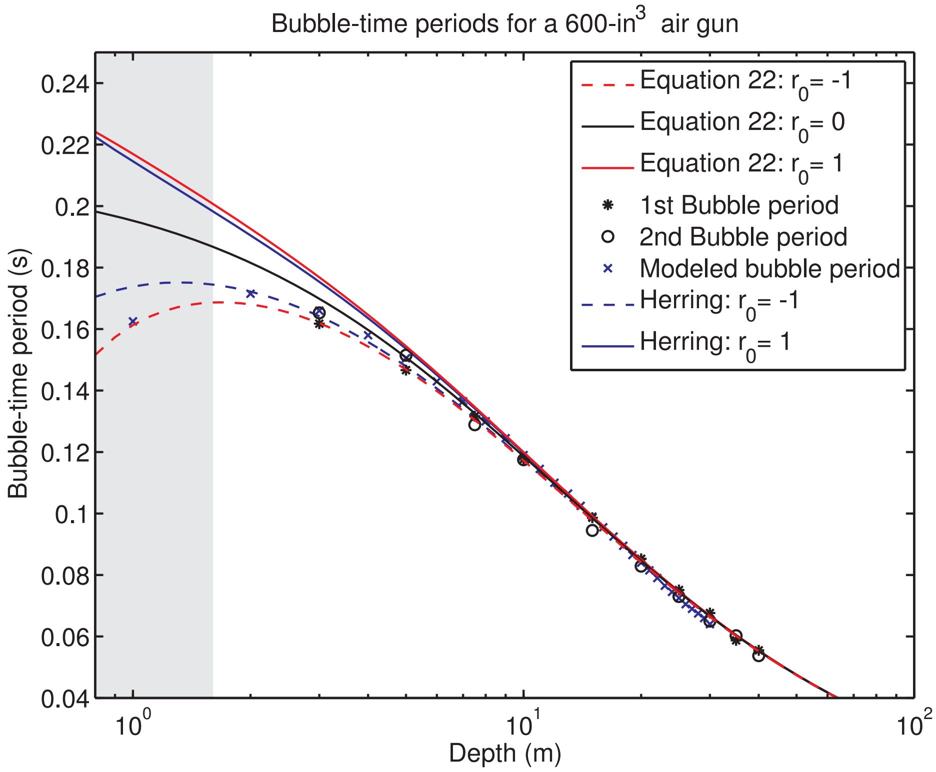

Figure 3.4: Bubble-time periods from a 600-in^3 air gun fired at different depths, from air-gun modeling and from the Rayleigh-Willis equation with and without indicated correction-terms. The gray area indicates where $\kappa \leq 4$.

The bubble-time periods were picked between the primary and first bubble and between the first and second bubble for each depth. The measured bubble-time periods are shown together with the estimated bubble-time periods using equation 3.22, equation 3.23, the best-fit Rayleigh-Willis curve (equation 3.1) and the modeled bubble-time periods from a commercial air-gun modeling software in Figure 3.4. We see that the measured bubble-time periods fit the depth dependence of the Rayleigh-Willis formula quite well at depths deeper than 7.5 m, and that the bubble-time periods at shallower depths fit the corrected Rayleigh-Willis formula very well.

To demonstrate the source scaling law we estimate the source signature at 30 m from signatures measured at other depths. Figure 3.5 shows the source signatures used for this analysis, along with the estimated signatures and the difference between the measured and the estimated signatures for 5 m depth difference. The corresponding signatures and differences in the frequency domain are shown in Figure 3.6. Figures 3.7 and 3.8 show the equivalent plots for a 10 m depth difference. We see that the signatures estimated from

± 5 m depth have NRMS-differences around 5% between the estimated and measured signature at that depth. The source signature estimated from a source signature fired at ± 10 m difference has an NRMS-difference around 8 % between the measured signature at that depth. Figure 3.9a shows the NRMS-differences between estimated 20-m signatures using data from all other depths as input and the measured 20-m signature. Source scaling was done with and without the correction of equation 3.22 to the Rayleigh-Willis equation. We observe that the NRMS-error decreases significantly when we use the correction term, ~ 10 % for the signature estimated from the 3-m signature. This improvement is most pronounced for shallow source depths. This is expected since these equations represent corrections due to the free surface. It is clear that a correction term is needed, however, the results from using the two different correction terms (equations 3.22 and 3.23) are very similar. Equation 3.23 from Herring (1941) requires knowledge of the average radius of the bubble (R_a), while equation 3.22 require that we know R_{EQ}. Since R_{EQ} is a function of the initial source depth, firing pressure and gun volume it is more practical to use. The gas constant γ is needed for both.

Figure 3.9b shows the estimated signatures using equation 3.22 for the source scaling. Note that we have chosen 20-m depth as a reference depth. Similar results (relative) are found if we use for instance 10 m as reference depth. In Figure 3.9b we see that the bubble-pulses from the different depths are well-aligned in time. We also observe that the pressure amplitude of the bubble pulses decreases with depth.

3.4 The effect of the hydrophone instrument response on source scaling

In the process of estimating a source signature by using source scaling, we map the amplitude and phase from one frequency in the measured signature to a different frequency in the signature we try to estimate ($\hat{f} = f/a$). This method is therefore sensitive to frequency dependent alterations to the signal, i.e. filters. We can observe large differences at low frequencies in both phase and amplitude in Figure 3.6b and c. We think that this can partially be attributed to the instrument response of the hydrophone used in this experiment, in addition to low signal-to-noise ratio at these frequencies. The typical instrument response (transfer function) for a hydrophone has a roll-off in amplitudes below a certain natural frequency and corresponding phase-shifts. The amplitude and phase at a given frequency in the source signature is scaled and rotated by the hydrophone response when it is recorded. When the amplitude and phase at this frequency are mapped to a different frequency, the amplitude scaling and phase rotation will follow as well. It will appear as if the estimated signature was recorded with a hydrophone response that is scaled ($H(\hat{f}) = H(f/a)$, where H is the hydrophone response). This will result in errors at the frequencies affected.

To show how a hydrophone instrument response may affect the results of source scaling we present a simple example: We create a synthetic data set of notional source signatures

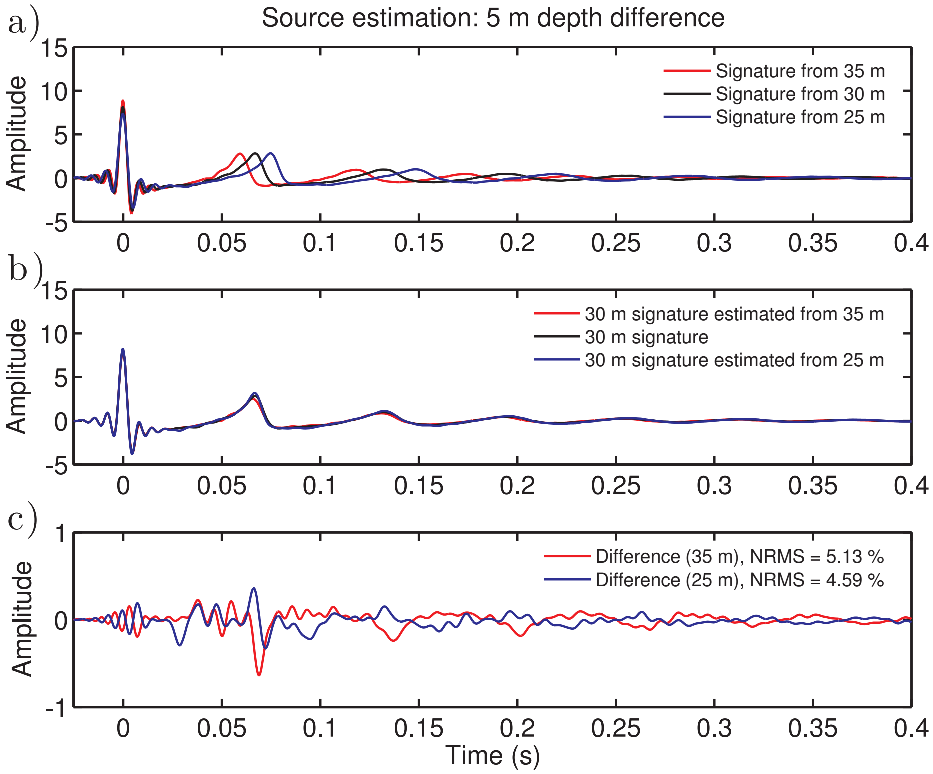

Figure 3.5: a) The source signatures from 25, 30 and 35 m. b) 30 m-signatures estimated from signatures measured at 25 and 35 m, respectively, shown together with the measured signature from 30 m. c) The difference between the estimated and measured signature.

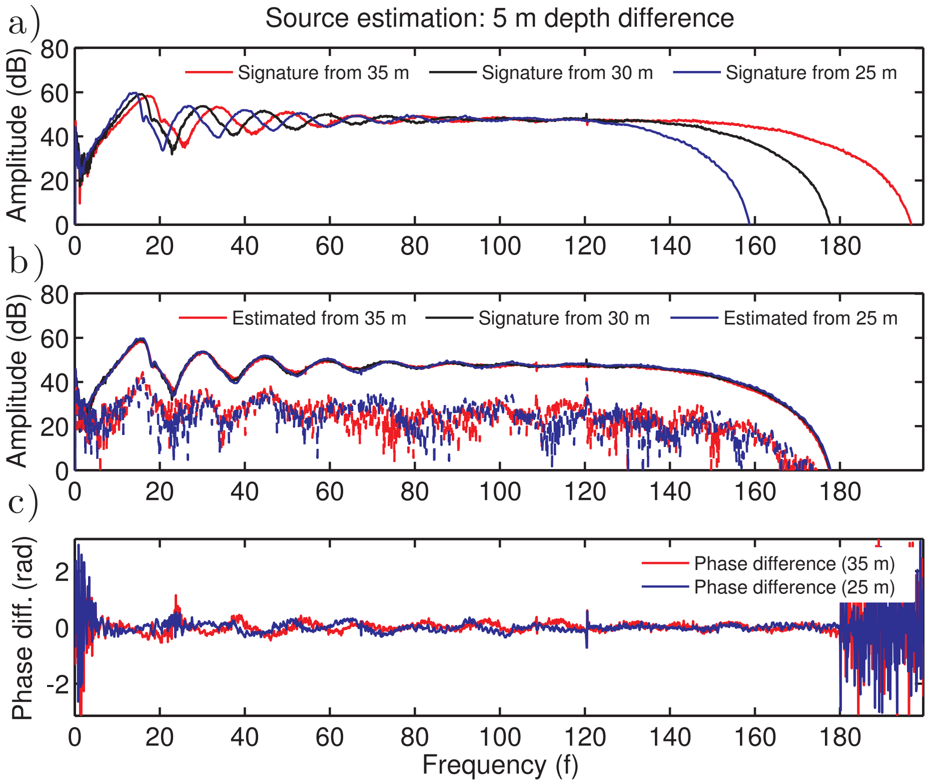

Figure 3.6: a) The amplitude spectra of the source signatures from 25, 30 and 35 m. b) Amplitude spectra of the estimated 30 m signatures from 25 and 35 m, respectively, shown together with the spectrum of the measured signature from 30 m. The amplitude differences between the estimated and measured signatures are shown in dashed lines. c) The difference in phase between the measured signature at 30 m and the signature estimated from 25 and 35 m.

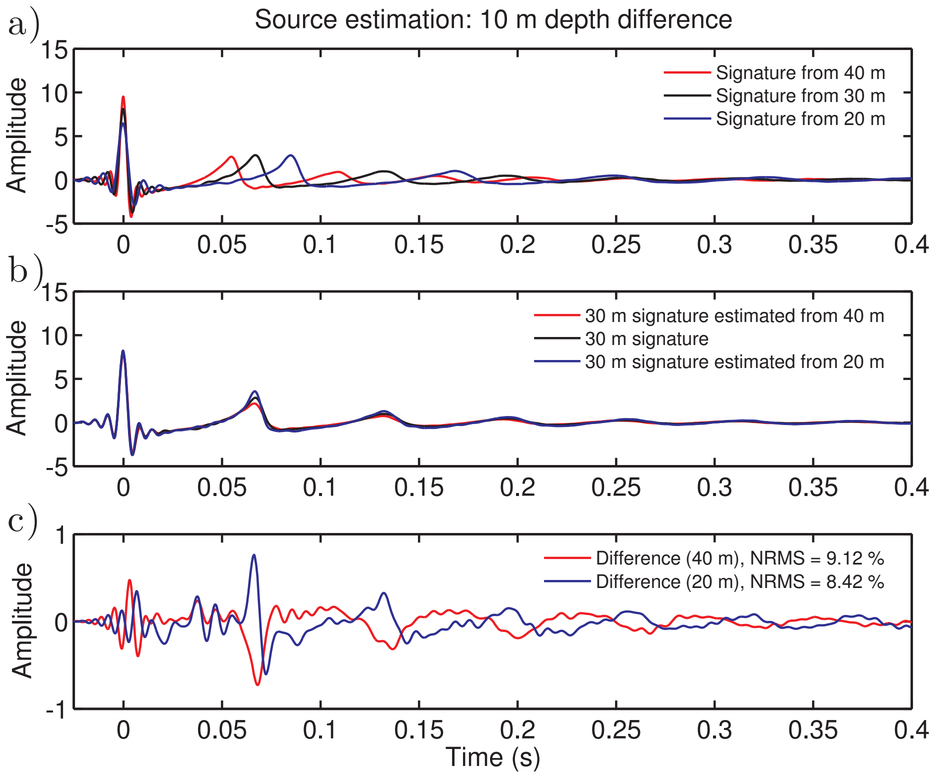

Figure 3.7: a) The source signatures from 20, 30 and 40 m. b) 30 m-signatures estimated from signatures measured at 20 and 40 m, respectively, shown together with the measured signature from 30 m. c) The difference between the estimated and measured signature.

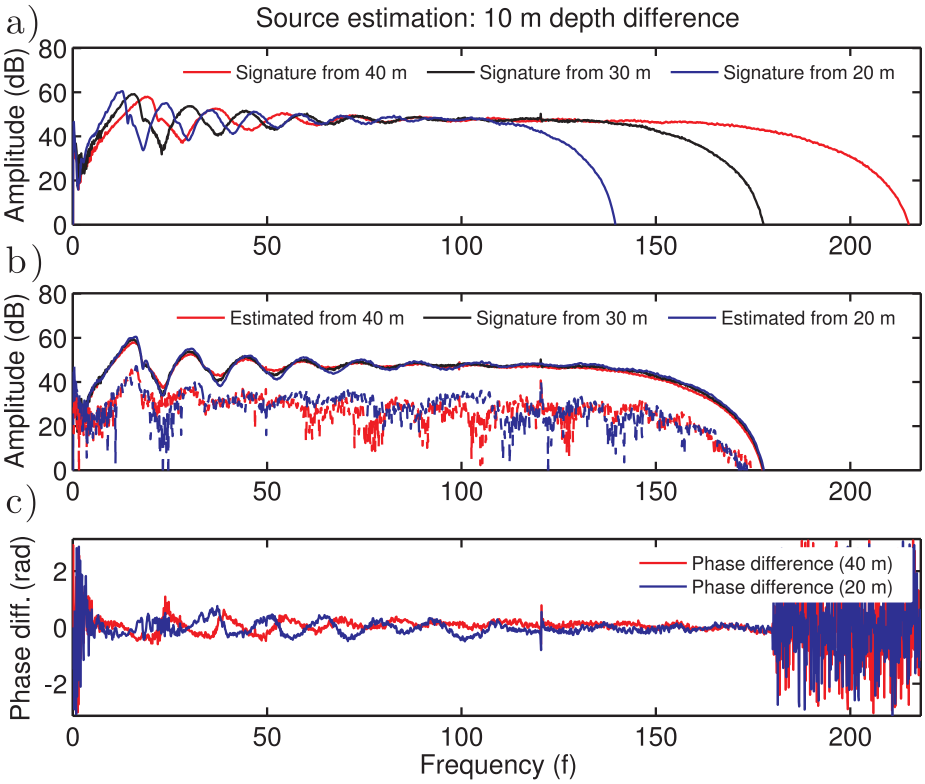

Figure 3.8: a) The amplitude spectra of the source signatures from 20, 30 and 40 m. b) Amplitude spectra of the estimated 30 m signatures from 20 and 40 m, respectively, shown together with the spectrum of the measured signature from 30 m. The amplitude differences between the estimated and measured signatures are shown in dashed lines. c) The difference in phase between the measured signature at 30 m and the signature estimated from 20 and 40 m.

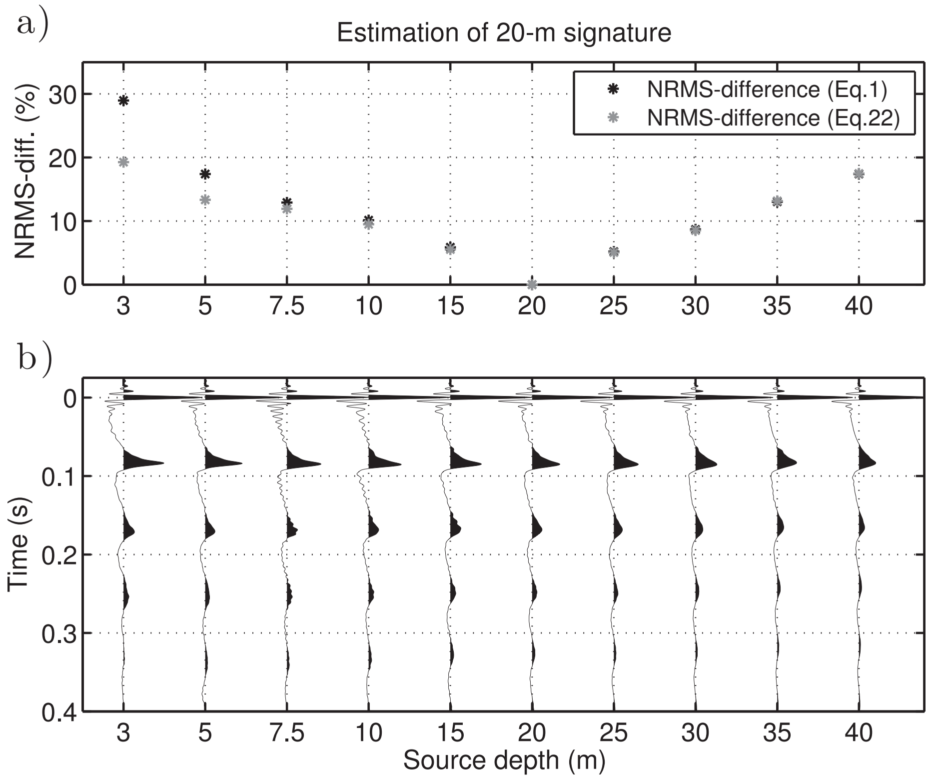

Figure 3.9: a) The NRMS-difference between the estimated 20-m signatures from the indicated source depths and the measured 20-m signature. The NRMS values are extracted in a 0.4 s window. b) A portion of the estimated 20-m signatures from the indicated depths.

from an air-gun fired at different depths. This is done by using the average signature from Figure 3.9b , and then remove an instrument response given by:

$$H(f) = \frac{1}{1 - if_0/f}, \tag{3.26}$$

where f is the frequency, f_0 is the natural frequency of the hydrophone and i is the imaginary unit. The resulting signature was scaled to other depths using source scaling as presented here (with equation 3.22), and the same instrument response was added to each of the different signatures. Assuming that source scaling works, these signatures now represent the type of signatures we record in field using the same hydrophone. Here we used $f_0 = 5Hz$. The same type of analysis that was done for the real data (Figure 3.9) was performed on the synthetic data set. The result is shown in Figure 3.10. We note that since we have used the same source scaling twice, back and forth, the only difference is the effect of the hydrophone instrument response. In Figure 3.10a we observe that the effect of the hydrophone gives the same kind of behaviour of the NRMS-differences versus difference in source depth as seen in the real data example. Furthermore, Figure 3.10b shows that the predicted source signatures is changing appearance, especially around the bubble pulse ($\sim$0.1 s). This is also what we see in Figure 3.9b.

3.5 Discussion

Our findings suggest that the source signature from an air gun fired at a given depth can be estimated from a measured source signature from the same air gun fired at a different depth. Good results are obtained for depth variations up to 10 m. The NRMS-difference increases almost linearly with the depth difference between the depth where we try to estimate a signature and the depth of the signature we use for the estimation. There are probably many causes for the differences between the measured and estimated signatures presented here. Random noise is certainly present, but some of the differences are more systematic. As seen in Figure 3.3, there are residual ghosts after deghosting and stacking the signatures from the same depths. Since the ghost event is not part of the notional source signature it will not scale, and residual ghosts will contribute to the difference. The travel-time for the ghost event is dependent on the source depth and therefore the difference between measured and estimated signatures as presented here will have residual ghosts from both amplitude and travel-time "errors". Furthermore, the process of deghosting is more vulnerable to noise when the source depth is shallow. This is because the direct event and the ghost event have almost similar magnitudes which makes the signal-to-noise ratio poor at specific frequencies. This will result in notional source signatures with more noise. This problem can probably be reduced by using near-field measurements instead of quasi-near-field measurements in this kind of analysis.

The limit from Chahine (1977) that $\alpha \gg 2.5$ will correspond to approximately $\kappa \gg 10$ which means that our theory is not valid for the 600-in^3 air gun unless it has a source depth greater than 3 m. In the data presented here the shallow-most source is positioned at 3

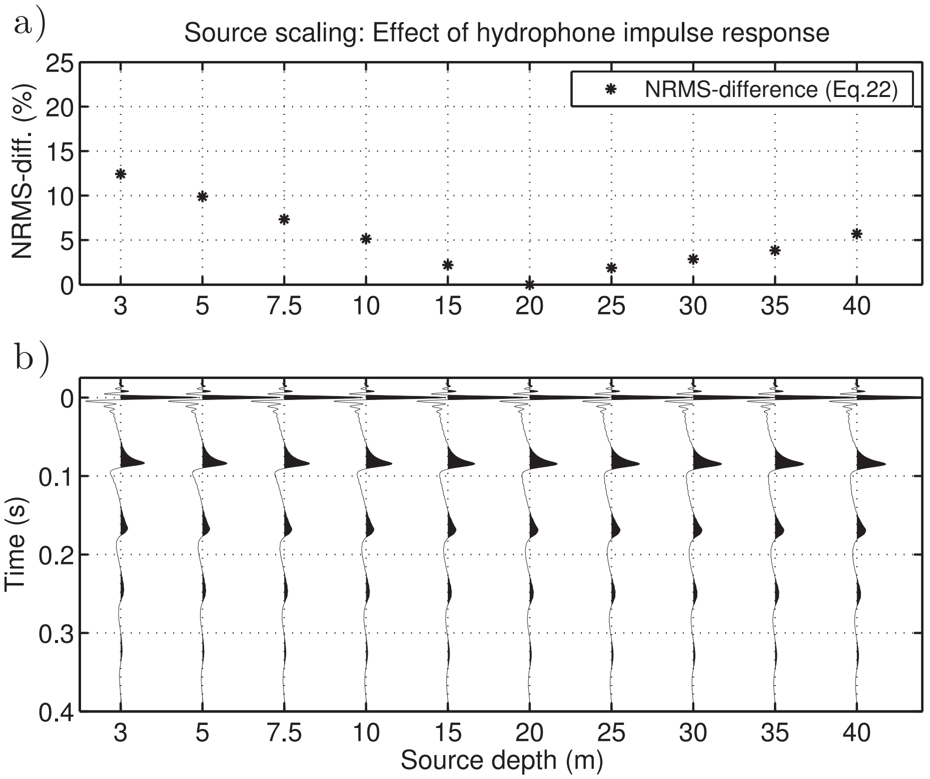

Figure 3.10: This Figure shows the same as in Figure 3.9 but for synthetic data as described in the text. a) The NRMS-difference between the estimated 20-m signatures from the indicated source depths and the 20-m signature. The NRMS values are extracted in a 0.4 s window. b) A portion of the estimated 20-m signatures from the indicated depths.

m. It is also from this depth where the error is biggest when source scaling is performed. However, our results show that when the correction term is used in the source scaling, the error from the source at 3 m is not much bigger than the error from source from 40 m when trying to estimate a 20-m signature (see Figure 3.9). Even though the limit from Chahine (1977) may not be fulfilled, our simple method performs very well.

Our example on how the hydrophone instrument response will affect the result from source scaling shows that the measured data should be corrected for the hydrophone response prior to performing source scaling. Unfortunately, we did not have the instrument response for the hydrophone used in this field experiment. Other frequency dependent alterations that may affect the signal in this experiment are attenuation and the actual value of the free-surface reflection coefficient. The measurements are recorded 20 m below the air gun and the difference in attenuation between the different firing depths is expected to be small. However, the ghost event from the shot fired at 40 m has traveled more than three times the distance compared the ghost from the shot fired at 3 m. This might be of importance. The free-surface reflection coefficient is frequency dependent, and this is probably the major cause for the residual ghosts in the notional source signatures in Figure 3.3.

From a practical point of view, deriving precise notional source signatures during real acquisition conditions, with e.g. swell, firing time variations, air leakage and air-gun swing, might be quite difficult. What we foresee is to derive notional source signatures from near-field measurements acquired in a controlled setting. This experiment can be repeated many times to obtain good quality notional source signatures at a reference depth in an ideal setting. This data can then be compared to near-field data from field acquisition and robust parameters, such as the bubble-time period, can be used to say something about the variation in depth relative to the reference data. This information can then be used as input to source scaling of the notional source signatures that was obtained in the controlled setting to design a signature suitable for the de-signature process. This can be done on a shot-to-shot basis. We think that a de-signature strategy like this might be more robust than using notional source signatures derived from each shot directly. This is because the notional source signatures estimated from the controlled experiment(s), by using source scaling, may contain less noise. The source scaling law can be used in source de-signature between sequential shots as described above. This would be very important for VSDA seismic data (Haavik and Landrø, 2015), where the source depth is deliberately varied between sequential shots. Source depth variations are also common in conventional seismic acquisition and may for instance cause large errors in repeatability between time-lapse surveys (Andorsen and Landrø, 2000).

The source scaling law is very simple to use when the only difference between the measured signal and the desired signal is the firing depth. This is because the stretch or squeeze in time is proportional to the ratio between bubble-time periods which can be found from the Rayleigh-Willis formula, or from a modified version of the Rayleigh-Willis formula (equation 3.23 or 3.22) if the air gun is close to the free surface. Here we have used the source scaling law to estimate changes in the signature with respect to depth variations, but the source scaling as presented here, with equation 3.24 and 3.25, predicts that it should be able to perform the same analysis between signatures fired with different initial pressures, volumes, at different temperatures (see Landrø, 2014) or a combination of these and source depths. The validity of this is, however, not demonstrated here.

As shown here, this method can be used to model how the signature from a given air gun, and potentially an air-gun array, will change with source depth. This can be used as an alternative to conventional air-gun modeling when reference notional source signatures are known. Due to its simplicity, we think that source scaling may greatly simplify inversion schemes involving forward modeling of air-gun signatures. Examples of this may be to find the optimal sequence of firing depths in a VSDA sequence (see Haavik and Landrø, 2015) or the optimal source depths in a slanted or multi-level air-gun array (see Shen et al., 2014).

It is important to specify that the source ghost does not scale in general, and the analysis presented here is for the notional source signatures. Ziolkowski (1986) presents specific conditions for when the source ghost scales with depth as well.

3.6 Conclusion

We have tested the accuracy of the source scaling law for a single air gun with respect to the source depth. Our study using quasi-near-field measurements of a large single air gun fired at depths ranging from 3 to 40 m shows that the source scaling law works very well for predicting the signatures from the same air gun fired at different depths. We have shown that by using a modified version of the Rayleigh-Willis formula, which includes a correction term for when the air gun is fired close to the free surface, gives better results in estimating the source signatures. When estimating the notional source signature from an air gun fired at a given depth from notional source signatures recorded at other depths, we find NRMS-differences down to $\sim$ 5-6 % for ± 5 m difference in source depth and 8-12 % for a difference of ± 10 m. In comparison, the average NRMS-differences between raw measurements from the same source depth without deghosting is $\sim$5 %. For most applications we find that the source scaling law is sufficiently accurate to be used to predict source signatures at various depths, given that the source signature is known or measured at a given reference depth. This may be used as an alternative to conventional air-gun modeling.

3.7 Acknowledgements

We acknowledge Lundin Norway AS for financial support to Kjetil E. Haavik's PhD project. We would like to thank Statoil ASA for contributing with the source signatures. We thank the Norwegian Research Council for financial support to the ROSE consortium

at NTNU. Furthermore, we thank three anonymous reviewers for comments and suggestions that improved this manuscript.

3.8 Appendix: Relationship between bubble parameters

In our model for bubble motion close to a free surface we use $\kappa = 2b/R_{EQ}$ as the parameter that controls how large the correction term to the bubble-time period is. Equation 3.22 is derived assuming that the bubble walls of the two potentials are not overlapping, e.g. $\alpha = b/R_m > 1$ which approximately corresponds to $\kappa > 4$. This restriction comes from our model using two potentials (equation 3.13). In addition to this, a stricter limit is posed in Chahine (1977), that $\alpha >> 2.5$ for this model based on the method of images to be valid for describing interaction between the free surface and a bubble. Figure 3.11a shows the relationship between R_m and R_{EQ} for 600-in^3 air gun fired at different depths modelled using the Rayleigh equation with $\gamma = 1.13$. Figure 3.11b shows the corresponding values of κ and α.

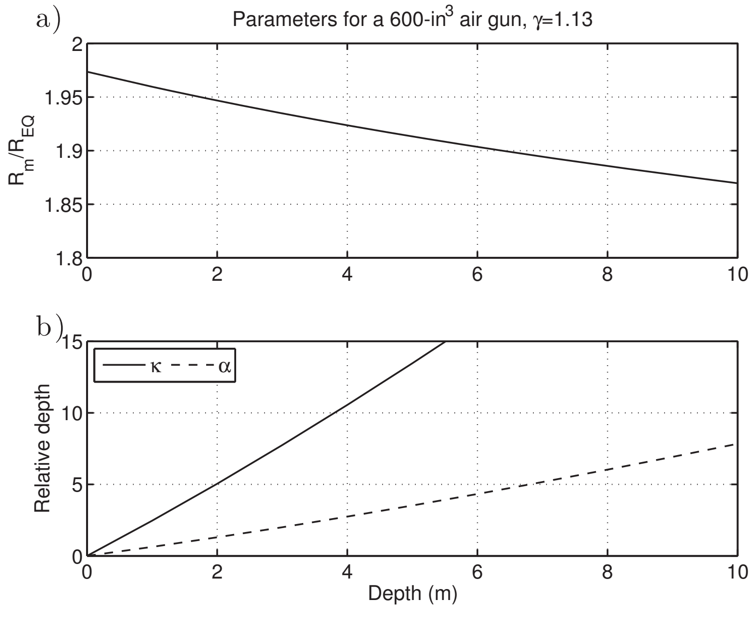

Figure 3.11: a) The ratio between R_m and R_{EQ} for different source depths for a 600-in^3 air gun assuming Rayleigh bubble motion b) $\alpha = b/R_m$ and $\kappa = 2b/R_{EQ}$ for different source depths for a 600-in^3 air gun assuming Rayleigh bubble motion.

Chapter 4

Variable source depth acquisition for (an overall) improved signal-to-noise ratio in marine broadband seismic data: A modeling study*

Kjetil Eik Haavik and Martin Landrø
Norwegian University of Science and Technology, Trondheim, Norway

4.1 Abstract

Marine seismic data acquisition has conventionally been carried out with a source array positioned at a single depth. The resulting source-ghost notch is often taken as the limit for the bandwidth of the data. In broadband seismic data acquisition, multi-level sources are now being used to fill in these notches. Here we present a modeling study where variable source-depth acquisition (VSDA) is compared to conventional single-level source and multi-level source acquisition. Our results show that an overall (not all over) improvement of signal-to-noise ratios are obtained using VSDA compared to the other source strategies. Due to the nature of VSDA, having different far-field signatures for different shots, the amplitude versus offset behaviour of the VSDA is not ideal. In stacked images, these variations are mostly seen in very shallow reflectors (< 0.3 s).

---

* *Paper submitted to GEOPHYSICS August 2016*

4.2 Introduction

The interest for broadband seismic data has led to several new configurations and acquisition strategies for the marine seismic source. The key objective of these source configurations, or strategies, is to mitigate the long-standing problem related to the source-side ghost. The source ghost cause deep notches in the frequency spectra of the far-field signatures, and the recorded seismic data will therefore have poor signal to noise ratio (S/N) at frequencies in the vicinity of these notch frequencies. The notch frequencies are determined by the towing depth of the source. Changing the depth of an air-gun source results in a change in the frequency spectra of the output pressure produces by air-guns. This change can be described qualitatively by stretching or squeezing the amplitude spectrum from a given airgun with respect to the frequency axis because of the change in hydrostatic pressure (Haavik and Landrø, 2016). When a source is positioned deep, the ghost response is favorable towards low frequencies, but the corresponding change in the amplitude spectrum is making the total low-frequency output close to unaffected (Hegna and Parkes, 2011; Hopperstad et al., 2012; Landrø and Amundsen, 2014a), at least below 5–6 Hz. Hegna and Parkes (2011) showed that a gain of up to 16 dB can be achieved in the interval from 7–30 Hz by towing a 1200 in^3 array at 20 m compared to 6 m. The drawback of deep source tow is that the first ghost notch will be positioned within the usable bandwidth for seismic imaging.

The marine source-side broadband strategies that have been implemented in commercial seismic acquisition, experimentally tested or suggested are: Multi-level source arrays (Hopperstad et al., 2008b; Parkes and Hegna, 2011; Sablon et al., 2013; Shen et al., 2014), dipole-sources (Meier et al., 2015) and VSDA (Haavik and Landrø, 2015). In VSDA, the source depth is different from shot to shot to introduce notch diversity, and has not been tested experimentally yet.

Receiver-side deghosting of marine seismic data has been mitigated in at least four different ways: Deghosting of conventional - single-level - streamer acquisition through processing, Over/Under acquisition (Parrack, 1974; Posthumus, 1993), multi-component acquisition (Berni, 1982; Tenghamn et al., 2007) and variable depth streamer acquisition (Ray and Moore, 1982; Soubaras and Dowle, 2010; Soubaras, 2012). There are several similarities between the different broadband source strategies and the broadband receiver-side strategies. The reciprocal experiment to over/under streamer acquisition with a single-depth source, is for the source side, to acquire two shot gathers at the same position with sources at two different depths and receivers on a single level (e.g. Moldoveanu, 2000; Egan et al., 2007). The data acquired with receivers on a single level using multi-level source would result in data that corresponds to summation of the data recorded on the over and under streamer using a single level source, i.e., the data from the two source depths are not separated. Different strategies time-synchronization for the sources at different depths exist to separate the primary and ghost or to align the primaries (Parkes and Hegna, 2011; Hopperstad et al., 2008b). The reciprocal experiment on the source side to using multi-component streamer, is to use a source array that consists of both dipoles and monopoles (Robertsson et al., 2012). However, at present time, no dipole sources with sufficient strength exist. The reciprocal source strategy to using variable-depth streamer acquisition is VSDA. While the impulse response of the hydrophones does not change significantly with depth, the response of the air-guns do. Good results are obtained with variable-depth streamer acquisition (Soubaras and Dowle, 2010; Soubaras, 2011, 2012; Salaun et al., 2016), but its reciprocal experiment has not been tested in field or with proper modeling.

The purpose of this work is to present a comparison study where different source strategies are tested. Here, we perform a comparison of three different source strategies by modeling 2.5D seismic data for frequencies up to 200 Hz. The different source approaches we test are: Multi-level source (MLS) arrays, variable source depth acquisition (VSDA) (Haavik and Landrø, 2015) and conventional - single level - source array (SLS). Although, more complicated seismic modeling methods exist, such as finite difference, finite element and FK methods, the modeling here is performed using Kirchhoff modeling in a constant velocity medium. This method is chosen because: 1) it is computationally fast when we want to model a broad range of frequencies and reflectors that are not flat. 2) we are free to choose events being modelled. In this way we isolate the effect of the source-side strategies on the final image, so that the comparisons will be easier.

4.3 Theory

Interference between the down-going wave and the reflected up-going wave (the ghost reflection) from the source, cause notches in the frequency spectra in recorded wavefield. The position of the notches are dependent on the depth of the source z and the take off angle. The ghost response for a monopole source is given as (Amundsen, 1993):

$$g(z,k) = 1 - r_0 \exp{(2ik_z z)}, \tag{4.1}$$

where r_0 is the free surface reflection coefficient, i is the imaginary unit, $k_z = \sqrt{\frac{\omega^2}{c^2} - k_r^2}$ is the vertical wavenumber in the water layer, $\omega = 2\pi f$ is the angular frequency, k_r the radial wavenumber and c being the velocity in water. The position of the ghost notches are given by:

$$f_n = \frac{c}{2z\cos\theta}n, \quad \text{for} \quad n = 0, 1, 2, \ldots, \tag{4.2}$$

where θ is the take-off angle from vertical. Conventionally, the source depth has been chosen based on the target for the seismic acquisition, to avoid notches in the usable bandwidth. In modern broadband marine acquisition, it is becoming more common to use source arrays that are distributed both in time and in depth to avoid deep notches in the spectra. Figure 4.1 shows the zero offset ghost responses for a SLS at 6 m, a MLS at 6 m (2/3 strength) and 9 m (1/3 strength), and the mean spectra for VSDA with source depths 3.75, 7.5, 11.25, 15 and 18.75 m, all sharing a common notch at 200 Hz. Haavik and Landrø (2015) proposed an inversion scheme to find the optimal source depths for

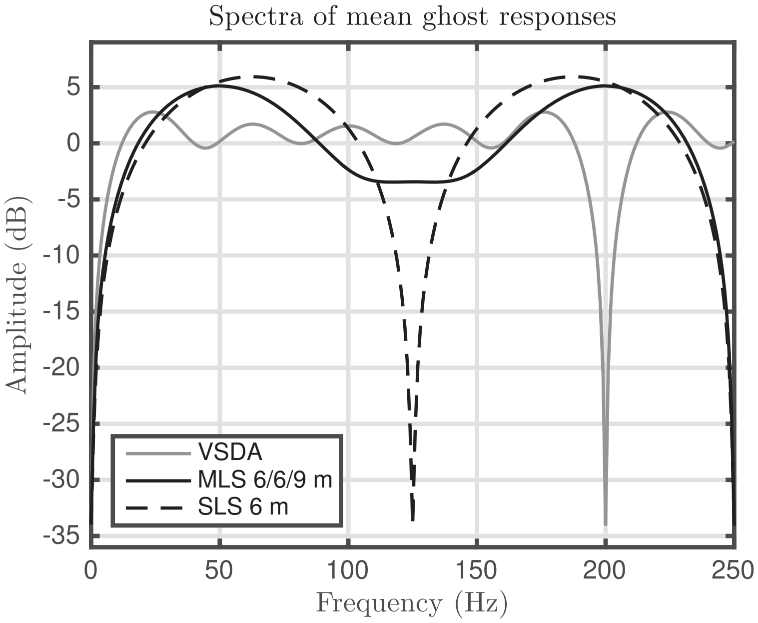

Figure 4.1: Vertical ghost responses for sources at 6 m (dashed), 6 (2/3) and 9 (1/3) m source (black) and the mean spectra of 5 source depths (grey) at 3.75, 7.5, 11.25, 15 and 18.75 m illustrating stacked VSDA data.

VSDA. However, they used data from a single large air gun, thus having several notches resulting from the bubble period itself. For a tuned air-gun array, the inversion for optimal source depths is not as important as having complimentary source-ghost functions.

The amplitude spectrum of the output pressure waveform for an air-gun source vary with source depth. The natural frequency of the bubble motion is increasing, and qualitatively, the whole amplitude spectrum is stretched with respect to the frequency axis when the source depth is increased (Willis, 1941; Haavik and Landrø, 2016). The shift in natural frequency for an air-gun signature when changing the depth from z_1 to z_2 can be given as:

$$f_2 = f_1 \left(\frac{10 + z_2}{10 + z_1} \right)^{5/6} . \tag{4.3}$$

where $f_i = \tau_i^{-1}$, and τ_i being the bubble-time period at depth i. For example, an air-gun with peak frequency of 6 Hz at a depth of 3.75 m, will have a peak frequency at 11 Hz for 18.75 m.

4.4 Modeling

We use Kirchhoff modeling in a constant velocity medium to synthesize shot gathers for primary reflections over the reflectivity model shown in Figure 4.2. First, we model the impulse response for three different kinds of source strategies: VSDA, MLS, and conventional SLS. The source ghosts are correctly included by using the method of images, or mirror source approach (Lloyd, 1834). Furthermore, we model data with no receiver-side ghost, to isolate the effect of the source strategies. The data are generated by convolving the impulse responses from the model with source signatures that corresponds to sum of all notional source signatures from an air-gun array positioned at the respective depths. The notional source signatures are modeled using a commercial air-gun modeling software. A tuned air-gun array consisting of 28 air guns with a total volume of 4100 in^3 (67.2 l) is used. The amplitude spectra of the sum of the notional source signatures at the respective depths and the vertical far field signatures for the different depths (or type of strategy) is shown in Figure 4.3a and b, respectively. We observe in Figure 4.3a that the peak frequency increases with increasing source depth. Although not easy to see in the figure, the peak frequency increases from 6 Hz for the source at 3.75 m to 11 Hz for the source at 18.75 m, and the corresponding amplitude for the peak frequency value is down 3.5 dB. The diversity of ghost notches can clearly be seen in Figure 4.3b, except for the spectrum of the MLS (6/6/9 m) far-field signature where the notches are reduced. Furthermore, we see that for the deep sources (11.25 to 18.75 m), the shift of the peak frequency along with the ghost response being more favorable towards low frequencies results in high amplitudes in the bandwidth 7–15 Hz, compared to the other sources. This is the same as shown in Hegna and Parkes (2011).

For the MLS, we model data from sources at 6 m and 9 m, and add them together using a 2/3 weight on the 6 m data and 1/3 weight for the 9 m data. The 9 m data is given a static time shift, that corresponds to aligning the primary vertically downwards with the 6 m data. We model 256 shot gathers for each source strategy. The shot separation is 18.75 m, the receiver spacing is 12.5 m, and the streamer is 2000 m long, with a minimum offset of 25 m. The data is modeled over a local model that covers the source and receiver spread, in addition to 800 m to both sides. A noise data set containing 256 "shot gathers" with different realizations of pink noise is added to the respective shot gathers, giving the same noise for all the different source strategies. Furthermore, we model a data set containing only the impulse response of the model (shots) without any ghosts or source signatures. This data set is used as reference. Normal move-out (NMO) corrected common mid-point (CMP) gathers from the three different strategies are shown in Figure 4.4. In Figure 4.4, we can observe that the noise is equivalent for all strategies. Furthermore, the different source signatures that are used in VSDA, and how this affects the continuity of the ghost events in a given horizon is clearly visible in Figure 4.4c. The ghosts in VSDA make local dipping events from the flat primaries.

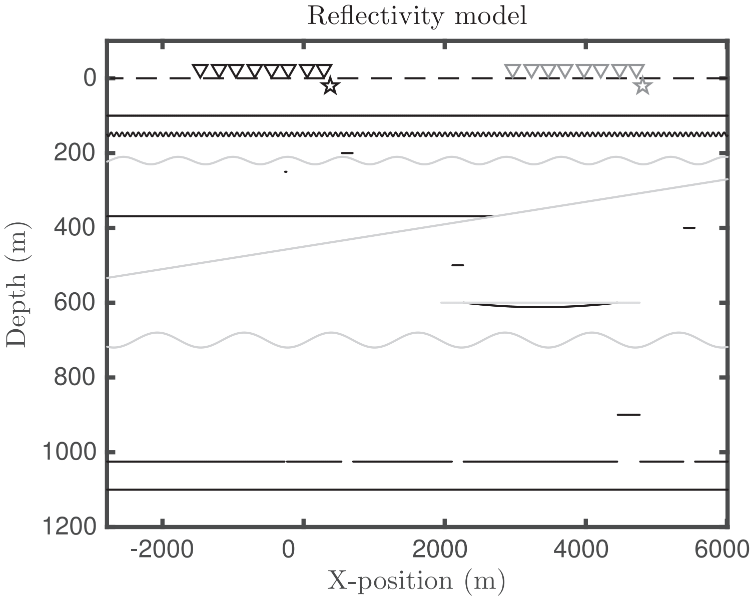

Figure 4.2: Reflectivity model used in modeling of seismic data. The black star and triangles illustrates the first source and receiver positions and the grey star and triangles illustrates the last source and receiver positions. The grey reflectors have negative polarity and the black reflector have a positive polarity. The dashed line is the reference depth.

4.5 Processing and Results

To keep the comparison between the different source strategies as fair as possible, we use a very simple processing flow:

1. Re-datuming to mean sea level (MSL)
2. 1-Dimesional designature/deghosting
3. Sort to common mid-point gathers
4. Amplitude recovery (multply with t)
5. Kirchhoff pre-stack time migration
6. Residual move-out correction
7. Outer mute for migration-stretch > 30 %
8. Stack

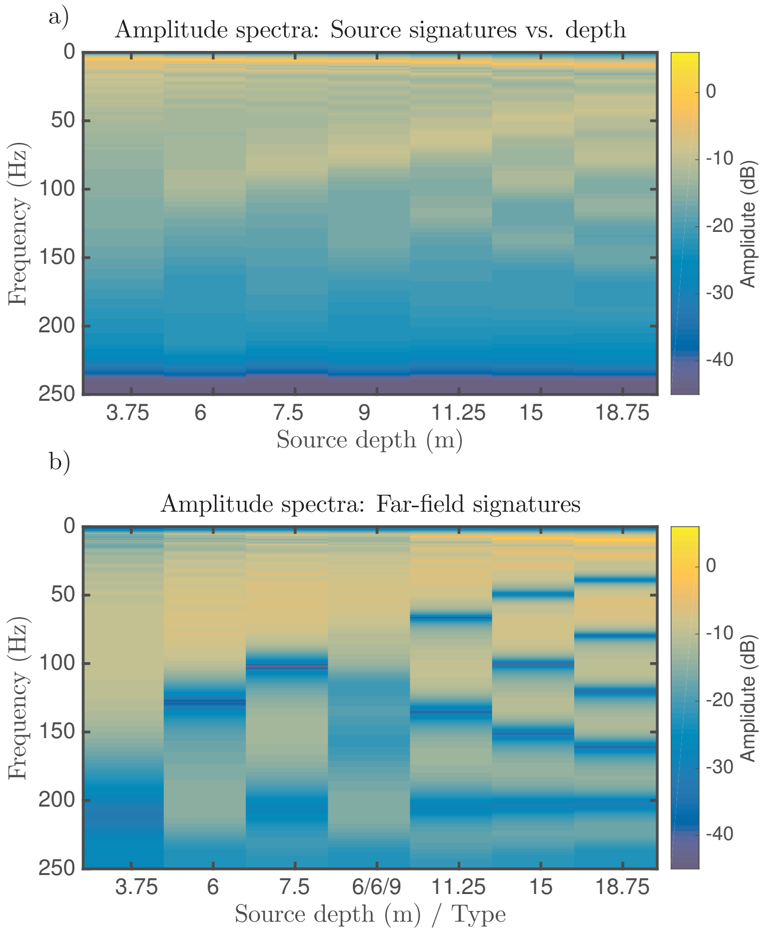

Figure 4.3: a) Amplitude spectra for the sum of all notional source signatures at the respective depths. b) Amplitude spectra of the far-field signatures vertically below the source. 3.75, 7.5, 11.25, 15, 18.75 m for VSDA, 6/6/9 m for MLS and 6 m for SLS.

The re-datuming is done by applying the following time shift to the data:

$$\Delta t_r(t_0, x) = \Delta t_s \left(1 + \frac{1}{2} \frac{x^2}{t_0(t_0 + \Delta t_s)c^2}\right) \tag{4.4}$$

where Δt_s corresponds to travel time for a wave to propagate from the source depth to mean sea level and t_0 is the travel time at zero offset. For the MLS (6 and 9 m), the time shift corresponding to the travel time for the 6 m source is used. The deghosting is performed in common-shot domain as a damped deconvolution with the inverse of the

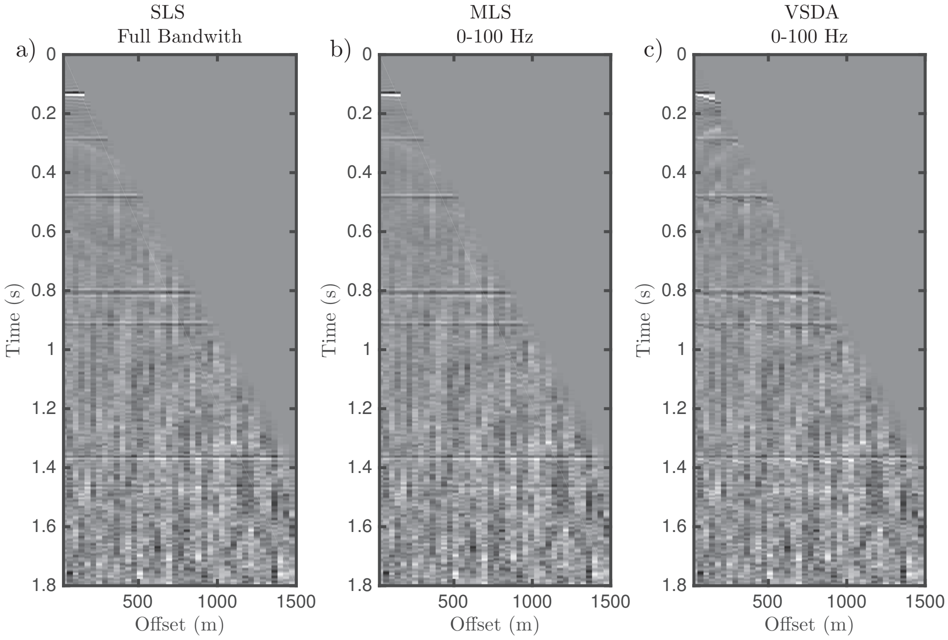

Figure 4.4: NMO-corrected CMP gathers for 6 m source (SLS) in a), 6/6/9 m source (MLS) in b) and VSDA c). The noise is the same for the three datasets. Note the different source signatures along the same reflectors for VSDA, particularly seen along the reflectors at 0.8 s and 1.3 ms.

respective ghost functions, for the SLS it is given as:

$$G^{-1}(\omega, z) \approx \frac{G^{*}(\omega, z)}{G^{*}(\omega, z)G(\omega, z) + \epsilon(\omega)}, \tag{4.5}$$

where $G(\omega, z)$ represents the ghost response for source depth z, ω is the angular frequency, ϵ is a damping term that is based on the noise level, and the superscript $*$ denotes complex conjugate. For the MLS, we use:

$$G_M^{-1}(\omega) \approx \frac{G_M^{*}(\omega)}{G_M^{*}(\omega)G_M(\omega) + \epsilon(\omega)}, \tag{4.6}$$

where $G_M(\omega)$ is the combined one-dimensional ghost response for the MLS (6/6/9 m). A least-squares (LS) type deconvolution (Soubaras and Dowle, 2010) is used on the VSDA data:

$$G_j^{-1}(\omega, z_j) \approx \frac{G^{*}(\omega, z_j)}{\frac{1}{N}\sum_{i=1}^{N} G^{*}(\omega, z_i)G(\omega, z_i) + \epsilon(\omega)}. \tag{4.7}$$

Here, z_j is the source depth for the source used in the $j'th$ shot gather, N is the number of shots in a sequence of different source depths, here equal to five. The same damping

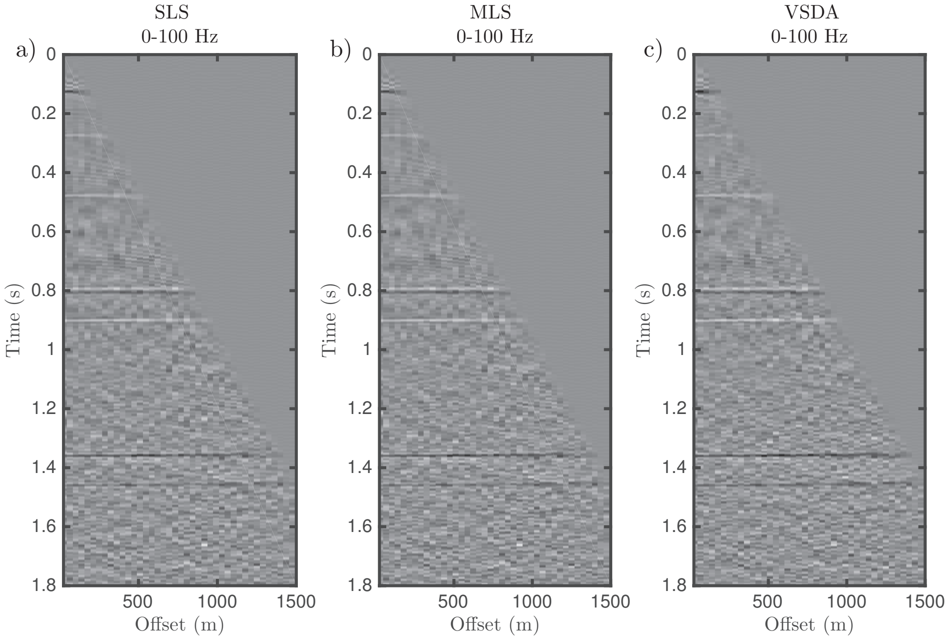

Figure 4.5: Common image gathers for SLS in a), MLS in b) and VSDA in c). Observe there are no apparent variation in the wavelet along the different reflectors, as seen clearly in Figure 4.4c.

term is used for the VSDA, as for the MLS and the SLS. No noise attenuation is applied, except for the damping term in the deghosting step. The noise gathers were also processed in the exact same processing flow as the data with noise, giving us the opportunity to compare noise levels in the processed images. The reference data are processed without redatuming, designature and deghosting.

Migrated common image gathers (CIG) at the same mid-point position as in Figure 4.4 are shown in Figure 4.5. We observe that the data from the different strategies appears very similar. The variations of the wavelet along the same reflectors, as seen in Figure 4.4c are not that apparent in the migrated CIG in Figure 4.5c. This is because the migrated images contain data from several shot-gathers, thus from more than one signature for the VSDA. The amplitudes along the reflector at approximately 1.35 s are shown in Figure 4.6 after subtracting the corresponding noise data, to isolate the effect of the source strategies have on the amplitude versus offset (AVO) behaviour. We can clearly see the large variations in amplitude for the VSDA data. When the data is smoothed with a window of five data points, corresponding to the five different source depths, the correct AVO behaviour is recovered.

The stacked migrated images are shown in Figure 4.7 for the frequency band 3 - 200 Hz and in Figure 4.8 for frequencies between 3 and 15 Hz. Due to the resolution, smaller

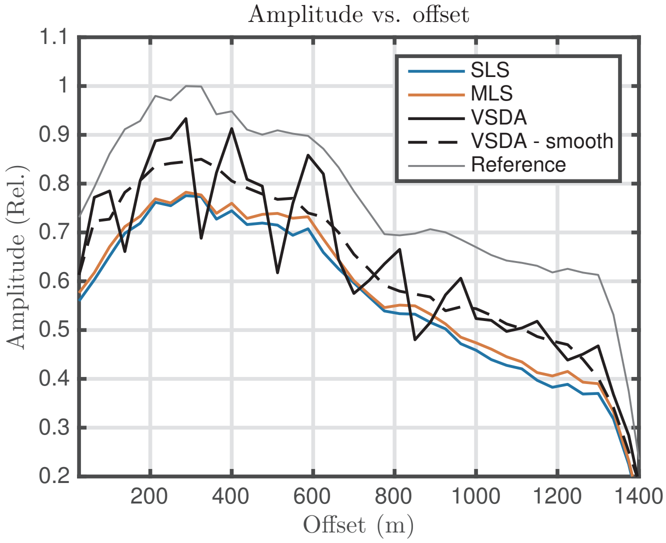

Figure 4.6: Amplitude versus offset curves for the reflector at approximately 1.35 s. The amplitudes are from noise free CIG, and normalized to the maximum of the reference data.

images of the frequency band between 100 and 150 Hz are shown in Figure 4.9. All the stacked images have been multiplied with $t^{0.6}$ for the purpose of normalizing the amplitude of the images with respect to depth, and are displayed using the same color map in the respective figures. In Figure 4.7, all three source strategies appear quite similar, but we observe that there is a more pronounced low-frequency halo surrounding the reflectors, especially at approximately 0.9 s (sinusoidal reflector) and 1.35 s, for the VSDA data (Figure 4.7c) than in the other strategies. This is also what we can observe in the reference data in Figure 4.7d. In the frequency band between 3 and 15 Hz, in Figure 4.8, we observe that the images from SLS and MLS in Figure 4.8a and b, respectively, have significantly lower S/N than the VSDA in Figure 4.8c. We can also observe that the first reflector in Figure 4.8c has periodic variations in amplitude with x-position. In the bandwidth between 100 and 150 Hz, we can observe differences between all three source strategies. As expected, the image from the SLS at 6 m with a ghost notch at 125 Hz has significantly more noise than the other two images. We remind the reader that the deconvolution that is used is damped, and that the damping parameter is a trade-off parameter between lots of noise and signal, or no signal and some noise. A large damping parameter will attenuate noise, but the signal will not be properly recovered. If no damping is used, the signal will be recovered (in theory), but the noise will be blown up and completely cover up the signal. Here we have chosen the damping so that we obtain results that are acceptable, and still recover some of the signal. The symmetrical side–lobes in Figure 4.9a is due to imperfect recovery of the signal. This is less pronounced in Figures 4.9b,c and d. Visually, the VSDA image appear to have more energy in the given bandwidth, and the reflectors

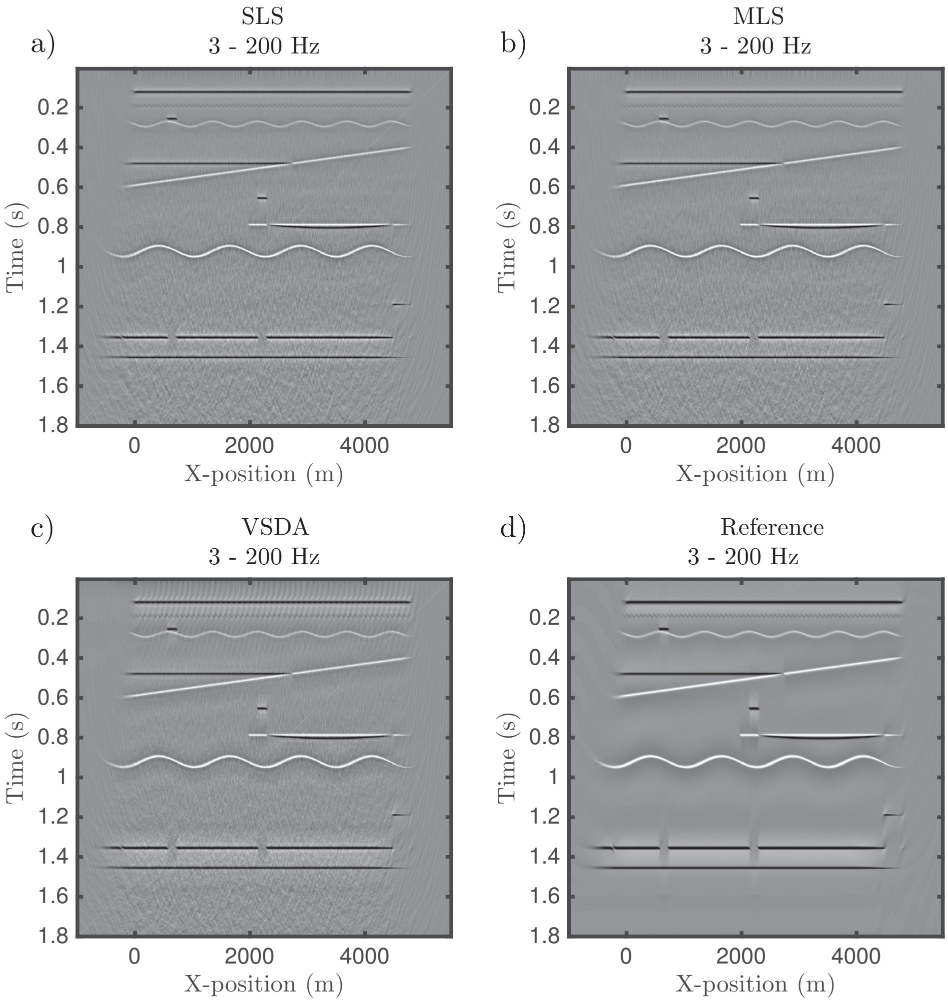

Figure 4.7: Full bandwidth stacked migrated images of the SLS data in a), MLS data in b), VSDA data in c) and the target image in d).

are more continuous and brighter (see Figure 4.9c).

The amplitude spectra of the migrated images are shown in Figure 4.10a. The most prominent feature is the oscillations in the spectra. The period of the oscillations are 10 Hz, and corresponds to travel time between the two deep reflectors that are positioned 0.1 s apart. Events that are separated by a given distance in time give rise to oscillatory behaviour in the frequency domain. We can observe that the spectra from all the source strategies have this behaviour up to approximately 100 Hz. Above 100 Hz, the amplitude spectra for the VSDA is lower than for the SLS and MLS, with exception in the vicinity of the ghost notch at 125 Hz for the SLS. However, the VSDA data continues with the oscillatory trend up to 150 Hz, indicating that the S/N is higher for VSDA image than for the other strategies in this frequency band. In the reference amplitude spectra the oscillatory behaviour is seen in the full bandwidth. For frequencies between 7 and 15 Hz, the VSDA data have up to 5 dB gain over MLS and 6 dB gain over SLS. This is also apparent in Figure 4.8. The S/N is possible to study when the noise is known. We processed the noise gathers in the exact same processing flow for the respective data sets, and can be subtracted from the data sets to obtain noise-free data. The ratio between the amplitude spectra of the noise-free data and the amplitude spectra of the noise is shown in Figure 4.10b. We note that this is not a measure of how much signal the respective data sets contain relative to the reference data, but a measure of the S/N in the resulting data. In the frequency band from 5 to 31 Hz, the VSDA data have the highest S/N. In the window between the two first vertical black lines in Figure 4.10b, 31 to 50 Hz, the MLS data have the highest S/N. In the window between the two last vertical black lines in Figure 4.10b, 50 to 98 Hz, the SLS data have the highest S/N. Above this the VSDA data has the highest signal to noise ratio.

For very shallow reflectors, the fold, or number of traces that contributes to the stacked image, is very low due to stretch-mute, and this often results in poor images at these depths. For VSDA, this might be even worse because the resulting signatures at different offsets are different. The VSDA image should contain a high fold so that all the different signatures are stacked into the image. A zoomed view of the shallow part of the stacked images are shown in Figure 4.11. Figures 4.11a,b and c are divided into two parts. A minimum offset of 137.5 m is used in the part to the left of the black line illustrating more realistic seismic acquisition geometry, and a minimum offset of 25 m is used in the parts to the right of the black line. We observe that in all the stacked, images where a minimum offset of 137.5 m is used, the amplitudes are weaker in the most shallow parts, compared to when the full offset range is used. This is expected as less energy is stacked into the image. We can observe variations in the wavelet along the first two reflectors in the VSDA image in Figure 4.11c, but this is not apparent in the reflector that appears as a gentle through at approximately 0.3 ms, or for deeper reflectors. In these shallow parts of the image, SLS and MLS results in a better image.

4.6 Discussion

Our modeling study indicates that acquiring seismic data with variable source depths can result in images that are of high fidelity and have better S/N at frequency bands from 6 to 15 Hz and from 100 to 150 Hz compared to a standard source at 6 m and a multi-level source at 6/6/9 m. We have shown that the VSDA do not suffer from having different signatures in stacked migrated images, at times greater than 0.25 s. High S/N in the VSDA images is due to the notch diversity on the source side. The extra boost seen in low frequencies (6–15 Hz) is because of the deep sources. Deep tow results in a ghost function that is favorable towards lower frequencies, in addition to pushing the peak frequency of

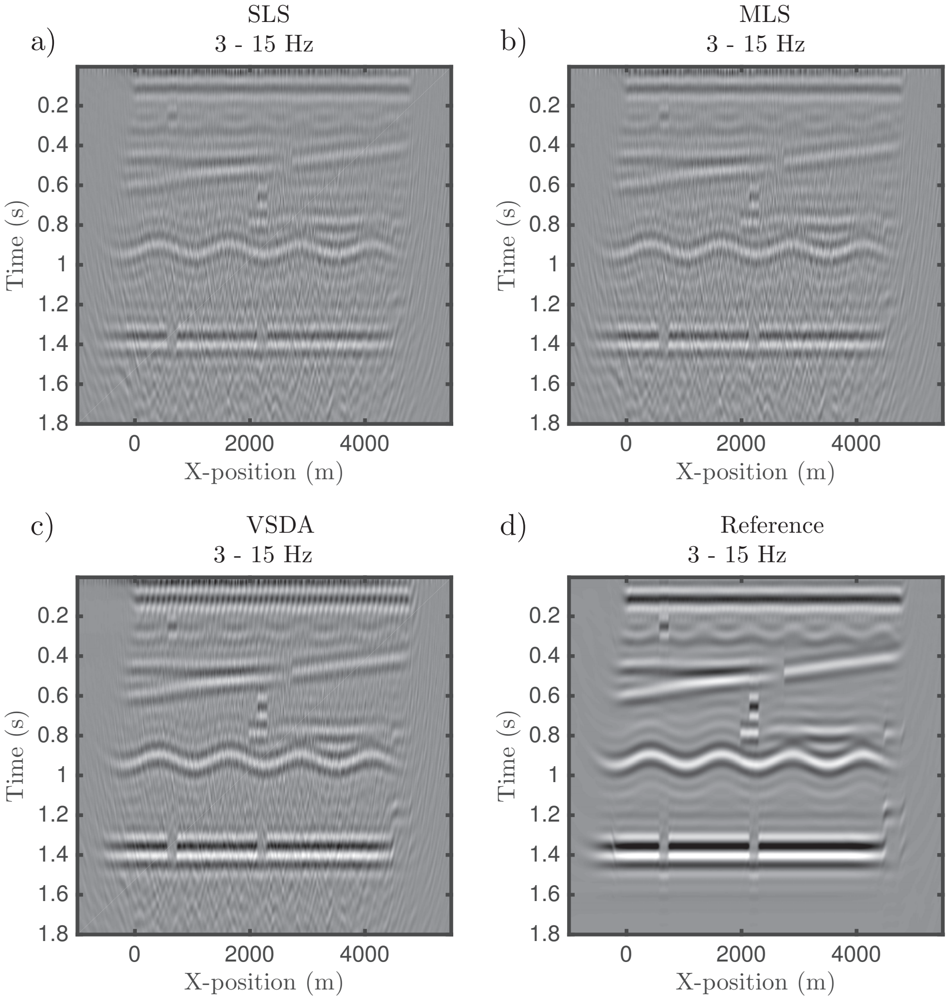

Figure 4.8: Stacked migrated images of the SLS data in a), MLS data in b) and VSDA data in c) for the frequency range between 3 and 15 Hz.

the air-gun source into towards the frequencies where the ghost amplifies the signal. The amplitude at 11 and 120 Hz for the source used here, is respectively 13 dB and 10 dB higher when the source is positioned at 18.75 m and 3.75 m compared to the 6/6/9 m. That is 4.5 and 3.5 times more energy at those frequencies, respectively. If we assume that the S/N is proportional to the square-root of the number of traces, it will require about 20 and 12 traces of the MLS data to obtain the same S/N as for one trace at the respective depths in VSDA. These numbers are of course approximate, but it shows that acquiring seismic data with different source depths will result in good S/N over a broad bandwidth.

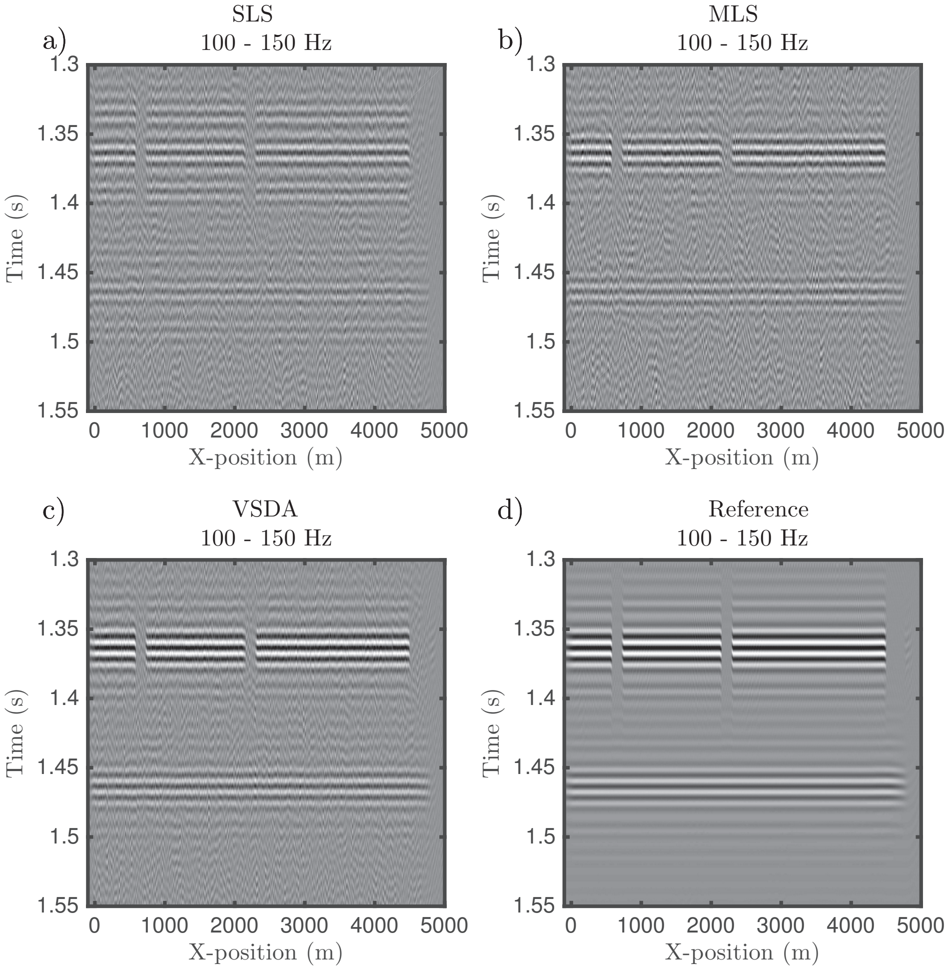

Figure 4.9: Window of the deeper two reflectors in the model in stacked migrated images of the SLS data in a), MLS data in b), VSDA data in c) and the reference data in f) for the frequency range between 100 and 150 Hz.

The least-squares deghosting used on the VSDA data is a natural choice when complimentary ghost functions are used (Soubaras, 2012). The phase of the data is corrected for, and the amplitudes are weighted in the frequency bands with high S/N. However, for prestack data analysis, such as amplitude versus offset (AVO) analysis, the LS-deghosting will not give the correct amplitudes with respect to frequency. From the example presented here, it is clear that the AVO behaviour of the VSDA data is not as optimal as for the other two strategies (see Figure 4.6). With a simple smoothing in the offset direction we recover the correct AVO-behaviour from the VSDA data. Many AVO inversion or attribute-generation schemes are based on a least-squares fit to some amplitude function

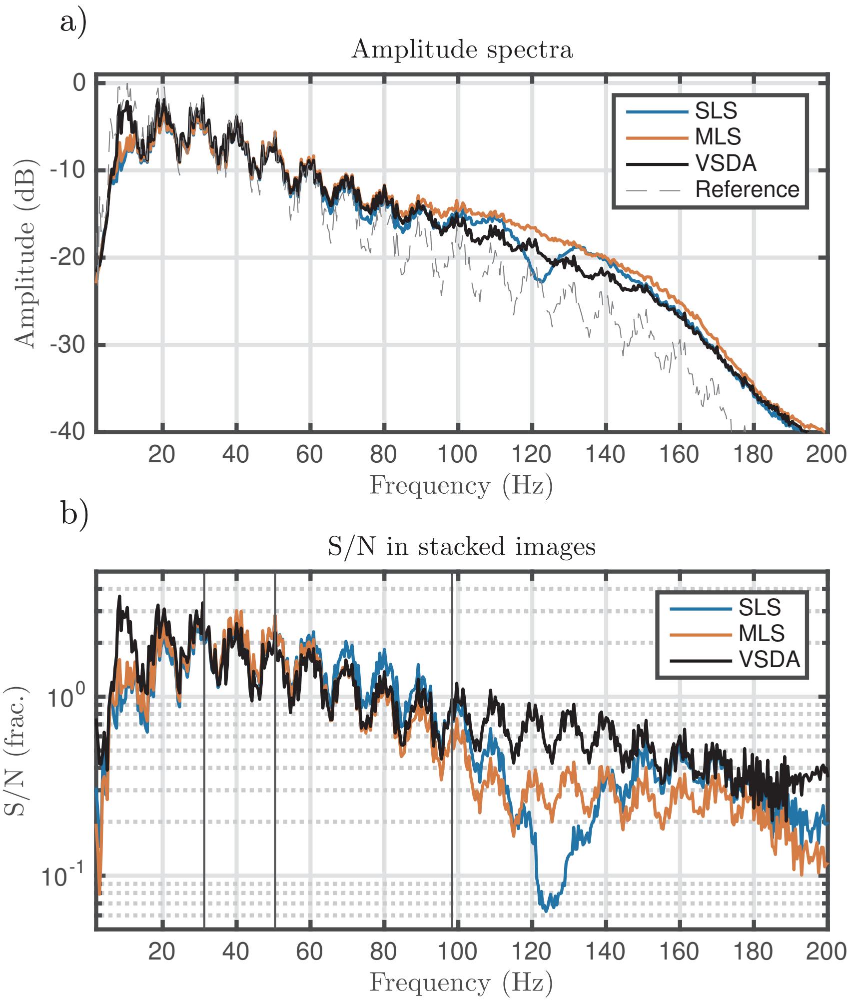

Figure 4.10: a) Amplitude spectra from the stacked data sets. The oscillations with period of 10 Hz seen the spectra are related to the two events that are present at approximately 1.35 and 1.45 s - 0.1 s apart. b) The signal to noise ration of the stacked images. The noise have been subtracted from the noisy data prior finding this ratio.

versus angle (Buland and Omre, 2003; Chopra and Castagna, 2014), and we think that a least-squares method may be able to pick up the AVO behavior despite the variations from trace to trace. This is not shown here. A joint-deconvolution of migrated and mirror-migrated images, as proposed in Soubaras (2012), for variable-depth streamer data could also useful for VSDA. Other source side deghosting and designature algorithms based on inversion exist (e.g. Wang et al., 2015; Fu et al., 2015), and may be used for VSDA data on a shot-to-shot basis. This, however, has not been demonstrated here. A problem that may arise when performing conventional deghosting on a shot-to-shot basis is that we are amplifying noise at all notch frequencies. A possible solution to this might be to "borrow" energy to fill these notches from neighbouring traces.

For the ultra low-frequency end of the spectra ($f < 5Hz$), VSDA does not improve the S/N when using an air-gun source. This is because the spectrum of the source change when we change the source depth. To benefit from the deep-tow ghost response, a source that does not change its amplitude spectra with source depth must be used. A potential candidate for this is the marine vibrator source (Baeten et al., 1988; Tenghamn, 2006; Pramik et al., 2015). Experimental data for a vibrator with a usable bandwidth in the range from 5–100 Hz, show that the natural frequency change from 15 to 16 Hz when the source depth is changed from 5 to 100 m depth, and can be considered constant in depths the between 8 and 25 m (R. Tenghamn, personal communication, 2016).

In the simple example provided here, we have not included attenuation, i.e., frequency dependent damping of the signal (e.g. Futterman, 1962; Kjartansson, 1979). However, attenuation (and dispersion), often have a huge impact on the final images. The attenuation of the seismic signal is frequency dependent, and the signal is progressively more attenuated going from low to high frequencies in the data. The degree of attenuation is also dependent on the media the waves are propagating through (Q) and the total travel time. For events arriving from deep reflectors in earth will therefore contain less high frequency energy than events arriving from shallow depths. In real seismic data noise is always present. The S/N dictates whether or not it is reasonable to perform different types of processing to the data, e.g. perform deghosting or compensate for attenuation. The S/N for given source strength and noise level depends on the total travel time for the wave and the frequency. There always exist a depth (for stacked data) for each frequency where the S/N is to poor to extract data through processing. By increasing the S/N we push this surface to deeper parts giving the opportunity to recover more high frequencies in deeper parts of the resulting image.

We have not discussed any practicalities related to acquisition of variable source-depth seismic data. A possible solution can be depth-controlling devices for the sources. For example, in flip-flop shooting, where it might be possible to have the two arrays operating in two different depth-ranges. Several seismic acquisition companies are now performing acquisition with more than two source arrays behind the seismic vessel; up to five source arrays (Hager, 2016). It should therefore be possible to have five source arrays positioned stationary at five different depths.

4.7 Conclusion

We have presented a simple example of data modeled with different source strategies; conventional single-level, multi-level source, and variable source-depth acquisition (VSDA). The modeling shows that all strategies provide good migrated images, but amplitude spectra of the resulting images differ between the three strategies. The multi-level source and the variable depth source strategies provide a better and flatter spectra than the single-level source. VSDA provides better S/N in the frequency bands from 7 to 14 Hz and from 100 to 200 Hz. While the uplift seen in stacked images of VSDA data compared to multi-level source data is clear, VSDA comes at the cost of different wavelets along the same reflectors in common image gathers. This may cause difficulties for pre-stack analysis, but not for stacked images. The data modeled with VSDA show imprint of the different source signatures and ghost functions in the shallow-most parts of the final stacked image. At times larger than 0.25 s, this imprint is not visible as the fold of the data being stacked into the final image is increasing with depth.

This study shows that variable source-depth acquisition has the potential for improving the S/N over a broad bandwidth in seismic data.

4.8 Acknowledgements

Thanks to Lundin Norway AS for financial support to Kjetil E. Haavik's PhD project. We would like to thank the Norwegian Research Council for financial support to the Rose Consortium. K. E. Haavik thanks the Norwegian Petroleum Directorate (NPD) for their hospitality during his stay there.

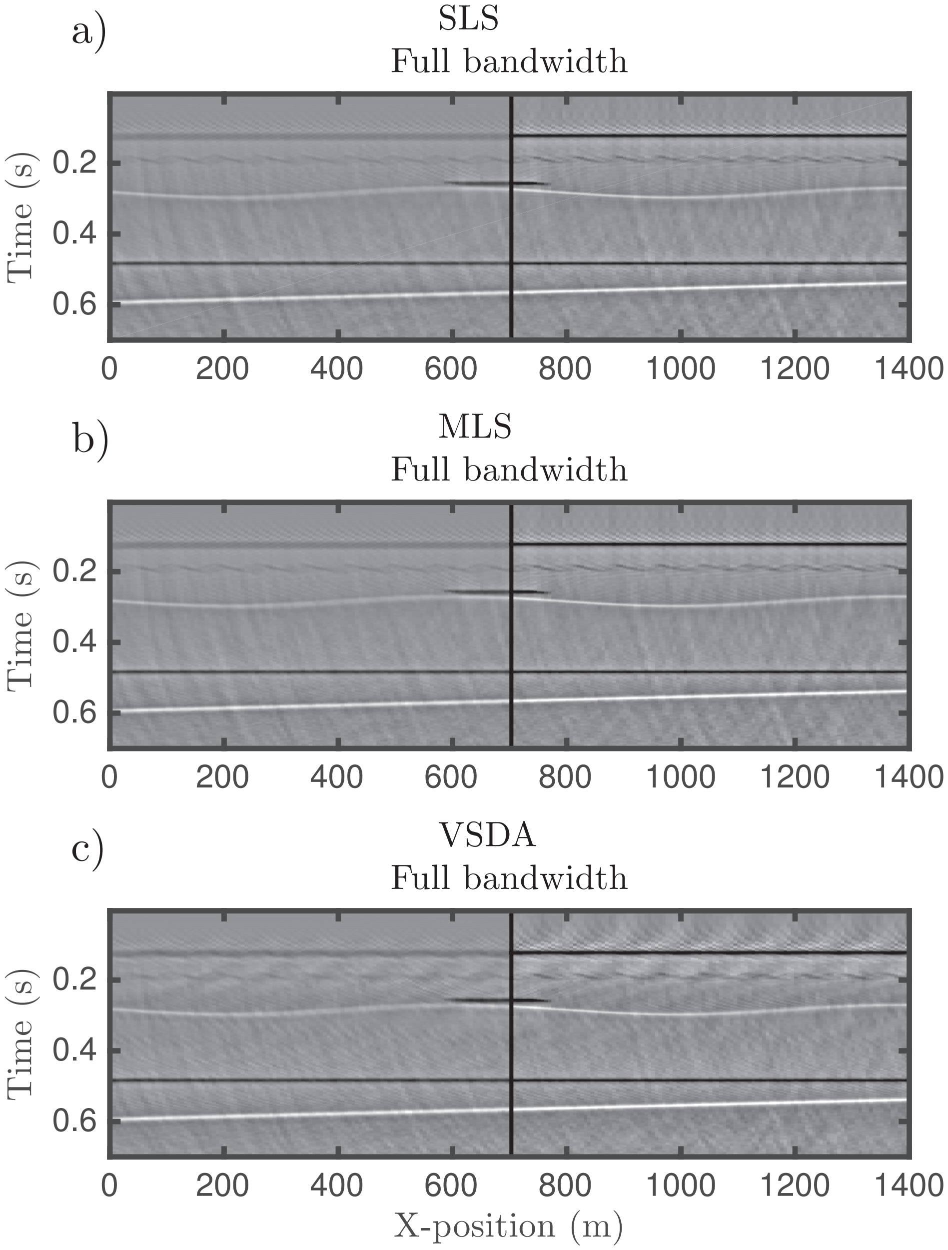

Figure 4.11: Zoom in on shallow parts of the stacked images for the SLS in a), MLS in b) and VSDA in c). The parts to the left of the vertical black lines are stacked sections with minimum offset is 137.5 m, and the part to the right have a minimum offset of 25 m.

Chapter 5

Implementation of marine seismic source wavefields in finite-difference methods using wavefield injection*

Kjetil Eik Haavik, Espen Birger Raknes and Martin Landrø
Norwegian University of Science and Technology, Trondheim, Norway

5.1 Abstract

We have developed a method for implementing source wavefields in finite-difference (FD) schemes for marine seismic modeling, migration and inversion. By using the wavefield injection technique, it is possible to inject arbitrary source wavefields into a FD grid. We have assumed that the notional source signature from each gun in an air-gun array and their positions are known. The source wavefield is extrapolated to a specified surface below the true source positions using analytical Green functions. On this surface, both pressure and its vertical derivative are inserted into the finite-difference grid. The wavefield propagating from this surface will then propagate downwards and appear as if it came from the true source position. The source positions do not need to coincide with the FD-grid points, and the free-surface reflection coefficient for the source-ghost can be specified, i.e., deviate from -1 and be frequency dependent. These features are possible because of the analytical extrapolation step. The presented method allows modeling of any kind of marine seismic source as long as the notional source signature and radiation pattern from each individual source element is known. A simple full-waveform inversion example shows that it is important to honor the source geometry in forward modeling of seismic data.

Paper published in GEOPHYSICS, Vol.81 No. 5. T211–T219. DOI: 10.1190/geo2016-0026.1. Parts of this work was presented at the 84th SEG Annual Meeting in 2015

5.2 Introduction

Coarse-grid finite-difference (FD) methods (e.g. Virieux, 1986; Holberg, 1987) have been used extensively in seismic modeling, migration and full waveform inversion (FWI), in the past decades. With increasing computer power, even large 3D seismic data sets can now be migrated and inverted using methods such as reverse-time migration (RTM) and FWI, respectively. Due to the nature of the FD-method, correct positioning of seismic sources might be challenging as the source positions may not coincide with the grid points. Modern seismic air-gun arrays may consist of 30 - 40 separate air guns or clusters positioned at different depths and spanning large areas, whereas the source used in FD modeling and imaging methods is often as simple as a single monopole source injected into a single node on the grid. The source signature emitted from large air-gun arrays exhibit variations with direction both with respect to take-off angle and azimuth. These variations cannot be accounted for by injecting a single monopole source into the FD scheme because it does not honor the true source geometry.

To overcome this problem, several solutions have been proposed. Landrø et al. (1993a) use a fixed number of effective FD sources to model the output from an air-gun array in FD modeling. In their method, the effective FD sources consist of monopole and dipole sources that were injected at grid cells surrounding the true source array. They use an inversion scheme to minimize the error between the modelled wavefield and the measured wavefield on a mini streamer or an artificial plane below the sources. Mittet and Arntsen (2000) use optimized band-limited versions of the Dirac delta function (referred to as the cardinal sine function or sinc function), to distribute the energy from the true source position to the surrounding grid nodes. Hicks (2002) uses Kaiser-windowed sinc functions for the same purpose. Both of these methods require appropriate coefficients for the band-limited delta function used by Mittet and Arntsen (2000) and for the optimal length of the Kaiser-window used by Hicks (2002).

By representing the source wavefield through a representation theorem, it is possible to introduce the source wavefield in the FD grid using a surface integral. This is referred to as wavefield injection or the method of multiple point sources (Mittet, 1994; Robertsson and Chapman, 2000; Amundsen and Robertsson, 2014; Broggini and Robertsson, 2014). Here, we use the wavefield injection method recently reviewed in Amundsen and Robertsson (2014) as a tool for implementing wavefields from any kind of marine source configuration in FD methods through a hybrid approach (e.g. Alterman and Karal, 1968). We assume that the source signature and the position of each element in an air-gun array are known for a given source configuration. The total wavefield, in particular the pressure and its vertical derivative, resulting from all the source and ghost source elements are calculated at a specified surface below the true source position. This is done analytically using Green functions in the water layer. The analytically calculated wavefield is then injected into the FD grid at the depth of the specified surface using the wavefield injection technique. The analytical extrapolation step gives the flexibility to implement arbitrary sources that are positioned above this injection surface, and we are free to choose the free-surface reflection coefficient.

We suggest to use notional source signatures obtained from near-field measurements (Ziolkowski et al., 1982) at each air gun in an air-gun array or from air-gun modeling to calculate the wavefield at a given surface. We assume that the source wavefield can be described adequately through notional source signatures. Laws et al. (1998) showed that both the notional source method (Ziolkowski et al., 1982) and the mini-streamer method (Landrø and Sollie, 1992) gave excellent results for conventional arrays. However, for compact air-gun arrays there is a risk that the near-field to far-field extrapolation method might introduce errors (Landrø et al., 1991).

We show that this method works adequately for introducing wavefields in FD methods. Furthermore, we present a simple acoustic FWI example where we show that by not honoring the source geometry in forward modeling will lead to poor inversion result compared to the results when the true source geometry is honored. This difference is more pronounced when higher frequencies are included in the inversion.

5.3 Marine sources in FD-modeling

To implement the wavefield resulting from any marine source array in a FD scheme we use a hybrid approach (e.g. Alterman and Karal, 1968). We extrapolate the wavefield analytically from each individual source element down to the specified injection surface S and use superposition to obtain the total wavefield from all source elements on S. The analytically obtained wavefield is then injected on S in the FD grid. If we consider a homogeneous half space, the resulting wavefield from this injection process will only propagate downwards as long as the injection surface is chosen to be below the true source positions. If the injection surface is chosen to be below the receivers, there will not be any direct wave present in the recorded wavefield. This is because the wavefield will only propagate downwards, i.e., never propagate past the receivers. For an earth model that is not homogeneous, the wavefield resulting from this injection will appear as if it was introduced as sources at the true source positions, apart from the absence of the direct waves in the medium above the injection surface. Figure 5.1 shows a schematic view of the proposed method. There are two steps in this method: Analytical extrapolation of the source wavefield to S (Figure 5.1a) and injection of this wavefield into the FD grid on S (Figure 5.1b).

5.3.1 Wavefield injection

The pressure field in an unbounded homogeneous acoustic medium, $P(\mathbf{x}, t)$, generated by N monopole sources obeys the acoustic wave equation:

$$\frac{1}{c^2}\frac{\partial^2}{\partial t^2}P\left(\mathbf{x}, t\right) - \nabla^2 P\left(\mathbf{x}, t\right) = \sum_{i=1}^{N} S_i(\mathbf{x} - \mathbf{x}_i, t). \tag{5.1}$$

The source term is given as

$$S_i(\mathbf{x}-\mathbf{x}_i,t) = c^{-2}\delta\left(\mathbf{x}-\mathbf{x}_i\right)s_i(t), \tag{5.2}$$

where $s_i(t)$ is the i'th notional source signature from source element positioned at $\mathbf{x}_i$, $\delta(\mathbf{x})$ is the Dirac delta function, and c is the velocity of sound in the medium. If we are only concerned with the wavefield below the injection surface S, equation 5.1 can be written in terms of equivalent source terms (Morse and Feshbach, 1953) as

$$\frac{1}{c^2}\frac{\partial^2}{\partial t^2}P\left(\mathbf{x},t\right) - \nabla^2 P\left(\mathbf{x},t\right) = s^m(\mathbf{x},t) + s^d(\mathbf{x},t), \tag{5.3}$$

where $s^m(\mathbf{x},t)$ and $s^d(\mathbf{x},t)$ are the monopole and dipole source terms, respectively, at a point $\mathbf{x}$ and a time t. These are given, respectively, as (Amundsen and Robertsson, 2014)

$$s^m(\mathbf{x},t) = \int\limits_S \frac{1}{\rho}\frac{\partial P_s(\zeta,t)}{\partial n}\delta(\mathbf{x}-\zeta)\mathrm{d}S(\zeta) \tag{5.4}$$

and

$$s^d(\mathbf{x},t) = \int\limits_S \frac{1}{\rho}P_s(\zeta,t)\frac{\partial\delta(\mathbf{x}-\zeta)}{\partial n}\mathrm{d}S(\zeta), \tag{5.5}$$

where S is the injection surface positioned at a depth z_s, n is the normal vector to S, ρ is the density assumed constant on S, and $P_s(\mathbf{x},t)$ is the pressure from the source. It is clear that both the pressure and its vertical derivative are required on the surface S to use this source representation. Furthermore, S should in theory be a closed surface; but for a wavefield that is purely outgoing, this surface can be truncated without introducing large errors to the injected wavefield in the model below this surface. This is done by extending the injection surface out in absorbing boundaries around the numerical model to avoid aperture effects (e.g. Zhen et al., 2009).

5.3.2 Extrapolation using Green functions

The total acoustic pressure field, and the solution to equation 5.1, at a point $\mathbf{x}$ due to N monopole sources positioned at $\mathbf{x}_i$ can be written in terms of Green functions (Morse and Feshbach, 1953) as

$$P_s(\mathbf{x},t) = \sum_{i=1}^{N}\int\limits_V g(\hat{\mathbf{x}},t;\mathbf{x}_i) * S_i(\hat{\mathbf{x}}-\mathbf{x}_i,t)\mathrm{d}V(\hat{\mathbf{x}}), \tag{5.6}$$

where $g(\hat{\mathbf{x}},t;\mathbf{x}_i)$ is the Green function in a 3D homogeneous medium (V) relating the response from a point $\hat{\mathbf{x}}$ to a point $\mathbf{x_i}$, and $*$ denotes temporal convolution. For a half

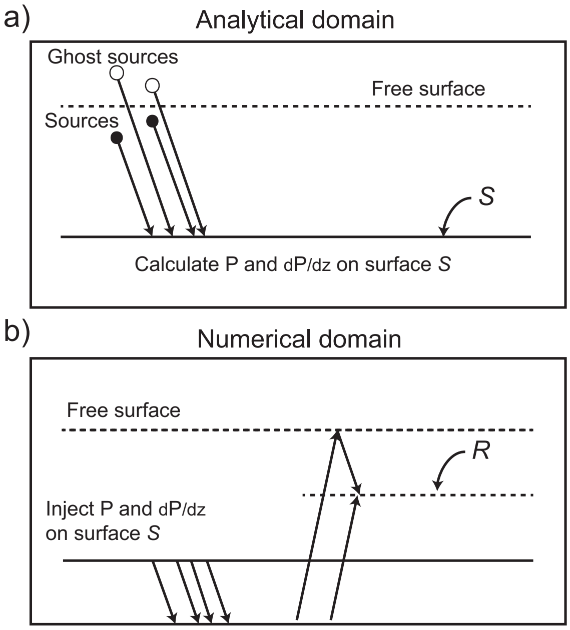

Figure 5.1: a) Analytical extrapolation of the source signature from each source and mirror (ghost) source to the surface S. b) The extrapolated signal is injected into the finite-difference grid. The wavefield propagates downwards from this surface as if the sources were injected at their true position at the correct time.

space below a free surface, we can use the method of images (Lloyd, 1834) and write the total Green function for the direct wave and the ghost reflection as:

$$g_t(\mathbf{x}, t; \hat{\mathbf{x}}) = g(\mathbf{x}, t; \hat{\mathbf{x}}) + R(t) * g(\mathbf{x}, t; \hat{\mathbf{x}}'), \tag{5.7}$$

where

$$g(\mathbf{x}, t; \hat{\mathbf{x}}) = \frac{1}{4\pi} \frac{\delta(t - \tau)}{|\mathbf{x} - \hat{\mathbf{x}}|}, \tag{5.8}$$

$R(t)$ is the frequency dependent free-surface reflection coefficient, $\hat{\mathbf{x}}' = (x, y, -z)$ is the image point of $\hat{\mathbf{x}} = (x, y, z)$, $\tau = |\mathbf{x} - \hat{\mathbf{x}}|/c$ and $\tau' = |\mathbf{x} - \hat{\mathbf{x}}'|/c$ are the traveltimes for the direct and ghost events, respectively. We have chosen to write the reflection coefficient as a temporal filter to show how a frequency-dependent reflection coefficient can be included. For a reflection coefficient equal to negative 1 we use $R(t) = -\delta(t)$. If $R(t)$ take the shape of a frequency dependent filter, it cannot be a zero-phase filter as this will introduce non-causality in the contribution from the ghost source. This will not be discussed any further here.

The wavefield injection method require the knowledge of the normal derivative of the pressure on the injection surface (equation 5.4). The normal derivative of the pressure along a horizontal surface can be found through the gradient of the Green function. At a constant depth it is given as (e.g. Landrø et al., 1993a)

$$\frac{\partial g(\mathbf{x},t;\hat{\mathbf{x}})}{\partial z} = \frac{z-\hat{z}}{|\mathbf{x}-\hat{\mathbf{x}}|^2} g(\mathbf{x},t;\hat{\mathbf{x}}) - \frac{1}{c}\frac{z-\hat{z}}{|\mathbf{x}-\hat{\mathbf{x}}|}\frac{\partial g(\mathbf{x},t;\hat{\mathbf{x}})}{\partial t}. \tag{5.9}$$

Here, we assume straight rays from the source and ghost source, to the point $\mathbf{x}$. The Green function and the vertical derivative of the Green function will be more complicated if the velocity in the water layer is not constant. Ray tracing may for instance be used to find the Green function if the velocity profile in the water layer is known.

5.3.3 Implementing wavefield injection

Implementation of the wavefield injection is done on a staggered-grid FD scheme that is second order in time and twelfth order in space. The monopole source term in equation 5.4 is added to the stress grid at the given depth. The derivative of the delta-function in equation 5.5 must be approximated. This can be done by using a high order central difference operator given as

$$\frac{\partial \delta(z)}{\partial z} P(z) \approx \sum_{i=1}^{M} P(z)\alpha_i \frac{\delta(z+i\Delta z)-\delta(z-i\Delta z)}{\Delta z}, \tag{5.10}$$

where α_i are differentiator coefficients and Δz is the grid sampling in the z direction of the spatial FD grid and M is the operator half-width. Here, for simplicity, we have omitted the dependency on other variables than z. We use Taylor series-based differentiator coefficients for the injection, and operators that are based on a group-velocity criterion (Holberg, 1987) in the FD-scheme. The pressure is added to the stress grid above and below the injection surface S as indicated in equation 5.10. Since we are truncating the surface S (i.e. not closed surface), we extend the injection surface out in an absorbing boundary (e.g. Zhen et al., 2009). Furthermore, we find that the half-width in equation 5.10 should at least equal the half-width of the FD operators in the FD-modeling scheme to obtain good injection results. The result of having a too small half-width in equation 5.10, is that parts of the wavefield will propagate upwards, while it ideally should only propagate downwards. Here, we use half-widths of eight and six in equation 5.10 and in the FD-modeling scheme, respectively. The sampling criteria for the wavefield injection is the same as the sampling criteria for the modeling scheme with respect to grid-points per shortest wavelength and dispersion.

5.4 Analytical versus injected wavefields

A test of the proposed method requires that we know both the notional source signatures from an air-gun array (Ziolkowski et al., 1982) and the wavefield produced by this source at a given depth. Unfortunately, we do not have this kind of field data available. What we can compare, however, is the wavefield from the method presented here at a given depth below the injection depth to the analytical wavefield extrapolated to the same depth. The result from a comparison as this will only show how good our implementation of the wavefield injection is, not how this method work on real data.

The air-gun array used for this test consists of 28 air guns in three sub-arrays positioned at a depth of 7.5 m and is spanning an area that is 40 m in the towing direction and 16 m in the direction perpendicular to the towing direction. This source design is similar to what is used in commercial seismic acquisition, besides from the length of the array which we have chosen to be longer to illustrate the directivity effects here, and in the FWI example below. The air guns have volumes ranging from 40 to 300 inch^3 (0.65 – 4.91 l) and the notional source signatures were modeled using a commercial air-gun modeling software. The notional source signatures from the 28 guns are shown in Figure 5.2. The source signatures have been filtered with a 45 Hz high-cut Butterworth filter. The analytical wavefields in this example are calculated using analytical Green functions and convolution.

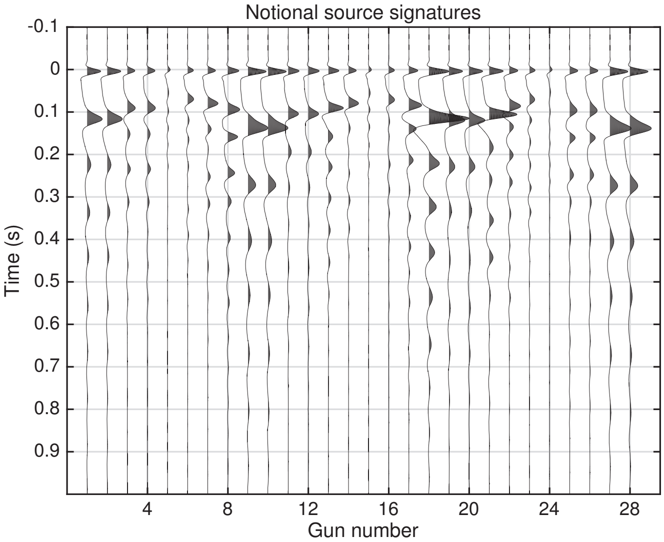

Figure 5.2: The notional source signatures that is used in modeling of seismic data. The signatures have been filtered with a high-cut filter at 45 Hz. The volumes of the guns range from 40 to 300 inch^3 and the array spread out 40 m in the in-line direction and 16 m in cross-line direction.

The injection surface for this example is 50 m below the free surface, and the spatial grid sampling is $\Delta x = \Delta y = \Delta z = 5$ m. We use a constant velocity of 1500 m/s to mimic seawater. We note that the array does not coincide with the grid points in the cross-line direction. Snapshots of the wavefield along the in-line direction at the center of the array are shown in Figure 5.3 at four different time steps. This figure shows that the injected wavefield is in practice only propagating downwards from the injection surface. This shows that the injection of an analytical wavefield works very well. At time 0.05 s we observe that the wavefield exhibits no clear directivity. At times 0.15 s, 0.25 s and 0.35 s, we can clearly observe the directivity of the source wavefield. The observed directivity is related to three different effects: The ghost reflection, spatial distribution of the sources and differences between the notional source signatures. The latter is by itself not a cause for directivity, but in combination with spatial distribution of sources, this will increase the directivity. The reason why the directivity is more apparent at later times than for early times is because the primary pulse from all the separate guns are aligned in time, while the bubble-pulses are not (see Figure 5.2). The wavefield is extracted at 100 m below the free surface and compared to the analytical wavefield at the same depth. The wavefield extracted at 100 m from the FD modeling, the analytically calculated wavefield and the difference between them are shown in Figure 5.4. We observe that the differences are strongly correlating with the amplitude of the signal. The signal recorded at zero offset (center of the source array) at 100 m is shown in Figure 5.5a together with the analytical signal and the difference between the two. The corresponding amplitude spectra is shown in Figure 5.5b together with the phase difference between the modeled and the analytical signal. The normalized root-mean-square (NRMS) difference between the modeled and analytical signal is 0.22% for the trace shown in Figure 5.5b. We see that the difference is increasing with frequency. Relatively large differences are seen below 5 Hz, but the amplitude of the signal at those frequencies is very low. This is also what we see in the plot of the phase difference. The cause for these differences are probably twofold: First, the coefficients that we use in the approximation to the vertical derivative in equation 5.10 may not be ideal. The coefficients used here are Taylor based, and it may be that other coefficients can result in even better injection. Second, errors may be a result of inaccurate numerical integration of the notional source signatures prior to the extrapolation step. The differences are in general small.

5.5 FWI using true source geometry

FWI is a classical inverse method for estimating model parameters affecting wave propagation based on minimizing the difference between measured and modeled seismic data (Tarantola, 1984; Mora, 1987; Virieux and Operto, 2009). The minimization is performed using a local gradient-based optimization method. FWI is a non-linear and ill-posed (in the Hadamard sense) problem. Thus, many solutions to the inverse problem exist. To mitigate this problem, Bunks et al. (1995) perform inversion in time domain and use a multi-scale scheme that starts the inversion using a coarse grid and low temporal frequencies. After a number of iterations on this grid, the inversion process is continued on a denser grid and with a broader frequency band. Sirgue and Pratt (2004) perform inversion in frequency domain and discretize the frequencies in an efficient way to cover all the wave-numbers in the model, thus reducing the number of temporal frequencies used in

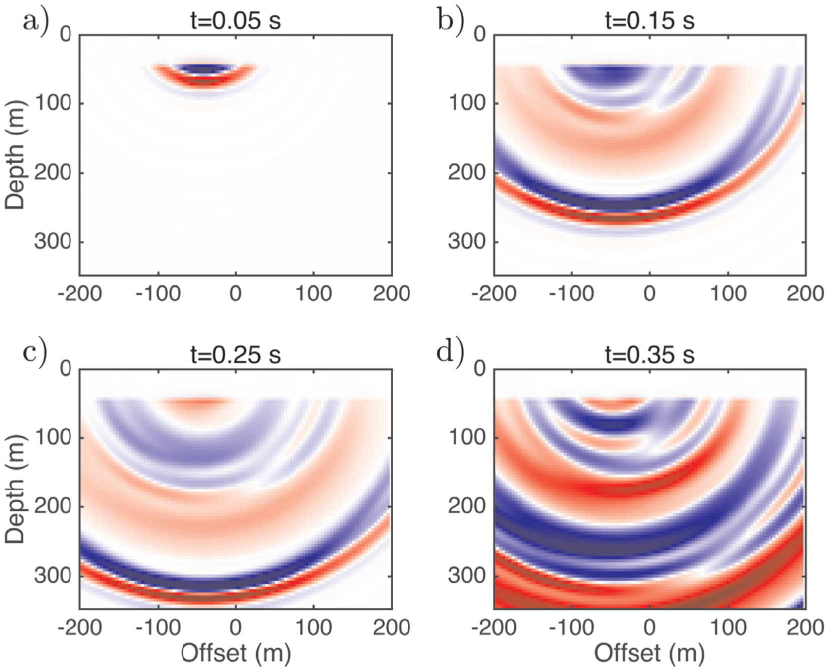

Figure 5.3: Snapshots of the injected wavefield along the in-line direction through the center of the array at times 0.05 s (a), 0.15 (b), 0.25 (c) and 0.35 s (d). Source directivity can most clearly be seen at the later time steps.

the inversion. FWI has succesfully been applied to 2D seismic data (Pratt et al., 1996), 3D seismic data for both acoustic and elastic parameters (e.g. Warner et al., 2008; Raknes et al., 2015) and time-lapse seismic data (e.g. Raknes and Arntsen, 2014).

For FWI, it is important to know the source used in acquisition of the seismic data as the forward modeled data will be a function of both model parameters and the source. To illustrate how the inversion is affected by not using the correct source geometry, we present a simple 2D acoustic inversion example. The velocity model used to generate synthetic data has $N_z N_x$ = 175 × 750 grid points with grid sampling of $\Delta x = \Delta z = 2$ m and is shown in Figure 5.6a. A constant density of 1000 kg/m^3 is used for simplicity. This velocity model is based on an outcrop of collapsed Mesozoic strata and associated infill deposits at Kvalvågen on Spitsbergen. Despite being from a different location, the concept of using outcrops for advanced seismic modeling and processing is presented in Johansen et al. (1994, 2007). The initial velocity for the inversion (Figure 5.6b) is a smoothed version of the true model: Triangle-weighted smoothing in both x- and z-direction. The water column in this smoothed velocity model was replaced by the true velocity in the water column. The source that is used to generate the data consist of a 40-m long array

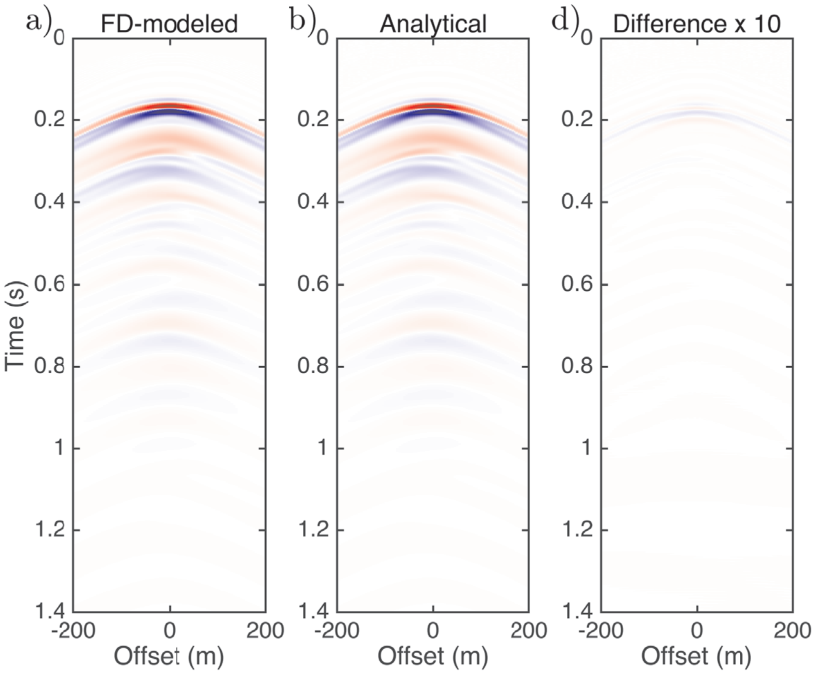

Figure 5.4: a) Recorded FD modeled wavefield at 100 m. b) Analytical wavefield at 100 m. c) Ten times the difference between a) and b).

consisting of 28 air-guns with source signatures as shown in Figure 5.2. The shot sampling is 20 m. The source depth is 7.5 m, the injection depth is 64 m and the receiver depth is 40 m. The receiver sampling is 2 m. The data is modeled without a free surface, but the source-side ghost is included in the source wavefield that is injected. The sources are filtered with a high-cut filter with a 45 Hz cut-off frequency prior to calculating the analytical fields needed for wavefield injection. These fields are calculated using Green functions for 2D media. The injection surface is located below the recording surface to avoid the direct wave in the modeled data. The reason for this choice is based on the fact that the greatest difference between the data modeled with and without the true source geometry is in the direct wave, which we think is of less interest when we investigate how the inversion of other waves are affected by the source directivity. The direct wave is shown for the 3D case in Figure 5.4. The modeled data is inverted twice; first by using the true source geometry and second by using a single point source, positioned at the center of the true array. We refer to the latter as the single-point approximation of the source. The same notional source signatures are used in both inversions. We use 74 shots distributed evenly over the model and receivers positioned over the entire model. Here, FWI is performed sequentially in different bandwidths. We start in the band 0–7 Hz and continue with 0–14 Hz, 0–20 Hz and 0–27 Hz. This is done by applying a

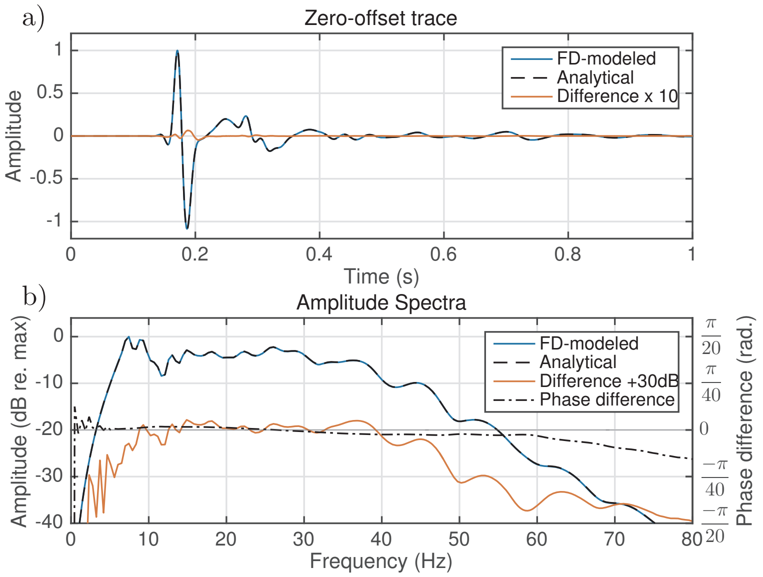

Figure 5.5: Zero-offset recording at 100 m depth. a) FD modeled and analytical signal in time together with the difference multiplied with 10. The data has been normalized to first peak. b) Amplitude spectra of the FD modeled signal, analytical signal, the difference between the two +30 dB, and the phase difference between the FD modeled and analytical signal.

bandpass filter to both the data and the source, respectively, prior to the inversion. In each frequency band, we perform a number of iterations and stop if we cannot find a step length that satisfy our criterion for reducing in the misfit. We use the quasi-Newton method L-BFGS (Limited-memory Broyden, Fletcher, Goldfarb, and Shannon; See Nocedal and Wright [2006]), for minimizing the difference between forward modeled and measured (synthetic) data. We use the same grid sampling in all frequency bands. We do not allow the inversion to update the velocity in the water layer, where it is assumed to be known.

The velocity models resulting from the different inversions are shown in Figure 5.7. We observe that the models resulting from the first frequency band (0–7 Hz) are very similar when the two different sources are used. Although the velocity models using the different sources in the inversion are quite similar after the 0–14 Hz bandwidth, we start to notice differences in the first high velocity layer at approximately 200 m and that a low velocity region appears in the deepest part at $x = 500$ m (see arrow 1 in Figure 5.7c). When higher frequencies are included, larger differences are seen between the inverted velocity models from the two different sources (see Figure 5.7e, f, g and h). A clear result is that when the single-point source approximation is used, we get large edge effects. This is because the difference between the source wavefields will be larger at greater angles, and the velocity model update on the edges is calculated from very few gradients/shots were the single-

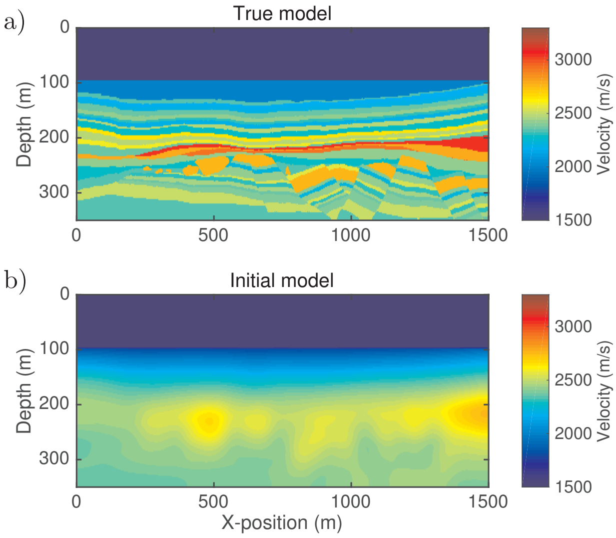

Figure 5.6: a) True velocity model used in generating seismic data. b) Initial model used for FWI. The vertical exaggeration of these figures is 2.

point source approximation is closer to the true source. In the middle of the model this error will be less pronounced because the model update is an average of many gradients from more shots were the single-point source approximation is close to the true source. The gentle trough that starts at approximately 120 m depth to the left of the model and ends at the sea floor to the right, is smeared out in the velocity model from the inversion with the single-point approximation of the source. This is almost perfectly recovered when the true source geometry is used (see arrow 2 in Figure 5.7h and j). Furthermore, high velocity layers form at, and below, the sea floor when the single-point approximation of the source is used. This can clearly be seen in Figure 5.7e and Figure 5.7g, arrow 3. This is because the inversion will try to compensate for the directivity by altering the model in a way that has nothing to do with true model. We think these velocity errors in the shallow parts will cause the wavefield below them to be farther away from the wavefield in the true model. When higher frequencies are included in later iterations, these will be more sensitive to these shallow errors and the resulting wavefield below these features will be even farther away from the true wavefield. This may lead to cycle skipping. This will also contribute to updating the velocity model in a wrong direction at deeper parts, and since directivity is more pronounced on high frequencies, the FWI will continue to update the velocities in the shallow parts in a wrong direction. The cause for these differences is related to the source, since this is the only difference between the two inversions. All this boils down to the fact that a single-point source cannot fully reproduce the wavefield resulting from a source array. Hence it is not possible to forward model the correct data since we do not honor the source geometry.

5.6 Discussion

By using the presented method, it is possible to implement the source wavefield from any source configuration, assuming that the notional source method gives an adequate representation of the source wavefield at a given depth below the true source. We think this method will be very suitable to use in RTM of seismic data acquired with, e.g., multi-level sources (Cambois et al., 2009; Sablon et al., 2013; Shen et al., 2014) or variable source depth acquisition (VSDA) (Haavik and Landrø, 2015). The image resulting from RTM will then contain data migrated with a better estimate of the source wavefield. The reflectors should then, depending on the velocity model and the estimate of the source wavefield, be imaged with a zero-phase wavelet. This is independent of the imaging condition that is used (cross-correlation or deconvolution, e.g., Poole et al. (2010)).

Amundsen and Robertsson (2014) suggest to use the total down going wavefield, including direct wave, ghosts and surface-related multiples (SRMs), as the source wavefield and the total up going wavefield as the backwards propagated field in RTM. By doing this they eliminate the need for elimination of SRMs and designature prior to RTM. However, their method require measurements of both pressure and particle velocity beneath the source array. As pointed out by Amundsen and Robertsson (2014), the direct wave is rarely obtained with sufficient fidelity to properly characterize it. As the typical air-gun array source is directive, the direct wave measured along a streamer in a conventional seismic acquisition setup (source in front of the streamer) will not contain the correct signatures for the wavefield propagating downwards, which most of the recorded events will have. To be able to use the method of Amundsen and Robertsson (2014) for small offsets, the acquisition setup must be changed so that the wavefield can be recorded below the source. The method presented here may be used to complement the method of Amundsen and Robertsson (2014) in the way that it can be used to model the direct wave where no streamer recordings are available.

Amundsen and Robertsson (2014) state that wavefield injection in a higher order staggered grid requires recordings of multi-component data along several recording levels. We have shown here that the wavefield injection works well for higher-order FD schemes using pressure and its normal derivative at a single level only. Good results are obtained as long as the length of the higher-order approximation to the derivative of the delta function is at least as long as the operator used in the FD-modeling scheme. However, there is a difference between the analytically calculated and the injected wavefields at some depth below the injection surface. This error is small, but we think that the benefits of using a higher order FD-scheme are clear (e.g. Alford et al., 1974; Dablain, 1986; Wu et al., 1996).

The signal emitted from an air-gun array often exhibit directivity in azimuth and take-off angle. How the air guns are distributed in an air-gun array controls the directivity. Source arrays can be designed to exhibit close to no azimuthal directivity (Hopperstad et al., 2001). Since most air-gun arrays are designed to be as non-directive as possible, at least in a cone below the source, directivity will be more pronounced on far-offset data and for shallow geology. For sources that exhibit weak or no directivity, this method will not result in any great changes to the image or inversion results. If we can handle more directive sources, it might be possible to use more radical air-gun array designs that can be optimized with respect to, e.g., maximum output down- and backwards (the latter for conventional streamer acquisition) or minimum output to the sides. This could also have an environmental benefit, as less energy will propagate in the water layer. An example of this is high frequency noise caused by ghost-cavitation (Landrø et al., 2011, 2016). This type of noise is in the frequency range above 1 kHz and is not interesting for seismic imaging, but might cause stress for marine mammals. This type of noise can be reduced by placing sub-arrays further away from each other (Landrø et al., 2016).

This method can be used to model more realistic seismic data, e.g. true source directivity of air-gun arrays and frequency-dependent ghost reflection. This could be an appropriate tool for testing source-side deghosting and designature algorithms. Other marine sources may also be implemented using this method; for example, marine vibrators or other directive sources such as dipole sources (see Meier et al., 2015). The marine vibrators generate a source wavefield that is directive in nature (see Pramik et al., 2015). Due to movement of the source during acquisition, Doppler effects may also influence the data from moving vibrators (Dragoset, 1988). Both these effects may be included in the source wavefield implementation presented here.

We think the proposed method for implementing source wavefields will be very suitable for FWI. This is because the whole wavefield is considered in the inversion process and therefore no need to remove SRMs or perform designature. The benefits of this method will probably be largest for problems that require high accuracy, such as time-lapse analysis for reservoir parameters and FWI where reflection and refraction data are used. High resolution FWI of conventional streamer seismic data for shallow geology may see an uplift. The latter, will probably contribute to more accurate forward modeled wavefields in deeper parts of the velocity model, which may improve FWI for deeper layers as well. For problems such as RTM with relatively low frequencies, we do not think this method will give any significant uplift. The synthetic FWI example presented here illustrates the strong influence source directivity has on the inversion results. Although, for a different kind of inversion for elastic parameters, Helgesen and Landrø (1993) also show that the source directivity has a strong influence on amplitude versus offset inversion results.

If the free-surface boundary condition in the FD scheme is implemented correctly, $R = -1$ (e.g. Mittet, 2002), we would probably not see large discrepancies between the method presented here and the method in Mittet and Arntsen (2000). However, it is well known that the free surface reflection coefficient is dependent on the sea state. It often deviates from -1 and may be frequency dependent (Laws and Kragh, 2002; Orji et al., 2013; Hardwick et al., 2014). Williams and Pollatos (2012) estimated the free surface reflection coefficient by averaging a number of traces and found it to be -0.87 $\pm$ 0.07 for the first ghost and even less for the ghost of the ghost (ghost at the receiver side of the source ghost). In the method proposed here, as opposed to Mittet and Arntsen (2000) and Hicks (2002), we have the flexibility to include a better estimate of the free-surface reflection coefficient for the source-side ghost.

5.7 Conclusion

We present a method for implementing arbitrary marine seismic source wavefields in FD methods. This method is based on a hybrid scheme, where we calculate the pressure and normal derivative of the wavefield at a given depth analytically, and then inject this wavefield into a FD grid using wavefield injection. In our method, any type of marine source or source array can be implemented assuming that the notional source signature, position and radiation pattern for the individual source elements are known. The method allows for choosing the free-surface reflection coefficient on the source side, which have been shown to often deviate from -1 and be frequency dependent. Furthermore, since this method honors the source geometry and use the notional source signatures from the individual source elements, the directivity of an air-gun array is included in the modeled source wavefield.

Our results show that our method works satisfactorily, and that the resulting wavefield at a given depth is close to equivalent to the wavefield analytically extrapolated to the same depth.

Our simple inversion example shows that ignoring the directivity of the sources will not affect the inversion results when only low frequencies are used. However, when higher frequencies are included, the inversion results starts to deviate from the true velocity and artifacts are introduced. The example also shows that as long as the true source wavefield is used in forward modeling of data, good inversion results are obtained.

5.8 Acknowledgements

Thanks to Lundin Norway AS for financial support to Kjetil E. Haavik's PhD project. We thank the Norwegian Research Council for financial support to the ROSE Consortium. K. E. Haavik thanks the Norwegian Petroleum Directorate (NPD) for hospitality during his stay there. Ståle Johansen and the IGD group at NTNU are acknowledged for providing the velocity model used in the FWI example. K. E. Haavik thanks Marlies Vasmel at ETH for fruitful discussions on wavefield injection. The reviewers: Filippo Broggini, Daniel Koehn, and one anonymous, are acknowledged for their comments and suggestions that improved this manuscript.

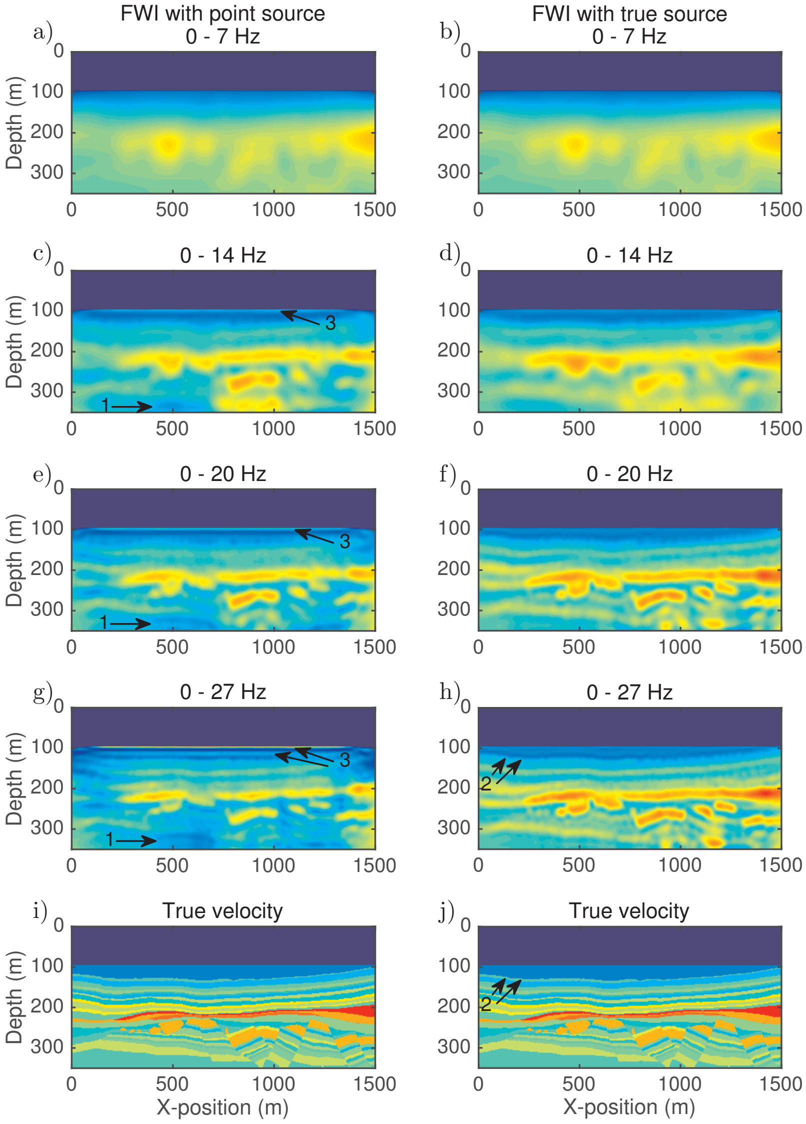

Figure 5.7: The velocity models to the left are the result of inversion where a point-source approximation of the true source has been used. The velocity models to the right are inversion results where the true source wavefield has been used. Figure a), c), e) and g) are the inverted velocity models for the frequency bands 0 – 7 Hz, 0 – 14 Hz, 0 – 20 Hz and 0 – 27 Hz. b), d), f) and h) are the inverted velocity models for the frequency bands 0 – 7 Hz, 0 – 14 Hz, 0 – 20 Hz and 0 – 27 Hz, respectively. The color scale that is used is the same as in Figure 5.6. The true velocity model used in generating seismic data is shown for simpler comparison in i) and j). The numbered arrow indicated features that are discussed in the text. The vertical exaggeration of these figures is 2.

Chapter 6

Wavefield separation using seismic apparition on towed streamer data with distributed source arrays: Site survey and conventional survey in one go?*

Kjetil Eik Haavik and Martin Landrø
Norwegian University of Science and Technology, Trondheim, Norway

6.1 Abstract

Separation of wavefields is an important processing step of seismic data acquired with simultaneous sources. Here, we apply the newly introduced seismic apparition methodology to separate marine seismic data acquired with distributed source arrays (DSA) with periodical shooting patterns for towed streamer data, and explore the potential of acquiring conventional and site-survey data simultaneously. The seismic apparition method is a signal-processing only technique and allows for perfect separation as long as the data are well sampled. The seismic apparition is here performed in the common offset domain, where the reflectors are seen primarily with gentle dips. We provide an example on conventional data and site-survey data acquired separately are summed to synthesise simultaneous source data. We show that the separation method works adequately for the provided example, assuming that the deep part of the conventional shot record can be neglected. The method should in theory also work for the deep parts of conventional data, as long as the data is well sampled.

Revised manuscript submitted to GEOPHYSICS August 2016

6.2 Introduction

Simultaneous source acquisition has been utilized to optimize seismic acquisition with respect to survey time (Beasley, 2008; Hampson et al., 2008; Ibrahim and Sacchi, 1995; Abma et al., 2015; Kumar et al., 2015; Zhan et al., 2015; Langhammer and Bennion, 2016). In simultaneous source acquisition, a second or/and third source array are typically fired with random time delay/dither compared to the first array. By sorting this kind of data in different domains (common mid-point, common offset, common receiver gathers), the second and/or third source(s) appear random and can be separated out using, *e.g*, a sparse inversion method (Abma et al., 2015). A special type of simultaneous source acquisition is blended acquisition proposed by Berkhout (2008), where the simultaneous sources also are fired at different source positions. Berkhout (2012) also proposed to acquire blended seismic data with distributed source arrays (DSA), where several narrowbanded sources are distributed in space and time, instead of fewer broadband sources. This allows for optimum sampling intervals for the respective narrowbanded sources (e.g. Berkhout, 2012; Caporal et al., 2015; Tsingas et al., 2016). Here, we present an application of the seismic apparition method, recently proposed by Robertsson et al. (2016a), to perform wavefield separation of towed streamer seismic data acquired with simultaneous DSA. The apparition methodology is here applied in the common offset domain. We present an example where we synthesise simultaneous acquisition of conventional and site survey data from field data. As opposed to previous methods, where random ditherers are used between different sources, the apparition method is based on periodic shot interval in time or space (Robertsson et al., 2016a).

6.3 Theory

Seismic apparition is a signal processing approach for separating signals which are sampled differently (Robertsson et al., 2016a,b,c; Pedersen et al., 2016). The basis for this methodology is the nature of the sampling functions that are used. The sampling function, or comb function, is given as:

$$s(x, \Delta x) = \sum_{i=-\infty}^{\infty} \delta(x - i\Delta x), \tag{6.1}$$

where Δx is the sampling interval in the x-direction. The Fourier transform of the comb function is given as:

$$S(k, \Delta x) = \sum_{i=-\infty}^{\infty} \delta(k - i2k_N), \tag{6.2}$$

where k is the wavenumber, or frequency, and $k_N = 1/2\Delta x$ is the Nyquist wavenumber. If a record consist of two signals that are sampled differently, then the periodicity in the wavenumber domain will be different for these two:

$$p(x) = p_1(x)s(x, \Delta x) + p_2(x)s(x, 2\Delta x), \tag{6.3}$$

where $p(x)$ consist of the signal $p_1(x)$ and $p_2(x)$ sampled at Δx and $2\Delta x$ intervals, respectively. In the wavenumber domain this can be written as:

$$P(k) = P_1(k) * S(k, \Delta x) + P_2(k) * S(k, 2\Delta x), \tag{6.4}$$

with $*$ denoting convolution. This is illustrated in Figure 6.1. We observe that the wavenumber spectrum of the signal sampled at $2\Delta x$ is apparated, or "ghostly" apparent around $k = \pm k_N$, and separated from the signal sampled at Δx in Figure 6.1f, while the spectrum around $k = 0$ consist of both signals. From this, it is clear that by careful numerical surgery, we can find the amplitude spectrum from the signal sampled at $2\Delta x$, shift it to $k = 0$ and subtract to separate the signal sampled at Δx. This procedure can be done as long as the wavenumber spectra of the different signals do not overlap, i.e., both signals are well sampled. This can also be done for more than two signals that are sampled differently. Figure 6.1f can be thought of as the wavenumber spectrum for a given frequency in fk-domain.

Robertsson et al. (2016a) formulate signal apparition in terms of modulation function that is convolved on a trace-by-trace basis to a regular data set. The modulation function is given as:

$$m(x) = \frac{1}{2}\left(1 + e^{i\pi x}\right) + \frac{1}{2}A(\omega)\left(1 - e^{i\pi x}\right), \tag{6.5}$$

where $A(\omega)$ is the apparition filter. If $P_2(\omega, k)$ is the normalized discrete Fourier transform of $p_2(\omega, x)$ over x-direction, then we can write the convolution between $m(x)$ and $p_2(\omega, x)$ in fk-domain as:

$$H(\omega, k) = \frac{1 + A(\omega)}{2} P_2(\omega, k) + \frac{1 - A(\omega)}{2} P_2(\omega, k - k_N). \tag{6.6}$$

$A(\omega) = e^{i\omega\tau}$ corresponds to a time delay τ of every other trace in the data, and $A(\omega) = 0$ corresponds to muting every other trace in the data. The modulation function separates the original data into two data sets sampled at half the sampling rate of the original data. Thus making the periodicity in the wavenumber domain half of the original data. The signal cones around wavenumbers $k = 0$ and $k = k_N$ are linked through the filter $A(\omega)$, and by knowing the signal around $k = k_N$ we can find the signal at $k = 0$.

6.4 Apparition strategy for simultaneous acquisition of DSA

Site surveys typically have denser shot sampling than conventional seismic data, and we therefore think it is of interest to examine the potential of acquiring site-survey data simultaneously with conventional seismic data. If we assume that the site-survey shot sampling Δx is half the shot sampling of the conventional data, then two site-survey shots are fired for every single shot of conventional data. For data viewed in the common offset domain, sorted to align the site-survey data, the conventional data will appear with alternating

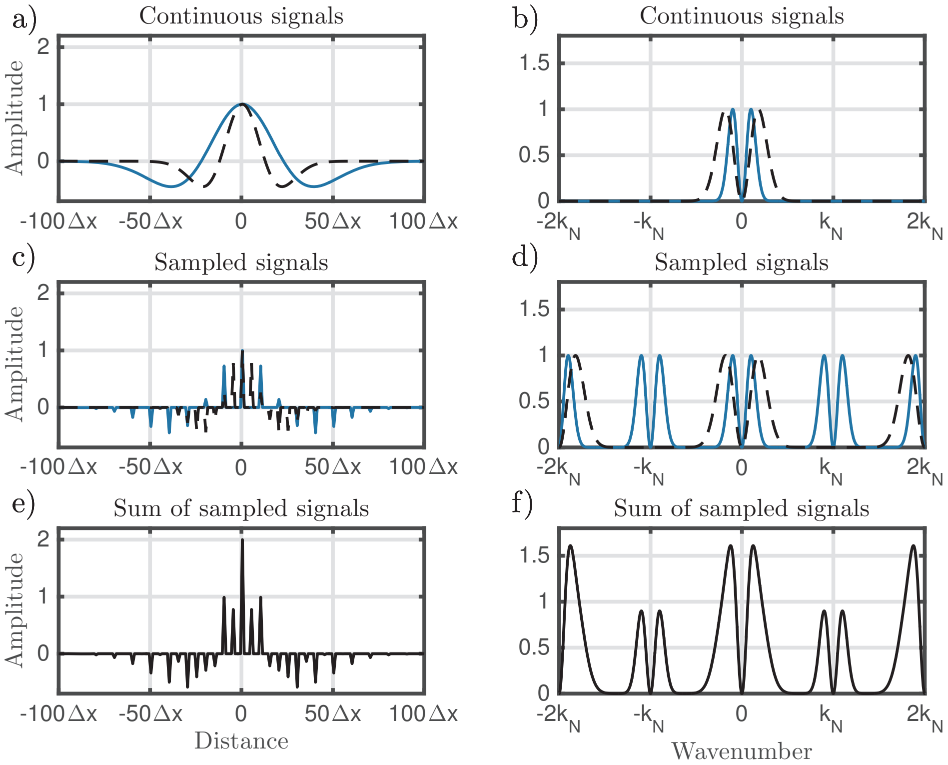

Figure 6.1: a) $p_1(x)$ and $p_2(x)$ in space domain, b) The wavenumber spectra of the two signals i a), c) The two signals in a) sampled with two different sampling distances in space. d) The wavenumber spectra for the sampled signals in c). We see that the two different signals overlap around $k = 0$, but have different periodicity. e) The sum of the signals in c). f) The wavenumber spectrum for the signal in e), where we observe that the spectra from the signal sampled at twice the sampling interval is separated from the other around the Nyquist wavenumber.

traces with the shallow and the deep parts of the conventional data, respectively. The ideal situation would be if the amplitudes of the deep part of the conventional data shot record are very small or negligible compared to the site-survey data and shallow part of the conventional data. In this situation, we could treat the data as illustrated in Figure 6.4 - as two signals sampled differently, or $A(\omega) = 0$ for the conventional data. However, in many cases the deeper part of the conventional data are desired signal, and few seismic surveys are designed to have several seconds of extra recording time as this reduce acquisition efficiency. There are no apparition filters, $A(\omega)$, that can relate the shallow part of the conventional data to its deeper. For the case described above we have not two, but three signals, site survey (SS) and conventional survey (CS), where CS divided into

CS_s and CS_d. Subscripts s and d indicates shallow and deep parts of CS, respectively.

In order to separate the full length of the conventional data, as well as the site-survey data, there exist several apparition strategies. Here we describe two of these strategies:

1) Shoot the site-survey source with shot interval Δx and the conventional source with shot interval $(2\Delta x)$ with a time shift applied to every other shot. By sorting the resulting data into common offset domain, with lengths in time corresponding to the length of two site-survey shot records, and transforming it into fk-domain, the conventional data will be apparated with filter $A(\omega) = e^{i\omega\tau}$. Since the data is sorted with two site-survey shots in each trace, the spatial sampling in common-offset gathers is now halved to $2\Delta x$. In this strategy, the the data will be split into signal cones that are reoccurring with two different periods: SS will be positioned around $k = 0$, and CS will be positioned at $k = 0$ and $\pm k_n$ with scale $1 + A(\omega)$ and $1 - A(\omega)$, respectively. Thus allowing for separation of the site-survey and the conventional survey if the data are well sampled. This strategy comes at the cost of halving k_N compared to Nyquist wavenumber given by the site-survey shot sampling, and may lead to more issues related to aliasing because the signal cones from the conventional and site-survey data are more likely to overlap in fk-domain.

2) Shoot the conventional source regularly $(2\Delta x)$ and the site-survey source with shot interval Δx with a time delay every fourth shot, corresponding in time with the deeper part of a conventional shot record. When the resulting data are sorted into common offset domain, aligned in time on the site-survey, we will have three different signals in the fk-domain:

1. SS sampled at Δx
2. CS$_u$ sampled at $2\Delta x$ (= sampled at Δx with $A(\omega) = 0$)
3. CS$_l$ sampled at $2\Delta x$ with $A(\omega) = e^{i\omega\tau}$

In this way, the data will split into cones of energy that are reoccurring with three different periods in the fk-domain. SS will be positioned around $k = 0$, CS_s will be positioned at $k = 0$ and $k = \pm k_N$, and CS_d will be positioned at $k = 0$ and $k = \pm k_n$ with scale $1 + A(\omega)$ and at $k = \pm k_N/2$ and $k = \pm 3k_n/2$ with scale $1 - A(\omega)$. As long as the data are well sampled it is now possible to separate the three different parts of the signal. The signal cones from CS_s and SS are in this approach separated by twice the distance in fk-domain compared with the signal cones in the first strategy. CS_d have the same distance from SS as in the first strategy, but the main difference between the methods is that deep parts of the conventional data have in general lower frequencies than in the full section, which should therefore make the second strategy perform better.

Now by, using the latter example we describe how the data can be separated. The process is done for all offset classes on common-offset gathers (COGs) in fk-domain. Separation using the apparition method is performed as follows:

1. Define an area over f and k in the fk-domain where the signal that is sparsest sampled is isolated. For CS_d this is around $k = \pm k_N/2$.

2. Scale this part of the signal with the corresponding scale, $1 - A(\omega)$, and shift it to $k = 0$. This process will separate CS_d, remove the time shift and implicitly interpolate the signal to Δx
3. Take the separated signal obtained in step 2, shift and scale it to $\pm k_n/2$ with scale $1 - A(\omega)$, and $k = \pm k_n$ and $k = 0$ with scale $1 + A(\omega)$. This process will decimate and re-apply the time-shift to CS_d.
4. Subtract the signal obtained in step 3 from the original data. This process eliminates CS_d from the data.
5. Define an area over f and k in the fk-domain from the previous step where the signal from CS_s is isolated (around $k = \pm k_N$).
6. Shift this part of the signal to $k = 0$. This process will separate CS_s and implicitly interpolate it to Δx.
7. Take the separated signal obtained in step 6, shift to $k = \pm k_n$ and $k = 0$. This process will decimate the signal again.
8. Subtract the signal from step 7 from the signal obtained in step 4 to eliminate CS_s.
9. Now, all three parts are separated.

The two strategies described above, will in theory give perfect separation of the different parts of the data, as long as its well sampled. A third strategy is to use slope-based and frequency filters to separate the deep part of the conventional data from the site-survey data. This separation can for instance be performed in shot gathers containing CS_d and SS using high resolution radon transforms (e.g. Sacchi and Ulrych, 1995). With this hybrid-separation strategy, there are no requirements for the time delay of every fourth shot of the site-survey, as illustrated in strategy 2, and can for instance be changed with no time delay or even random time dithering. In the example provided below, we assume that we have used this hybrid strategy and only consider the site survey and shallow parts of the conventional data.

6.5 Synthetic field data example

A test of the proposed method on synthetic simultaneous data consisting of real conventional towed-streamer data and real site-survey data acquired separately is performed. The data used for this example comprise of a conventional 2D line acquired over the Edvard Grieg field in the North Sea, and a 2D site-survey line acquired over the 2/4–14 blowout well in the Central North Sea (Landrø, 2011). The shallow geology in both places consists of sub-glacial erosional valleys and iceberg ploughmarks (e.g. Haavik and Landrø, 2014), giving rise to numerous diffractions and high-angle reflections in the two data sets. The shot spacing is 12.5 m and 25 m for the site-survey and the conventional data, respectively. The receiver spacing is 12.5 m in both data sets. We are limited in recording time, maximum offset and number of shot records to the respective values of the site survey, which is 2048 ms, 1200 m and 640 shot records, respectively. In the conventional data set, a high cut filter at 200 Hz (at 370 dB/Oct) was used during acquisition.

To synthesise simultaneous source data, we do the following steps: Apply a 5 Hz low-cut filter to both data sets to remove swell noise. Interpolate conventional data from 2 ms sampling to 1 ms sampling. Add the top 2048 ms of the conventional data. We assume that the deeper part of the conventional survey is filtered out or negligible in strength compared to the site-survey and the upper part of the conventional data. The resulting data set is shown in Figure 6.2 in form of a COG and a shot gather where both site survey and conventional data are present. The corresponding fk-spectra to the COG in Figure 6.2a is shown in Figure 6.3, where we can observe that the signals from the two different surveys have different periodicity. We see that the dominant parts of the spectra are focused in narrow vertical columns around integers values of the Nyquist wavenumber (k_N=0.04 m^{-1}). However, the more low-amplitude regions in these signal cones, at high wavenumbers, are overlapping to a certain degree. Although the conventional survey had a high-cut filter applied during acquisition, which could limit the amount of overlap in the fk-spectra, it can be seen from Figure 6.3, the amplitudes from the conventional survey is rapidly decaying with frequency above 100 Hz.

For the separation process on this data we start at step 5 in the list described in the previous section. This is because we assume that CS_d is already filtered out. We use a sine-tapered box-car filter to isolate the signal cone from the CS_s in the fk-domain. The full temporal frequency bandwidth is used. The original data, separated data and the difference between the original and separated data in zero-offset COGs are shown in figures 6.4 and 6.5 for the conventional and site surveys, respectively. Visually, there are no larger differences between the original and separated wavefields from the conventional survey (Figure 6.4) that correlate with any high energy event. For this COG, the NRMS-difference is approximately 16 %. In Figure 6.5c, only every other trace from the data are plotted due to every other trace in the separated site survey being exactly the same as in the original (every other shot is site survey only) the NRMS-differences are calculated from the whole survey. In Figure 6.5 we observe the same type of behaviour as we see for the conventional survey, in Figure 6.4. Although the noise levels seems a bit higher than the NRMS-difference of 35 %, there is not any strong correlation between the difference and any high energy events. The cause for the apparently low NRMS difference is because every other trace in the separated data being exactly the same as the original. The original data, separated data and the difference between the original and separated data in resulting shot gathers are shown in figures 6.6 and 6.7 for the conventional and site surveys, respectively. In the shot gathers we observe that the separation performs very well for the conventional survey, with NRMS-difference of about 7 % relative to the original survey, while the NRMS-difference is about 64 %, between the original and separated site surveys in (Figure 6.7d). We can see from Figure 6.6 and Figure 6.7 that a noise burst at approximately 200 m offset originally in the site survey, has moved into the conventional survey after separation. Furthermore, some highly dipping events at large offset and times appear in the separated conventional survey.

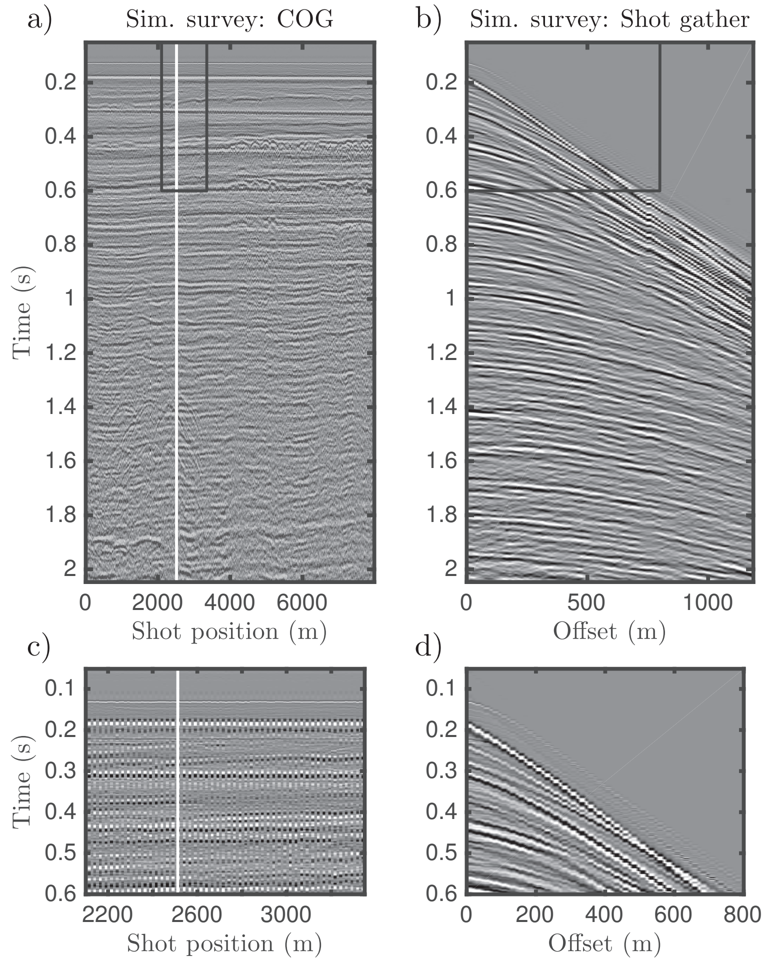

Figure 6.2: a) Minimum-offset COG from the synthesised simultaneous source data set. b) Shot gather from the synthesised simultaneous source data set. The corresponding position is indicated with a white line in a). c) A zoom up of the black box in a). d) A zoom up of the black box in b).

6.6 Discussion

We have presented how the seismic apparition methodology, presented by Robertsson et al. (2016a), can be used to acquire both site survey and conventional seismic data simultaneously. The test of the proposed method on synthetic simultaneous data consisting of real conventional towed-streamer data and real site-survey data acquired separately shows that the method works very well on "real" data, when assuming that the deeper part

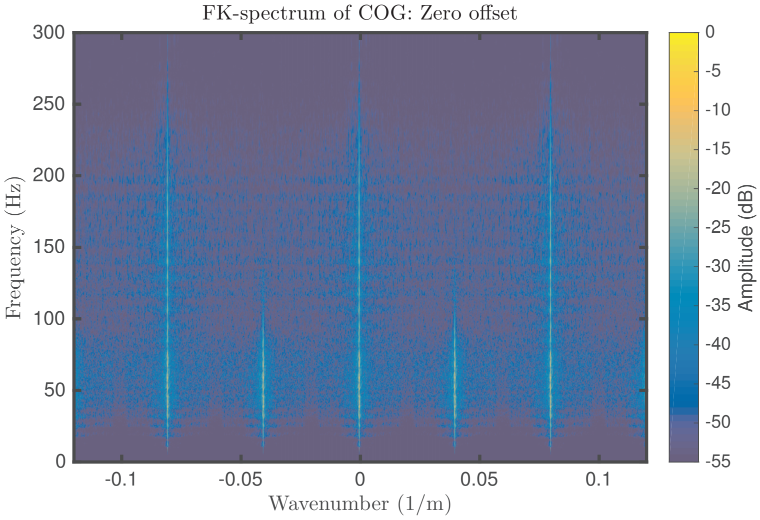

Figure 6.3: fk-spectra of minium-offset COG from the synthesised simultaneous data used in the "real" data test. The periodicity of different source sampling can clearly be seen in the wavenumber direction.

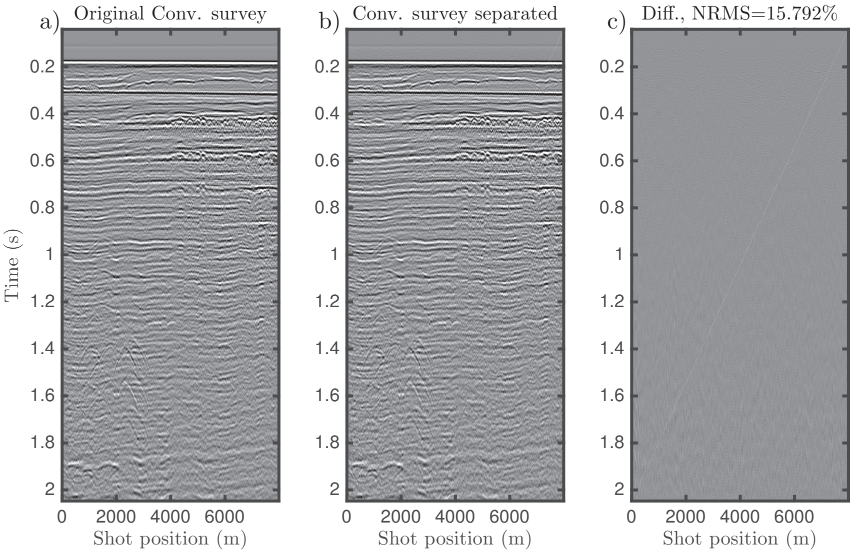

Figure 6.4: a) Minimum-offset COG from the original conventional survey, b) Minimum-offset COG from the conventional survey after separation and c) Difference between a) and b).

of the conventional data is separated out by other means or negligible. These results are very encouraging as the method is simple to implement and computationally fast. With only about 7 % NRMS difference between the original conventional survey and the separated conventional survey in shot gathers, it may be possible to obtain an additional site survey data set. Although this data set has much larger NRMS-differences from its original data (∼64%), it has the potential to improve shallow imaging significantly. We note again, that no de-noising or cosmetics are applied to the data prior or post separation. Because the separated shot gathers look quite good, we expect the NRMS-differences between stacked images to be reduces compared to in COGs as presented here.

Again, we point out that the example provided here is not from field data acquired in the proposed way, and the results may therefore not directly be representative for the results when the deeper part of the conventional data is also considered. However, we will present a thought example of the proposed acquisition. Lets assume that a seismic vessel is acquiring data with a speed of 5 knots (∼ 2.5 m/s), and we want to shoot the site-survey source every 12.5 m and the conventional source every 25 m. This gives 5 s to record conventional and site-survey data before the next site-survey shot is fired. For the deeper 5 s of the conventional data, there will therefore always be a new site-survey shot. In this case, the deeper part of the conventional data will have move-out behaviour and frequency content very different from the site-survey data. This is because of several reasons: The wavefield from the conventional source at these times will reflect from deep geology, and be more low frequent in nature because of attenuation. Furthermore, the site-survey source is often more high frequency in nature. In the second strategy proposed above,

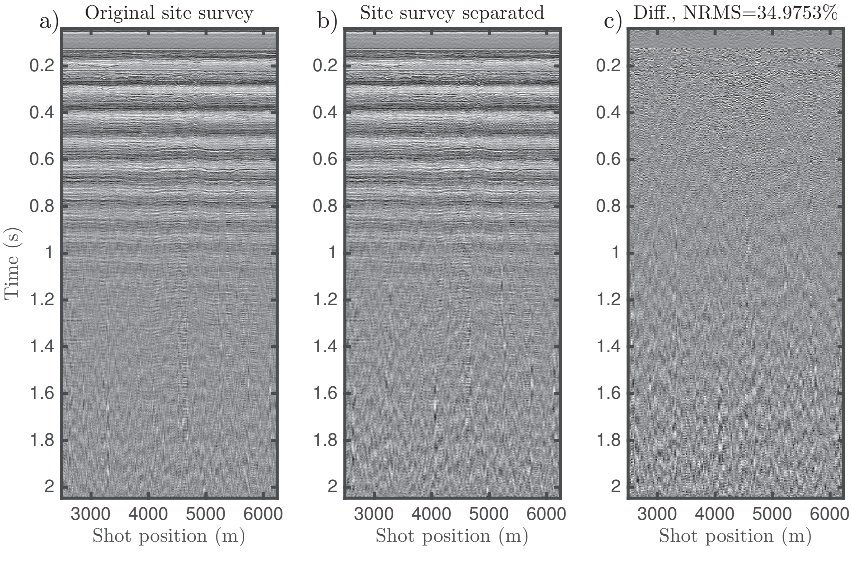

Figure 6.5: a) Minimum-offset COG from the original site survey, b) Minimum-offset COG from the site survey after separation and c) Difference between a) and b).

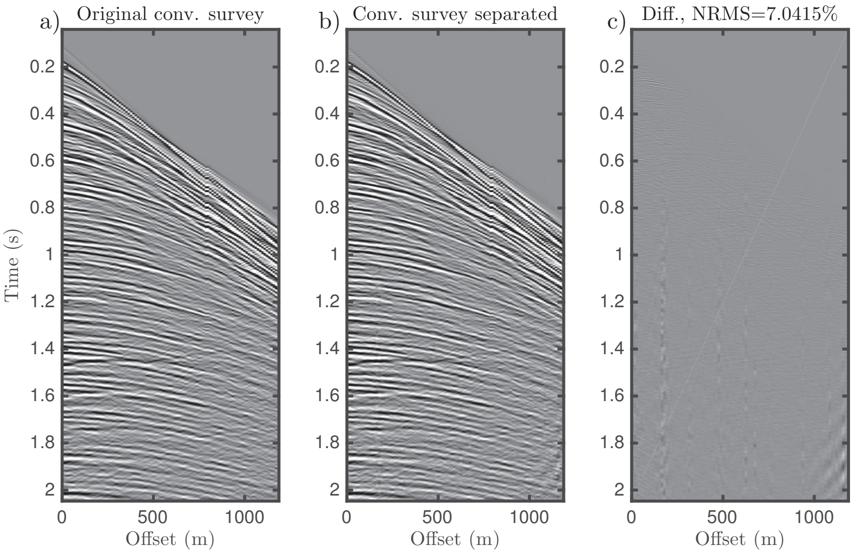

Figure 6.6: a) Shot gather from the original conventional survey, b) Conventional survey shot gather after separation and c) Difference between a) and b).

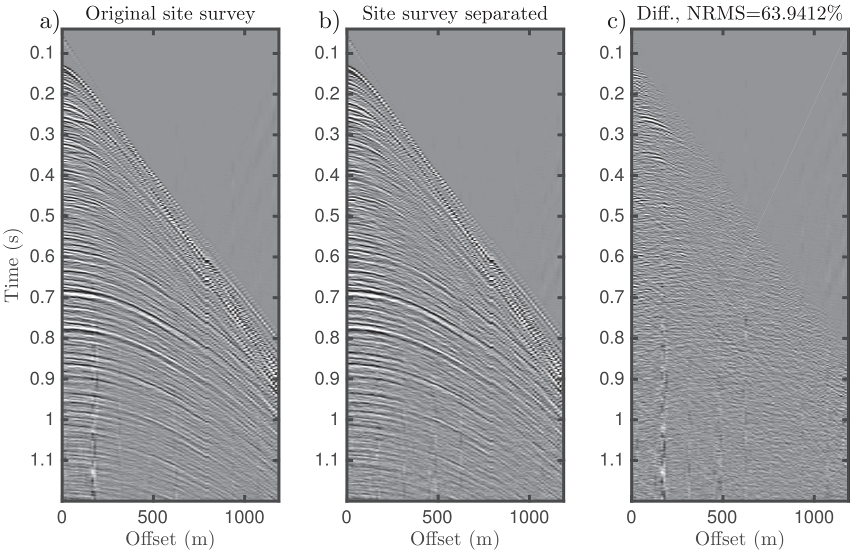

Figure 6.7: a) Shot gather from the original site survey, b) Site survey shot gather after separation and c) Difference between a) and b).

the signal of the deeper part of the conventional data is distributed around $k = \pm k_N/2$. If the deep part of the conventional data have low-frequency content compared to the site-survey, it will be better isolated in the fk-domain and make the separation process better.

Another possible solution to this problem, as presented in the third strategy above, is to use more traditional separation methods such as slope-based filters (radon or fk) and frequency filters to separate the deep part of the conventional data from the site survey data. Because there are no requirements for the regular time delay on every fourth site-survey shot in this approach, random dithering can for instance be used together with existing separation methods (e.g. Ibrahim and Sacchi, 1995; Abma et al., 2015; Kumar et al., 2015; Zhan et al., 2015; Langhammer and Bennion, 2016). This will not be theoretically accurate, as the two apparition strategies presented above, but may be a more practical approach. When the apparition methodology is used with time delays, $A(\omega) = e^{i\omega\tau}$, its scaling function $1 - A(\omega)$ corresponds to deghosting. Thus being unstable for frequencies in the vicinity of 0 Hz and notch frequencies given by integer multiples τ^{-1}. While the notches above 0 Hz can be pushed to high frequencies by reducing the delay time τ, the notch at 0 Hz cannot be avoided in the first and second acquisition strategies.

Seismic apparition in the common offset domain is a natural choice: If the geology consist of flat layers, this method would be perfect since all events in this domain would be flat, *i.e.*, all frequencies would be sampled according to the Nyquist criterion (Nyquist, 1926; Shannon, 1949). Since this is normally not the case, aliasing will occur for diffractions and reflectors that are dipping. For seismic apparition in the common offset domain, it is the shot separation distance that is the spatial sampling parameter. The degree of aliasing is related to shot separation, frequency content from the sources, the angle of dipping reflectors, and the positions of diffractors. The lowest velocity that we may see in a COG is half the velocity of the water, however, for close to flat geology, the velocities in this domain are close to infinite. For relatively low frequencies, the distributions in the fk-domain from the sources with different shot separations will not overlap, and can be used in interpolation schemes to guide interpolation of aliased energy (e.g. Spitz, 1991; Yu et al., 2015; Andersson et al., 2016). Other approaches might be to use a sparse inversion method (e.g. Abma et al., 2015) or adaptive subtraction (e.g. Liu et al., 2014), to obtain the highest frequencies. The highest frequency one can sample in COG is related to the Nyquist sampling in shot interval:

$$f_{max} = \frac{c}{2\Delta s \sin\theta}, \tag{6.7}$$

where θ is the apparent angle of a reflector in common offset domain and Δs is the shot interval. When it is the shot sampling that is apparated, or sampled differently, the apparition framework can be used in other domains as well, such as common receiver and common mid-point domains. It might be that energy coming from diffractions and dipping layers could be better handled in these domains, and that a processing approach that combines these domains may improve the overall separation. However, this is not shown here.

The example provided here is in 2D. However, the method should work independently of the streamer position, as long as the streamer have the same relative motion as the sources during acquisition. This is because seismic apparition is a signal-processing only technique. Mis-positioning of source and receivers, or firing-time delays, may give rise to rapid variations from trace to trace in the COGs, and hence high wavenumbers that could easily be aliased. This is depicted in Figure 6.8, where we see how the jittery behaviour in the site-survey data influences the difference between the original and separated wavefield for the conventional and site-survey in Figure 6.8c and d, respectively.

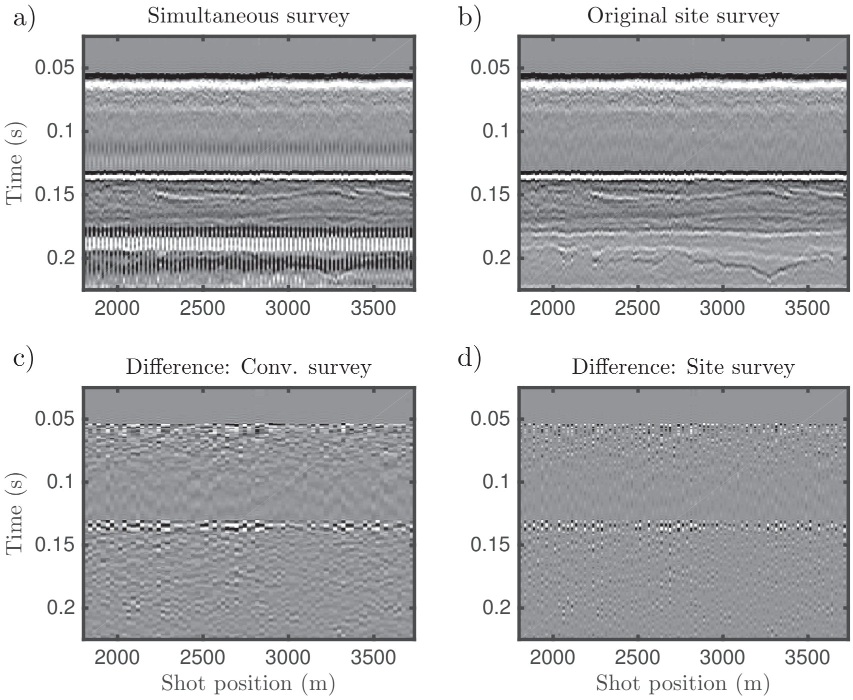

Figure 6.8: Common offset gathers for zero offset: a) Synthesised simultaneous source data, b) Original site survey data, c) Difference between original and separated conventional data d) Difference between original and separated site-survey data.

Noise is always present in seismic data. Noise is additive for the apparition methodology, meaning that when we extract data from around k_N and shift is to around $k = 0$, the noise from around k_N will follow. The noise that was present in this region will then map onto different wavenumbers when shifted to $k = 0$. This means that we might introduce noise that have different dips than the original noise which might be what we see in Figure 6.6. In the example provided here, it is noise from two data sets. Thus, the noise levels are actually higher than they would be if both data sets were acquired simultaneously.

We foresee that the proposed method can be used in separation of different sources in multi-purpose seismic acquisitions, such as, acquisition of data using a dedicated low-frequency source along with conventional data, or site-survey data along with conventional marine acquisition, as in the second example. The latter can for instance be done by towing a smaller source array inside the streamer/receiver spread that is fired at half the shot interval as the conventional source. By doing this, it could be possible to obtain zero offset as well as negative offsets data, with respect to towing direction. If carried out simultaneously as a 3D survey, this strategy could make it possible to acquire 3D site survey data simultaneously with conventional seismic data. This has a huge upside, as most operators are required to acquire site-survey data prior to drilling. If the high-frequency need is covered with the site-survey source, the main source array could be designed with emphasis on the low-frequency end of the spectrum. This will reduce overlapping in fk-domain at high frequencies and make the separation process even better, in addition to the possibility of benefiting from increased low frequency data. The two real data sets that we used in the example are acquired with different receiver depths that are chosen as optimal for the respective survey targets. Choosing optimal streamer depth based on the site-survey targets may lead to sub-optimal data for the conventional survey, or vice versa, for a hydrophone-only streamer acquisition. This problem would be solved by using multi-component streamers, where separation of up- and down-going waves can be achieved (e.g. Amundsen, 1993).

6.7 Conclusion

We have presented a method for separating site-survey and conventional data acquired simultaneously. We have applied the proposed method to synthetic marine towed-streamer seismic data where site-survey and conventional seismic data are acquired simultaneously. When assuming that the deeper part of the conventional data is negligible, we obtain very good separation results. The apparition is here performed on common offset gathers. The separation results will depend on the relationship between the complexity of the geology and the shot separation, as the method is limited by the apparent dip of the events in COG being sampled properly. Further feasibility studies, including full-length data, dealiasing of COGs and real data over more complex geology, are needed before we can conclude that it is possible to acquire site-survey data along with conventional data.

6.8 ACKNOWLEDGMENTS

We thank the sponsors of the ROSE Consortium and the Norwegian Research Council for financial support. K.E.H thanks Lundin Norway for financial support to his PhD project. Furthermore, the Norwegian Petroleum Directorate is acknowledged for their hospitality during K.E.H.s stay there. Statoil ASA and Lundin Norway AS are acknowledged for the seismic data used in this work. K.E.H. thanks J.O.A. Robertsson for an inspiring presentation in Vienna that triggered this work.

Chapter 7

Concluding remarks

The main objective of this doctoral work has been to explore the potential of acquiring marine seismic data where the source depth is varied from shot to shot to further improve marine broadband seismic data. This is a natural extension and contribution to the vast amount of research that has been published on broadband seismic data acquisition in the past two decades. This study has been limited in the amount of real seismic data suitable to investigate the potential of VSDA, and synthetic data have been used to provide examples of VSDA.

Chapter 2, describes the theoretical background for VSDA. In this work, an inversion is used to find the optimal source depths for a sequence of shots that yield a white frequency spectrum in the average source wavefield that propagates down in the subsurface. Quasi near-field data from an air-gun fired at different depths are used to show that VSDA gives seismic data sets that have flatter, or "whiter", frequency spectra when data from several shots are stacked.

The depth dependency of source signatures from a single air gun is studied in Chapter 3. An empirical relationship that relates the source signature from an air gun fired at a given depth to another depth is presented. A scaling law is used to relate the signatures from different depths, with the ratio between bubble-time periods, as predicted by the Rayleigh-Willis equation, used as scale. A correction factor is derived for the bubble-time period when a bubble is close to the free surface. Tests of the empirical relationship show that the method works well as long as the difference in depth is not too large ($< \pm 10$ m). The correction term results in better estimation of the source signature for shallow source depths. This method, can for instance, be used to correct for variation in the source depth during the designature process or to rapidly perform modeling of source signatures at different depths, when the source signature from one depth is known.

The modeling study presented in Chapter 4 shows that VSDA may result in high signal-to-noise ratios over a broader bandwidth, compared to conventional single-level source and a multi-level source. This is at the cost of having slightly different wavelets along the same reflectors in common-image gathers. This results in a worse starting point for pre-stack seismic data analysis, such as, AVO analysis. However, the correct AVO behaviour was recovered using a simple smoothing operation in the offset direction. The problem related to different wavelets is less visible in stacked images, but give rise to lower quality data in low-fold areas, e.g., for very shallow geology.

In Chapter 5, a method for implementing arbitrary source wavefields in marine finite-difference methods is presented. In this work, a combination of analytical Green functions and the wavefield injection technique makes it possible to implement the source wavefield originating from arbitrary source positions. An inversion example shows that being able to forward model the correct data is important when trying to invert for the model parameters. This method can be used to model VSDA data when the source depths do not coincide with the FD grid, which is often the case. The main difference between the method presented here and others (see Chapter 5) is the possibility to choose the free surface reflection coefficient on the source side.

From the research presented here, we may conclude that VSDA can improve the signal-to-noise ratio over a broad bandwidth, compared to using a conventional single-level source or a broadband multi-level source. This method requires more detailed knowledge of source depths, notional source signatures and will probably give rise to more involved processing steps prior to velocity estimation and imaging. Higher signal-to noise ratios in the high-frequency range will push the limits of where we can compensate for attenuation to deeper targets. VSDA with conventional air-gun arrays will not give an uplift in the low-frequency end of the spectra (< 5–7 Hz) because of the counteracting effects from the source ghost and the change in bubble-time period when the source depth is changed.

I suggest that diversity in the source ghost and signatures may make the final image less dependent on accurate deghosting and designature operators. This is because errors resulting from inaccurate deghosting or designature processes are not systematically repeated for all the shots in the data. Small errors in these operations for VSDA, is more likely to be stacked out because of the diversity.

Currently, the most popular broadband source strategy is the multi-level source, for example, using two sub arrays at 6 m and a third at 9 m. This way, the deepest ghost notch from the 6 m source is filled. A major difference in the data obtained from VSDA and multi-level sources is that every shot record has deep notches in the VSDA data. However, these notches are positioned at different frequencies for the different source depths (except for the notch at zero Hz). VSDA is in a way complying with the ghosts rather than fighting it. The focus, when discussing the ghost reflection, is often its resulting ghost notch. In fact, there are positive sides to the ghost, merely that parts of the frequency band is gained up to 6 dB (a doubling). In VSDA, it is possible to design the surveys so that all frequency bands are gained to some extent. In comparison, the 6/6/9 m multi-level source, as presented above, will in fact reduce the total output in a frequency band between 50 to 125 Hz compared to a single-level source at 6 m.

Possible extensions of the doctoral work related to VSDA are:

- **Field test of VSDA.** By performing a field test of VSDA along with other types of acquisition strategies, such as multi-level source and conventional source, we would obtain a better foundation for comparing different strategies. This is the ultimate test for VSDA.

- **More complex modeling of VSDA data.** 3D modeling over more realistic models, accompanied with more realistic processing flows will give better insight into different strengths and weaknesses of VSDA.
- **Optimal sources for VSDA.** For tuned air-gun arrays, it is more important to have complimentary ghost functions than complimentary source signatures. However, optimizing the volumes and firing pressure of air guns for the sources positioned at different depths may contribute to further improving VSDA. This would require a more difficult inversion process than the one presented in Chapter 2.
- **Frequency dependency of free-surface reflection coefficients.** In the examples shown here a constant free-surface reflection coefficient is assumed. As discussed in Chapter 5, this is probably not the case. At least for high frequencies. I think that the frequency dependency of the free-surface reflection coefficient will be affected by the source depth. The reason for this is when the source is positioned very close to the free surface, linear approximations will not be sufficient in describing the physics because the pressure and components of motion will be too large. To study this, the full Navier-Stokes equations and the motion of the free-surface should be considered.

The major challenges that VSDA may be facing are related to the following:

- **Operationally difficult to acquire.** With current depth control for marine sources, changing the source depths is not possible during acquisition. A dedicated depth-controlling device must be developed, or several source arrays positioned stationary at different depths must be used.
- **Difficulties for pre-stack analysis of data.** The petroleum industry is conservative. AVO-analysis is established as a routine tool in exploration and field monitoring. If VSDA has difficulties in such analysis, it could make VSDA a less tempting technology, even though other benefits are provided.

A part of this thesis is devoted to other themes than VSDA. In Chapter 6, a test of the newly proposed apparition methodology (Robertsson et al., 2016a) is performed in the common-offset domain in separation of site survey and conventional seismic data acquired simultaneously. When assuming that the deeper part of the conventional data is negligible, we obtain very good separation results. Further investigation of different apparition strategies and full-length records are needed. This was not possible due to time-constraints during this PhD. Issues related to aliasing are likely to occur in this method. The lowest apparent velocity that can be seen in common-offset gather is half the velocity of the water ($\sim$750 m/s). However, for flattish geology, this method should work quite well. More studies on dealiasing/interpolation for common-offset gathers are needed to make sure that the method can work in more complex geological settings.

Separation of wavefields recorded from simultaneous sources is required for conventional seismic imaging and impedance inversion. For FWI, however, this might not be as strict. Crosstalk between the different sources result in unphysical artifacts in the calculated gradients that are used to update the velocity model. In Chapter 5, FWI was carried out with a source array with a length of 40 m. In this example, crosstalk between the wavefields from the different sources is most definitely occurring, but the study shows that good results are obtained as long as the source wavefield is modeled correctly. Therefore, I think that data resulting from simultaneous acquisition of site survey and conventional data, as proposed in Chapter 6, may be used directly in FWI if the source wavefields are modeled correctly. On the other hand, the current state of the art in FWI of real data is limited in computational power and memory requirements to relatively low frequencies. Up to 30 Hz in 2D acoustic FWI (Mancini et al., 2016). In this range of frequencies the separation process proposed in Chapter 6 will probably suffice.

In Appendix A, a new model for how iceberg ploughmarks act as a trapping mechanism for gas in Quaternary sediments is proposed. This study is mostly based on interpretation of conventional 3D seismic data that lack high frequencies and resolution in the shallow sediments. A few 2D site-survey lines were available to this study, and they clearly demonstrate the uplift in interpretability that site-survey data provide in shallow geology. Operators are, in many countries, obliged to acquire site-survey data prior to drilling wells to assess potential geohazards. By acquiring site-survey data alongside of conventional data, the cost of a separate survey could be saved, in addition to providing better knowledge of the shallow geology.

In seismic acquisition in general, the demand for ultra-low frequency data (<5–7 Hz) is probably the biggest challenge. For marine seismic acquisition at present time, the source wavefield is limited in low-frequencies by two factors: The low-frequency output from air-gun arrays and the source ghost. The exploration geophysics community's current understanding is that the effect of the source ghost and the change in low-frequency signal from air guns is close to perfectly canceling when the depth of the source is changed (Hopperstad et al., 2012; Landrø and Amundsen, 2014b). This results in no change for the low-frequency output from the source. VSDA with air guns, along with other air-gun based broadband sources, are therefore incapable of pushing the low-frequency end of spectrum further towards zero Hz. Hopperstad et al. (2012) find that the only way of getting more low-frequency energy from air guns is to increase to total amount of air used in the sources, i.e., use bigger guns and higher pressure. In order to get more low-frequency energy, I think, new sources must be developed. Research on marine dipole sources will hopefully result in a step-change in low-frequency marine sources in the future. The source ghost is beneficial for low frequencies because of the radiation pattern for dipole sources. If we cannot beat the ghost, we should at least take advantage of it.

Appendix A

Iceberg ploughmark illuminated by shallow gas in the Central North Sea *

Kjetil Eik Haavik and Martin Landrø
Norwegian University of Science and Technology, Trondheim, Norway

A.1 Abstract

Conventional 3D seismic data provides direct evidence for glacial influence during the early Pleistocene sedimentation in the Central North Sea. We identify iceberg ploughmarks as dim linear to curve-linear features in three early Pleistocene horizons that have high reflection amplitude compared to adjacent horizons. The anomalous horizons are interpreted to be reflections from thin sandy layers saturated with gas. The gas acts as a contrast liquid illuminating the thin sand layers. The reason for this is the difference in acoustic properties between water and gas saturated sand layers. The combination of thin bed effects and shallow gas makes the iceberg ploughmarks easily detectable as dim features in seismic reflection amplitude maps. Our interpretation is based on analysis of real seismic data, well logs and modeled seismic response. The methods we use include interpretation of horizons followed by extraction of reflection amplitudes, well log analysis, pre-stack amplitude versus offset analysis of high resolution 2D seismic data and time-lapse analysis of seismic. Seismic modeling is performed to study interactions between thin sand beds, shallow gas and iceberg ploughmarks. A new trapping mechanism for shallow gas is presented and seismic modeling of this trap strengthens our interpretation. The trap is created by iceberg ploughmarks in sandy layers that are covered by finer and less permeable sediments. For this area we find that conventional seismic interpretation is superior to the much used method of studying seismic time-slices for detection of iceberg

---

[*] Paper published in Quaternary Science Reviews, Volume. 103, number 1 (November 2014); P. 34–50. DOI:10.1016/j.quascirev.2014.09.002

ploughmarks, both with respect to time and detectability. This study shows that the interpreter should look for high amplitude horizons with amplitude variations laterally when trying to detect iceberg ploughmarks.

A.2 Introduction

Icebergs are created by calving ice sheets or glaciers at their marine or lacustrine margins. Interaction between icebergs and the seafloor may result in linear to curve-linear depressions between parallel berms, and are often referred to as iceberg scours or iceberg ploughmarks (Woodworth-Lynas et al., 1991). The berms are built by the displaced sediments from the depression. This process can be seen at the present day East Greenland continental shelf (Syvetski et al., 1992; Dowdeswell et al., 1993). Buried Iceberg ploughmarks in the North Sea were first reported by Stoker and Long (1984) and later by others (e.g. Graham et al., 2007; Kuhlmann and Wong, 2008; Haavik and Landrø, 2013; Dowdeswell and Ottesen, 2013). Identifying buried iceberg ploughmarks in seismic data is a much used method to determine whether or not the buried sediments are deposited during a period of glacial influence. Analysis of buried iceberg ploughmarks provide information about the flow direction of the icebergs and potentially their source area. The density of ploughmarks is related to the rate of iceberg production, and should be linked to the dynamics of the ice sheet that produce them (Dowdeswell and Forsberg, 1992). The North Sea Basin has been subsiding throughout the Quaternary, and a close to complete sediment record is preserved in the Central North Sea (Gatliff et al., 1994; Ottesen et al., 2014). These sediments hold key information to map the behavior of the surrounding ice sheets during former glaciations.

Shallow gas has been observed in association with buried iceberg ploughmarks in various ways (Gallagher and Heggland, 1994; Kuhlmann and Wong, 2008; Haavik and Landrø, 2013). Haavik and Landrø (2013) proposed a method for how iceberg ploughmarks act as a trapping mechanism for shallow gas in sand layers. In this paper we describe this trap in more detail and the effect thin gas filled sand layers have on imaging of iceberg ploughmarks. We use seismic data to investigate early Quaternary sediments in the Central North Sea and identify linear to curve-linear features interpreted as buried iceberg ploughmarks in the 2/4 block at approximately 56°4'N and 3°8'E. The interpreted ploughmarks are identified in sediments deposited between the Upper Regional Unconformity equivalent (URU) and the Base Naust equivalent as used in Dowdeswell and Ottesen (2013) and Ottesen et al. (2014). We use several geophysical tools such as amplitude vs. offset analysis (AVO), conventional seismic interpretation and time-lapse seismic (4D), together with seismic modeling. The different geophysical tools are explained in Section A.4. Here, we use the Quaternary period as formally ratified by the International Commission on Stratigraphy (ISC) that starts at 2.58 Ma and includes the Gelasion stage (Gibbard et al., 2010). We will refer to continuous seismic reflections from geological boundaries as horizons, and we refer to any interface between to different geological layers as a reflector. This paper is organized so that we present the methods and how we obtain our results in the

Section A.4 and comment on them in the

A.3 Background

A.3.1 Historical setting

The study area is located in the 2/4 block in the Central North Sea (see Figure A.1). In this area shallow gas has been identified as vertical structures and chimneys on seismic reflection data in Paleogene and Neogene sediments over most of the known hydrocarbon reservoirs (D'Heur, 1987; Pekot and Gersab, 1987; Granli et al., 1999). Shallow gas in the Quaternary sediments has been identified within seismic (Lie and Larsen, 1991; Haavik and Landrø, 2013), and also encountered in several exploration wells drilled in this area (according to NPD Fact Pages (2014), wellbore 2/1-1, 2/4-13, 2/4-15 and 2/4-16). A major underground blow out took place when Saga Petroleum drilled the 2/4-14 well into a Jurassic reservoir in 1989. It was estimated that 0.4 MSm^3 of oil and 196-367 MSm^3 of gas had been flowing from the reservoir and into shallow formations before the blow out was killed with assistance from the 2/4-15 relief well after 326 days (Remen, 1991). Lie and Larsen (1991) identified new amplitude anomalies on seismic lines that were re-acquired after the blow out. This was probably the first 4D seismic acquired offshore Norway (Bjørlykke, 2011, Chapter 19). These anomalies were located at approximately 490 m and 840 m below mean sea level and interpreted as the two main recipients for the hydrocarbons from the blow out. The accident has given and will continue to give scientists the opportunity to study the seismic expression of fluid flow in shallow sediments.

The reader is referred to Landrø (2011) for further reading on the 2/4-14 blow out.

A.3.2 Geological Setting

The North Sea was an intracratonic basin during Cenozoic times. With the exception of a narrow seaway that connected the North Sea with the Norwegian-Greenland Sea, landmasses confined the basin: The Fennoscandian shield to the East and Northeast, Central Europe to the South and British Isles to the West (Ziegler, 1988, 1990; Jordt et al., 1995; Sørensen et al., 1997; Huuse et al., 2001; Anell et al., 2011). During most of Paleogene and Neogene, the Central North Sea Basin received sediments from the surrounding landmasses. Continuous subsidence of the basin and uplift of the land areas has governed the evolution of the Central North Sea. An almost complete Cenozoic sediment record is preserved in the central parts of the basin (Ziegler, 1990; Anell et al., 2011). The most accepted model for sedimentation is that the Central North Sea was filled by pro-deltaic and deltaic sediments sourced from North in Oligocene times, gradually rotating clockwise, to supply from Northeast and East in the late Miocene and Pliocene and from East and

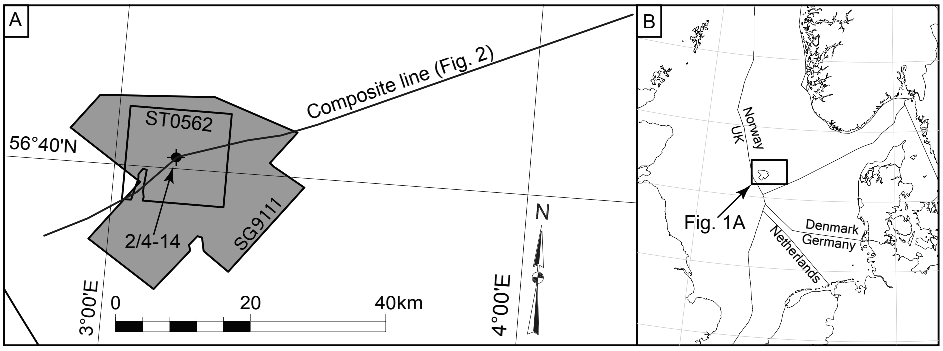

Figure A.1: (A) A map of the study area in the Central North Sea showing the position of the data used in this paper. The position of the 2/4-14 well is indicated together with the position of a composite seismic section and the outline of two 3D seismic cubes, SG9111 from 1991 and ST0562 from 2005. (B) Location map. Our study area is highlighted with a black box.

Southeast in early Pleistocene times (Spjeldnes, 1975; Cameron et al., 1993; Jordt et al., 1995; Sørensen and Michelsen, 1995; Sørensen et al., 1997; Anell et al., 2011; Ottesen et al., 2014). Anell et al. (2011) pointed out that this model was to simple and that sediments were also supplied from the Shetland Platform and Fennoscandia at varying rates throughout this period.

In early Quaternary, the great European rivers provided sediments that filled in the basin from South and Southeast (Bijlsma, 1981; Gibbard, 1988) at the same time as fluvial sediments from the UK area filled the basin from the West (Ottesen et al., 2014). Sediments were also supplied from Denmark from East (Sørensen et al., 1997). The early Quaternary sediments in the North Sea are mainly fluvio-deltaic to marine (Cameron et al., 1987; Long et al., 1988). During the middle and late Quaternary, glacial input to the North Sea was provided by the Scandinavian and British ice sheets that characterized the sediment sources in this period (Stoker et al., 2005). The mid to late Quaternary sediments are related to many cycles of glacial and interglacial periods resulting in inter-bedding of glaciogenic and marine deposits (Jansen and Sjøholm, 1991).

The sediments and erosional features produced in the North Sea basin during the middle to late Quaternary glacial cycles have been studied by many scientists (e.g. Long et al., 1988; Rise et al., 2004; Graham et al., 2010; Stewart and Lonergan, 2011). The North Sea has been inundated by ice sheets several times the last 0.5 Ma, and many generations of buried tunnel valley systems have been mapped in the North Sea (e.g. Cameron et al., 1987; Huuse et al., 2001; Praeg, 2003; Stewart and Lonergan, 2011). Tunnel valleys are erosional features that are formed below ice sheets (Ó Cofaigh, 1996). Several reconstructions of North Sea ice sheet from the late Pleistocene has been proposed (e.g. Ehlers, 1990; Graham et al., 2011; Clark et al., 2012). Less material is published on the early Pleistocene glaciations in the North Sea (Ehlers and Gibbard, 2008). In the Central North Sea, ice-rafted debris (IRD) have been identified in cuttings and cores from the early Quaternary sediments (Eidvin et al., 1999), and iceberg ploughmarks are interpreted in seismic data continuously through early Quaternary sediments (Dowdeswell and Ottesen, 2013) providing strong, but indirect evidence for glacial influence during this period (Ottesen et al., 2014). The buried iceberg ploughmarks observed in the early Pleistocene sediments in the Central Norths Sea show a principal flow direction in a North-South direction and source of these icebergs was probably a Scandinavian ice sheet (Dowdeswell and Ottesen, 2013). Based on comparison between the dimensions of the early Quaternary iceberg ploughmarks in the Central North Sea with the iceberg ploughmarks observed from modern polar continental shelves, Dowdeswell and Ottesen (2013) conclude that the ploughmarks observed in the Central North Sea are formed in relatively deep water (200-500 m).

A.3.3 Shallow gas

Gas present in sediments down to 1000 m is referred to as shallow gas (Davis, 1992). Shallow gas in sedimentary basins can have biogenic and/or thermogenic origin. Thermogenic gas is the term used for gas that is generated when organic matter is degraded under high temperature and pressure, and biogenic gas is the term used for microbial degradation of organic matter resulting in gas. Determining the origin of the gas can be done through isotope analysis of gas samples (Floodgate and Judd, 1992). There are several motivating factors for identifying shallow gas: (1) Shallow gas can be used in hydrocarbon exploration as an indicator that there is a working petroleum system present (e.g. Heggland, 1998). (2) Shallow gas is a potential geohazard for drilling operations. Gas may be present in pressurized pockets, trapped beneath low permeability shale and form a blow out hazard (Sillis and Wheeler, 1992). (3) Shallow gas may be produced (Peon discovery in the Norwegian Sea). (4) Shallow gas reduces the seismic velocity of the sediments significantly. Including knowledge of shallow gas when making velocity models will improve seismic imaging (Sernpere and Hardy, 1998).

The use of conventional 3D seismic data has proven valuable for identifying shallow gas (Gallagher and Heggland, 1994; Sallisbury et al., 1996). Shallow gas has many expressions in seismic data and descriptions of these can be found in e.g. Judd and Hovland (1992) and Løseth et al. (2009). Two of most obvious gas effects that can be seen in seismic data are bright spots due to gas accumulation, and chimneys due to dispersed gas that reduce the velocity of the affected sediments and obscure the image (e.g. Arntsen et al., 2007).

A.4 Database and methods

A.4.1 Data

The data sets available for this study are two industry 3D seismic cubes, 2D regional lines and high resolution 2D lines from site surveys. The two 3D data sets SG9111 and ST0562 were acquired in 1991 and 2005, respectively, and the 2005 cube is fully embedded within the 1991 cube. They have been acquired along different sail lines and processed differently. The bin-size in the both the 3D data sets are 12.5 m x 25.0 m and the temporal sampling is 4 ms. The 3D data sets are processed to zero phase wavelet and the central frequency is about 45 Hz in the shallow parts. Interpretation of the 3D seismic data is only available in full-stack migrated versions, which means that no information about angle dependant reflection amplitudes are available (see Section A.4.4 on AVO). The quality of the 3D data sets are poor in the shallow parts that are studied here. This is because few or none of the processing steps have been optimized for the shallow parts. Despite this, the 3D data is still very useful for this study. The 2D high resolution lines are from the SG8845, SG8910 and ST09322 site/monitor surveys and have a common mid-point (CMP) separation of 6.25 m, an offset range from 41 m to 1200 m and the temporal sampling is 1 ms. The wavelet is processed into a zero-phase wavelet and the central frequency is close 70 Hz. Some of the 2D lines are available in pre-stack format. The regional seismic 2D lines used in this study are CAST-90-122A and UG97-112. They have CMP separation of 12.5 m and the temporal sampling is 4 ms. The wavelet for these lines are mixed phase wavelet and the central frequency is between 25-40 Hz. A sparse set of well logs are available from the area. This reason for this is that most of the wells have not been logged in the shallow parts. Gamma ray logs are available in the shallow parts from wells 2/4-10, 2/4-13, 2/4-16 and 2/4-17. A Sonic log is available from the 2/4-16 well. The data set is provided by the sponsors of the LOSEM consortium at NTNU. The outline of the 3D data sets and the regional line are shown in Figure A.1.

A.4.2 Regional stratigraphy

A representative Southwest-Northeast trending seismic composite line across the Southern part of the Norwegian North Sea is shown in Figure A.2. This line is composed of the lines CAST90-122A, a random profile through the SG9111 and the UG97-122 line, indicated in Figure A.2. In this study we have picked four geological horizons on a regional scale. The purpose of this is to set the studied interval in relation to previous work. Three of the horizons are tied to the interpretation in Figure 4 from Anell et al. (2011). These horizons are BASE NEO 2, BASE NEO 3 and BASE NEO 4, and corresponds to the Mid-Miocene Unconformity (MMU), the Base Naust equivalent and the Upper Regional Unconformity (URU) equivalent that are the names used in this paper, respectively. The Mid Miocene Unconformity corresponds to the base of the Nordland Group after Deegan and Scull (1977) and is a well described regional unconformity in the North Sea (e.g.

Jordt et al., 1995; Michelsen, 2001; Sørensen et al., 1997). The Base Naust and the URU are horizon that are well defined in the Norwegian sea (Dalland et al., 1988; Rise et al., 2005; Ottesen et al., 2009) and were extended from the Norwegian sea to the North Sea in Dowdeswell and Ottesen (2013). On the mid-Norwegian Shelf the Naust Formation is mainly of glacial origin and its base is about 2.75 Ma (Rise et al., 2005), older than base of Quaternary. The age of URU is close to the Brunhes-Matuyama magnetic boundary at 0.78 Ma (Stoker et al., 1983) in the Norwegian sea, and its equivalent in the North Sea is probably younger than this (Ottesen et al., 2014). The URU is the boundary between the early and middle Pleistocene. The fourth horizon that was picked is called Gas Level 1, and is the deepest horizon where we identify dim linear to curve-linear features in a high amplitude background as described in Section A.4.3.

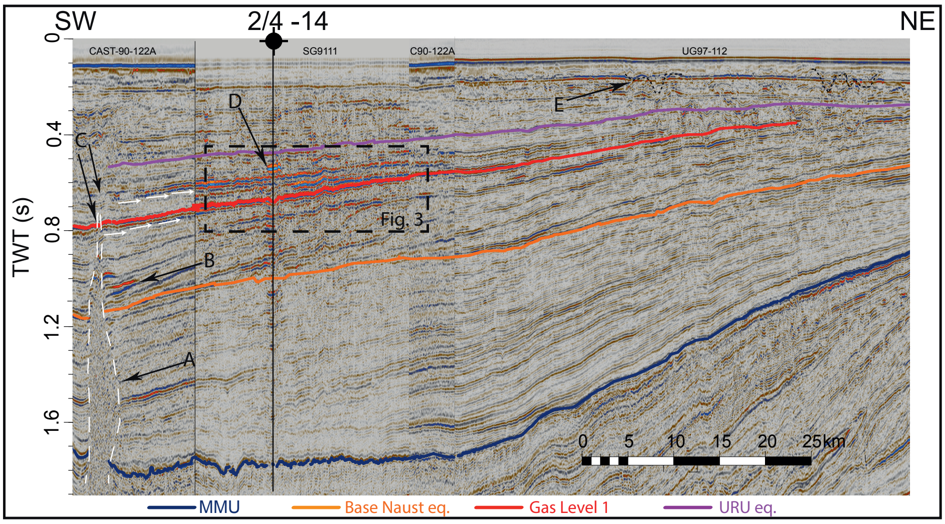

Figure A.2: A composite seismic profile as shown in Fig. A.1. Base NEO2, Base NEO3 and Base NEO4 are horizons that are tied to previous work in the North See(see Anell et al., 2011, Fig.4). Gas Level 1 is the deepest of the three horizons which are further studied in this paper (see Section A.4.3). The position of the 2/4-14 well bore is indicated. Arrows: (A) A gas chimney that shows that gas from deeper strata has migrated vertically. (B) Bright spots indicate accumulation of gas in porous sediments. (C) Possible entry points for lateral migration for the shallow gas in the sand layers investigated in this work. Possible lateral migrations routes from the gas chimney are indicated by white arrows. (D) The amplitude anomaly at 550 ms is a known gas accumulation with gas from the 2/4-14 underground blow out. (E) Tunnel Valleys in the middle and late quaternary.

A.4.3 Iceberg ploughmark detection

A much used method to detect buried iceberg ploughmarks in seismic data has been through step-wise time slicing through 3D cubes and identifying linear to curve-linear features (e.g. Dowdeswell and Ottesen, 2013). Here, we identify three dipping horizons in the seismic that have anomalous amplitudes and exhibit amplitude variations laterally. These horizons are positioned between 500 ms and 700 ms and have been picked within the 1991 3D seismic data set. A close up of these horizons are shown in Figure A.3. The horizons were picked on zero crossing in a filtered version of the cube, and attributes were extracted from the seismic data along these horizons afterwards. The filter that was used was a spatial and temporal smoothing filter. Picking zero crossings proved to be simpler and more robust than picking on peak (maximum positive amplitude) or trough (maximum negative amplitude). The reason for this is probably because of the great lateral amplitude variations that makes it hard for tracking algorithms to continue tracking. The horizons corresponding to Gas Level 1 and 3 in Figure A.3 could be traced through the entire data set, while the horizon corresponding to Gas Level 2 is truncated towards Northeast. In this region, careful picking was performed to ensure that the layers that were positioned above or below the original horizon continued to stay above or below the picked horizon. The position of the truncation is indicated with an arrow in Figure A.3 (and a dashed white line in Figure A.6). Root-Mean-Squared (RMS) amplitudes were extracted from the unfiltered seismic cube in an 18 ms window centered on each of the picked reflectors. Different attributes (e.g. variance, coherency) were tested, but we found that the RMS amplitude attribute gave the best result for visualizing these dim linear to curve-linear features.

A two-way travel-time map of the horizon corresponding to Gas Level 1 is shown in Figure A.4. The RMS amplitude attribute maps generated from the three levels in Figure A.3 are shown in figures A.5, A.6 and A.7. Time slices that cut through these features at two different constant travel times are shown for the purpose of comparison with the method used here in Figure A.8, and the position of these are indicated by white dashed boxes in Figure A.5, A.6 and A.7. The dim linear to curve-linear features observed in the three gas levels were interpreted one by one and directional analysis was performed by mapping the orientation of each of these. The interpreted dim linear to curve-linear features from all three gas levels are presented in Figure A.9 with corresponding rose diagrams showing the orientation of the features.

A.4.4 Amplitude versus offset analysis

Amplitude versus offset (AVO) analysis is a method that can provide information about lithology and fluid content based on angle dependent reflection coefficients (Smith and Gidlow, 1987; Hampson and Russell, 1990). A pre-stack high resolution 2D seismic line from 1988 was used in the AVO analysis. The data was sorted into common mid points (CMP) and the reflector corresponding to Gas Level 2 was picked for analysis. CMPs

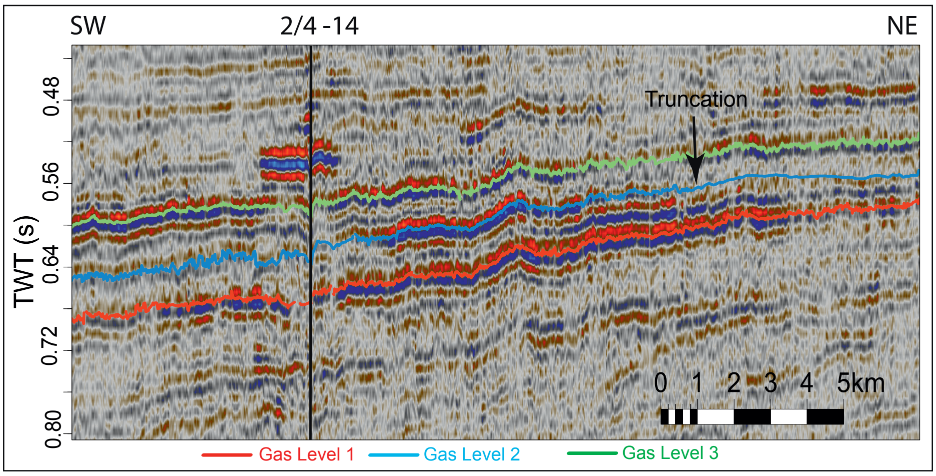

Figure A.3: Shallow seismic profile showing the three anomalous horizons Gas Level 1 (red), Gas Level 2 (blue) and Gas Level 3 (green). These Horizons have been picked through the SG9111 data set. This section is the part of Figure A.2 that runs through the SG9111 3D seismic data shown in Figure A.1. The position where Gas Level 2 truncates is indicated with an arrow.

from two areas that are shown in Box 1 and Box 2 in Figure A.10A were used in the AVO analysis. The position of this 2D line is superimposed on the RMS amplitude map from Section A.4.3 shown in Figure A.10C. RMS amplitudes were extracted from a 10 ms window, and corrected for both geometrical spreading and attenuation. Compensation for attenuation loss was done using a constant Q model with peak frequency f_p = 70 Hz, Q = 70 and the travel-time was estimated by a simple straight ray-tracing procedure. The same rays were also used when correcting for geometrical spreading. Finally, the amplitudes were multiplied by -1 to change the polarity back to negative, as we would expect from a reflection from the boundary between shale and a poorly consolidated sand that is saturated with gas. This was done because the result of the RMS process is always a positive number. The gamma ray log from the shallow parts of 2/4-16 well is shown in Figure A.10B. The interval marked in Blue, at approximately 560 m, has been interpreted as a 6 m thick sandy layer. We interpret this as sand because of the low gamma ray count. This layer correspond to Gas Level 2 in Section A.4.3. We observe low gamma ray values around 530 m, 580 and 605 m. The layers at 530 m and 605 m correspond to Gas Level 1 and 3, respectively.

AVO modeling was performed in order to compare the field data to different scenarios of pore fluids. Our hypothesis is that the strength of the amplitudes in the three gas levels are related to the pore fluids. To model AVO responses, a model consisting of two layers was used: A porous sandstone layer below a layer of shale. P-wave velocity (α) was chosen based on well logs. S-wave velocity (β) and density (ρ) are also required for the AVO-

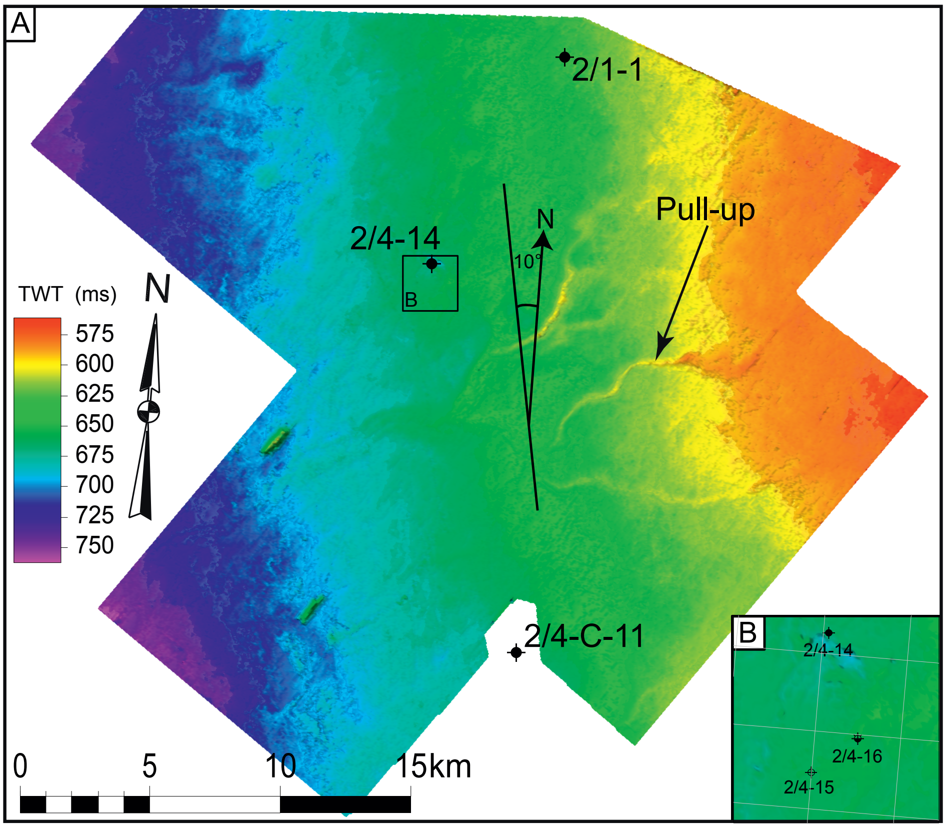

Figure A.4: (A) A Two-way travel time map of the horizon corresponding to Level 1 in Section A.4.3. The units are in milliseconds. The layer has an average dip of 0.3° towards Southwest. The strike angle is 10 ° Northwest. The arrow indicates pull-up that is associated with high velocity infill of tunnel valleys (e.g. Ó Cofaigh, 1996) that are located in Middle to Late Quaternary sediments positioned above. The position of the 2/1-1, 2/4-14 and 2/4-C-11 wells are indicated, and a close up of the wells that are positioned in the vicinity of the 2/4-14 well is shown in (B).

modeling, but were not available from logs. To get an estimate of S-wave velocities in both layers we used the empirical relationship given by Han (1986), which uses P-wave velocity as input. Velocities for sandstone saturated with both water and methane gas, and mixtures of the two, were found using fluid substitution (Gassman, 1951). Velocities were found for two different types of saturations: gas uniformly distributed in water and for patches of concentrated gas in water background. These types are referred to as uniform and patchy saturation, respectively. The reflection coefficients were calculated using an approximation to the equations in Zöppritz (1919) given in Shuey (1985). A brief summary of how to perform AVO analysis and the equations needed for this process

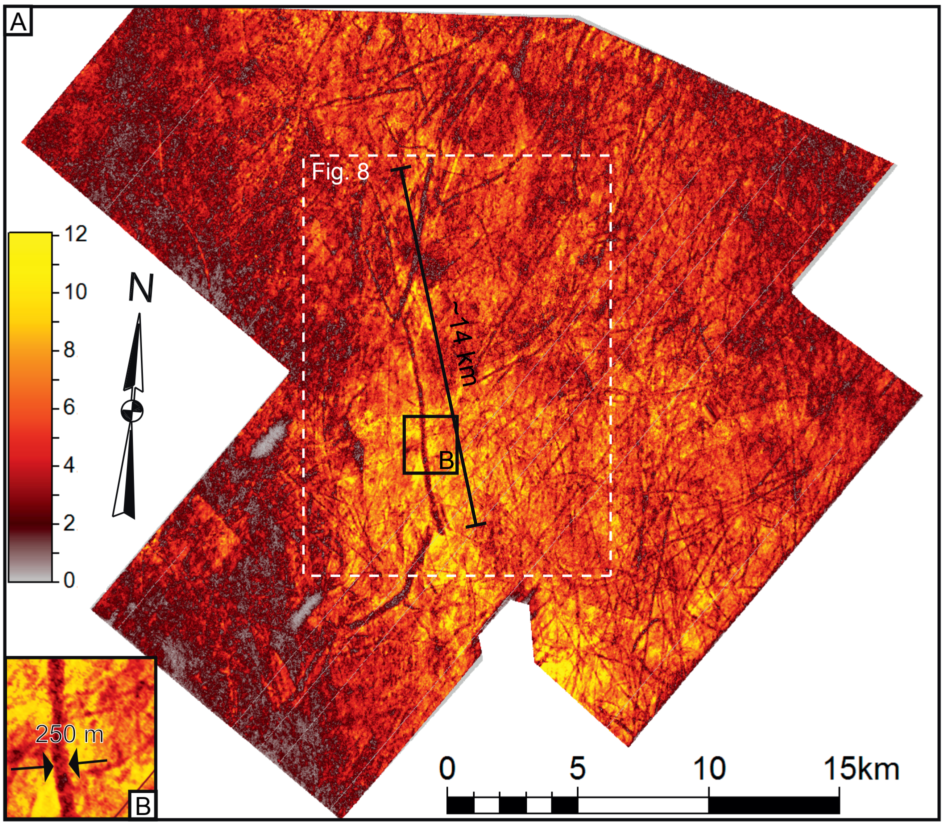

Figure A.5: (A) RMS amplitude map extracted from the unfiltered SG9111 data in a 18 ms window around the horizon corresponding to Level 1 in Section A.4.3. The black scale shows the length of the largest continuous dim line that is approximately 14 km long. The width of this dim line is found to be up to 250 m if they are measured between the high amplitudes on both sides. A close up of how and where the width is measured is shown in (B). The area inside the dashed with Figure A.8 box is shown together with a time slice at 680 ms in Figure A.8 A1 and B1, respectively.

is given in Appendix 1. The parameters used for the water saturated sandstone layer was $\alpha_{sw} = 1900\ m/s$, $\rho_{sw} = 2.07\ g/cm^3$ and porosity $\phi = 0.35$. For the shale layer we used $\alpha_{sh} = 2100\ m/s$, $\rho_{sh} = 2.13\ g/cm^3$. The field data was normalized to the modeled data. This was done by finding a scaling factor that scaled the regression line from the data points from the presumed water filled zone to the amplitudes calculated for the scenario where the sandstone is saturated with 100 % water. This scaling factor was then applied to all data points.

The data from the AVO analysis of the pre-stack high resolution 2D data are shown together with modeled AVO response in Figure A.11.

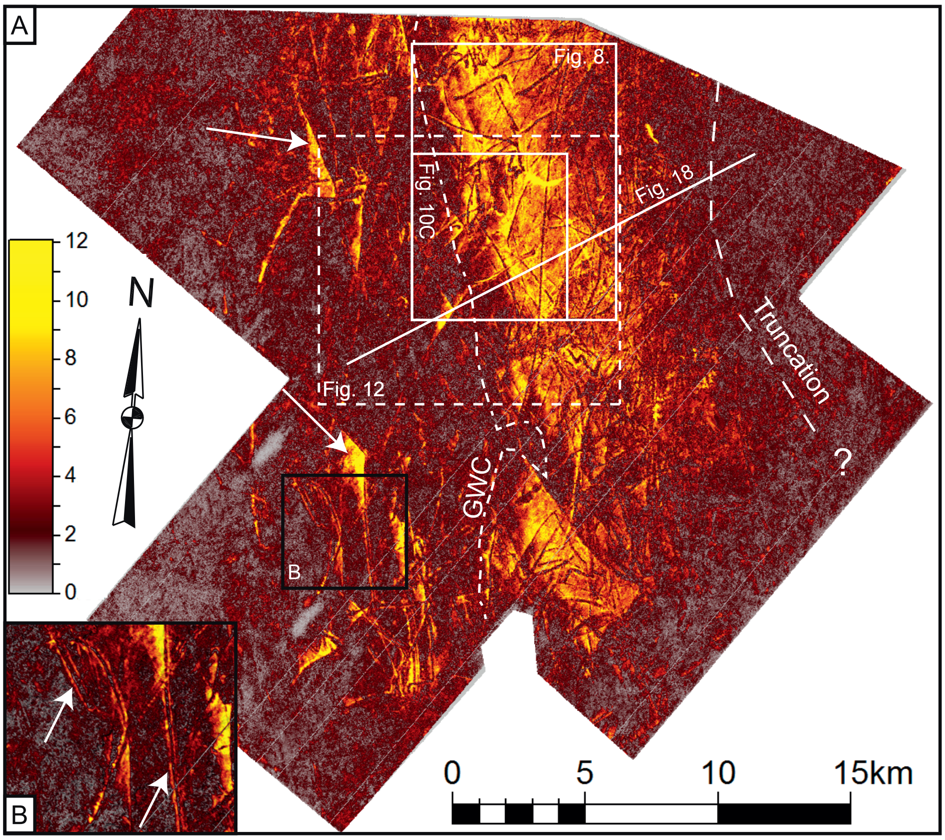

Figure A.6: (A)RMS amplitude map extracted from the unfiltered SG9111 data in a 18 ms window around the horizon corresponding to Level 2 in Section A.4.3. The truncation of the reflector corresponding to Gas Level 2 is indicated along. The GWC line is the approximate boundary of the high amplitude belt that is seen in close to North-South trend. The arrows are indicating some of the triangular shaped anomalies that can be observed in this map. Larger figures are available of the indicated boxes. The area inside the dashed with Figure A.8 box is shown together with a time slice at 600 ms in Figure A.8 A2 and B2, respectively. (B) High amplitude curve linear features are indicated with white arrows. These features are seen in pairs. (B) Is a close up of the black box in (A).

A.4.5 Time-lapse seismic (4D) analysis

Time-lapse, or repeated seismic is a commonly used tool in the petroleum industry when designing infill production or injection wells and deciding on injection/production strategy for hydrocarbon reservoirs (Greaves and Fulp, 1987; Landrø et al., 1999). When two seismic data sets are acquired over the same area with a given time period in between, they can provide insight into how geology, fluid content and pressure may have changed

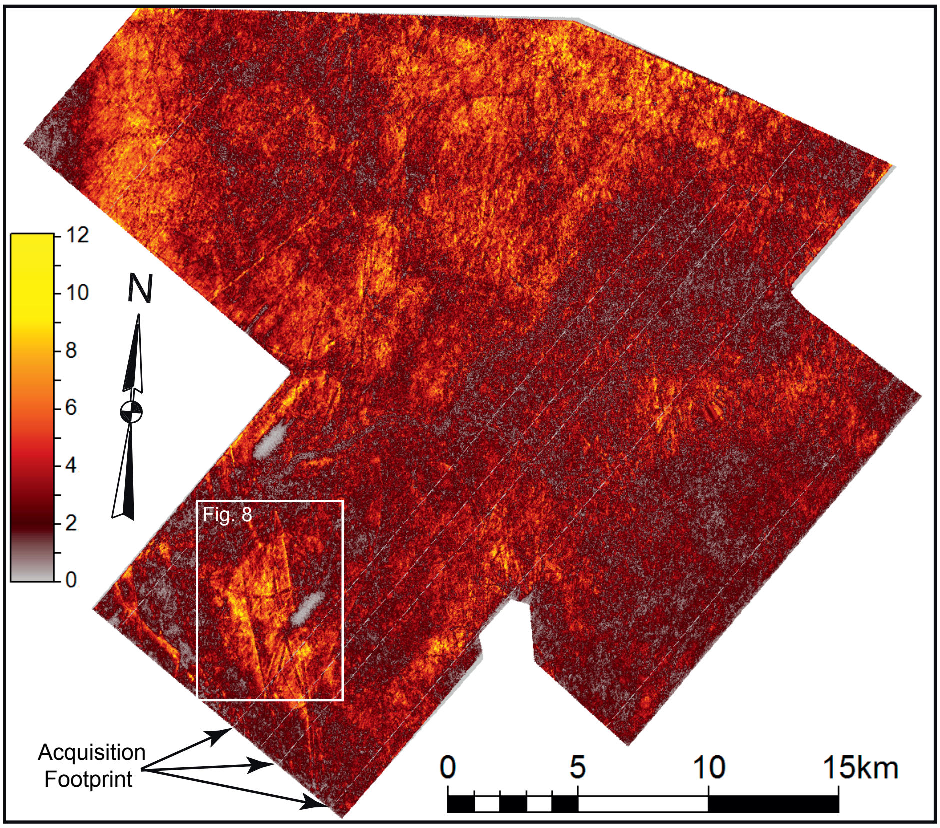

Figure A.7: RMS amplitude map extracted from the unfiltered SG9111 data in a 18 ms window around the horizon corresponding to Level 3 in Section A.4.3. Dim lines can be seen in the high amplitude areas. Acquisition footprints are seen as parallel dim lines running in the towing direction. The area inside the dashed with Figure A.8 box is shown together with a time slice at 600 ms in Figure A.8 A3 and B3, respectively.

over this period (Landrø, 2001). Here we perform time-lapse studies on the two 3D seismic data sets acquired in 1991 and 2005, respectively, and on three 2D high resolution seismic lines that are acquired over the same physical line in 1988, 1990 and in 2009.

The two-way travel-times (TWT) down to a given geological reflector are different in the 1991 and 2005 3D seismic data sets, on a regional scale. This difference is not related to any changes in the geology over this period, but a result of different processing work flows that have been applied to the respective data sets, and most important, the velocity models used for imaging of the two data sets are known to be different. This difference makes it essential to recognize and pick the same geological reflector and perform attribute analysis in both data sets. The horizon corresponding to Gas Level 2 (in Section A.4.3) was picked throughout the 2005 3D seismic data set and the same procedure for extracting RMS

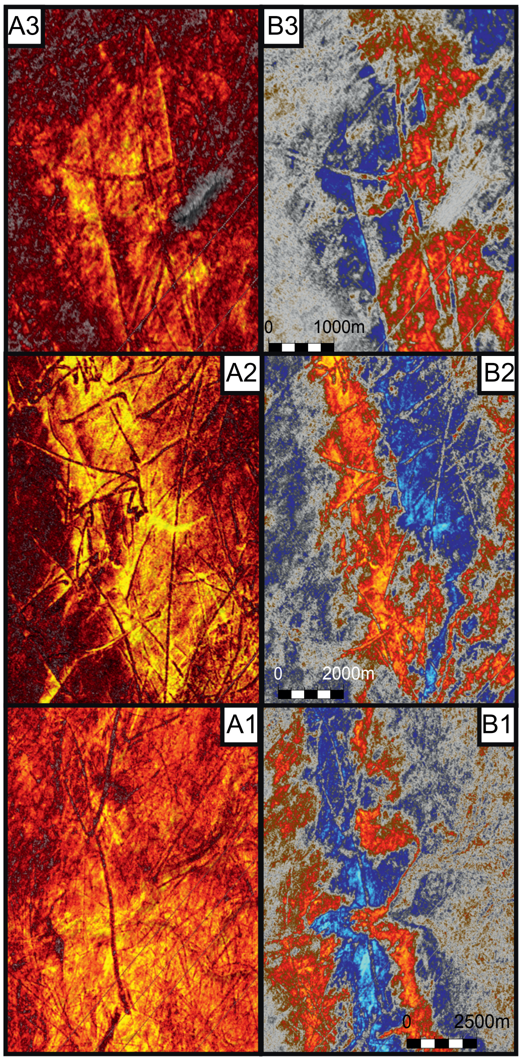

Figure A.8: Comparison of the detectability of linear to curve-linear features in the map generated from from the different gas levels and time slices. The amplitude map from Gas Level 1 (A1) and a time slice at 680 ms (B1) from the position indicated in Figure A.5, in the 1991 3D data. (A2) and (B2) are the amplitude map from Gas Level 2 and a time-slice from 600 ms, respectively, from the position indicated in Figure A.6. (A3) and (B2) are the same as (A2) and (B2) for Gas Level 3. The position indicated in Figure A.7. The same color map is used in all amplitude maps.

amplitudes as discussed in Section A.4.3 was carried out. Since the two 3D seismic data sets are acquired and processed differently they have different range of amplitudes.

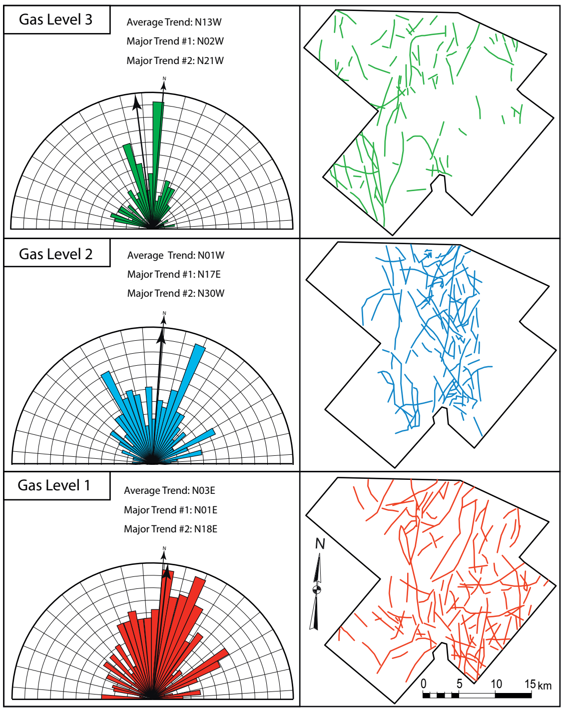

Figure A.9: The interpreted dim curve-linear to linear features with corresponding Rose diagrams showing the distributions of directions and average directions in black arrows for Gas Level 1, Gas Level 2 and Gas Level 3. The small black arrow in the rose diagrams indicates North. The rose diagrams are only one-sided, but the measurements are uni-directional. The rose diagrams are weighted by the lengths of the ploughmarks.

This difference in amplitudes is depth dependent and could not be adjusted for globally. However, a local scaling of the 2005 data set at the investigated level was performed to ensure that the amplitude range in the two data sets are comparable, at least in a qualitative way, in a 4D sense. We stress that with such significant differences between the data sets and their processing work flow it is the qualitative differences we can identify, such as a new amplitude distribution, and not a numerical value for a change in saturation or pressure. The RMS amplitude maps from Gas Level 2 from 1991 and 2005 are shown in Figure A.12.

The high resolution 2D lines were analyzed for time-shifts. The time-shifts down to the horizon corresponding to Gas Level 1 in Section A.4.3 was measured from 1988 (before the blow out) to 1990 and 2009, respectively. This was done using a cross-correlation method where the maximum correlation time lag between the two traces, centered on a specific horizon, is assumed to be the time shift (e.g. Langseth and Landrø, 2012). Time-shifts down to a seismic horizon give information about changes that have occurred in

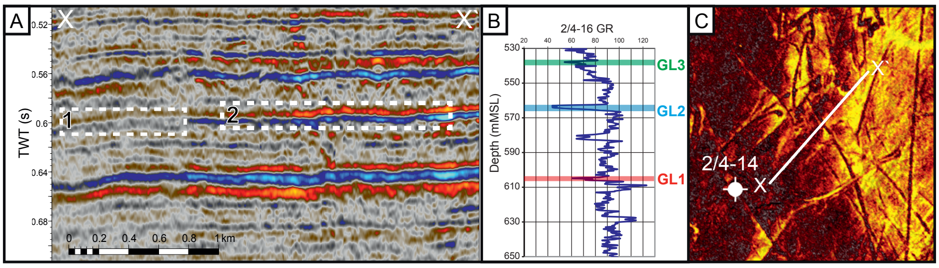

Figure A.10: (A) A shallow seismic profile showing the areas where AVO analysis has been performed. The presumed water filled and gas filled zones are indicated in Box 1 and 2, respectively. (B) Gamma ray log from the 2/4-16 well indicating sand layers around 530 m, 560 m, 580 m and 605 m. The colored intervals corresponds to Level 1 (Red), Level 2 (Blue) and Level 3 (Green) in Section A.4.3. (C) Part of the amplitude attribute map from Level 2 shown in Figure A.6 where the position of the seismic profile in (A) is indicated. Yellow indicates high amplitude and gray low.

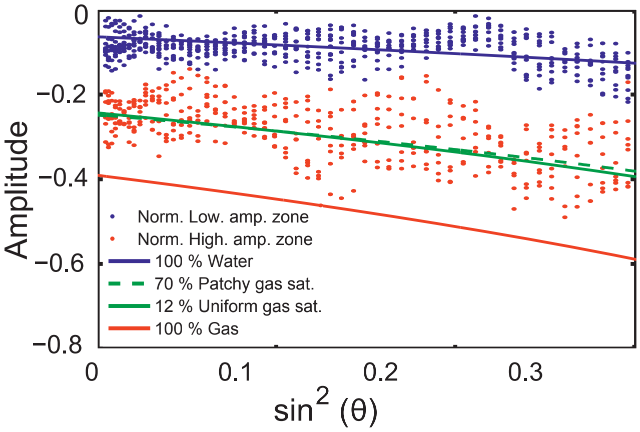

Figure A.11: AVO data from the low amplitude zone in Box 1 (Blue dots) and high amplitude zone in Box 2 (Red dots), in Figure A.10. The data has been corrected for geometrical spreading and attenuation and then normalized to the modeled AVO data as described in Section A.4.4. The lines represent the modeled AVO response from an interface between two layers, shale above sand, where the sand has different saturations of gas and water, indicated by the legend.

the overlying sediments during the period between the data sets were acquired, but do not give information about the exact depth of the change. The time-shifts are shown together with the position of the 2D line used for this analysis in Figure A.13.

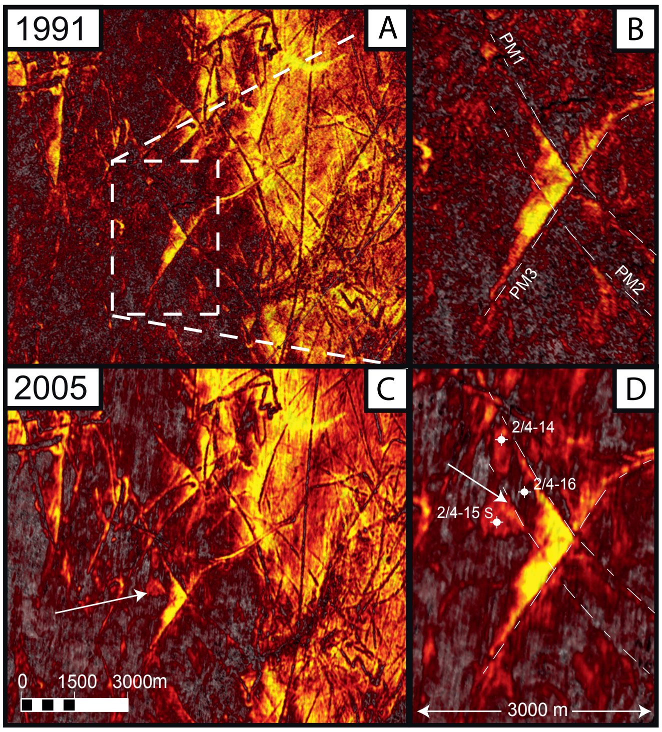

Figure A.12: (A) RMS amplitude map from Gas Level 2 extracted from the 1991 3D seismic data set. (B) Close up of the dashed white box in (A), showing a triangular shaped anomaly in vicinity of the 2/4-14 well. The thin dashed lines called PM1, PM2 and PM3 are interpretation of the dim curve-linear features that we see in the amplitude maps. (C) and (D) are the equivalents of (A) and (B), but for the 2005 3D data set. The position of the 2/4-14, -15 and -16 are indicated. An anomaly is present around the 2/4-15 well in (D) in the 2005 data set and is not present in the 1991 data set. This anomaly terminates towards the dashed line PM2 from (B) that are imposed onto (D), see white arrow.

A.4.6 Seismic response of thin sand layer

Tuning is the term used by the seismic interpretation community for interference between seismic reflections (e.g. Widess, 1953; Meissner and Meixner, 1969). If two reflectors, as the top and base of a sand layer, are closely spaced we would not necessarily be able to separate the two reflections in a seismic section. The appearance of the total seismic response from the two reflectors is dependent on the distance between the two reflectors and the frequency content of the seismic signal. Rayleigh's criterion for vertical resolution is a quarter of the wavelenght λ of the dominant or peak frequency and often used as the

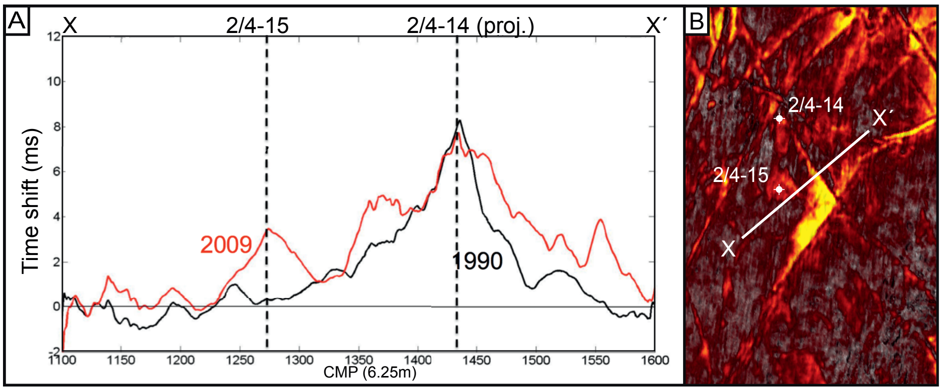

Figure A.13: (A) Time shifts to the reflector corresponding to Level 1, in Section A.4.3, from before the blow out in 1988 to 1990 (black line) and 2009 (red line), respectively. The separation between the Common Mid Poitns (CMP) is 6.25 m, and the total profile is 2.5 km. These time-shifts are found from time-shift analysis of repeated high resolution 2D lines. The time-shifts seen at the projection (proj.) of the 2/4-14 well is due to the gas in the 490 m layer seen at approximately 550 ms in Figure A.3. We also observe an increased time-shift from 1990 to 2009 below the 2/4-15 well. (B) Part of the amplitude attribute map from Level 2 shown in Figure A.6. The position of the 2D line used for time-shift analyses is indicated by the white line, and the 2/4-14 and -15 wells are shown.

resolution criteria in seismic (Sheriff, 1985), which is given as:

$$D_m = \frac{\lambda}{4} = \frac{\alpha}{4f_p}. \tag{A.1}$$

Where α is the P-wave velocity in the layer and f_p is the peak frequency of the seismic data. The vertical resolution above is defined as the limiting distance the reflectors have to be apart to still be resolved. The ability to resolve geological features is dependent on both resolution in time and space. The horizontal resolution is often taken as the 1. Fresnel diameter:

$$D = \sqrt{\frac{2z\alpha_{avg}}{f}} \tag{A.2}$$

where z is the depth down to the geology that is being imaged and α_{avg} is the average velocity down to z. For our 3D data set, if we assume $z = 600\ m$, $f_p = 45\ Hz$ and $\alpha_{avg} = 1900\ m/s$, the horizontal resolution is 110 m. However, the horizontal resolution in migrated 3D seismic data is about a quarter of the wavelength (Brown, 1999), but is dependent on noise and spatial sampling (Sheriff, 1985). The horizontal and vertical resolution in 3D data sets analyzed here, using these criteria, are both close to 10 m, and this corresponds to a temporal resolution of approximately 10 ms. This horizontal resolution is smaller than the bin cells in the 3D data, which means that the bin size will be the limiting factor controlling the horizontal resolution. Figure A.14 shows a comparison between the 1991 3D seismic and a high resolution 2D line from a site survey over one of the triangular shaped anomalies seen in Figure A.6A.

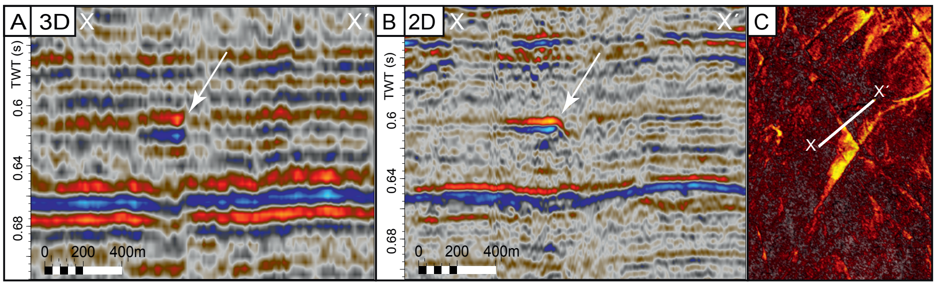

Figure A.14: Seismic sections across the triangular shaped anomaly in Level 2 from the SG9111 3D seismic cube in (A) and High resolution 2D line from the SG8910 survey in (B). (C) Amplitude map from Level 2 showing the triangular shaped anomaly and the position of the seismic sections in (A) and (B). The arrow indicate the position of the edge of the ploughmark in (A) and (B).

A wedge model consisting of a sand wedge in surrounding shale was generated. Seismic modeling using the convolution method was performed with a 45 Hz Ricker wavelet as source. Figure A.15 shows the seismic response of this wedge model, where the sand is saturated with 100 % water in (B) and 12 % gas in (C). The maximum amplitudes from the water and gas case are extracted and shown together with thickness of the wedge in (D). The velocities and densities used in Section A.4.4, was also used in this model.

To test the detectability of iceberg ploughmarks in seismic data, a 2D finite difference modeling approach was used to generate synthetic seismic data (e.g. Virieux, 1986). The model that was used had vertical sampling Δz = 0.2 m and horizontal sampling Δx = 2 m. A 45 Hz Ricker wavelet with sampling $\Delta t = 8 * 10^{-5}$ s was used as source pulse. A line source was used to generate zero offset data. The data was then partially stacked in the horizontal direction to mimic binning, and then re-sampled to Δx = 24 m and Δt = 4 ms. This was done in order to resemble more realistic seismic acquisition. The data was then migrated using a post-stack Kirchhoff migration algorithm with a constant velocity. A 1D sinc interpolation was performed in order to make the synthetic seismic appears more similar to the seismic sections that are displayed in seismic interpretation softwares that are commonly used today. The models we use consist of a sand layer with 15 depressions in it that has the shape of a parabola. The width of the depressions were all 50 m, which equals the average width of ploughmarks earlier described in the early Pleistocene by Dowdeswell and Ottesen (2013), and the depths range from 1 to 15 m. Three different thicknesses of the sand layer was modeled, 2 m, 6 m and 10 m, to see how tuning affect imaging of iceberg ploughmarks. RMS-amplitudes were then extracted in a 18 ms long window centered on the zero crossing of each of the migrated sections. Figure A.16 shows the modeled seismic response for the 15 depressions in sand layers of 2 m, 6 m, and 10 m.

2D finite difference modeling was also performed on a conceptual model of Gas Level 2. This result is shown in Figure A.18 and discussed in Section A.6.

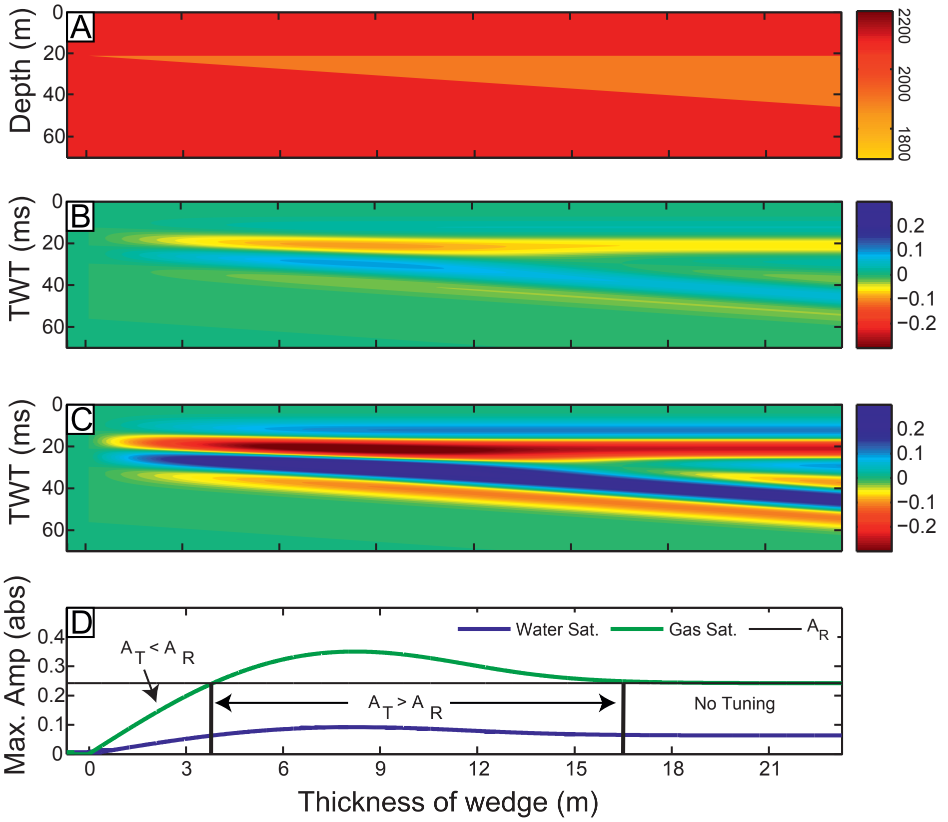

Figure A.15: (A) The P-wave velocity model used in modeling. The shale layer (red) is 2100 m/s and the velocity of the sand (orange) is 1900 m/s for water filled case and 1400 m/s for the gas case. The thickness of the sand is up to 23 m (B) Synthetic seismic of the water filled case. (C) Synthetic seismic for the gas filled case, with 12% uniform gas saturation as found from fluid substitution analysis described in Section A.4.4. (D) The maximum amplitude from (B) and (C), and the thickness of the wedge versus the wedge X-position. A_T and A_R are the Tuning amplitude and the amplitude of a resolved separate reflection. When the thickness of the wedge is between 3.6 m and approximately 16.4 m, A_T is greater than the A_R. The difference in amplitude between the gas case and the water case significant for

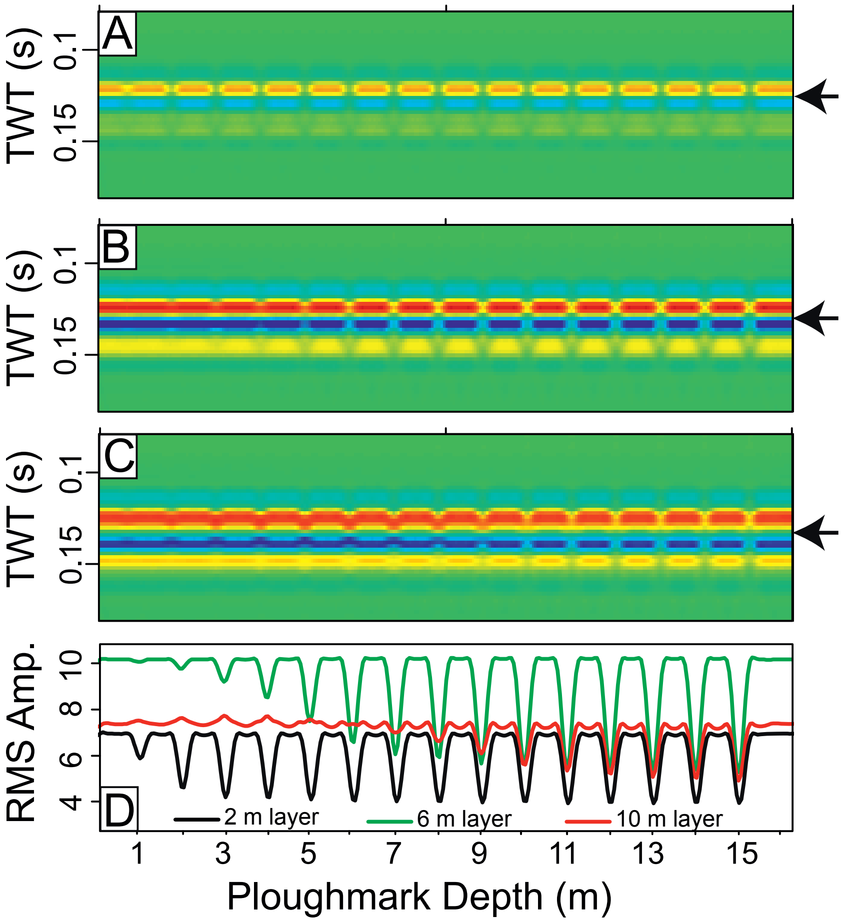

Figure A.16: (A), (B) and (c) are the migrated and interpolated synthetic seismic sections from thin sand layers that have 15 depressions in them ranging from 1 to 15 m. The widths of the depressions are all 50 m. The thickness of the sand layer is 2 m in (A), 6 m in (B) and 10 m in (C). The same color map is used in (A), (B) and (C). RMS amplitudes were extracted in a 18 ms window centered on the time indicated by the black arrows and are shown in (D).

A.5 Results and Interpretation

A.5.1 Regional stratigraphy

The Mid-Miocene Unconformity (MMU) is a high amplitude reflection in most of the North Sea. The overlying sediments of late Miocene and Pliocene are downlapping on the MMU reflection. The MMU horizon is the blue marker in Figure A.2. The Base Naust equivalent horizon is not a high amplitude or clear reflection in the data set, but can be inferred from the downlapping of the latest Pliocene and early Pleistocene prograding delta sediments overlying this horizon, see orange marker in Figure A.2. The Upper Regional Unconformity equivalent is difficult to identify in the Central North Sea because the sediments above the URU are conformable with the URU. Our pick of the URU horizon is extrapolated from Figure 4 in Anell et al. (2011) and is the purple marker Figure A.2. We are not very confident in our pick of the URU. The horizon called Gas Level 1 is a high amplitude horizon in our data set and is the red marker in Figure A.2.

In the regional profile in Figure A.2, we observe a vertical dim zone (indicated by arrow A) where the crossing horizons appear distorted. This zone cuts through the MMU and the Base Naust equivalent horizons, and appears to terminate above or below the Gas Level 1 horizon. We also observe anomalously high amplitude horizons, indicated with Arrow B, that extend up to 5 km away from this distorted vertical feature. We interpret this vertical distorted feature as a gas chimney, and the high amplitude anomalies extending out of this chimney as gas accumulations. We identify horizons that have higher amplitude than the surroundings in close vicinity of the top of the interpreted gas chimney. These horizons are brighter on the up-dip side (Northeast) of the gas chimney and we suggest that these are permeable sand layers that act as a migration route for gas. Possible entry points to the two horizons are indicated with Arrow C, and white arrows are positioned directly below these horizons in Figure A.2. We also observe over-deepened structures interpreted as tunnel valleys (arrow E in Figure A.2).

A.5.2 Iceberg ploughmarks

From the TWT map, in Figure A.4, we find that Gas Level 1 has an average dip of 0.3° towards West-Southwest, assuming an average velocity of 1900 m/s down to this horizon. Gas Level 2 and 3 have average dips of 0.2° in the same direction. The strike of the dips are 10°Northwest. An overburden velocity effect referred to as a pull-up can be observed in the TWT map in Figure A.4A. This pull-up is associated with high velocity tunnel valley infill in overlying early Quaternary sediments.

By studying the amplitude attribute maps in Figure A.5, A.6 and A.7 we observe low amplitude linear to curve-linear features in a more high amplitude background. Some of the features exhibit a very predictive nature, while others have abrupt changes. Loops and cross-cuttings are also observed. These features exhibit the same appearance as iceberg ploughmarks that are observed at the modern high latitude shelves. These features are therefore interpreted to be buried iceberg ploughmarks. The interpretation of iceberg ploughmarks and the directional analysis (Figure A.9) show that the average trend of drifting icebergs was close to North-South for all three levels. However, we observe that the ploughmarks in Gas Level 2 can be described by two main trends, and that these trends are equally deviating away from the strike angle of the dip of the horizon with about 25°.

In the amplitude map from Gas Level 1 (Figure A.5), we observe a distribution of amplitudes that is highest around the Southernmost part of the white dashed box and then gradually decrease away. Dim lines can be seen across most of the map, but are more difficult to be interpreted or not visible in the westernmost part where the amplitudes are weak. The largest ploughmark is about 250 m wide and several individual ploughmarks have lengths that exceed 10 km (Figure A.5). The width of the ploughmark was measured between the high amplitudes, perpendicular to the dim line. This is shown in Figure A.5B.

The RMS amplitude map extracted from Gas Level 2 (in Figure A.6A) shows a different nature than Gas Level 1. We observe that the areas towards West and East are dim, and that there is a belt of high amplitudes in a trend that is close to the strike angle of the dip, and almost parallel to the line where the horizon truncates towards east (indicated by a dashed line and labeled "Truncation" in Figure A.6). This high amplitude belt stops towards West approximately at the dashed line labeled GWC in Figure A.6. High amplitude anomalies that are triangular in shape and positioned down-dip of cross-cutting dim curve-linear features are observed in the dimmer areas, West of the GWC line, and are indicated by arrows in Figure A.5A. We also observe high amplitude curve-linear events that occur in pairs, as seen in Figure A.6B, they have the same nature spatial nature as the ploughmarks that are interpreted from the dim linear features and are also interpreted as iceberg ploughmarks. The width of these high amplitude lines are up 60 m, when measuring between the low amplitude sides (opposite to Figure A.5B).

The RMS amplitudes from Gas Level 3 (Figure A.7) are in general lower than the amplitudes observed in Gas Level 1 and 2. The nature of the amplitudes in Gas Level 3 is similar to those seen in Gas Level 1 in the upper half of the map, and a nature that is more equal to the triangular shaped anomalies observed in Gas Level 2 are observed in the white box in Figure A.7.

A.5.3 Amplitude versus offset analysis

We observe that the data points from the low amplitude zone (blue dots) and from the high amplitude zone (red dots) plot in separate regions in the amplitude vs. angle plot in Figure A.11. The reflection amplitudes from the high amplitude zone is more negative at zero offset and have a steeper gradient (i.e changing more rapidly with angle) than in the data from the low amplirude zone. This type of response is referred to as a class III AVO response (Rutherford and Williams, 1989), which is a typical AVO response for unconsolidated gas-filled sands below harder shale. The scatter of data points observed in Figure A.11 is expected from real seismic data. Noise in the seismic data and small variations in geology and/or gas saturation at the different positions (CMPs) will cause this behavior. In the data set analyzed here we probably observe a combination of these effects.

The modeled AVO responses for the simple model described in Section A.4.4 are shown for different gas saturations and types of saturation in Figure A.11. The modeled response for 100 % water saturated rock fit the data from the presumed water filled zone, which is expected because we normalized the data to the presumed water filled zone. However, the data is only normalized using a scalar and we still observe that the trend of the data fit the modeled AVO response very good. Modeling with 100 % gas in the pores result in an AVO response that do not to fit the data points. We find that AVO Modeling with 12 % uniform saturation or 70 % patchy gas saturation gave best fit with the data from the high amplitude zone. The AVO analyses therefor indicate that the sand layer is partially saturated with gas where high amplitudes are observed, and that the saturation is somewhere in range from 12 % to 70% depending on how the gas is distributed in the sand layer, patchy, uniformly or a combination.

A.5.4 Time-lapse analysis

RMS amplitude maps from Gas Level 2 (Section A.4.3) are shown for both the 1991 and the 2005 3D seismic data sets in Figure A.12. The two maps are very similar in nature and the same dim linear to curve-linear crossing features can be recognized in both. We observe that the 2005 data set appears more smoothed and has less noise compared to the 1991 data set. The most obvious difference between the two maps is the new amplitude anomaly around the position of the 2/4-15 well, that is indicated with an arrow in Figure A.12C. We see that the triangle shaped anomaly appears brighter towards its easternmost margin and that it seems that the new high amplitude anomaly, around the 2/4-15 well, is stopping towards an interpreted iceberg ploughmark. This ploughmark is less visible in the 2005 data than the 1991 data, but can be inferred from the North-Northeast edge of the new high amplitude and from the dim line inside the triangular shaped anomaly, the interpreted ploughmarks are indicated by dashed white lines in Figure A.12 B and D. A new amplitude anomaly in a sand layer shows that the seismic velocity at this position in this layer has been lowered from 1991 to 2005, resulting in a higher reflection coefficient.

The time-shift analysis performed on the 2D high resolution line shows that the greatest time-shifts are located directly below the projection of the 2/4-14 well, see Figure A.13A. This time-shift is positioned below one of main recipients of gas from the 2/4-14 blow out positioned at 490 m below mean sea level, and has been studied previously (e.g. Lie and Larsen, 1991; Langseth and Landrø, 2012). This gas filled sand is indicated by Arrow D in Figure A.2. A larger time-shift can be observed below the 2/4-15 well in the period from 1988 to 2009 compared to the period 1988 to 1990. This implies that there has been a reduction in the velocity in the overlying sediments between 1990 and 2009. The observed time-shifts below the 2/4-15 well are up to 3 ms.

The time-shift below 2/4-15 suggest that there is a reduction in the velocity above Gas Level 1 and the new amplitude anomaly observed in Gas Level 2 shows that the velocity of the sand in Gas Level 2 has been reduced and the reflection strength has increased because of this. An interpretation that explain both of these observations is that gas from the 2/4-14 blowout has migrated up along the 2/4-15 well and entered Gas Level 2. However, if we attribute the maximum observed time-shift of 3 ms to a change in saturation in the 6 m thick sand layer, it implies a reduction of the velocity in the order of 900 m/s. A more sound interpretation is that gas from the 2/4-14 blowout has saturated thin sand layers and/or damaged formation around the 15 well in addition to charging Gas Level 2 with gas. Based on the data available, this fluid flow must have taken place between 1991 and 2005.

A.5.5 Seismic response of thin sand layer

The reflection response from a thin sand layer depends on its thickness and the frequency content of the seismic data. Figure A.15 shows that when the thickness of the sand layer is between 3.6 m and 16.4 m, its tuning amplitude A_T will be greater than the amplitude of a resolved top or base reflection, A_R, when using a 45 Hz Ricker wavelet. The tuning is independent of the fluid fill, but the amplitude will be proportional to the reflections coefficient. The reflection coefficient for the gas saturated case is 3.8 times as strong as for the water saturated case, and Figure A.15D shows that the response from gas filled sand layer, if it is thicker than 2 m, will be higher than the response from a water filled layer at maximum tuning thickness. Maximum tuning thickness for a Ricker wavelet with peak frequency $f_p = 45$ Hz occurs at 8.2 m. In Figure A.14 we observe that to the left of the high amplitude anomaly (indicated with arrows) we are able to continue interpret the high amplitude reflector, in both the data sets, where it dims to the left. This line very close to the 2/4-16 well where the sand layer is 6 m thick. Since this horizon can be interpreted where it is water filled, our tuning analysis suggest that we should be able to interpret, at least, a 2 m thick gas filled sand layer as well.

Modeling of depressions in thin sand layers show that iceberg ploughmarks that are 50 m wide can be visible in layers as thin as 2 m (Figure A.16A), using the method of extracting RMS amplitudes. When the sand layer is 6 m thick, its total response has a high amplitude, and the depressions can be spotted as dim zones if the ploughmark is deeper than 3 m and easily detected if the depth exceeds the layer thickness (Figure A.16B). Figure A.16C) shows that the detectability of iceberg ploughmarks will be reduced when the thickness of the layer is higher than maximum tuning thickness. However, at this thickness we start to see the depressions of the ploughmarks when they are deeper than 1 m.

The RMS amplitudes shown in Figure A.16D shows that the amplitude of the seismic signal at the position of iceberg ploughmarks are in general lower than the amplitude in surrounding, unaffected layer. However, by studying the RMS amplitudes extracted from the the 10 m thick sand layer, we observe two things: When the depression is less than 4 m deep, there is an increase in amplitude and when the depression is deeper than 6 m there is an increase in amplitude on the edges of the depressions. These two observations can be explained by tuning effects. The 10 m thick layer is thicker than the maximum tuning thickness, and whenever a depression in the layer makes the total thickness go toward maximum tuning, its amplitude will increase.

A.6 Discussion

There may be several explanations for high amplitude horizons in a seismic section. Large contrasts in lithology or fluid fill between sedimentary layers will result in a high reflection coefficient and correspondingly bright reflectors in a stacked seismic image. Examples of this can for example be sediments on bedrock, silisiclastic sediments on salt or hard carbonates, or sand/shale on coal. In this study, we present results that give good indications that the observed high amplitude horizons in the early Pleistocene sediments studied in this paper are due to gas accumulations in thin sand layers. AVO analyses show a clear separation between the data from the low amplitude and high amplitude zones (Box 1 and 2 in Figure A.10), and the AVO response from the high amplitude zone is a typical response from a gas saturated sand layer (Rutherford and Williams, 1989; Shuey, 1985; Avseth et al., 2005). Furthermore, time-lapse analysis indicate that gas from the 2/4-14 blowout has been flowing into the sands of Gas Level 2 some time in the interval from 1991 to 2005 (Figure A.12). In addition to showing that gas from the 2/4-14 blow out has entered a new sand layer, it gives us a very good indication of how gas or hydrocarbons in Gas Level 2 appears in seismic. The fact that the new gas accumulation exhibits the same nature as the surrounding anomalies, strengthens our interpretation that the observed high amplitude anomalies in the studied interval are related to shallow gas.

The seismic modeling show that iceberg ploughmarks should be detectable in seismic data as dim features, and that ploughmarks should be observable in sand layers as thin as 2m in the 3D data sets used here. A factor that influence the ability to detect the ploughmarks is the depth of the ploughmark. If the depth of ploughmark exceeds the thickness of the sand layer it is positioned in, it will be detectable in RMS amplitude maps. The modeling shows that when the layer is thicker than the depth of the ploughmark its detectability is reduced compared to the latter case (Figure A.16). The noise level in the seismic data set will also have an impact on the detectability of iceberg ploughmarks. We can not detect variations that are smaller than the noise level. However, by extracting RMS values in a window we do a form of stacking that will enhance coherent signal and reduce non-coherent noise. This will increase the differences between high and low amplitude zones in the horizons under investigation and therefore the detectability of iceberg ploughmarks.

The triangular shaped anomalies observed in Gas Level 2 (Figure A.6) have earlier been interpreted as a result of relict ploughmarks acting as a trapping mechanism for shallow gas (Haavik and Landrø, 2013). This trap is the result of icebergs that have ploughed down in a sandy sea floor, followed by deposition of finer sediments that can act as a seal, or that the icebergs have ploughed down in sand that lies beneath shale. To form a trap, two of the ploughmarks must cross each other or one ploughmark must be part of an ellipse or a semicircle (Figure A.17). The sandy layer must, at least, locally, have a dip to generate volume where gas can be trapped. Furthermore, we think think that the angle between the trend of the iceberg ploughmarks and the strike of the dipping layer should be close, but not equal, to give the traps a large storage potential. If the trend of the ploughmarks are close to perpendicular to the strike of the dip the storage potential will be lower, see Figure A.17. The parallel high amplitude lines, shown in Figure A.6B, must have a different explanation. The modeling suggest that an increase in amplitude will occur when an iceberg ploughmark decreases the total thickness of a layer into tuning thickness (Figure A.16D), but this increase appears to be in the order of a few percent and cannot explain the observations. The parallel high amplitude lines are positioned in a low amplitude background area and the RMS amplitude from these features are ranging from 2 to 5 times as high as the background amplitudes. This suggests that the surroundings are water filled, while the high amplitude lines are gas filled. An explanation for this can be that the ploughmarks has berms that are high enough to trap gas and wide enough to be observed. In that case, the width of the berms can be over 60 m wide. This explains why the lines are parallel too; that berms are positioned on both sides of the depression. Woodworth-Lynas et al. (1991) reported that the crests of modern iceberg ploughmarks can reach up to 6 m above the seafloor.

The reason why we see this sort of trap in Gas Level 2 is probably a combination of several factors. The ploughmarks observed in this layer have two main directional trends and these trends have the same small deviation from the strike of the dip, giving the traps a good storage potential. The gamma ray response from the layer corresponding to Gas Level 2 is low compared to that of Gas Level 1 and 3 (Fig. A.10C). This is indicating that this sand layer is cleaner than the other layers. Clean and poorly consolidated sandstones are usually correlated with high permeability and porosity (Nelson, 1994), and this means that the sands of Gas Level 2 may act as an effective migration route for the gas. The gas traps will appear very strong and stand out from the surroundings if less gas is trapped in heterogeneities inside the sand layer.

Our interpretation is that the sand layer of Gas Level 2 is pinching out towards East and form a reservoir that is filled with gas. We interpret the GWC line in Figure A.6 to be the approximate gas-water contact. When gas has entered the sand layer of Gas Level 2, it has migrated up-dip towards Northeast. Some of the gas gets trapped in the smaller triangular shaped anomalies discussed above, and the rest is filling the stratigraphic trap. This shallow gas reservoir appears to extend out of the 3D data set available for this study, at least to the North. Figure A.18A shows a seismic line running perpendicular to the belt of high amplitudes and also across one of the triangular shaped anomalies, and the reflector of Gas Level 2 is highlighted. A schematic model for how the gas is trapped in Gas Level 2 is shown in Figure A.18B and synthetic seismic of this model is shown in Figure A.18C.

The regional seismic profile in Figure A.2 indicates that the shallow gas observed in Gas Level 1, Gas Level 2 and Gas Level 3 has been sourced from deeper strata, with the exception of the gas from the 2/4-14 blowout, and therefore has thermogenic origin. Vertical gas migration can be inferred from the interpreted gas chimney and we think that horizontal migration occurred through the observed high amplitude shallow sandy layers (see Figure A.2). However, we do not exclude the possibility that parts of the gas have biogenic origin.

We have not discussed the possibility that the sand layers studied here are filled with oil.

These sand layers are very thin and an oil response might not been detected by well logs. The belt of high amplitudes in Gas Level 2 has an area over 570 km^2 and appears to continue further out of the data set. The conceptual model in Figure A.18 may be a new, far-fetched, Quaternary exploration play in the Central North Sea.

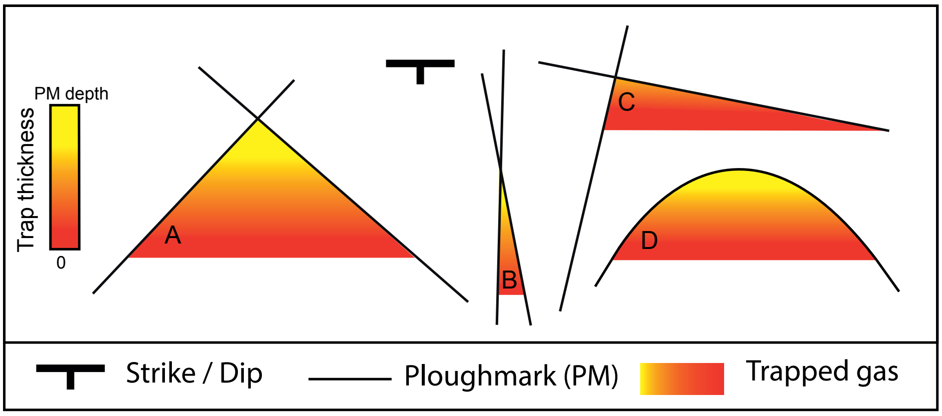

Figure A.17: This figure shows possible traps generated by iceberg ploughmarks seen from above. The strike (East-West) and dip (South) of the layer that the iceberg ploughmarks are situated in is indicated. The storage capacity of the traps created by the iceberg ploughmarks are related to the trend or trends of the ploughmarks relative to the strike of the dipping layer. When the angle between the trends of the ploughmarks and the strike angle are low, or relatively low as in (A) more gas can be trapped than if the angle is high as in (B). If the ploughmarks have trends that are very different compared to the strike angle, as in (C), it will lower the storage capacity compared to (A). Another possible trap can be wavy ploughmarks as in (D). The trap thickness or the height of the column of fluid it can trap is indicated by the color bar. The maximum height this type of trap can have is the depth of the ploughmark at its highest point (e.g. where the ploughmarks cross).

The iceberg ploughmarks that have been identified in this paper are positioned between roughly 470 m to 700 m depth below mean sea level and positioned above the interpreted Base Naust equivalent horizon (Figure A.2), and the directional trend of the iceberg ploughmarks in this data set is consistent with the observations in Stuart and Huuse (2012) and Dowdeswell and Ottesen (2013). In the Central North Sea the Base Naust equivalent horizon is about 2.7 Ma and have been correlated to the 2/4-C-11 well at approximately 700 m depth in Ottesen et al. (2014) and 980 m in Eidvin et al. (1999) and (Eidvin et al., 2013). The 2/4-C-11 well is positioned 12 km South of the 2/4-14 well and its position is indicated in Figure A.4 right outside the 3D seismic data set available for this study. Our interpretation of the Base Naust equivalent horizon at the 2/4-14 well gives a depth below mean sea level of roughly 950 m, when using an average velocity of 1900 m/s down to this horizon. This is in good correspondence with the depth from Eidvin et al. (1999). However, there is an ambiguity in the depth of the Base Naust equivalent in the this study and Eidvin et al. (1999) and to the one in Dowdeswell and Ottesen (2013) and Ottesen

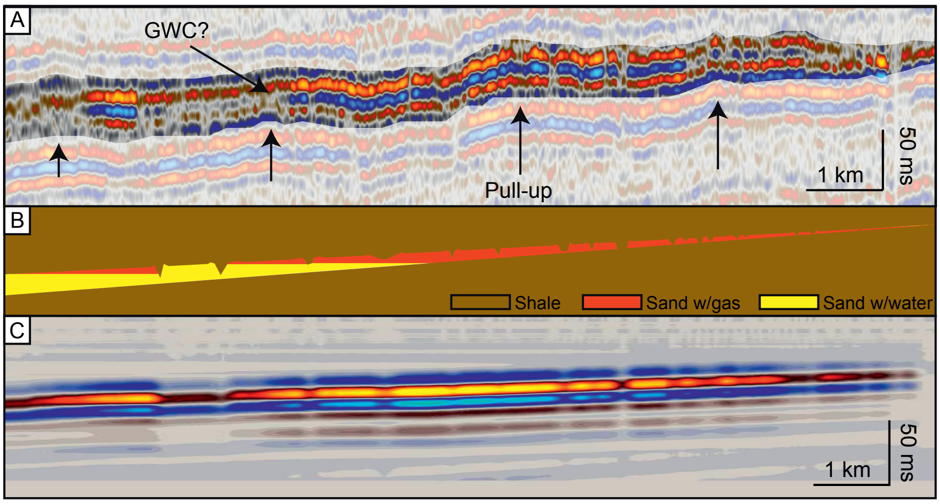

Figure A.18: (A) A random line from the SG9111 3D data set which position is indicated in Figure A.6. The line is running from Southwest towards Northeast from right to left. The reflection and close surroundings of Gas Level 2 is highlighted. The vertical arrows are indicating pull-ups in the seismic. The pull-ups are overburden velocity effects and make the apparent topography of the geology differ from its real. A possible gas to water contact is indicated with arrow GWC. (B) A conceptual model for Gas Level 2. A sand layer pinching out in surrounding shales and saturated with gas in two different traps; ploughmark trap and a stratigraphic trap. The sand layer is 7 m at its thickest (to left) and have several depressions that represent iceberg ploughmarks. (C) Synthetic migrated seismic section of the model in (B). The modeling procedure is explained in Section A.4.6.

et al. (2014). This ambiguity makes it difficult to date the iceberg ploughmarks identified here. By using the depth of the Base Naust equivalent horizon from Figure 4 in Ottesen et al. (2014) we find that the ploughmarks identified in this study can be as old as 2.7 Ma. If we compare the horizon that corresponding to Gas Level 1 in Figure A.2 to earlier interpretations from this area, Figure 6 in Huuse (2002) and Figure 4 in Michelsen (2001), we find that the ploughmarks should be close to 1.8 Ma based on their interpretation. In comparison, about 200 km further to the South, Kuhlmann and Wong (2008) described an interval heavily influenced by iceberg ploughing which they dated to be around 1.9 Ma. A more detailed stratigraphic study is needed to date the interval properly.

Eidvin et al. (1999) found small quantities of ice-rafted material in the cores and cuttings in the early Pleistocene section of the 2/4-C-11 well compared to sediments at comparable depths in the northern North Sea. This was interpreted as if this area was less influenced by icebergs than the areas in the Northern North Sea. In contrast to findings of Eidvin et al. (1999), (Dowdeswell and Ottesen, 2013) and this study show that the early Pleistocene sediments in the Central North Sea are heavily influenced by icebergs.

The sediments of the Naust Formation in the Central North Sea are rather fine grained, probably distal deposits from fluvial and glacio-fluivial sources in South and Southeast (Ottesen et al., 2014), and the ploughmarks observed in the Central North Sea are probably formed in relatively deep water (Dowdeswell and Ottesen, 2013). In this study we find multiple thin sand layers in the Naust formation, and that these layers are embedded in finer sediments that are sealing. These sands have probably been deposited in deep water, and we speculate that sediment failure in the delta fronts of the fluvial systems to the South and Southeast are the sources of these sands. The sand layers may have been covered in finer sediments prior to the generation of the ploughmarks, as long as the ploughmarks are deep enough to penetrate into the sands we should be able to observe them in seismic. The three different layers may therefore be a result of periods with very high sedimentation rates causing the delta front instabilities (Adams and Roberts, 1993; Benvenuti et al., 2012).

The method for detecting iceberg ploughmarks using time-slices through the seismic data have shown great results (e.g. Dowdeswell and Ottesen, 2013). However, a shortcoming of that method is that it is not able to correctly resemble a palaeo-seafloor, especially if the layers under investigation have topography or are affected by overburden velocity effects (e.g. pull-ups as seen in Figure A.4). The choice of method for detecting iceberg ploughmarks should be based on the topography in the area. It is clear, from the comparison made in Figure A.8, that the method of time-slicing is able to detect buried ploughmarks in this area. However, by manually picking horizons, we assure that the interpreted iceberg ploughmarks are roughly of the same age. We are also able to interpret more iceberg ploughmarks because of this.

We have shown that conventional picking of seismic reflectors followed by amplitude attribute analysis can give beautiful images where iceberg ploughmarks can easily be detected. The method works very well where gas is illuminating shallow sand layers giving locally high amplitude horizons in the seismic. This method is extremely fast using auto tracking algorithms that are available in most of the seismic interpretation softwares used today. Using the described method on a larger data set may give insight into the spatial and temporal distribution of iceberg ploughmarks through a larger sediment record. This may in provide further insight into glaciations of the early Pleistocene.

A.7 Conclusions

- Sandy layers probably deposited in deep water during early Pleistocene are visible as high amplitude horizons in seismic data. The high amplitudes are associated with gas in these layers, which is supported by geophysical analysis and seismic interpretation.
- By picking these high amplitude sandy layers in 3D seismic data and performing amplitude attribute analysis we obtain maps where iceberg ploughmarks can easily

be detected as dim linear to curve-linear features, showing that the sandy layers was deposited under glacial influence.

- For the three early Pleistocene sand layers studied here we find that the iceberg ploughmarks have a principal direction in a close to a North-South trend. The age of these ploughmarks are probably around 1.8 Ma.
- AVO-analysis confirms that high amplitude anomalies are most likely caused by the presence of shallow gas.
- The shallow gas present in the sand layers under investigation are most likely of thermogenic origin, and a result of migration from deeper layers.
- Two types of hydrocarbon traps are observed in this data set. One of the traps is a stratigraphic pinch out. The other trap is a result of buried iceberg ploughmarks, and is to our knowledge, the only place where this type of trap has been documented.
- Gas from the 2/4-14 blowout in 1989 has migrated further into a new sand layer. Analysis indicate that this migration happened between 1991 and 2005.

Acknowledgements

We would like to thank Kjersti Eidissen for processing the AVO data used in this study. We acknowledge the Norwegian Research Council for financial support to the Rose project at NTNU. We acknowledge the sponsors of the Long term seismic monitoring (LOSEM) project for financial support: BayernGas, BP, CGG, Det Norske, Lundin Norway, Petrobras, Statoil and Total. We acknowledge Lundin Norway AS for financial support for Kjetil E. Haavik's PhD Project. We also acknowledge Dag Ottesen for valuable advice and feedback. Furthermore, the reviewers, Helge Løseth and Margaret A. Stewart, are acknowledged for useful comments and suggestions that improved this manuscript.

A.8 Appendix: Amplitude versus offset modeling

The equations used in AVO-modeling are presented in this Appendix.

A.8.1 Angle dependent reflection coefficients

Amplitude versus offset analysis is a method where angle dependent reflection-coefficients are used to make inferences about the rock properties, mineralogy and fluid content. Reflection coefficients that vary with angle is an effect of the energy distribution over a boundary. By imposing the boundary conditions that two layers have welded contact, Zöppritz (1919) derived the equations for how the energy from an incident wave will be distributed in reflected, transmitted and converted waves. A widely used approximation to the Zöppritz equations for P-wave reflection was given by Shuey (1985) as:

$$R(\theta) = R(0) + G\sin^2(\theta) + F\tan^2(\theta)\sin^2(\theta) \tag{A.3}$$

where:

$$R(0) = \frac{1}{2}\left(\frac{\Delta\alpha}{\overline{\alpha}} + \frac{\Delta\rho}{\overline{\rho}}\right) \tag{A.4}$$

$$G = \frac{1}{2}\frac{\Delta\alpha}{\overline{\alpha}} - \frac{2\overline{\beta}^2}{\overline{\alpha}^2}\left(\frac{2\Delta\beta}{\overline{\beta}} + \frac{\Delta\rho}{\overline{\rho}}\right) \tag{A.5}$$

$$F = \frac{1}{2}\frac{\Delta\alpha}{\overline{\alpha}} \tag{A.6}$$

and $\overline{x} = (x_1 + x_2)/2$, $\Delta x = x_2 - x_1$ for $x_i = \alpha_i$, β_i, ρ_i where subscript i indicate the layer number. We see that the P-wave velocity α, S-wave velocity β and density ρ for both layers are needed to model the angle dependent reflection coefficient given in Eq.A.3.

A.8.2 Gassman fluid substitution

Fluid substitution is done, using the equations given by Gassman (1951), to predict the effective elastic muduli, or velocities, of a porous and permeable rock saturated with different fluids. In order to perform fluid substitution we need to know the S-wave velocity β, P-wave velocity α, density ρ,porosity ϕ and bulk modulus of the solid K_s and the fluid saturating the pores K_{f_1}. Furthermore, the Bulk modulus and density of the fluid we would like to saturate the rock with are required. The procedure is given by e.g Avseth et al. (2005):

1. Find the effective bulk and shear moduli from velocities and density for a rock saturated with a fluid 1, here indicated by subscript 1:

$$K_1 = \rho_1\left(\alpha_1^2 + \frac{4}{3}\beta_1^2\right) \tag{A.7}$$

$$\mu_1 = \rho_1\beta_1^2 \tag{A.8}$$

2. Use the equations from Gassman (1951) to find the bulk modulus to the rock saturated with fluid 2, K_2:

$$\begin{aligned}\frac{K_2}{K_s - K_2} - \frac{K_{f_2}}{\phi\,(K_s - K_{f_2})} &= \\ &\frac{K_1}{K_s - K_1} - \frac{K_{f_1}}{\phi\,(K_s - K_{f_1})}\end{aligned} \tag{A.9}$$

3. According to Biot theory the shear modulus μ remain unchanged.

$$\mu_2 = \mu_1 \tag{A.10}$$

4. Calculate the bulk density of the rock saturated with fluid 2.

$$\rho_2 = \rho_1 + \phi\left(\rho_{f_2} - \rho_{f_1}\right) \tag{A.11}$$

5. Calculate the velocities for the rock saturated with fluid 2.

$$\alpha_2 = \sqrt{\frac{K_2 + \frac{4}{3}\mu_2}{\rho_2}} \tag{A.12}$$

$$\beta_2 = \sqrt{\frac{\mu_2}{\rho_2}} \tag{A.13}$$

These velocities can then be used in e.g. AVO-modeling.

A.8.3 Bulk modulus and density of fluid mixtures

Often the gas or oil saturation in rocks are not 100 %. To model the properties of fluids that consist of more than one phase we use averages. For gas solved in water it is often assumed that the two phases experience the same pressure when a seismic wave propagate through it and the effective bulk modulus can be given by the "iso-stress" or Reuss average (Avseth et al., 2005):

$$K_{f_m}^R = \left(\frac{S_{f_1}}{K_{f_1}} + \frac{S_{f_2}}{K_{f_2}}\right)^{-1} \tag{A.14}$$

Where K_{f_m}, K_{f_1} and K_{f_2} are the bulk modulus of the mixture of fluids given by Reuss average, the bulk modulus of fluid 1 and the bulk modulus of fluid 2, respectively. S_{f_1} and S_{f_2} are the amount of fluid 1 and fluid two each fluid and $S_{f_1}+S_{f_2} = 1$. The average given in Eq. A.14 is often used for gas solved in water, i.e uniformly mixed fluids. However, the geometrical distribution of the gas may be quite different in nature. If the gas is distributed as larger patches in a background of water then another average is often used, the Voigt average:

$$K_{f_m}^V = S_{f_1}K_{f_1} + S_{f_2}K_{f_2} \tag{A.15}$$

The average given in Eq. A.15 is used when the patches of gas are on a scale that is larger than a critical scale (Mavko and Mukerji, 1998). This critical scale is dependent on the permeability of the rock, bulk modulus and viscosity of the fluid, and the frequency of the seismic (wavelength). Mavko and Mukerji (1998) find that the use of Eq.A.15 in fluid substitution give good results for patchy saturation.

The density of the fluid mixture is given for both uniform and patchy saturation mixtures as:

$$\rho_{f_m} = S_{f_1}\rho_{f_1} + S_{f_2}\rho_{f_2} \tag{A.16}$$

The density ρ_{f_m} and bulk moduli $K^R_{f_m}$ or $K^V_{f_m}$ are used in fluid substitution depending on the type of saturation, i.e the mixture of fluids. When free gas is present in the system, patchy saturation is likely to occur (Sengupta, 2000).

A.8.4 Empirical relationships for S-wave velocity and density

Often we do not have all the parameters that are required for AVO modeling. We then rely on empirical relations that can give us estimates of the unknown parameters through the parameters we know. To get an estimate of S-wave velocity β in both layers, we used the empirical relationship given by Han (1986) which uses P-wave velocity α as input:

$$\beta = 0.793\alpha - 786.8 \tag{A.17}$$

This empirical relationship is found for clean unconsolidated sandstones at 40 MPa confining pressure.

The density for a brine saturated poorly consolidated sandstone is here estimated by the use of the density of Quartz ρ_Q and brine ρ_w together with an assumed porosity ϕ.

$$\rho = \rho_Q\,(1 - \phi) + \rho_w\phi. \tag{A.18}$$

Another way of estimating the density is through the empirical relationship from Gardner et al. (1974), who found that the density can be estimated using the P-wave velocity α as:

$$\rho = 0.23\alpha^{0.25}. \tag{A.19}$$

Appendix B

Other work performed during this PhD

This Appendix contains a list over other scientific work performed during this 3-year period, that was found to not directly fit into this thesis.

- **Conference abstract** Using geophone components to obtain ultralow frequency seismic signals at long offsets. *Presented by Martin Landrø at the 83rd SEG meeting.* See Landrø et al. (2014).
- **Conference abstract** Analysis of Shallow Gas in the Ekofisk Area. *Presented at the 75th EAGE Meeting by Kjetil E. Haavik*. see Haavik et al. (2014).
- **Conference abstract** Monitoring changes in the overburden - some observations from using various 2D and 3D seismic time lapse data sets. *Presentet by Martin Landrø at the Time-lapse workshop at the 77th EAGE meeting*. See Haavik and Landrø (2015b).
- **Conference abstract** Correcting air gun source signatures for variation in sea water temperature *This was presented at the 3rd EAGE workshop on Permanent Reservoir Monitoring by Kjetil E. Haavik.* See Haavik and Landrø (2015a)
- **Conference abstract** Discriminating between oil and gas exploiting the amplitude dimming a the rim. *This was presented at the SEG annual meeting by Kjetil E. Haavik.* See Landrø and Haavik (2015).

References

Abma, R., D. Howe, M. Foster, M. T. Imtiaz Ahme and, Q. Zhang, A. Arogunmati, and G. Alexander, 2015, Independent simultaneous source acquisition and processing: Geophysics, **80**, WD37–WD44.

Adams, C. E. J., and H. H. Roberts, 1993, A model of the effects of sedimentation rate on the stability of Mississippi delta sediments: Geo-Marine Letters, **13**, 17–23.

Agudo, O. C., P. Caprioli, and D.-J. van Manen, 2016, A spatially compact source designature filter: Geophysics, **81**, V125–V139.

Aki, K., and P. G. Richards, 2002, Quantitative seismology, 2 ed.: Universeity Science Books.

Alford, R. M., K. R. Kelly, and D. M. Boore, 1974, Accuracy of finfite-difference modeling of the acoustic wave equation: Geophysics, **39**, 834–842.

Alterman, Z., and F. C. Karal, 1968, Propagation of elastic waves in layered media by finite difference methods: Bulletin of the Seismological Society of America, **58**, 1.

Amundsen, L., 1993, Wavenumber–based filtering of marine point–source data: Geophysics, **58**, 1335–1348.

Amundsen, L., and J. O. A. Robertsson, 2014, Wave equation processing using finite–difference propagators, part 1: Wavefield dissection and imaging of marine multicomponent seismic data: Geophysics, **79**, T287–T300.

Andersson, F., K. Eggenberger, D. van Manen, J. O. A. Robertsson, and L. Amundsen, 2016, Seismic apparition dealiasing using directionality regularization: SEG Technical Program Expanded Abstracts 2016.

Andorsen, K., and M. Landrø, 2000, Source signature variations versus repeatability - A study based on zero-offset VSP experiment: Journal of Seismic Exploration, **9**, 61–71.

Anell, I., H. Thybo, and E. Rasmussen, 2011, A synthesis of Cenozoic sedimentation in the North Sea: Basin Research, **23**, 1–26.

Arntsen, B., and J. M. Carcione, 2000, A new insigth into the reciprocity principle: Geophysics, **65**, 1604–1612.

Arntsen, B., L. Wensaas, H. Løseth, and C. Hermanrud, 2007, Seismic modeling of gas chimneys: Geophysics, **72**, SM251–SM259.

Avseth, P., T. Mukerji, and G. Mavko, 2005, Quantitative Seismic Interpretation: Cambridge University Press.

Baeten, G., J. Fokkema, and A. Ziolkowksi, 1988, The marine vibrator source: First Break, **6**, 285–294.

Barker, D., and M. Landrø, 2012, Simple expression for the bubble-time period of two clustered air guns: Geophysics, **77**, A1–A3.

———, 2013, Estimation of bubble time period for air-gun clusters using potential isosurfaces: Geophysics, **78**, P1–P7.

Beasley, C. C., 2008, A new look at marine simultaneous sources: Leading Edge, **27**, 914–917.

Benvenuti, K., H. Kombrink, J. H. ten Veen, D. K. Munsterman, F. Bardi, and M. Benvenuti, 2012, Late Cenozoic shelf delta development and Mass Transport Depositsin the Dutch offshore area – results of 3D seismic interpretation: Netherlands Journal of Geosciences, **91**, 591–608.

Berkhout, A. J., 2008, Changing the mindset in seismic data acquisition: Leading Edge, **27**, 924–938.

———, 2012, Blended acquisition with dispersed source arrays: Geophysics, **77**, A19–WA23.

Berni, A. J., 1982, Marine seismic system.: U.S. Patent,, **Patent No.: US 4520467**.

Bijlsma, S., 1981, Fluvial sedimentation from the Fennoscandian Area into the North-West European Basin during the Late Cenozoic: Geol. Mijnb., **60**, 337–345.

Bjørlykke, K., 2011, Petroleum Geoscience: From Sedimentary Environments to Rock Physics: Springer Vorlag.

Blake, J. R., and D. C. Gibson, 1981, Growth and collapse of a vapour cavity near a free surface: Journal of Fluid Mechanics, **111**, 123–140.

Brink, M., and M. Svendsen, 1987, Marine seismic exploration using vertical receiver arrays: A means for reduction of weather downtime: 57th Annual International Meeting, SEG, Expanded Abstracts, 184–187.

Broggini, F., and J. O. A. Robertsson, 2014, FD injection utilizing the wavefields generated by marchenko redatuming: A target-oriented approach: SEG Technical Program Expanded Abstracts 2014, 3297–3302.

Brown, A. R., 1999, Interpretation of three–dimensional seismic data: AAPG, **42**.

Buland, A., and H. Omre, 2003, Bayesian linearized avo inversion: Geophysics, **68**, 185–198.

Bunks, C., F. M. Saleck, S. Zaleski, and G. Chavent, 1995, Multiscale seismic waveform inversion: Geophysics, **60**, 1457–1473.

Cambois, G., A. Long, G. Parkes, T. Lundsten, A. Mattsson, and E. Fromyr, 2009, Multi-level airgun array - a simple and effective way to enhance low frequencies in marine seismic: 71^{th} EAGE Conference and exhibition, S001.

Cameron, T. D. J., J. Bulat, and C. S. Mesdag, 1993, High resolution seismic profile through a late Cenozoic delta complex in the southern North Sea: Marine and Petroleum Geology, **10**, 591–599.

Cameron, T. D. J., M. S. Stoker, and D. Long, 1987, The history of Quaternary sedimentation in the UK sector of the North Sea: Journal of the Geological Society, **144**, 43–58.

Caporal, M., G. Blaquière, and A. J. Berkhout, 2015, Seismic acquisition with dispersed source arrays: first results: SEG Technical Program Expanded Abstracts 2015, 170–175.

Chahine, G. L., 1977, Interaction between an oscillating bubble and a free surface: Journal of Fluid Engineering, **99**, 709–716.

Chopra, S., and J. P. Castagna, 2014, Avo: Society of Exploration Geophysicists.

Clark, C. D., A. L. C. Hughes, S. L. Greenwood, C. Jordan, and H. Sejrup, 2012, Pattern and timing of retreat of the last British-Irish Ice Sheet: Quaternary Science Reviews, **44**, 112–146.

Cole, R. H., 1948, Underwater explosions: Princeton, Princeton Univ. Press.

Dablain, M. A., 1986, The application of high-order differencing to the scalar wave equation: Geophysics, **51**, 54–66.

Dalland, A., D. Worsley, and K. Ofstad, 1988, A lithostratigraphic scheme for the Mesozoic and Cenozoic succession offshore mid- and northern Norway: NPD Bull. No., **4**.

Davis, A. M., 1992, Shallow gas: an overview: Continental Shelf Research, **12**, 1077–1079.

Day, A., T. Klüver, W. Söllner, H. Tabti, and D. Carlson, 2013, Wavefield-separation methods for dual-sensor towed-streamer data: Geophysics, **78**, WA55–WA70.

Deegan, C. E., and J. B. C. Scull, 1977, A standard lithologic nomenclature for the Central and Northern North Sea: Institute of Geological Sciences Report 77/25, Norwegian Petroleum Directorate Bulletin, **1**, 33.

Dhelie, P. E., J. Lie, V. Danielsen, and A. Myklebostad, 2014, Broadband for everyone - increasing notch diversity using variable streamer profiles: 76^{th} EAGE Conference and exhibition, Tu ELI2 15.

D'Heur, M., 1987, "Albuskjell":Geology of Norwegian oil and gas fields North Sea: Graham and Trotman Ltd., Edited by: Anthony Mansell Spencer.

Dowdeswell, J. A., and C. F. Forsberg, 1992, The size and frequency of icebergs and bergy bits derived from tidewater glaciers in Kongsfjorden, northwest Spitsbergen: Polar Research, **11**, 81–91.

Dowdeswell, J. A., and D. Ottesen, 2013, Buried iceberg ploughmarks in the early Quaternary sediments of the central North Sea: A two-million year record of glacial influence from 3D seismic data: Marine Geology, **344**, 1–9.

Dowdeswell, J. A., H. Villinger, R. J. Whittington, and P. Marienfield, 1993, Iceberg scouring in Scoresby Sund on the East Greenland continental Shelf: Marine Geology, **111**, 37–53.

Dragoset, W. H., 1988, Marine vibrators and the doppler effect: Geophysics, **53**, 1388–1398.

———, 2000, Introduction to air guns and air-gun arrays: the Leading Edge, **19**, 892–897.

Egan, M., K. G. El-Kasseh, and N. Moldoveanu, 2007, Full deghosting of obc data with over/under source acquisition: 77th Annual International Meeting, SEG, Expanded Abstracts, 53–56.

Ehlers, J., 1990, Reconstructing the dynamics of the North-west European Pleistocene ice sheets: Quaternary Science Reviews, **9**, 71–83.

Ehlers, J., and P. L. Gibbard, 2008, Extent and chronology of Quaternary glaciation: Episodes, Geological Society of India, **31**, 211–218.

Eidvin, T., F. Riis, E. S. Rasmussen, and Y. Rundberg, 2013, Investigation of Oligocene to Lower Pliocene Deposits in the Nordic Area. : NPD Bull. No., **10**.

Eidvin, T., F. Riis, and Y. Rundberg, 1999, Upper Cainozoic stratigraphy in the Central North Sea (Ekofisk and Sleipner fields): Norsk Geologisk Tidsskrift, **79**, 97–128.

Ewing, W. M., 1957, Elastic waves in layered media: McGraw-Hill.

Floodgate, G. D., and A. G. Judd, 1992, The origin of shallow gas: Continental Shelf Research, **12**, 1145–1156.

Fokkema, J. T., and P. M. van den Berg, 1993, Seismic applications of acoustic reciprocity: Elsevier science publishers B.V.

Fossen, H., and R. Gabrielsen, 2005, Strukturgelogi: Fagbokforlaget.

Fu, Z., N. Du, H. Shen, P. Wang, and N. Chazalnoel, 2015, Source deghosting for synchronized multi-level source streamer data: 85nd Annual International Meeting, SEG, Expanded Abstracts, 4595–4599.

Futterman, W. I., 1962, Dispersive bode waves: Journal of Geophysical Research, **67**, 5279–5291.

Gallagher, J. W., and R. Heggland, 1994, Shallow gas evaluations based on conventional 3-D seismic data: 56^{th} EAGE Conference and Exhibition, **Vienna**.

Gardner, G. H. F., L. W. Gardner, and A. R. Gregory, 1974, Formation velocity and density – the diagnostic basics for stratigraphic traps: Geophysics, **39**, 770–780.

Gassman, F., 1951, Über die Elastizitat poroser Medien: Veirteljahrsschrift der Naturforschen den Gesellschaft in Zürich, **96**, 1–23.

Gatliff, R. W., P. C. Richards, K. Smith, C. C. Graham, M. McCormac, N. J. P. Smith, D. Long, T. D. J. Cameron, D. Evans, A. G. Stevenson, J. Bulat, and J. D. Ritchie, 1994, UK offshore regional report: The geology of the Central North Sea: (British Geological Survey).

Gibbard, P. L., 1988, The history of the great northwest European rivers during the past three million years: Journal of Quaternary Science, **318**, 559–602.

Gibbard, P. L., M. Head, M. J. C. Walker, and The subcommision on Quaternary Stratigraphy, 2010, Formal ratification of the Quaternary System Period and the Pleistocene Series Epoch with a base at 2.58 Ma: Philosophical Transactions of the Royal Society of London, **25**, 96–102.

Giles, B. F., 1968, Pneumatic acoustic energy source: Geophysical Prospecting, **16**, 21–53.

Giles, B. F., and R. C. Johnston, 1973, System approach to air-gun design: Geophysical Prospecting, **21**, 77–101.

Gilmore, F. R., 1952, The growth or collapse of a spherical bubble in a viscous compressible liquid: California Institute of Technology, Report, NO, **26**, 4.

Graham, A. G. C., L. Lonergan, and M. S. Stoker, 2007, Evidence for Late Pleistocene ice stream activity in the Witch Ground Basin, central North Sea, from 3D seismic reflection data: Quaternary Science Reviews, **26**, 627 – 643.

———, 2010, Depositional environments and chronology of Late Weichselian glaciation and deglaciation in the central North Sea: Boreas, **39**, 471 – 491.

Graham, A. G. C., M. S. Stoker, L. Lonergan, T. Bradwell, and M. A. Stewart, 2011, The Pleistocene glaciations of the North Sea Basin: In: Ehlers, J.; Gibbard, P.L.; Hughes, P.D., (eds.) Quaternary glaciations : extent and chronology : a closer look., **Developments in Quaternary Science, 15**, 261–278.

Granli, J. R., B. Arntsen, A. Sollid, and E. Hilde, 1999, Imaging through gas-filled sediments using marine shear-wave data: Geophysics, **64**, 668–677.

Greaves, R., and T. Fulp, 1987, Three–dimensional seismic monitoring of an enhanced oil recovery process: Geophysics, **52**, 1175–1187.

Haavik, K., and M. Landrø, 2013, Ice scours as trapping mechanism for shallow gas: 75^{th} EAGE Conference and Exhibition incorporating SPE EUROPEC, **London**.

Haavik, K. E., K. Eidissen, and M. Landrø, 2014, Analysis of shallow gas in the ekofisk area: 76^{th} EAGE Conference and exhibition, Tu G102 03.

Haavik, K. E., and M. Landrø, 2014, Iceberg ploughmarks illuminated by shallow gas in the Central North Sea: Quaternary Science Reviews, **103**, 34–50.

———, 2015a, Correcting air gun source signatures for variation in sea water temperature: Third EAGE Workshop on Permanent Reservoir Monitoring 2015, Tu C01.

———, 2015b, Monitoring changes in the overburden – some observations from using various 2d and 3d seismic time lapse data sets: 77^{th} EAGE Conference and exhibition - Workshop, WS02–A03.

———, 2015, Variable source depth acquisition for improved marine broadband seismic data: Geophysics, **80**, A69–A73.

———, 2016, Estimation of source signatures from air guns fired at various depths: A field test of the source scaling law: Geophysics, **81**, P13–P22.

Hager, E., 2016, Multi-source design and penta source case study from the NWS Australia: ASEG Technical Program Extended Abstracts, Accepted.

Halliday, D. F., 2013, Source-side deghosting: A comparison of approaches: SEG Technical Program Expanded Abstracts 2013, 67–71.

Hampson, D., and B. Russell, 1990, AVO inversion: Theory and Practice: SEG Technical Program Expanded Abstracts, 1456–1458.

Hampson, G., J. Stefani, and F. Herkenhoff, 2008, Acquisition using simultaneous sources: Leading Edge, **27**, 918–923.

Han, D.-H., 1986, Effects of porosity and clay content on acoustic properties of sandstones and unconsolidated sediments: PhD thesis, Stanford University.

Hardwick, A., H. Masoomzadeh, J. Gromotka, P. Cox, and R. Gilbert, 2014, Broadband processing in the Norwegian Barents Sea — Practical aspects of deghosting in a challenging marine environment: SEG Technical Program Expanded Abstracts 2014, 4223–4226.

Heggland, R., 1998, Gas seepage as an indicator of deeper prospective reservoirs. A study based on exploration 3D seismic data: Marine and Petroleum Geology, **15**, 1.

Hegna, S., and G. Parkes, 2011, The low frequency output of marine air-gun arrays: SEG Technical Program Expanded Abstracts 2013, 77–81.

Helgesen, J., and M. Landrø, 1993, Estimation of elastic parameters from AVO effects in the tau-p domain: Geophysical Prospecting, **41**, 341–366.

Herring, C., 1941, Theory of the pulsations of the gas bubble produced by an underwater explosion: New London, Conn. Columbia Univ., Div. of National Defense Research, OSRD report, 236.

Hicks, G. J., 2002, Arbitrary source and receiver positioning in finite-difference schemer using kaiseer windowed sic functions: Geophysics, **67**, 156–166.

Holberg, O., 1987, Computational aspects of the choice of operator and sampling interval for numerical differentiation in large-scale simulation of wave phenomena: Geophysical Prospecting, **35**, 629–655.

Hopperstad, J. F., R. Laws, and E. Kragh, 2008a, Fundamental principles of isotropic marine source design: 70th Annual International Conference and Exhibition, EAGE, Extended Abstracts, B025.

———, 2008b, Where is the center of a multidepth marine source array?: 78th Annual International Meeting, SEG, Expanded Abstracts, 40–44.

———, 2012, Hypercluster of airguns – more low frequencies for the same quantity of air: 74th Annual International Conference and Exhibition incorporating SPE EUROPEC, EAGE, Extended Abstracts, Z011.

Hopperstad, J. F., J. R. Synnevåg, and P. Vermeer, 2001, An azimuth-invariant source array: 71th Annual International Meeting, SEG, Expanded Abstracts.

Huuse, M., 2002, Cenozoic uplift and denundation of southern Norway: insights from the North Sea Basin: Geological Society, London, Special Publications, **196**, 209–233.

Huuse, M., H. Lykke-Andersen, and O. Michelsen, 2001, Cenozoic evolution of the eastern North Sea Basin – new evidence from high-resolution and conventional seismic data: Marine Geology, **177**, 243–269.

Ibrahim, A., and M. D. Sacchi, 1995, Simultaneous source separation using a robust radon transform: Geophysics, **79**, V1—-V11.

Ikelle, L. T., and L. Amundsen, 2005, Introduction to petroleum seismology: Society of Exploration Geophysicists.

Jansen, E., and J. Sjøholm, 1991, Reconstruction of glaciation over the past 6 Myr from ice-borne deposits in the Norwegian Sea: Nature, **349**, no. 6310, 600–603.

Johansen, S. E., E. Granberg, D. Mellere, B. Arntsen, and T. Olsen, 2007, Decoupling of seismic reflectors and stratigraphic timelines: A modeling study of Tertiary strata from Svalbard: Geophysics, **72**, SM273–SM280.

Johansen, S. E., S. Kibsgaard, A. Andresen, T. Henningsen, and J. R. Granli, 1994, Seismic Modeling of a Strongly Emergent Thrust Front, West Spitsbergen Fold Belt, Svalbard: AAPG Bulletin, **78**, 1018–1027.

Jordt, H., J. I. Faleide, K. Bjørlykke, and M. T. Ibrahim, 1995, Cenozoic sequence stratifraphy of the central and northern North Sea: tectonic development, sediment distribution and provenance area: Marine and Petroleum Geology, **12**, 845–879.

Judd, A. G., and M. Hovland, 1992, The evidence for shallow gas in marine sediments: Continental Shelf Research, **12**, 1081–1095.

Kirkwood, J., and H. Bethe, 1942, The pressure wave produced by an underwater explosion.: OSRD Report NO. 588.

Kjartansson, E., 1979, Constant Q - wave propagation and attenuation: Journal of geophysical research, **84**, 4737–4748.

Knopoff, L., 1964, Q: Reviews of geophysics, **2**, 625–660.

Kologinczak, J., 1974, Stagaray system improves primary pulse/bubble ratio in marine exploration: Offshore Technology Conference.

Kragh, E., E. Muyzert, T. Curtis, M. Svendsed, and D. Kapadia, 2010, Efficient broadband marine acquisition and processing for improved resolution and deep imaging: First

Break, **29**, 464–469.

Kuhlmann, G., and T. E. Wong, 2008, Pliocene Paleoenvironment evolution as interpreted from 3D-seismic data in the southern North Sea, Dutch offshore sector: Marine and Petroleum Geology, **25**, 173–189.

Kumar, R., H. Wason, and F. J. Herrmann, 2015, Source separation for simultaneous towed-streamer marine acquisition – a compressed sensing approach: Geophysics, **80**, WD73–WD88.

Landrø, M., 2001, Discrimination between pressure and fluid saturation changes from time–lapse seismic data: Geophysics, **66**, 836–844.

———, 2011, Seismic monitoring of an old underground blowout - 20 years later: First Break, **29**, 845–879.

———, 2014, A practical equation for air gun bubble time period including the effect of varying sea water temperature: 76^{th} EAGE Conference and exhibition, We P04–01.

Landrø, M., and L. Amundsen, 2010, Marine seismic sources part I: Geo ExPro, **7**.

———, 2014a, Is it optimal to tow air guns shallow to enhance low frequencies?: Geophysics, **79**, A13–A18.

———, 2014b, Maximizing the Ultra–low Frequency Output from Air Guns: 76^{th} EAGE Conference and exhibition, Tu ELI2 09.

Landrø, M., L. Amundsen, and D. barker, 2011, High-frequency signals from air-gun arrays: Geophysics, **76**, Q19–Q27.

Landrø, M., and K. E. Haavik, 2015, Discriminating between oil and gas exploiting the amplitude dimming at the rim.: SEG Technical Program Expanded Abstracts 2015, 648–1652.

Landrø, M., K. E. Haavik, and L. Amundsen, 2014, Using geophone components to obtain ultralow frequency seismic signals at long offsets: SEG Technical Program Expanded Abstracts 2014, 233–237.

Landrø, M., R. Mittet, and R. Sollie, 1993a, Implementing measured source signature in a course grid finite-difference modeling scheme: Geophysics, **59**, 1852–1850.

Landrø, M., Y. Ni, and L. Amundsen, 2016, Reducing high–frequency ghost cavitation signals from marine air-gun arrays: Geophysics, **81**, Accepted for publication.

Landrø, M., O. A. Solheim, E. Hilde, and L. K. Strønen, 1999, The Gullfaks 4D seismic study: Petroleum Geoscience, **5**, 213–226.

Landrø, M., and R. Sollie, 1992, Source signature determination by inversion: Geophysics, **57**, 1633–1640.

Landrø, M., S. Strandenes, and S. Vaage, 1991, Use of near–field measurements to compute far–field signatures – evaluation of the method: First Break, **9**, 375–385.

Landrø, M., G. Zaalberg–Metselaar, B. Owren, and S. Vaage, 1993b, Modeling of water-gun signatures: Geophysics, **58**, 101–109.

Langhammer, J., and P. Bennion, 2016, Triple-source simultaneous shooting a future for higher density seismic?: 74th Annual International Conference and Exhibition incorporating SPE EUROPEC, EAGE, Extended Abstracts.

Langseth, E., and M. Landrø, 2012, Time–Lapse 2D interpretation of gas migration in shallow sand layers - Compared to reservoir simulation: International Journal of Greenhouse Gas control, **10**, 389–396.

Laws, R., and E. Kragh, 2002, Rough seas and time–lapse seismic: Geophysical Prospecting, **50**, 195–208.

Laws, R., M. Landrø, and L. Amundsen, 1998, An experimental comparison of three direct methods of marine source signature estimation: Geophysical Prospecting, **46**, 353–389.

Lie, A., and D. O. Larsen, 1991, Monitoring of an underground flow in well 2/4-14 by shallow seismic data: Proceedings: The 2/4-14 Experience transfer seminar, Stavanger.

Linden, D. A., 1959, A discussion of sampling theorems: Proceedings of the IRE, 1219–1226.

Liu, Z., B. Wang, J. Specht, J. Sposato, and Y. Zhai, 2014, Enhanced adaptive subtraction method for simultaneous source separation: 84th Annual International Meeting, SEG, Expanded Abstracts, 115–119.

Lloyd, H., 1834, On a new case of interference of the rays of light: Transactions of the Royal Irish Academy, **17**, 171–177.

Loewenthal, D., S. S. Lee, and G. H. F. Gardner, 1985, Deterministic estimation of a wavelet using impedance type technique: Geophysical Prospecting, **33**, 956–969.

Long, D., C. Laban, T. D. J. Streiff, T. D. J. Cameron, and R. T. E. Schüttenhelm, 1988, The sedimentary record of climatic variation in the southern North Sea: Philosophical Transactions of the Royal Society of London, **318**, 523–537.

Løseth, H., M. Gading, and L. Wensaas, 2009, Hydrocarbon leakage interpreted on seismic data: Marine and Petroleum Geology, **26**, 1304–1319.

Mancini, F., K. Prindle, T. Ridsdill-Smith, and J. Moss, 2016, Full-waveform inversion as a game changer: Are we there yet?: The Leading Edge, **35**, 445–451.

Mavko, G., and T. Mukerji, 1998, Bounds on low-frequency seismic velocities in partially saturated rocks: Geophysics, **63**, 918–924.

Meier, M. A., R. E. Duren, K. T. Lewallen, J. Otero, S. Heiney, and T. Murray, 2015, A marine dipole source for low frequency seismic acquisition: 85th Annual International Meeting, SEG, Expanded Abstracts, 181–185.

Meissner, R., and E. Meixner, 1969, Deformation of seismic wavelets by thin layers and layered boundaries: Geophysical prospecting, **17**, 1–27.

Michelsen, O., 2001, Late Cenozoic basin development of the eastern North Sea Basin: Bulletin of the Geological Society of Denmark, **43**, 9–21.

Minneart, M., 1933, On musical air–bubbles and the sound of running water: Philosophical Magazine, **16**, 235–248.

Mittet, R., 1994, Implementation of the kirchhoff integral for elastic waves in staggered–grid modeling schemes: Geophysics, **59**, 1894–1901.

———, 2002, Free-surface boundary conditions for elastic staggered-grid modeling schemes: Geophysics, **67**, 1616–1623.

Mittet, R., and B. Arntsen, 2000, General source and receiver positions in coarse-grid finite-difference schemes: Journal of Seismic Exploration, **9**, 73–92.

Moldoveanu, N., 2000, Vertical source array in marine seismic exploration: 70th Annual International Meeting, SEG, Expanded Abstracts, 53–56.

Moldoveanu, N., N. Seymour, D. Manen, and P. Caprioli, 2012, Broadband Seismic Methods for Towed–streamer Acquisition: 74th Annual International Conference and Exhibition incorporating SPE EUROPEC, EAGE, Extended Abstracts, Z009.

Moore, I., B. Dragoset, T. Ommundsen, D. Wilson, C. Ward, and D. Eke, 2008, Simultaneous source separation using dithered sources: SEG Technical Program Expanded Abstracts 2008, 2806–2810.

Mora, P., 1987, Nonlinear two-dimensional elastic inversion of multioffset seismic data: Geophysics, **52**, 1211–1228.

Morse, P. M., and H. Feshbach, 1953, Methods of theoretical physics: McGraw-Hill.

Mueller, M. B., D. F. Halliday, D.-J. van Manen, and J. O. A. Robertsson, 2015, The benefit of encoded source sequences for simultaneous source separation: Geophysics, **80**, V133–V143.

Nelson, P. H., 1994, Permeability-porosity Relationships In Sedimentary Rocks: The Log Analysist. Society of Petrophysicists and Well-Log Analysts, **May**.

Nocedal, J., and S. J. Wright, 2006, Numerical optimization: Springer.

NPD Fact Pages, 2014, General information on exploration wellbores. Information extracted in july 2014.

Nyquist, H., 1926, Certain topics in telegraph transmission theory: Trans. AIEE, **47**, 617–644.

O'Brian, P. N. S., 1969, Some experiments concerning the primary seismic pulse: Geophysical prospecting, **17**, 511–547.

Ó Cofaigh, C., 1996, Tunnel valley genesis: Progress in Physical Geography, **20**, 1–19.

Oldenburg, D. W., and Y. Li, 2005, Inversion for applied geophyscis: A tutorial: Near-surface geophysics, SEG investigations in geophysics series No 13, editor Dwain Butler, **78**, 89–150.

Orji, O. C., W. Sollner, and L. J. Gelius, 2013, Sea surface reflection coefficient estimation: SEG Technical Program Expanded Abstracts, 51–55.

Ottesen, D., J. A. Dowdeswell, and T. Bugge, 2014, Morphology, sedimentary infill and depositional environments of the Early Quaternary North Sea basin (56° to 62°): Marine and Petroleum Geology, **56**, 123–146.

Ottesen, D., L. Rise, E. S. Andersen, T. Bugge, and T. Eidvin, 2009, Geological evolution of the Norwegian continental shelf between 61N and 68N during the last 3 million years: Norwegian Journal of Geology, **89**, 251–265.

Parkes, G., and S. Hegna, 2011, An acquisition system that extracts the earth response from seismic data: First Break, **29**, 81–87.

Parkes, G. E., A. Ziolkowski, L. Hatton, and T. Haugland, 1984, The signature of an air gun array: Computation from near-field measurements including interactions – practical considerations.: Geophysics, **48**, 105–110.

Parrack, A. L., 1974, Method of marine reflection-type seismic exploration: U.S. Patent,, **Patent No.: US 3979713 A**.

Pavey, G. M., and R. H. Pearson, 1966, Method and underwater streamer apparatus for improving the fidelity of recorded seismic signals: U.S. Patent,, **Patent No.: US 3290645 A**.

Pedersen, Åsmund S.., L. Amundsen, and J. O. A. Robertsson, 2016, Wavefield signal apparition, Part II - application to simultaneous sources and their separation: 78th Annual International Conference and Exhibition incorporating SPE EUROPEC, EAGE, Extended Abstracts.

Pekot, L. J., and G. A. Gersab, 1987, "Ekofisk": Geology of norwegian oil and gas fields north sea: Graham and Trotman Ltd., Edited by: Anthony Mansell Spencer.

Plesset, M. S., and A. Prosperetti, 1977, Bubble dynamics and cavitation: Annual Review Fluid Mechanics, **9**, 145–185.

Poole, T. L., A. Curtis, J. O. A. Robertsson, and D.-J. van Manen, 2010, Deconvolution imaging conditions and cross-talk suppression: Geophysics, **75**, W1–W12.

Posthumus, B. J., 1993, Deghosting using a twin streamer configuration: Geophysical Prospecting, **41**, 267–286.

Praeg, D., 2003, Seismic imaging of mid-Pleistocene tunnel-valleys in the North Sea Basin—high resolution from low frequencies: Journal of Applied Geophysics, **53**, 273–298.

Pramik, B., M. L. Bell, A. Grier, and A. Lindsay, 2015, Field testing the AquaVib: an alternate marine seismic source: 85th Annual International Meeting, SEG, Expanded Abstracts, 176–180.

Pratt, R. G., Z. M. Song, P. Williamson, and M. Warner, 1996, Two-dimensional velocity models from wide- angle seismic data by wavefield inversion: Geophysical Journal International, **124**, 323–340.

Raknes, E. B., and B. Arntsen, 2014, Time-lapse full-waveform inversion of limited-offset seismic data using a local migration regularization: Geophysics, **79**, WA117–WA128.

Raknes, E. B., B. Arntsen, and W. W. Weibull, 2015, Three-dimensional elastic full waveform inversion using seismic data from the sleipner area: Geophysical Journal International, **202**, 1877–1894.

Rattray, M., 1951, Pertubation effects on cavitation bubble dynamics: PhD thesis, California Institute of Technology.

Ray, H. C., and N. A. Moore, 1982, High resolution, marine seismic stratigraphic system: U.S. Patent,, **Patent No.: US 4353121 A**.

Rayleigh, L., 1917, On the pressure developed in a liquid during the collapse of a spherical cavity: Philosophical Magazine, **34**, 94–98.

Remen, A., 1991, Flow paths and shallow gas migration: Proceedings: The 2/4-14 Experience transfer seminar, Stavanger.

Rise, L., O. Olesen, K. Rokoengen, D. Ottesen, and F. Riis, 2004, Mid-Pleistocene ice drainage pattern in the Norwegian Channel imaged by 3D seismics: Quaternary Science Reviews, **23**, 2323–2335.

Rise, L., D. Ottesen, K. Berg, and E. Lundin, 2005, Large-scale development of the mid-Norwegian margin during the last 3 million years: Marine and Petroleum Geology, **22**, 33–44.

Robertsson, J. O. A., L. Amundsen, and Å. S. Pedersen, 2016a, Simultaneous source wavefield separation by signal apparition: Geophysical Journal International, **206**, 1301–1305.

———, 2016b, Wavefield signal apparition, Part I - theory: 74th Annual International Conference and Exhibition incorporating SPE EUROPEC, EAGE, Extended Abstracts.

Robertsson, J. O. A., L. Amundsen, Å. S. Pedersen, K. Eggenberger, F. Andersson, and D. van Manen, 2016c, Wavefield signal apparition: Simultaneous source separation:

SEG Technical Program Expanded Abstracts 2016.

Robertsson, J. O. A., and C. H. Chapman, 2000, An efficient method for calculating finite–difference seismograms after model alterations: Geophysics, **65**, 907–918.

Robertsson, J. O. A., D. Halliday, D. J. van Manen, I. Vasconcelos, R. Laws, K. Özdemir, and H. Grønaas, 2012, Full-wavefield, towed-marine seismic acquisition and applications: 74th Annual International Conference and Exhibition incorporating SPE EUROPEC, EAGE, Extended Abstracts, Z015.

Robertsson, J. O. A., I. Moore, M. Vassallo, K. Özdemir, D. van Manen, and A. Özbek, 2008a, On the use of multicomponent streamer recordings for reconstruction of pressure wavefields in the crossline direction: Geophysics, **73**, A45–A49.

Robertsson, J. O. A., D. van Manen, and R. Laws, 2008b, Seismic data acquisition and source-side derivatives generation and application: U.S. Patent 7,492,665 B2.

Rutherford, S. T., and R. H. Williams, 1989, Amplitude-versus-offset variations in gas sands: Geophysics, **54**, 680 – 688.

Sablon, R., T. Payen, H. Tonchia, R. Siliqi, X. Labarre, N. Salaun, and Y. L. Men, 2013, Ghost-free imaging combining synchronized multi-level source and variable-depth streamer.: SEG Technical Program Expanded Abstracts 2013, 72–76.

Sacchi, M. D., and T. J. Ulrych, 1995, High-resolution velocity gathers and offset space reconstruction: Geophysics, **60**, 1169–1177.

Salaun, N., V. Cavalie, P. Borisevitch, D. Hardouin, and A. W. (CGG), 2016, Enhanced 3d broadband processing - a case study from the edvard grieg field: 78th Annual International Conference and Exhibition incorporating SPE EUROPEC, EAGE, Extended Abstracts.

Sallisbury, R. S. K., M. R. Denley, and G. Douglas, 1996, The value of integrating existing 3D seismic into shallow gas studies: Proceedings: Offshore Technology Conference (OTC), Jouston Texas.

Sengupta, M., 2000, Integrating rock physics and flow simulation to reduce uncertainties in seismic reservoir monitoring: PhD thesis, Stanford University.

Sernpere, J. E., and P. B. Hardy, 1998, Reflection Tomography and Velocity Model Building in an Area Characterized by Shallow Gas: Proceedings: Offshore Technology Conference (OTC), Jouston Texas.

Shannon, C. E., 1949, Communication in the presence of noise: Proc. Institute of Radio Engineers, **37**, 10–21.

Shen, H.-L., T. Elboth, T. Gang, and L. Zhi, 2014, Modeling of multi-depth slanted airgun source for deghosting: Applied Geophysics, **11**, 405–417.

Sheriff, R., 1985, Aspects of seismic resolution: in: O.R. Berg, D.G. Woolverton (Eds.), Seismic Stratigraphy: II. An Integrated Approach to Hydrocarbon Exploration. AAPG memoir, **39**, 1–10.

Shuey, R. T., 1985, A simplification of the zöppritz equations: Geophysics, **50**, 609–614.

Sillis, G. C., and S. J. Wheeler, 1992, The significance of gas for offshore operations: Continental Shelf Research, **12**, 1239–1250.

Sirgue, L., and G. Pratt, 2004, Efficient waveform inversion and imaging: A strategy for selecting temporal frequencies: Geophysics, **69**, 231–248.

Smith, G. C., and P. M. Gidlow, 1987, Weighted stacking for rock property estimation and detection of gas: Geophysical Prospecting, **35**, 993–1014.

Sonneland, L., and L. E. Berg, 1985, A new method for separating wavefields in to up-and down-going components: Presented at the 47th EAEG Meeting, Budapest.

Sørensen, J. C., U. Gregersen, M. Breiner, and O. Michelsen, 1997, High-frequency sequence stratigraphy of the Upper Cenozoic deposits in the central and Southeastern North Sea areas: Marine and Petroleum Geology, **14**, 99–123.

Sørensen, J. C., and O. Michelsen, 1995, Upper Cenozoic Southeastern North Sea Basin: Bulletin of the Geological Society of Denmark, **43**, 74–98.

Soubaras, R., 2011, Method and device for processing seismic data: U.S. Patent,, **Patent No.: US 2011/0176384 A1**.

———, 2012, Pre-stack deghosting for variable-depth streamer data: SEG Technical Program Expanded Abstracts, 1–5.

Soubaras, R., and R. Dowle, 2010, Variabel-depth streamer - a broadband marine solution: First Break, **28**, 1328–1335.

Spitz, S., 1991, Seismic trace interpolation in the f-x domain: Geophysics, **56**, 785–794.

Spjeldnes, N., 1975, Palaeogeography and facies distribution in the Tertiary of Denmark and surrounding areas: Norges Geologiske Undersøkelse (NGU), **316**, 289–311.

Stewart, M. A., and L. Lonergan, 2011, Seven glacial cycles in the middle-late Pleistocene of northwest Europe: Geomorphic evidence from buried tunnel valleys: Geology, **39**, 283–286.

Stoker, M. S., and D. Long, 1984, A relict ice-scoured erosion surface in the Central North Sea: Marine Geology, **61**, 85–93.

Stoker, M. S., D. Praeg, B. O. Hjelstuen, J. S. Laberg, T. Nielsen, and P. M. Shannon, 2005, Neogene Stratigraphy and sedimentary and oceanographic development of the NW European Atlantic margin: Marine and Petroleum Geology, **22**, 977–1005.

Stoker, M. S., A. C. Skinner, J. A. Fyfe, and D. Long, 1983, Palaeomagnetic evidence for early Pleistocene in the central and northern North Sea: Nature, **304**, 332–334.

Strandenes, S., and S. Vaage, 1992, Signatures from clustered airguns: First Break, **19**, 305–312.

Stuart, J. Y., and M. Huuse, 2012, 3D seismic geomorphology of a large Plio-Pleistocene delta - Bright spots and contourites in the Southern North Sea: Marine and Petroleum Geology, **38**, 85–93.

Syvetski, J. P. M., A. B. Andrews, and J. D. Milliman, 1992, Icebergs and the seafloor East Greenland (Kangerlussuaq) Continental Margin: Arctic, Antarctic and Alpine Research, **3**, 52–61.

Tarantola, A., 1984, Inversion of seismic reflection data in the acoustic approximation: Geophysics, **49**, 1259–1266.

Telling, R., S. Denny, S. Grion, and R. G. Williams, 2014, Evaluation of a marine broadband slanted source: SEG Technical Program Expanded Abstracts, 62–76.

ten Kroode, F., S. Bergler, C. Corsten, J. W. de Maag, F. Strijbos, and H. Tijhof, 2013, Broadband seismic data — the importance of low frequencies: Geophysics, **78**, WA3–WA14.

Tenghamn, R., 2006, An electrical marine vibrator with a flextensional shell: Exploration Geophysics, **37**, 286–291.

Tenghamn, R., S. Vaage, and C. Borresen, 2007, A dual sensor towed marine streamer: Its viable implementation and initial results: SEG Technical Program Expanded Abstracts 2007, 989–993.

Tikhonov, A. V., and V. Y. Arsenin, 1977, Solution of ill-posed problems: John Wiley and Sons, Inc.

Tsingas, C., Y. S. Kim, and J. Yoo, 2016, Broadband acquisition, deblending, and imaging employing dispersed source arrays: The Leading Edge, **35**, 354—-360.

Vaage, S., K. Haugland, and T. Utheim, 1983, Signatures from single airguns: Geophysical Prospecting, **31**, 87–97.

Vaage, S., and B. Ursin, 1987, Computation of signatures of linear air gun arrays: Geophysical prospecting, **35**, 281–287.

Vaage, S. T., S. T. Tengham, and C. N. Borresen, 2008, System for combining signals of pressure signals and partical motion sensors in marine seismic streamers.: U.S. Patent,, **Patent NO.: US7359283 B2**.

van Melle, F. A., and K. R. . Weathernurm, 1953, Ghost reflections caused by energy initially reflected above the level of the shot: Geophysics, **18**, 793–804.

Virieux, J., 1986, P-SV wave propagation in heterogeneous media: Velocity-stress finite-difference method: Geophysics, **51**, 889–901.

Virieux, J., and S. Operto, 2009, An overview of full-waveform inversion in exploration geophysics: Geophysics, **74**, WCC1–WCC26.

Voinov, O. V., and V. V. Voinov, 1975, Numerical method of calculating nonstationary motions of an ideal incompressible fluid with free surfaces: Soviet Physics Doklady, **20**, 179.

Wang, P., K. Nimsaila, D. Zhuang, Z. Fu, H. Shen, G. Poole, and N. Chazaloel, 2015, Joint 3d source-side deghosting and designature for modern air-gun arrays: 77^{th} EAGE Conference and exhibition, Th N103 10.

Wang, P., and C. Peng, 2012, Premigration deghosting for marine towed streamer data using a bootstrap approach: 82nd Annual International Meeting, SEG, Expanded Abstracts, 1–5.

Wang, P., S. Ray, C. Peng, and Y. Li, 2013, Premigration deghosting for marine streamer data using a bootstrap approach in tau-p domain: 75^{th} EAGE Conference and exhibition, Th 08 13.

Wang, Q. X., K. S. Yeo, B. C. Khoo, and K. Y. Lam, 1996, Strong Interaction Between a Buoyancy Bubble and a Free Surface: Theoretical and Computational Fluid Dynamics, **8**, 73–88.

Warner, M., I. Stekl, and A. Umpleby, 2008, Efficient and effective 3D wavefield tomography: 70th European Association of Geoscientists and Engineers Annual Conference, 1059–1063.

Widess, M. B., 1953, How thin is a thin bed?: Geophysics, **38**, 1176–1180.

Williams, R. G., and J. Pollatos, 2012, Signal to noise – the key to increased marine seismic bandwidth: First Break, **30**, 101–105.

Willis, H., 1941, Underwater explosions, time interval between successive explosions.: Technical report, British report.

Wood, L. C., R. C. Heiser, S. Treitel, and P. L. Riley, 1978, The debubbling of marine source signatures: Geophysics, **43**, 715–729.

Woodworth-Lynas, C. M. T., H. W. Josenhans, J. V. Barrie, C. F. M. Lewis, and D. R. Parrott, 1991, The physical processes of seabed disturbance during iceberg grounding and scouring: Continental Shelf Research, **11**, 939—961.

Wu, W.-J., L. R. Linest, and H.-X. Lut, 1996, Analysis of higher-order, finite-difference schemes in 3D reverse-time migration: Geophysics, **61**, 845–856.

Yu, S., J. Ma, X. Zhang, and M. D. Sacchi, 2015, Interpolation and denoising of high-dimensional seismic data by learning a tight frame.: Geophysics, **80**, V119–V132.

Zhan, C., R. Malik, J. Specht, Z. Liu, and D. Teixeira, 2015, Deblending of continuously recorded OBN data by subtraction integrated with a median filter: 85th Annual International Meeting, SEG, Expanded Abstracts, 4673–4678.

Zhen, Q., L. Minghui, Z. Xiadong, Y. Yao, Z. Cai, and S. Jianyong, 2009, The implementation of an improved NPML absorbing boundary condition for elastic wave modeling: Applied Geophysics, **6**, 113–121.

Zhou, Z., M. Cvetkovic, B. Xu, and P. Fontana, 2012, Analysis of a broadband processing technology applicable to conventional streamer data: 74th Annual International Conference and Exhibition incorporating SPE EUROPEC, EAGE, Extended Abstracts, I06.

Ziegler, P. A., 1988, Evolution of the Arctic-North Atlantic and the Western Tethys: AAPG Memoir, **43**.

———, 1990, Geological Atlas of Western and Central Europe: Geological Society of London.

Ziolkowski, A., 1970, A method for calculating the output pressure waveform from an air gun: Geophysical Journal of the Royal Astronomical Society, **21**, 137–161.

———, 1993, Determination of the signature of a dynamite source using source scaling, part 1: Theory: Geophysics, **58**, 1174–1182.

Ziolkowski, A., and K. N. Bokhorts, 1993, Determination of the signature of a dynamite source using source scaling, part 2: Experiment: Geophysics, **58**, 1183–1194.

Ziolkowski, A., L. E. Lerwill, D. W. March, and L. Peardon, 1980, Wavelet deconvolution using a source scaling law: Geophysical prospecting, **28**, 872–901.

Ziolkowski, A., G. E. Parkes, L. Hatton, and T. Haugland, 1982, The signature of an air gun array: Computation from near–field measurements including interactions: Geophysics, **47**, 1413–1421.

———, 1998, Measurement of air-gun bubble oscillations: Geophysics, **63**, 2009–2024.

Ziolkowski, A. M., 1986, The scaling airgun array, including depth dependence and interaction: Geophysical prospecting, **34**, 383–408.

Zöppritz, K., 1919, Earthquake waves VII VIIb. About reflection and passage of seismic waves on surfaces of discontinuity: Göttinger Nachrichten (Royal Society of Sciences in Göttingen), **1**, 66–84.